

# **IMPLEMENTATION OF LASER ABLATION COATING REMOVAL TECHNIQUE FOR STEEL COMPONENTS ON VDOT BRIDGES**

---

A Thesis

Presented to

The Faculty of the School of Engineering and Applied Science

University of Virginia

---

In Partial Fulfillment

Of the Requirements for the Degree

Master of Science in Material Science and Engineering

By,

William Polk Moffat

August, 2019

# APPROVAL SHEET

This Thesis  
is submitted in partial fulfillment of the requirements  
for the degree of  
Master of Science

Author Signature: William Moffat

This Thesis has been read and approved by the examining committee:

Advisor: James M. Fitz-Gerald

Committee Member: Sean R. Agnew

Committee Member: Leonid V. Zhigilei

Committee Member: \_\_\_\_\_

Committee Member: \_\_\_\_\_

Committee Member: \_\_\_\_\_

Accepted for the School of Engineering and Applied Science:



Craig H. Benson, School of Engineering and Applied Science

August 2019

# Table of Contents

## Chapter 1 Introduction

1.1 Motivation.....	1
1.2 Industrial and Commercial Uses of LACR.....	3
1.3 Thesis Layout.....	10

## Chapter 2 Laser Material Interactions.....13

2.1 Introduction.....	13
2.2 Laser Ablation.....	14
2.3 Laser Cleaning.....	23

## Chapter 3 Experimental Setup.....34

3.1 Introduction.....	34
3.2 LACR Phase I: Laboratory Demonstration.....	34
3.3 LACR Phase II: Field Demonstration.....	37
3.4 LACR Phase III: Cleaning Tight Geometry Demonstration.....	40
3.5 LACR Phase IV: Testing for Lead Abatement.....	45
3.6 Preparation of Metallurgical Samples for Analysis .....	49
3.7 Coating Adhesion Testing.....	52
3.8 Mechanical Testing.....	54

## Chapter 4 Results.....56

4.1 Introduction.....	56
4.2 General Coating Removal Observations.....	57
4.3 Phase I Industrial Hygiene.....	59
4.4 Planar Surface Analysis.....	62
4.5 Cross Section Analysis.....	71
4.6 Microstructure.....	76
4.7 SEM and EDS Paint Composition Analysis.....	80
4.8 XRF and XRD Analysis of LACR Surfaces.....	94
4.9 Phase IV: LACR Testing for Lead Abatement.....	97

4.10 Coating Adhesion Testing.....	102
4.11 Surface Roughness.....	103
4.12 Mechanical Testing.....	104
Chapter 5 Discussion.....	113
5.1 Introduction.....	114
5.2 EI Group Industrial Hygiene.....	114
5.3 Laser Cleaning of Lead Paint.....	119
5.4 LACR Surface Analysis.....	122
5.5 LACR Cross Section Analysis.....	127
5.6 Coating Adhesion Analysis.....	135
5.7 Fatigue Testing.....	141
Chapter 6 Conclusions and Future Work.....	150
6.1 Conclusions.....	150
6.2 Future Work.....	153
Appendix A.....	155
Appendix B.....	164
References.....	168

## Abstract

One of the most common methods to mitigate corrosion of metallic structures is the application of paint coatings. However, with time and weathering, coatings deteriorate and require ongoing maintenance to ensure that they provide the necessary protection for the underlying metallic substrate. At the present, the Virginia Department of Transportation (VDOT) utilizes grit blasting to remove old coatings and provide a fresh surface for the reapplication of new coatings. This procedure is expensive due to containment structures such as tarps and scaffolding, traffic management, and physical load on the workers. In addition, the current process generates hazardous waste that is difficult to contain and remove. A relatively new technique termed *Laser Ablation Coating Removal (LACR)* has been developed that combines a hand-held laser ablation system with a high efficiency multi-filtration vacuum system. The LACR process incorporates a high-power pulsed laser operating in the near IR ( $\lambda=1064$  nm, pulse width 83 ns), and a multi-stage HEPA filtration system that provides the ability to remove coatings while reducing containment needs, meeting industrial hygiene safety requirements, along with a compact, confined modular filter disposable system.

The goal of this project was to evaluate if the use of LACR would provide VDOT with an acceptable new alternative for removing existing coatings. In this study, the LACR coating removal process was documented both in the laboratory and in the field for the feasibility of implementing this process on specific areas of VDOT bridges. There were two outstanding questions to be answered: first, whether VDOT could effectively implement LACR technology in coating removal operations on bridges, and second, to identify any additional coating removal techniques that VDOT should evaluate. To meet the goals of the research conducted here, the study was divided into four phases in collaboration with the Virginia Transportation Research Center (VTRC) and VDOT. The environmental and industrial hygiene requirements in Phases 1 and 2 were used to establish the viability of using LACR by VDOT. Each of the subsequent phases was then used to address questions and further develop LACR as a method for removing coatings from VDOT structures.

The Phase 1 study consisted of LACR processing that was performed in a controlled lab environment to remove lead-based paint and rust from heavily weathered I-beam sections made of A36 steel (ASTM A36 Standard Specification for Carbon Structural Steel). The sections were taken from a decommissioned bridge structure in the VDOT Lynchburg District. The bridge was put in service in the 1920s, prior to the implementation of grit blasting, and a layer of iron oxide (mill scale) was present below three layers of paint. Two comparison samples were also processed using the incumbent method of grit blasting. The Phase 2 study included an on-site (field) demonstration where LACR was evaluated on an in-service bridge structure in the VDOT Lynchburg District (off of Route 460 in Farmville, VA). In the Phase 3 study, sections of a bridge bearing were processed by LACR to determine whether the current system was capable of cleaning the surfaces of recessed areas of the bridge beam.

Results from electron and optical microscopy showed that LACR effectively removed multiple layers of paint and elemental hazards, including lead. I-beam cross sections showed that regions of the underlying mill scale layer (iron oxide) ranging from 20 to 100  $\mu\text{m}$  in thickness remained

on the surface with morphological evidence of melting and a solidification region on the order of 1  $\mu\text{m}$  in depth. Hardness measurements and tensile testing of the base metal, grit blasted, and laser cleaned samples showed that LACR has no detrimental effects on the surface or on the mechanical properties of laser cleaned bridge steel. Base metal and laser cleaned samples showed virtually no change in microhardness, both averaging about 139 HV from the surface through to the bulk of the steel. Tensile testing showed that both the yield and ultimate tensile strengths of base, grit blasted, and laser cleaned metal were 281 MPa and 440 MPa respectively, all on parity with that of ASTM A36 structural steel. Furthermore, fatigue testing of LACR samples shows no statistical difference in fatigue behavior from that of the base metal, with an endurance limit measured within the range of 300 MPa for laser cleaned steel, versus 269 MPa based on repeated loading conditions of base metal found in literature. Surface roughness was performed on LACR and grit blasted samples. Roughness values recorded parallel and perpendicular to the laser beam orientation averaged 5.26 and 5.41  $\mu\text{m}$  arithmetic average roughness,  $R_a$ . In comparison the grit blasted samples exhibited a  $R_a$  average surface roughness of 9.86  $\mu\text{m}$ . Pull-off adhesion testing on repainted LACR surfaces showed that there was little variation between the repainted samples following LACR or grit blasting, with average pull-off strengths of 1800 psi. After the cyclic testing, the majority of the pull-off failure occurred due to cohesion failure of the coating film. It is worth noting that the surface cleaning methods do not seem to affect the adhesion strength differently from each other. Based on this work, it was concluded that there was little variation in the adhesion strength between the two surface cleaning methods.

Industrial hygiene surveys conducted both remotely and in-person showed that no heavy metals or volatile organic compounds (VOCs) were detected during LACR. Lead levels were recorded to be at 0.0043  $\text{mg}/\text{m}^3$  for one laser operator and 0.0014  $\text{mg}/\text{m}^3$  for the other operator, both of which were well below the occupational safety and health administration (OSHA) action level (AL) of 0.03  $\text{mg}/\text{m}^3$ .

Metallurgical characterization was performed using optical microscopy, scanning electron microscopy (SEM), energy dispersive spectroscopy (EDS), x-ray fluorescence (XRF), and x-ray diffraction (XRD). Adhesion testing was performed with a pneumatic adhesion tensile testing instrument (PATTI) tester. Surface roughness was measured by mechanical profilometry using a Mitutoyo mechanical stylus. Tensile and fatigue testing was performed on a 22 kip Instron loadframe under pull-pull fatigue conditions of  $R = 0.1$  and at 10 Hz.

## **Acknowledgments**

First and foremost, I would like to thank my advisor, Professor Fitz-Gerald, for his continuous support and patience as I've worked my way through graduate school here at UVa. I can always count on him being available to talk to about research or anything else. In addition, I would like to thank Professor Agnew for his insights and contributions on discussing data throughout the project. I also would like to thank Md. Shamsujjoha, "Joha", for all his help with experiments and the knowledge and experience he has had to offer from his own research.

Steve Sharp has also had a large impact on this project, not only providing funding through VTRC but also through the contributions he brought from a VDOT perspective. Bill Ordell, also at VTRC, has helped immensely by showing me how to operate the mechanical testing frame.

I would like to thank Libby, Cecilia, Brian, and Mike Melia, Jonathan Skelton, and John Xia from the Fitz-Gerald lab.

Lastly, and most important of all, I would like to thank my family for always encouraging and supporting me to be the best that I can be.



# Chapter 1 Introduction

## 1.1 Motivation

One of the most common methods of preventing corrosion of steel bridge components is with the use of polymeric coatings. This is an effective corrosion mitigation technique, however with time, coatings require maintenance in order to effectively protect the underlying steel, as weathering and exposure can slowly deteriorate these coating systems and leave the steel vulnerable to corrosion. This can be seen near the ends of some bridge beams where excessive corrosion damage has occurred due to leaking deck joints resulting in frequent salt exposure. (Figure 1.1)<sup>[1]</sup>.



*Figure 1.1. Photographs showing beam end corrosion damage due to routine salt exposure. <sup>1</sup>*

In consideration of coating repairs, determining the optimal method for maintaining the coating system and protecting the structural steel can be complex and costly. This involves ensuring that the surface is prepared properly, as well as determining that the coating will adhere to the substrate, which is key for mitigating corrosion damage, (Figure 1.2)<sup>1</sup>. In addition, coating work in the field must meet worker field safety regulations as well as ensure environmental compliance through the proper containment of all materials (Figure 1.3)<sup>1</sup>.



*Figure 1.2. A bridge showing coating detachment due to weathering and exposure of bridge I-beams, highlighting the importance of coating adhesion.<sup>1</sup>*



*Figure 1.3. An example of bridge containment set up during a de-coating operation, which increases maintenance costs due to the time, materials, and labor required for assembly.<sup>1</sup>*

The Virginia Department of Transportation (VDOT) spends millions of dollars every year on bridge maintenance throughout the state, with bridge coating maintenance accounting for approximately 10% of this annual cost.<sup>2</sup> These costs include mobilization, traffic control, environmental protection, painting, and waste disposal. In order to reduce these maintenance costs, VDOT can reduce labor costs, improve capture efficiency of environmental contaminants, and reduce the amount of waste material that requires disposal.<sup>1</sup>

This project is aimed to evaluate the impact of laser ablation coating removal (LACR) during paint stripping of bridge components. The two main aspects of interest to VDOT are worker health and environmental safety, and the effects of LACR on the underlying substrate. These two points of interest were investigated with the latter focused on metallurgical investigations.<sup>1</sup>

## **1.2 Industrial and Commercial uses of LACR Technology**

Recently, laser cleaning has gained in popularity and use as a viable alternative to conventional cleaning methods such as sand or grit blasting, chemical stripping, or power sanding. Due to its advantages including smaller amounts of waste generation, more cost effective use, and selective coating removal, laser coating removal is becoming the method of choice for certain surface de-coating applications. Ranging in applications from art and sculpture cleaning and refurbishing<sup>3-9</sup>, paint and graffiti removal<sup>10</sup>, nuclear decontamination<sup>11</sup>, rust removal<sup>12-14</sup>, and coating removal on both aerospace<sup>15,16</sup> and marine structures<sup>17-19</sup>, laser ablation coating removal has found uses in a wide range of fields.

For example, the U.S. Navy has found laser cleaning applications for submerged ship surfaces, as well as dry parts of decking and ship superstructure, and even for such niche applications as cleaning test torpedoes. (Figure 1.4)<sup>20</sup>.

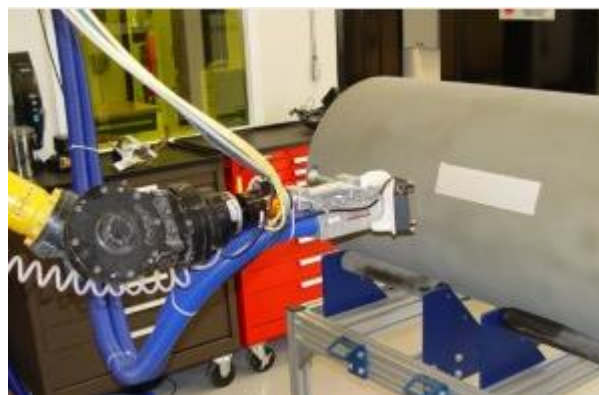


*Figure 1.4. Lasertronics laser system in use by the US Naval Undersea Warfare Center, Keyport, WA, for cleaning test torpedoes.<sup>20</sup>*

In commercial civilian settings laser cleaning has found uses in cleaning building facades, exteriors, and even sculptures and ornaments. The Philadelphia City Hall<sup>21</sup>, US Capitol Building (Figure 1.5)<sup>22</sup>, and Canadian Parliament building<sup>23</sup> are examples of prominent landmarks that have been successfully cleaned using LACR technology.

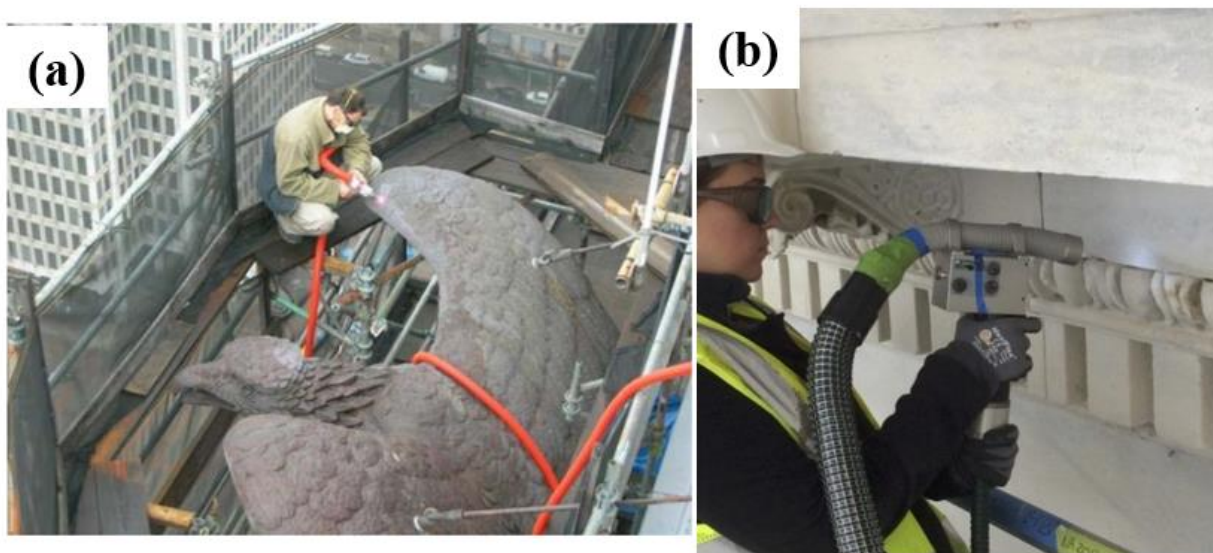


*Figure 1.5. (a) Laser surface cleaning of bronze statuary on the Philadelphia City Hall. (b) Laser cleaning exterior marble on the U.S. Capitol Building in Washington, D.C.<sup>21,22</sup>*

Aside from the U.S. Navy, another military branch that has had success with laser coating removal is the Air Force. The Air Force Research Lab (AFRL) has used a sequence of research phases throughout a Laser Coatings Removal Program to validate the efficacy and upgrade the sophistication of different laser cleaning methods on airplane parts. The goal of this program was to replace traditional methods such as sand or grit blasting, chemical paint removal, or power sanding (Figure 1.6)<sup>16</sup>, with laser coating removal which provides all the benefits mentioned earlier. This project at AFRL was split into three phases, each designed to test a different aspect pertaining to the implementation of LACR.



*Figure 1.6. Power sanding a paint coating from an off aircraft component. <sup>16</sup>*

AFRL Phase I of this project involved the use of a low power, light-weight, hand held laser system to clean aerospace parts, as shown in Figure 1.7<sup>16</sup>. AFRL was able to determine that this provided a cost effective, safety compliant, and selective stripping of the coating system that was environmentally friendly and increased the facility capacity.



*Figure 1.7. Hand held laser system used in phase 1 of the laser coatings removal program at AFRL<sup>16</sup>*

In addition, they were able to determine that there was no damage dealt to the substrate. Evaluated using 40, 120, and 500 W Nd:YAG and 250 W CO<sub>2</sub> handheld lasers, the system adequately removed paint from small areas and in nitpicking operations at a speed of about 14 in<sup>2</sup>/min. On clad aluminum substrates there was no penetration into the cladding, and no excessive surface roughness was noted. The adhesion properties were not adversely affected to the point of eliminating any of the lasers from consideration. Fatigue and tensile test results were similar to

published results from other stripping methods, as detrimental effects caused by laser stripping were no greater than those experienced using other stripping methods. Because of the success of this method several Air Force depots and the US coast guard have transitioned to handheld laser units. AFRL then proceeded to Phase II, employing robotic laser coating removal systems for large area off-aircraft coating removal.

AFRL Phase II involved developing a robotic laser coating removal system (RLCRS) to replace chemical and mechanical coating removal methods used on large off-equipment components. The major benefits of completing this phase included reducing the stripping time, therefore increasing production, as well as allowing for the replacement of chemical strippers such as MEK (methyl ethyl ketone), PMB (*p*-methoxybenzyl), and wheat starch. Figure 1.8<sup>16</sup> shows an image of the RLCRS system used in this phase of the study, and table 1.1<sup>16</sup> shows some of the consistent laser parameters that were used.



*Figure 1.8. The robotic laser coating removal system (RLCRS) that was used for phase 2 of the AFRL's laser coatings removal program. <sup>16</sup>*

This phase of the AFRL program used condemned parts from a KC-135 aircraft, and processing took place from March 3-6 2008. The parts were processed using a consistent set of parameters shown in table 1.1.

**Table 1.1: The laser parameters used in phase 2 of the AFRL project <sup>16</sup>**

<b>Units Measured</b>	<b>Value</b>
Laser Power(W)	6000
Laser power at Surface (W)	4500
Focused Spot Size (mm <sup>2</sup> )	4.4
Irradiance (kW/cm <sup>2</sup> )	102.3
Scan Rate (m/s)	7
Scan Width (mm)	127
Stand-Off (mm)	500
Sweep Rate (in/s)	2.75
Path Overlap (in)	0.125

Upon the completion of phase II the design and construction of RLCRS was successful and material testing demonstrated the safe use of RLCRS technology. Table 1.2<sup>16</sup> shows a comparison between the annual costs of the conventional chemical stripping method and for the use of the RLCRS, and it can be seen that there has been a decrease in every category after the implementation of RLCRS. There has since been interest from other facilities and services in acquiring robotic laser coating removal capabilities, and based on these positive results the Ogden Air Logistics Complex in Utah has commissioned the design and construction of an RLCRS for their facility.

**Table 1.2: The Cost Difference Comparison Between the Chemical Stripping Coating Removal Technique of the AFRL Program and the use of RLCRS <sup>16</sup>**

<b>Category</b>	<b>Annual Costs for Chemical Strip</b>	<b>Annual Costs for RLCRS</b>
Materials	\$114,000	\$20,410
Utilities	\$4,300	\$2,500
Waste	\$60,120	\$130
EHS	\$8,000	\$3,380
Labor (burdened rate)	\$9,560,260	\$2,180,300

Phase III of the AFRL program sought out to replace the laser automated de-coating system (LADS) with an Advanced Robotic Laser Coating Removal System (ARLCRS). The requirements of this advanced system include the ability to strip A-10, F-16 and C-130 radomes and other various candidate off-aircraft parts, and to integrate contour following robotics in order to maintain accurate stand-off and focal length distances. This required a turntable and robotic track system to access most part areas, and this all needed to be done with commercially available and production proven laser components. Phase III was more involved because it required robotic system design and construction which necessitated a robotics and integration company, evaluating a preliminary design, making modifications, finalizing them, and then performing testing and debugging before it could actually be implemented to compare it's performance against baseline data. For this application a high quality CO<sub>2</sub> laser was selected with an average output of 8kW of power. The robot system operated with no part specific programming and a bank of seven laser distance sensors that detect changes in part geometry. An advanced control logic dynamically adjusts input from sensors and adapts robot trajectory to maintain stand-off distance and perpendicularity to the part surface. Figure 1.9<sup>16</sup> shows an image of the system in use while laser cleaning an off aircraft component.

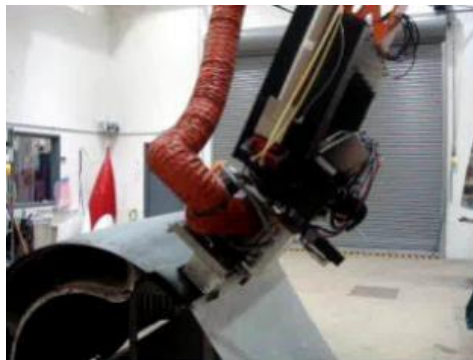


*Figure 1.9. The laser automated de-coating system (LADS) with the ARLCRS system removing paint from an off aircraft component. (AFRL)<sup>16</sup>*

The ARLCRS system began operation stripping F-16 radomes in April 2009, and improved stripping time from 4+ hours to strip an F-16 radome to about half an hour. Figure 1.10<sup>23</sup> shows the system in use on an F-16 radome.



*Figure 1.10. Laser cleaning of an F-16 radome using the LADS system. (AFRL)<sup>16</sup>*

ARLCRS provides a flexible platform for large-area coatings removal in which multiple geometries may be processed. The system was successfully transitioned to an Air Force depot, and is currently depainting F-16 Radomes with expected savings of over \$300,000 per year versus the RLCRS system, according to the AFRL. Table 1.3<sup>16</sup> summarizes the savings provided by the LADS and LADS II robotic laser cleaning systems. The Air Force has since been conducting testing and evaluation with other weapons system programs offices and engineering authorities to approve other components for this de-painting process. As of 2009 application is expanding to working with A-10 and F-22, B-2, and C-130 planes.

**Table 1.3: Comparison between the LADS and LADS II Robotic Laser Cleaning Systems, and Estimated Cost Savings<sup>16</sup>**

	<b>LADS</b>	<b>LADS II</b>	<b>Estimated Comparisons</b>
<b>Power Output</b>	6 kW pulsed	8 kW cont	Efficiency: 30-40% vs. 50-60%
<b>Power Consumption</b>	100 kW	77 kW	\$4,000 per year
<b>Annual Gas consumption (cylinders N, CO<sub>2</sub>, He)</b>	1435	2-3	\$ 71,000 per year
<b>Annual Maintenance Cost</b>	\$250 k/year	\$50 k/year	\$200,000 per year
<b>F-16 Radome Strip time</b>	5-6 man hrs	30-45 min	\$56,000 per year Or \$190,000 per year vs. chem. stripping
<b>Total savings for F-16 Radomes</b>	N/A	N/A	\$ 330,000 per year vs. LADS

Continuing with this trend of moving to laser paint stripping from conventional methods such as sand, grit blasting, or chemical stripping, VDOT has become interested in the possibility of using this technology for bridge de-coating operations. Despite all the advantages of this technology, it must be tested in a controlled manner before being adopted into full use. This testing includes industrial hygiene analysis in order to determine the environmental soundness and worker safety of the process, as well as metallurgical investigations of the laser cleaned substrate in order to ensure no damage is dealt to the substrate by the laser-solid interactions. These are the two main aspects studied in this work.

### **1.3 Research and Thesis Layout**

The proposed research in this project was divided and implemented in a series of four phases. Phase 1 consisted of laser cleaning painted bridge I-beam sections made of A36 steel (ASTM A36 Standard Specification for Carbon Structural Steel) removed from a decommissioned bridge structure in southern Virginia. Samples prepared from a traditional method, such as grit blasting,

were also produced and studied. Both the grit blasting and laser cleaning operations took place at Norton Sandblasting, located in Chesapeake Virginia. The operation was documented and recorded in addition to environmental hygiene data that was collected.

Phase 2 included an onsite field demonstration where LACR was tested on a standing bridge structure in Farmville, Virginia. Again an environmental hygiene survey was in place and the entire operation was documented and recorded.

In Phase 3 sections of a bridge bearing were transported to Norton Sandblasting, and another LACR test was performed. The purpose of this test was to determine whether the Adapt CL1000 Watt laser was capable of cleaning the surfaces of recessed areas of the bridge beam, which were at first difficult to reach in the field testing performed in Phase 2.

Phase 4 consisted of using the CL1000 laser system to test the effectiveness of lead removal from steel surfaces. In this phase VDOT employees performed the laser cleaning at the Norton Sandblasting location while various industrial hygiene tests were recorded. After the onsite lead removal operation using the CleanLaser system took place, pieces of the cleaned steel beams were transported to the University of Virginia where further laboratory analysis was conducted to measure the lead levels remaining on the surface.

Aside from the physical LACR demonstrations performed and material testing and characterization, a background literature review was conducted to investigate previous implementations of LACR and where it has been used successfully for industrial and popular use. This literature review also includes explanations of laser-solid interactions and laser based paint and rust removal. This background information and literature review is included in chapter 2.

Chapter 3, Experimental Setup, details the setups and experiments that were used throughout the project, both for LACR demonstrations in Phases I, II, and III, as well as material preparation for testing and characterization of LACR samples.

The Results are presented in Chapter 4, focused on the material characterization and testing performed at UVA. This includes results from surface and cross sectional analysis of LACR processed, grit blasted, and base material, as well as coating adhesion testing, roughness measurements, and mechanical testing. In addition to sample testing and characterization, general observations made during LACR demonstrations and results of the industrial hygiene survey from phase I are presented as here. This chapter also summarizes the industrial hygiene results from Phase IV, the testing for lead abatement completed by VDOT, as well as the laboratory analysis performed on the samples at the University of Virginia.

Chapter 5 discusses the results shown in the previous chapter. The discussion focuses on the state of the laser cleaned surface, and how laser processing results in the observed surface condition, in contrast to the grit blasted condition. The results of mechanical testing are discussed in detail, focusing on fatigue testing results and how the laser cleaning has any effect, if any at all, on the mechanical behavior of the steel. The details of how the industrial hygiene survey was conducted in Phase I are also discussed.

Chapter 6, Conclusions and Future Work, summarizes what was investigated and concluded from the research in this project, and future steps toward the study and implementation of LACR are also discussed. These include alternative methods to coating removal such as induction coating removal, as well as alternative laser systems that may offer superior performance compared to the laser systems tested thus far in the project.

## Chapter 2 Laser Material Interactions

### 2.1 Introduction

The process of laser cleaning is based on several complex mechanisms, including laser ablation, photodecomposition, and mechanical effects such as surface vibrations due to the impact of laser pulses. Laser ablation uses high energy pulses that are directed at a target to eject the surface layers of material. The processes contributing to laser ablation are complicated and can involve many different physical and chemical phenomenon at the same time. The effects of laser ablation can broadly be separated into three main categories; photothermal, where the heat generated by the laser pulse within the material dominates the interaction; photochemical, (photolytic), in which chemical processes dominate; and photophysical, in which both mechanisms are significant to the laser material interaction.<sup>24, 25</sup>

These terms depend on the process and mechanisms by which the laser light is absorbed by the material, which in turn depends on the characteristics of both the laser light as well as the type of material undergoing laser irradiation. Generally, photons will couple with the electronic states available in the material depending on the photon wavelength and will cause excitation of the electrons to higher energy levels. These higher energy electrons can then transfer energy to lattice vibrations, causing the material to heat up.

Whether a given material undergoes photothermal, photochemical, or a photophysical mechanism depends on the process of thermalization, or the material reaching thermal equilibrium after undergoing laser irradiation. To describe the thermalization process, a relaxation time,  $\tau_T$ , is used. The thermalization process includes the relaxation of the excited electron states back to ground energy levels by various mechanisms. The relative laser-induced excitation rate compared to the thermalization rate determines which absorption mechanism takes place.

The time it takes for materials to thermalize depends on the specific material and its electronic structure. For metals which contain many free electrons, thermalization is on the order of  $10^{-12}$  to  $10^{-10}$  seconds, whereas in non-metals without free electrons thermalization can slow to as much as  $10^{-6}$  seconds. When the laser-induced excitation rate is much lower than the thermalization rate, the details of the transient excited electron states are insignificant and the absorbed laser energy can be treated as being directly converting to heat. This case describes a purely photothermal process, and the material response is an increase in thermal energy. Conversely, if the laser excitation rate is high compared to the thermalization rate, many excited states can build up, leading to the direct breaking of chemical bonds, corresponding to photochemical processing. In purely photochemical processing, the temperature of the system remains relatively unchanged.

Despite the relatively well understood thermal character and photon driven reactions of photothermal and photochemical processes in general, laser processing can still be quite different from conventional heat sources and light sources in the case of photochemical reactions. This is largely due to the fact that laser driven processes can be localized in both space and time. Using lasers, small volumes of material can be imparted large amounts of energy in a short amount of time and thus the temperature can increase rapidly. This aspect is used in the application of laser cleaning, where the rapid rise of temperature causes the quick thermal expansion of the material, and in some cases vaporization and formation of plasma, forcing this region to separate, or ablate, from the bulk.<sup>24</sup>

## **2.2 Laser Ablation**

Laser ablation can be viewed as a mechanical process, in which the rapidly applied heat can cause thermal expansion and propagation of a pressure shockwave, which when applied effectively can be implemented in the removal of coatings. The laser ablation process can be schematically

represented as the rapid heating of the surface layers of the material undergoing ablation there by forming a plasma, which in turn creates a shockwave that ejects the ablated material outwards as fine particles. Ideally, the substrate below the coating that is targeted for removal is protected from damage by keeping the laser energy density below the damage threshold. Although the precise details of these events take place at exceptionally fast speeds and are challenging to accurately model and study, the overall process can be understood schematically as shown in figure 2.1.<sup>25</sup>

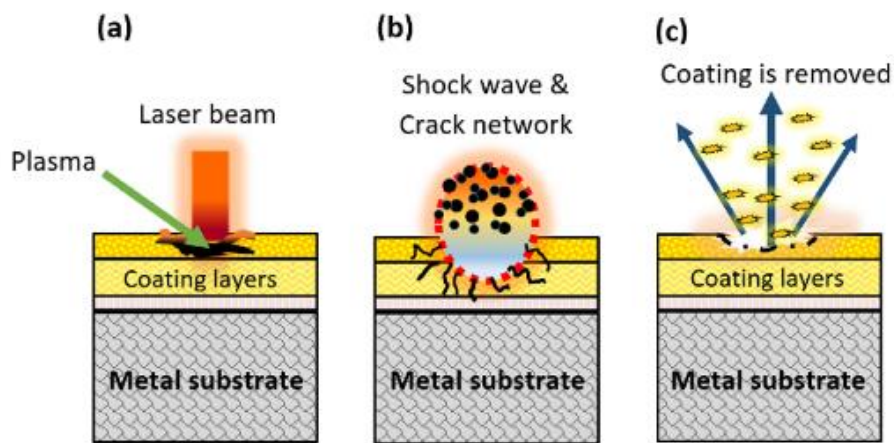


*Figure 2.1 Schematic depiction of the process of laser ablation as used for coating removal A.) The incoming laser pulse rapidly heats up the coating which causes a plasma to form. B.) The continually expanding plasma causes a shockwave to mechanically remove the volume of material that absorbs the laser light as well as spread pressure and thermal cracks throughout the adjacent material. C.) After the plasma has been generated the resulting pressure wave forces the ablated material in the form of particulate to expand outwards away from the surface. Diagram adopted from [25].*

When laser light strikes the surface of a material, a certain portion will be reflected from the surface due to a difference in the index of refraction, while the rest will be transmitted into the material. The amount of light that is reflected,  $R$ , depends on both the polarization and the angle of incidence  $\theta_i$  of the light as well as the indices of refraction of the materials  $n_1$  and  $n_2$ . The Fresnel equations [eq. 1]<sup>26</sup> can be used to calculate the reflection coefficients for the s-polarized and p-polarized components of the incident light:

$$[1] \quad R_s = \left[ \frac{E_r}{E_i} \right]^2 = \left[ \frac{n_1 \cos(\theta_i) - n_2 \cos(\theta_t)}{n_1 \cos(\theta_i) + n_2 \cos(\theta_t)} \right]^2$$

$$R_p = \left[ \frac{E_r}{E_i} \right]^2 = \left[ \frac{n_1 \cos(\theta_t) - n_2 \cos(\theta_i)}{n_1 \cos(\theta_t) + n_2 \cos(\theta_i)} \right]^2$$

which are related to the transmission coefficients through  $T_s = 1 - R_s$  and  $T_p = 1 - R_p$ . In the case of normally incident light on a flat surface the Fresnel equations reduce to the form [eq. 2]<sup>26</sup> :

$$[2] \quad R = R_s = R_p = \left( \frac{n_1 - n_2}{n_1 + n_2} \right)^2$$

Once light is inside the material, absorption of the light causes the intensity to decay with increased depth at a rate that is characteristic of the material's absorption coefficient,  $\alpha$ . In real materials  $\alpha$  is a function of wavelength and temperature, but for the case of constant  $\alpha$ , the intensity  $I$  decays exponentially with the depth  $z$ . This relation is described by the Beer-Lambert Law [3]<sup>26</sup>:

$$[3] \quad I(z) = I_0 e^{-\alpha z}$$

where  $I_0$  is the intensity just inside the surface after accounting for reflection loss. Another important parameter to define is the optical penetration, or absorption depth, defined as  $\delta = 1/\alpha$ , which is the depth in the material at which the intensity of the transmitted light drops to  $1/e$  of its initial value at the surface. Figure 2.2 shows the absorption depths as a function of wavelength in nanometers for different metals and semiconductors.<sup>26</sup> Since A36 is low carbon steel, the yellow colored iron line in the figure is a good representation of the steel used in this study, and a vertical dashed line at 1064 nm shows the wavelength that was in use by the CL1000 Nd:YAG laser that was used for LACR.

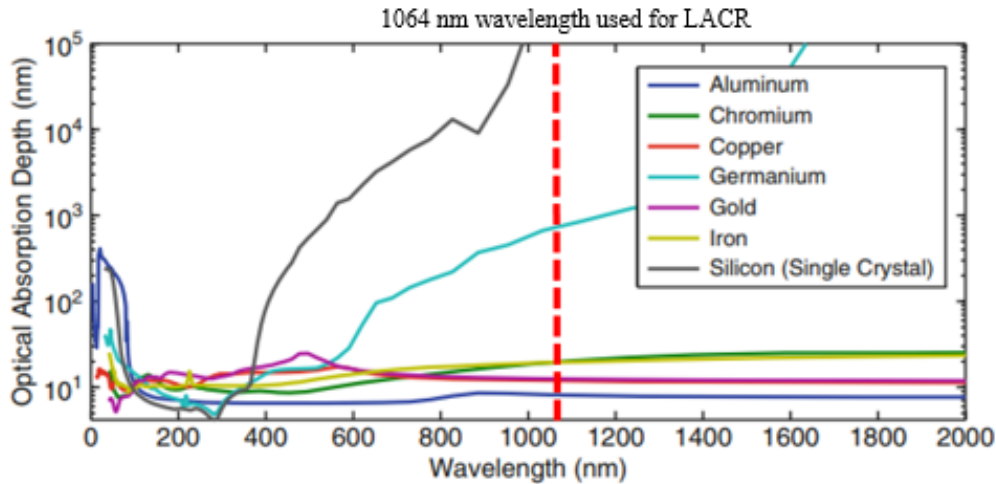


Figure 2.2. Optical absorption depths for several materials over a range of wavelengths. A dashed red line marks 1064 nm, the wavelength produced by the laser used for LACR. [26]

It can be noted that there is some appreciable variation in the absorption depth of different materials depending on the wavelength, with a minimum absorption depth located roughly in the UV range of the spectrum.

While the previous optical material data and equations previously discussed accurately model the interaction of light with different materials, they are based on unrealistic assumptions such as near perfectly flat polished surfaces, as well as clean interfaces between the medium the light is passing through (typically air) and the material in question. However in actuality, these situations are rarely encountered. For example, in this project the steel beams that underwent laser cleaning were not only contaminated with various paint layers, but with oxide rust scale that varied in thickness across the entire steel surface (as will be discussed in detail in later chapters). Because of this, it is difficult to precisely model the real time interaction of the laser beam with the I-beam surface.

Despite these challenges, some studies have attempted to determine the effect of realistic surface conditions (oxide layers, surface contaminants, and roughness) on the laser material interactions.

Figure 2.3 <sup>27</sup> diagrams how surface features can affect the absorptance of light onto metal substrates.

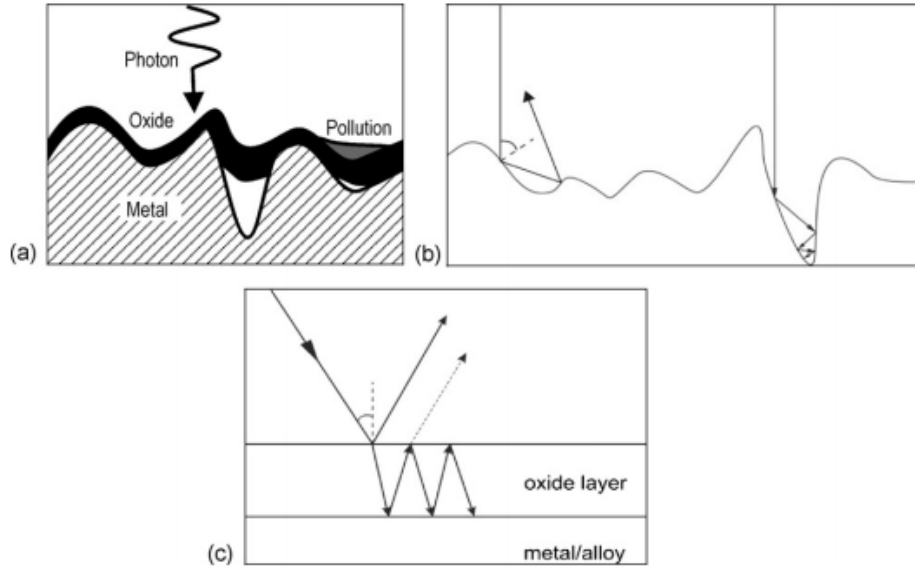


Figure 2.3. Various mechanisms which affect the absorptivity of real engineering surfaces: (a) a typical cross section of a metallic engineering surface. (b) high angle absorptance and multiple reflections due to surface roughness. (c) multiple reflections within an oxide layer. <sup>27</sup>

In photothermal processing, the ablation can be explained as a result in the quick elevation of temperatures and it is therefore important to be able to model the flow of heat inside a material.

The heat equation [eq. 4] <sup>26</sup> can be used to model the temporal and spatial evolution of the temperature field inside the material. The heat equation can be derived from conservation of energy and Fourier's law of heat conduction, which states that the local heat flux is proportional to the negative of the gradient of the temperature. In a coordinate system that is referenced to the laser beam, ie., fixed with the beam movement, the heat equation can be written as [4]:

$$\begin{aligned}
 [4] \quad & \rho(\mathbf{x}, T) c_p(\mathbf{x}, T) \frac{\partial T(\mathbf{x}, t)}{\partial t} - \nabla [k(\mathbf{x}, T) \nabla T(\mathbf{x}, t)] \\
 & + \rho(\mathbf{x}, T) c_p(\mathbf{x}, T) \mathbf{v}_s \nabla T(\mathbf{x}, t) = \mathbf{Q}(\mathbf{x}, t)
 \end{aligned}$$

where  $\rho$  is the mass density,  $c_p$  is the specific heat at constant pressure,  $\kappa$  is the thermal conductivity, and  $v_s$  is the velocity of the substrate relative to the heat source. The left side of the equation accounts for the evolution of temperature due to heat conduction as well as the convective term  $v_s$  to account for the shift in the reference frame of the laser. Framing the heat equation in terms of the laser light itself (in the reference frame of the laser beam) is advantageous for modeling laser ablation because often the laser beam is rastered over the material surface or some form of motion control is used to move the laser beam relative to the substrate, and writing the heat equation in terms of the laser helps to account for this. The  $Q$  term on the right side of the equation represents the heat sources and sinks through the volumetric heating rate.

The volumetric heating term  $Q(x,t)$ , is what initially drives the evolution of the temperature inside the material. Heat fluxes due to convection and radiation at the surface can be accounted for in the boundary conditions set for the particular problem, however in most cases laser irradiation is the main source of volumetric heating. Considering the different factors that account for the volumetric heating, the volumetric heating term can be written as [5]:

$$[5] \quad Q(\mathbf{x}, t) = g(x, y)f(z) q(t) + U(\mathbf{x}, t)$$

where  $g(x,y)$  represents the spatial shape of the beam's profile, a beam attenuation form  $f(z)$  is determined from the Beer-Lambert law in addition to the temporal shape  $q(t)$ , which could be a constant for a continuous wave laser, a pulse, or even a train of temporally shaped pulses, and the  $U(x,t)$  term which accounts for any chemical reactions or phase changes that occur.

The heat equation is a non-linear partial differential equation, and finding an analytic solution is difficult. Modeling using the heat equation is further complicated by the fact that optical and even some thermal properties can vary as a function of temperature and laser intensity. Therefore

determining quantitative information from the heat equation usually requires computational methods such as finite difference or finite element numerical analysis.

The laser ablation of organic materials, specifically polymers, has been a topic of intense research since 1982, due to its many potential applications. Ranging from thin film deposition techniques such as MAPLE (matrix assisted pulsed laser evaporation),<sup>28,29</sup> polymer surface processing and patterning for electronic materials,<sup>30,31</sup> microfluidic devices,<sup>32-34</sup> and even biomedical applications in surgery,<sup>35,36</sup> polymer laser ablation has been a subject of intense study.<sup>37,38</sup> The details of laser ablation of polymers depends on both the laser parameters, including the type of laser being used, as well as the optical and thermal properties of the material undergoing ablation. Figure 2.4<sup>26</sup> shows how the difference in the photo stability of two different polymers, despite both being the same type of polymers, polyimides, their response to laser irradiation can differ drastically.

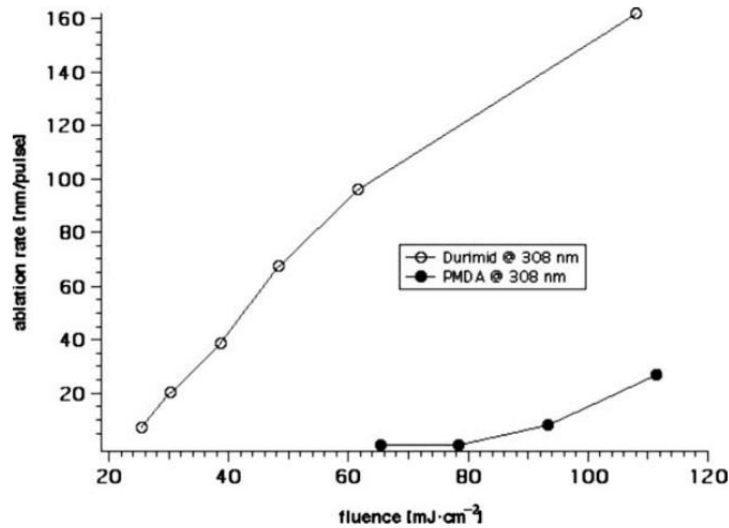


Figure 2.4. The ablation rates of a photosensitive polyimide (Duramid) and PMDA (kapton like polymer) at the irradiation wavelength of 308 nm.<sup>26</sup>

Lasers have different effects on the substrate as well. With CO<sub>2</sub> lasers the ablation threshold of a metallic substrate is higher than that of paint, allowing for the selective removal of paint coatings.

UV lasers have been shown to significantly decrease the thermal effects of laser ablation due to

the use of UV light which photolytically breaks apart the polymer bonds under the photochemical regime. High repetition rate Nd:YAG lasers are especially good for transporting laser light by optical fibre over long distances.

The main parameters characteristic of laser ablation are ablation rate, threshold fluence, and effective absorption coefficient. The ablation rate is defined as the amount of material removed from each laser pulse, and the threshold fluence is the minimum laser fluence needed to cause ablation to occur. Laser ablation is often described by the equation [eq. 6]:

$$[6] \quad d(F) = \frac{1}{\alpha_{eff}} \ln \frac{F}{F_{th}}$$

where  $d(F)$  represents the ablation rate per pulse,  $\alpha_{eff}$  is the effective absorption coefficient, and  $F$  is the laser fluence. Various methods for determining the ablation parameters exist, and depending on which method is used the resulting values can change.

For example the ablation rate can be defined as either the depth of the ablation crater after one pulse at a given fluence, or as the slope of a linear fit to a plot of the ablation depth versus the number of pulses for a given fluence. Values for the ablation rate do not just depend on the method of determination, but on the nature of the polymeric material itself. For example in some materials ablation does not start directly with the first pulse, but after multiple pulses, or multiple pulses are needed to create an ablation crater deep enough to measure. When ablation does not start with the first laser pulse, this process is referred to as incubation. It is due to the physical or chemical modifications of the surface from the first few laser pulses, which usually results in an increase in the absorption of the laser wavelength irradiation. Incubation is normally only observed for polymers with a lower absorption coefficient at the laser wavelength. Figure 3<sup>39</sup> shows the typical appearance of incubation in plots of ablation depth versus the number of pulses.

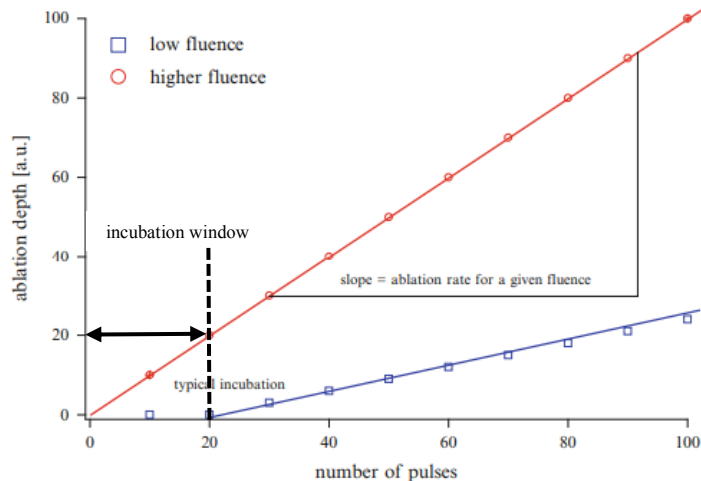


Figure 2.5 Plot of ablation depth vs. pulse number, which is used to determine the ablation rate for a given fluence. The typical feature of incubation, ie., ablation starts only after a certain number of pulses is shown for the lower curve. It is labeled with black lines as the incubation window.<sup>39</sup>

Different methods of ablation crater depth measurement can also influence the ablation parameters. Profilometric methods such as optical interferometry, mechanical stylus profilometry, or AFM, can provide sharp ablation threshold values, which are supported by reflectivity and acoustic measurements. In mass loss measurements, an “Arrhenius tail” becomes apparent in a region of the very low fluence regime, in which a linear increase of detected ablation products is observed, followed by a much quicker increase that coincides with the removal rates given by profilometric measurements. Even when all these different approaches are considered, it is often found that ablation rate cannot be defined with just a single set of parameters. To address this parameters can be defined within each fluence range where a certain ablation process dominates, therefore influencing the ablation rate. Figure 2.6<sup>39</sup> shows the generic scheme of how polymer ablation rate depends on the irradiation fluence, a typical behavior observed in most polymers.

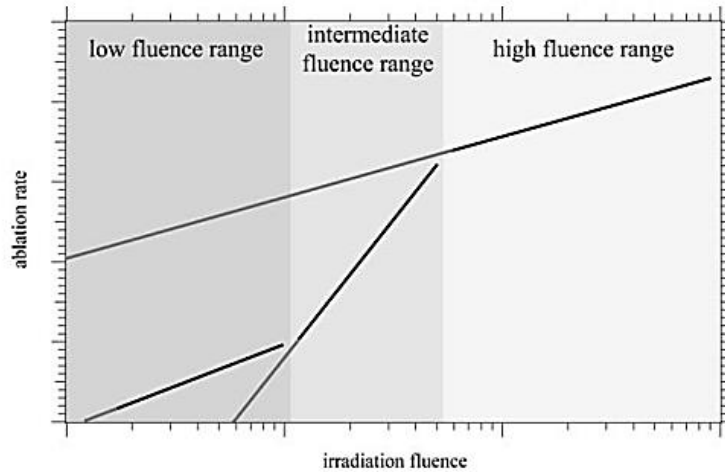


Figure 2.6 Schematic plot of the three fluence ranges which are typically observed for polymer. The three ranges are indicated with different shades of gray. <sup>39</sup>

In this plot, the intersection of the extending gray lines with the x-axis represent the threshold fluence for each fluence range, which in turn shows the schematic ablation rate, outlined in black lines. In addition to differing ablation rates within each fluence range, the effective absorption coefficient can also differ according to the fluence.

### 2.3 Laser Cleaning

The application of laser ablation to paint removal is not new, and previous research regarding the effectiveness of cleaning, and optimization of laser parameters has been performed. The implementation of laser ablation for laser cleaning has been studied before in many different circumstances and uses. <sup>11,5</sup>

A group in France, Francois Brygo et al., studied the effect of laser fluence, repetition rate, and pulse duration effects on the Nd:YAG laser ablation of grey epoxy paint from concrete. Using “etching curves”, graphs that give an indication of laser ablation efficiency by plotting the volume of material removed per laser pulse versus the laser fluence, the authors determined that higher repetition rates resulted in higher ablation efficiencies. Figure 2.7 <sup>40</sup> shows how the depth removed per pulse drastically increases with repetition rate.

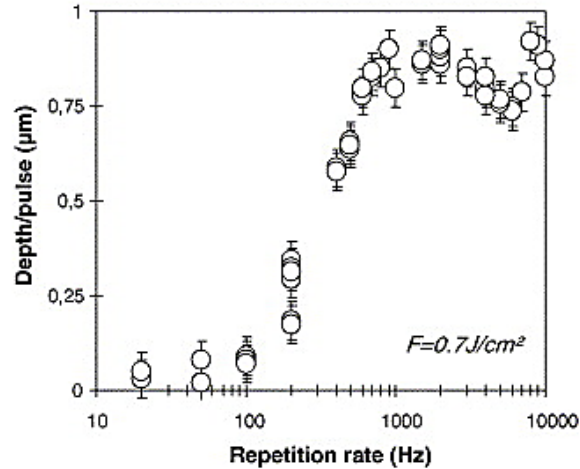


Figure 2.7. Depth per pulse as a function of the repetition rate for 100 pulses, at  $F = 0.7 \text{ J/cm}^2$  and 100 ns pulse duration. Depth per pulse increases as a function of the repetition rate due to heat accumulation in the material pulse per pulse in a “thermal confinement regime”.<sup>40</sup>

The researchers theorized that the accumulation of heat with the number of pulses at high repetition rate suggested that the ablation threshold fluence should decrease at higher repetition rates compared to lower repetition rates. Figure 2.8<sup>40</sup> shows that this was indeed the case.

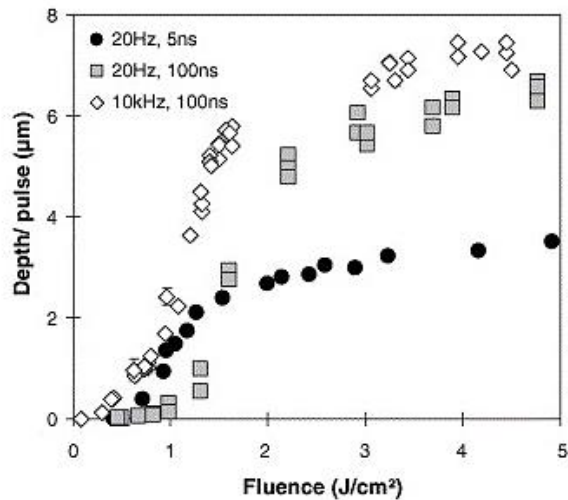


Figure 2.8. Depth per pulse as a function of the fluence for three sets of experimental condition: (1) 5 ns pulse duration, 20 Hz; (2) 100 ns pulse duration, 20 Hz; (3) 100 ns pulse duration, 10 KHz with 50 pulses. High repetition rate experiments were made with an air jet (5 bar pressure).<sup>40</sup>

The “air jet affect” is another variable that can influence the ablation efficiency. As the material is removed by the laser, the ejected material accumulates in front of the surface, and in the case of

high fluence a plasma plume forms in front of the surface. This accumulation can interfere with incoming laser light by adsorption and scattering, causing a decrease in the strength of the beam once it reaches the substrate. By using an air jet the debris could be blown out of the way of incoming laser light, therefore limiting the diminishing effect it has on laser ablation efficiency.

Another research group, Madhukar and coworkers,<sup>41</sup> tested both a continuous wave (CW) and a pulsed Yb-fiber laser to remove a red oxide and enamel paint from a stainless steel and an aluminum alloy substrate. The substrates were roughly  $35 \pm 5 \mu\text{m}$  in thickness and the effectiveness of different laser parameters in removing the paint without damaging the substrate was investigated. The authors found that the specific energy, defined as the amount of laser energy needed to remove a unit volume of paint before the onset of any substrate damage (which is also a measure of cleaning efficiency), was dependent on the laser processing parameters. The authors determined that for pulsed lasers (which were also used in this LACR study) the specific energy depended on both the time-length of each pulse as well as the time interval between the two successive pulses. At 1 kHz pulse frequency, the specific energy was found to be reduced with increase in duty cycle and the corresponding scanning speed, whereas at lower repetition rates such as 50-150 Hz and with 50% overlap between pulses, the specific energy was found to increase with increasing duty cycle. During the laser paint removal tests a plume was observed over the surface and this was attributed to the variation in specific energy, as the plume can absorb incoming laser irradiation and therefore affect the amount of laser energy that is delivered to the surface, resulting in the variations in specific energy. The dimensions of the plume as well as the particle density within it affect the amount of absorption, and the authors determined the absorption characteristics by applying Beer Lambert's Law.

Figure 2.9<sup>41</sup> shows optical micrographs of the bare stainless steel substrate surface and of paint removed tracks at different processing conditions. Because a ventilation or vacuum system was not in use, thin layers of ash remained on the sample surface, although the authors reported that this layer could easily be removed with light brushing or wiping with tissue paper. Figure 2.9c, 2.9d, and 2.9e show the laser cleaned surface at different laser processing conditions, and surface melting, complete paint removal, and partial paint removal are all shown respectively.

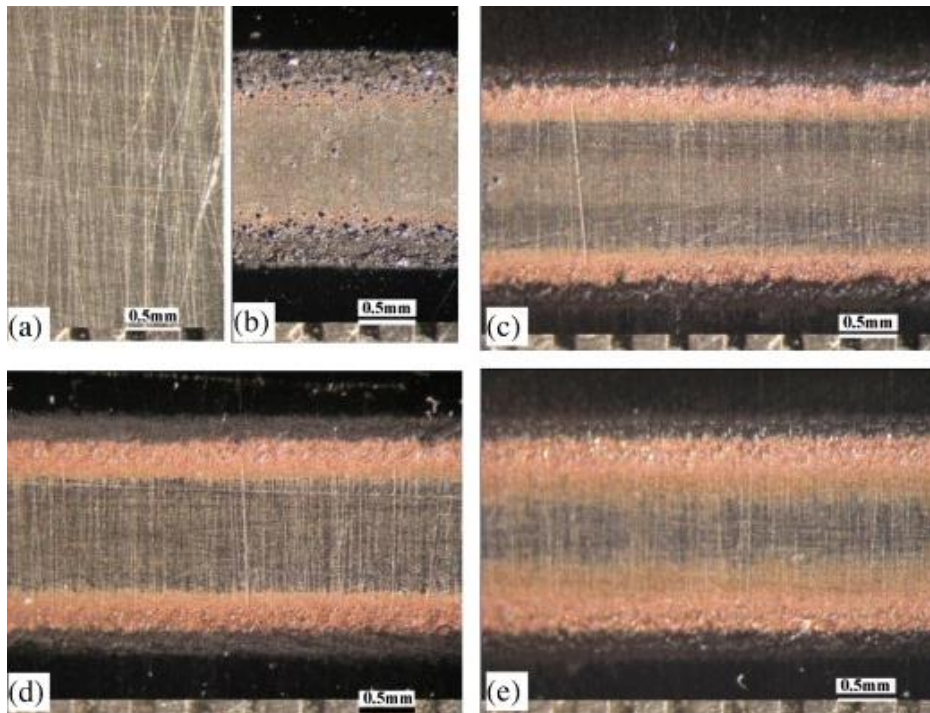


*Figure 2.9. (a) Photograph of the bare base metal prior to painting. (b) The laser cleaned surface showing the ash layer left behind on the surface after laser cleaning,  $v = 8000$  mm/min, (c) slight melting at the central zone of the laser cleaned track,  $v = 8000$  mm/min, (d) complete paint removal,  $v = 9000$  mm/min, and (e) partial paint removal,  $v = 14,000$  mm/min; residual ash has been wiped out in photographs (c) – (e), laser power = 300 W and continuous laser operation was used in each example.<sup>41</sup>*

Laser cleaning experiments performed by the group involving pulsed lasers used both high and low frequency pulse settings. At a high frequency of 1 kHz, the duty cycle (pulse on and off time) was varied generating pulses of 50 – 150  $\mu$ s duration, and with peak laser powers in the

1200- 1800 W range. Variations with laser scan speed and specific energy with duty cycle at different peak laser powers are shown in figure 2.10 (a-c) and 2.10(a-c)<sup>41</sup> for both stainless steel and aluminum alloy substrates respectively. The general trend the authors reported was that the laser scan (paint removal speed) increased with duty cycle as the pulse on-time and the input laser energy increased.

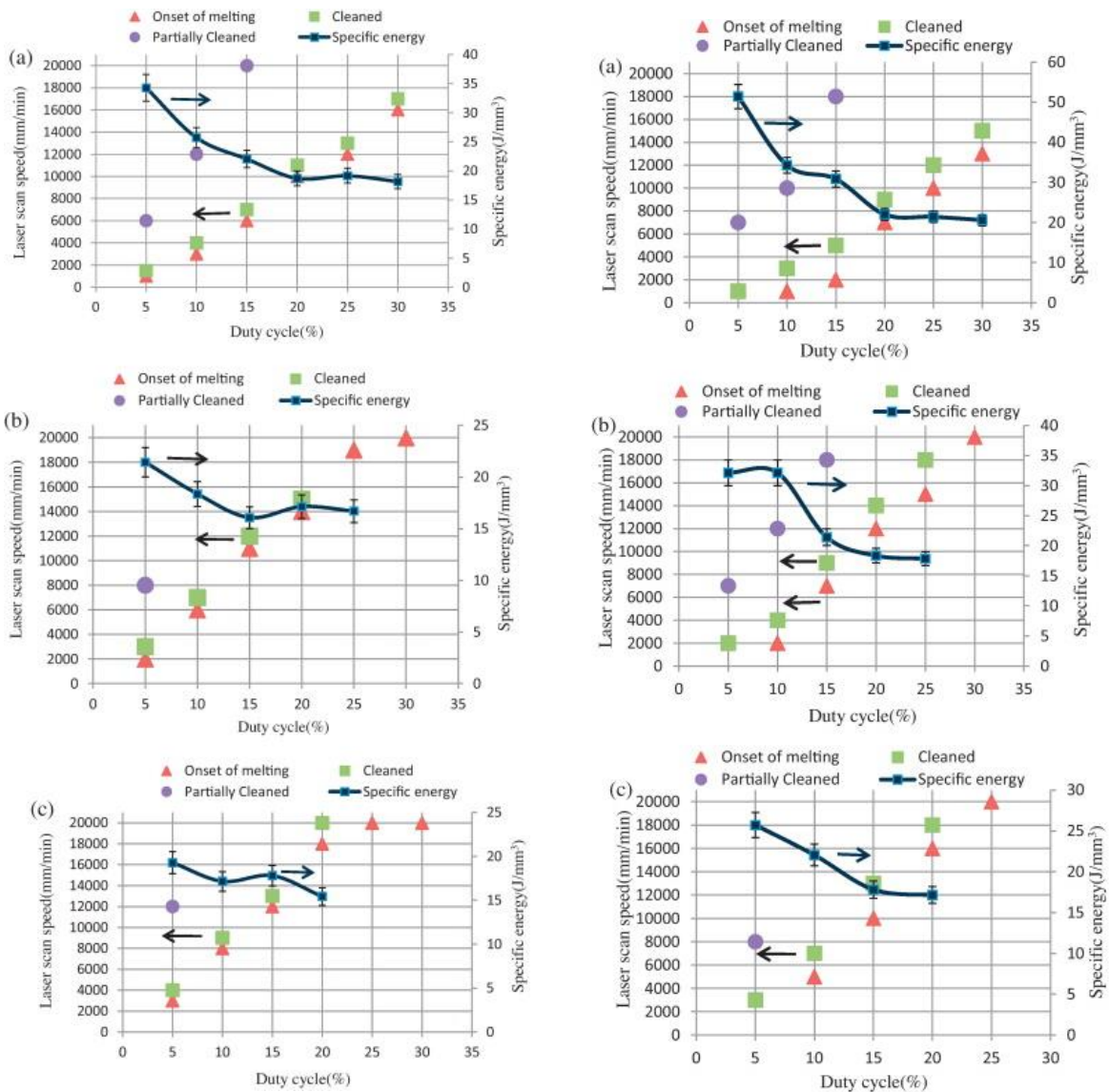


Figure 2.10 (left) and 9 (right) depicting the variation of laser scan speed and specific energy with duty cycle for different peak laser powers. Figure 8 (stainless steel substrate) and figure 9 (aluminum alloy substrate): (a) = 1200 W, (b) = 1500 W, (c) = 1800 W.<sup>41</sup>

The specific energy tends to decrease with increasing duty cycle, and it was found that the laser energy in a single pulse of duration of 10  $\mu\text{s}$  duration was not always sufficient to remove the entire thickness of the paint at the point of incidence, and therefore a number of pulses were required to completely remove the coating, especially when the duty cycle was low. For the stainless steel substrate the best laser parameters from a process efficiency standpoint were a specific energy of 15  $\text{J}/\text{mm}^3$ , at 20% duty cycle and 1800 W peak laser power. Likewise for the aluminum substrate, the best results were obtained at 17  $\text{J}/\text{mm}^3$  at 20% duty cycle and 1800 W peak laser power.

The authors concluded that there was a range of laser processing parameters that can be used to remove paint without damaging the substrate, but that the process efficiency or specific energy is not the same over the entire range. The specific energy was determined to range from 9.5 – 34.2  $\text{J}/\text{mm}^3$  for the stainless steel substrate for the experimental conditions the authors used. The specific energy needed to remove coating from the aluminum substrate was slightly higher than that needed for the stainless steel, and this was theorized to be due to the higher thermal conductivity of the aluminum compared to the steel (205.0 vs. 50.2  $\text{W}/\text{mK}$  respectively)<sup>42</sup>. Other researchers have reported no significant difference in paint ablation between aluminum and steel substrates, however in this case 100 nanosecond pulse duration were used instead of the millisecond range pulse durations that were used in this study. The authors rationalized that this could be due to the fact that the larger pulse duration time used in their experiment may have led to higher conduction heat loss which was reflected by the higher specific energy needed to remove the paint from the aluminum substrate.

A commonly used characterization technique in laser processing is laser induced breakdown spectroscopy, or LIBS, in which plasma created from laser material interaction is analyzed for the chemical composition of the material that is creating the plasma.

In order to determine the effectiveness of laser cleaning, various analytical techniques such as FTIR and LIBS have been used. By comparing the chemical composition, using LIBS and FTIR spectra before and after cleaning, the effect of the laser cleaning on the surface can be studied. Mateo et al.<sup>12</sup> cleaned brass surfaces coated with various contaminants such as varnish, ink, lacquer, and an oxide using a Nd:YAG laser, and used real time LIBS in the process to study the change in chemical composition during the cleaning. Figure 2.11<sup>12</sup> shows a depth profile of Cu, Si, and Zn as the number of laser pulses increases. This profile reflects a sand finished brass sample that was coated with ink. The copper was attributed to impurities in the ink, and the silicon was impregnated into the surface from the sand finishing. The Zinc corresponds to the ablation of brass, and can be used to confirm that the substrate has been reached and is being ablated.

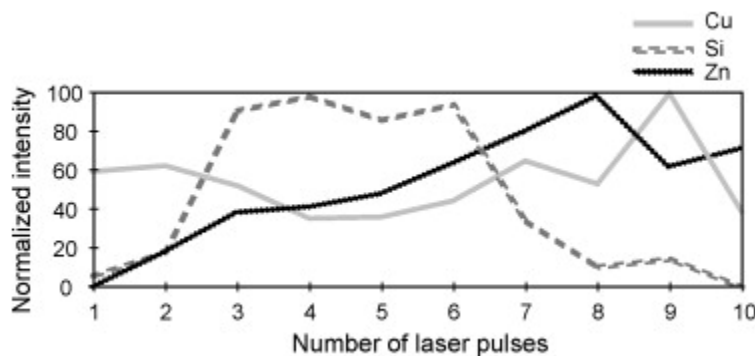


Figure 2.11. Depth profiles of Cu(I) 324.754 nm, Zn(I) 334.502 nm and Si(I) 288.158 nm emission lines corresponding to 10 consecutive laser pulses on a brass sample with sand finish coated by ink.<sup>12</sup>

In addition, FTIR (figure 2.12)<sup>12</sup> was used to analyze the surface both before and after the laser cleaning.

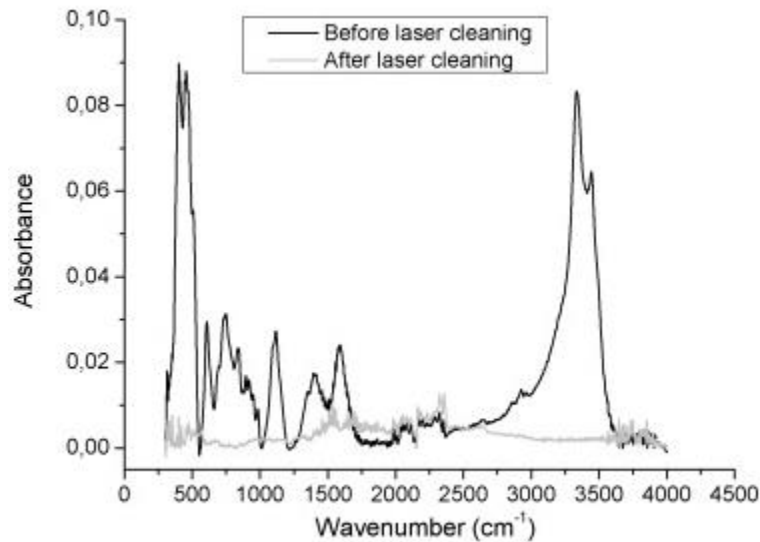


Figure 2.12. ATR-FTIR spectra of a brass sample with mirror finish coated by oxide before (dark line) and after (light line) laser cleaning.<sup>12</sup>

The peaks present before laser cleaning at around  $400 - 600 \text{ cm}^{-1}$  were attributed to copper and zinc oxides whereas the peaks around 3332 and 1092 corresponded to copper acetates. The rest of the peaks were attributed to zinc acetates which arose as by products to the oxidation procedure used in sample preparation.

The authors concluded that by using FTIR and LIBS the complete removal of the contamination layer could be confirmed and that optical microscopy even confirmed that the fine surface details such as scratches due to the sand finishing were still preserved.

Other groups have used laser cleaning for a variety of applications, such as Guan et al.,<sup>14</sup> who used a pulsed Nd:YAG laser to remove carbonaceous deposits from the heads of piston engines. The authors confirmed the cleaning by use of SEM, EDS, FTIR, and XPS. Figure shows the FTIR spectrum of the laser cleaned piston head, the original piston head, as well as spectra of a thin and thick contamination layer. It can be seen that the original piston's spectra is very close to that of the laser cleaned piston head. (see figure 2.13)<sup>14</sup>.

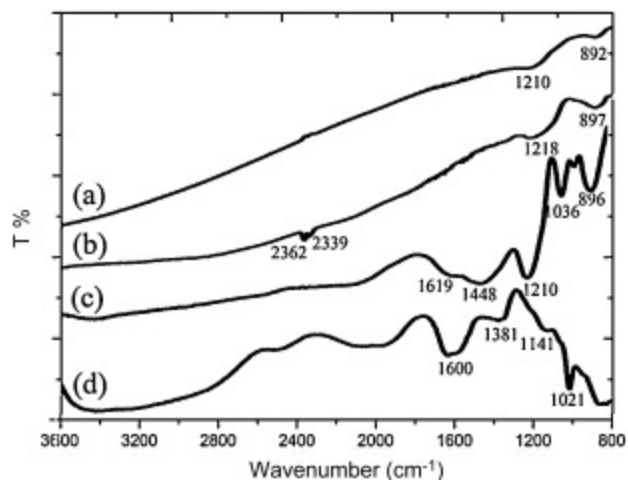


Figure 2.13. FTIR spectra collected from the surface of (a) steel substrate of the original piston, (b) laser cleaned surface, (c) thin contamination layer, and (d) thick contamination layer.<sup>14</sup>

The large peaks at 1210, 1036, and 890  $\text{cm}^{-1}$  were due to iron oxides and carboxylates that were found on the surface of the piston head. The tiny peaks at 2362 and 2339 were attributed to  $\text{CO}_2$  or  $\text{COOH}$  contamination due to atmospheric exposure.

Other groups have used excimer lasers to clean various types of marble for sculptures and statues, as well as structural marble. For example Maravelaki-Kalaitzaki et al.<sup>5</sup> used excimer lasers to clean black encrustation, soil and dirt, and biological deposits off of Pentelic marble from rubble in Athens, Greece, using SEM, FTIR, and LIBS to characterize the removal of the contaminants. The encrustation consisted of gypsum, black particles, iron oxides, soot, residual calcite, mica flakes, quartz, and even various types of lichen and fungi, all ranging from 20  $\mu\text{m}$  to several millimeters in thickness. These surface deposits accumulate on marble monuments situated outside due to the combined effect of chemical, physical, and biological processes, and although mostly accumulated on the surfaces of marble, the contamination can sometimes cause chemical damage up to a few millimeters within the sample due to the presence of cracks and fissures on the surface of the marble.

Figure 2.14<sup>5</sup> shows the FTIR spectra of the marble both before and after laser treatment. It is evident from the FTIR data that the amount of gypsum (Gy) has decreased after laser treatment while the amount of hemihydrate (H) and anhydrite (A) has increased. This alteration in the mineral structure is due to the laser treatment. LIBS was also used to monitor the change in composition as the laser treatment progressed. After gathering an initial composition spectrum before lasing the surface, this composition was observed to decrease with depth, indicating that the contaminating layer was being removed successfully. Particularly, a decrease in the amount of potassium was observed with further lasing, indicating the removal of biological material from the surface. Figure 2.15<sup>5</sup>, shows successive LIBS spectra with increased amounts of laser processing, corresponding to the depth within the sample from the surface. As depth (equivalent to pulse #) increases, the decreasing potassium peaks can be observed.

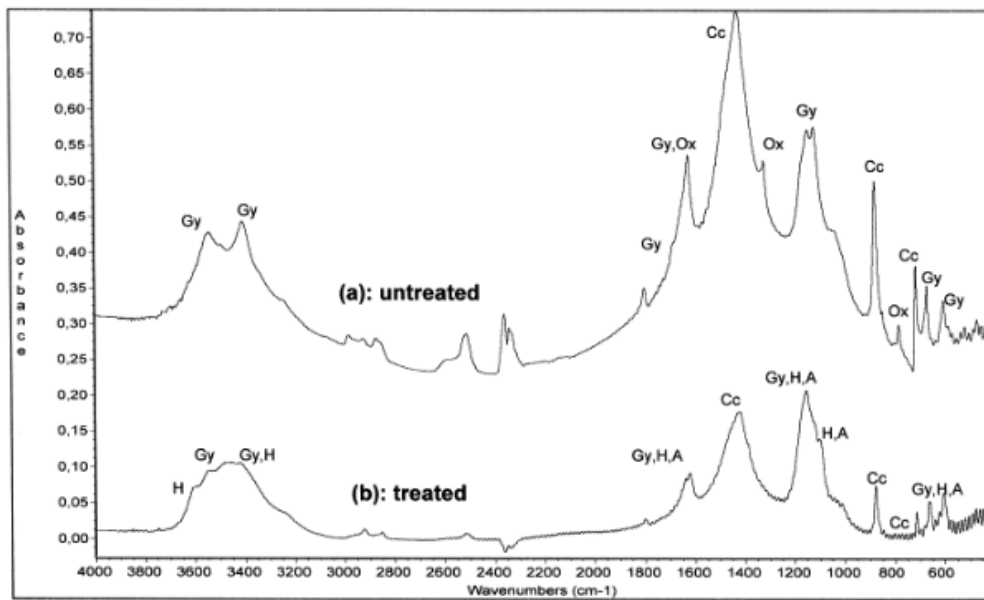
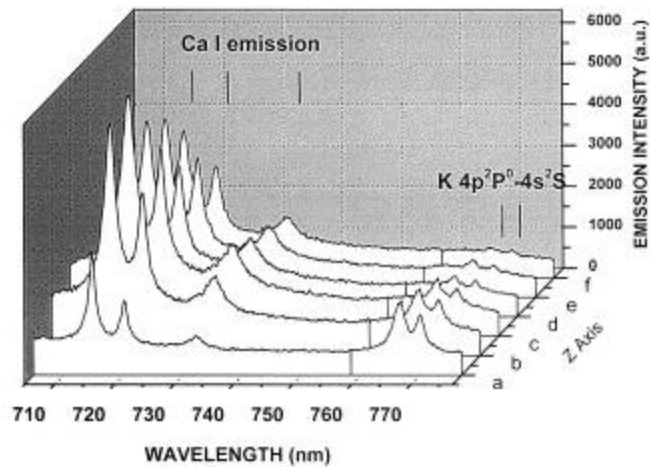


Figure 2.14. Spectra of a compact black crust before (a) and after treatment with a XeCl excimer laser (b), Gy – gypsum; Cc = calcite; Ox = calcium oxalate; H = hemihydrate; A = anhydrite.<sup>5</sup>



*Figure 2.15. Successive LIBS spectra during the KrF laser excimer assisted removal of biological crust on the Pentelic marble. The correspondence is (a) 1<sup>st</sup>-, (b) 2<sup>nd</sup>-, (c) 5<sup>th</sup>-, (d) 12<sup>th</sup>-, (e) 20<sup>th</sup>- and 32<sup>nd</sup>-pulse. <sup>5</sup>*

Laser cleaning has become an established technique among many application areas, however its implementation into new areas requires the validation of the effect of the laser light on the substrate. The effect of laser cleaning on bridge steel is examined in this study.

## **Chapter 3 Experimental Setup**

### **3.1 Introduction**

This project involved both industrial testing components at onsite and offsite locations, as well as detailed testing and characterization of processed samples. Offsite components took place at the Norton Sandblasting Facility, in Chesapeake, VA, and onsite components consisted of implementing the laser cleaning process at a bridge location in Virginia. In addition to these industrial tests, sample testing and characterization was completed at the University of Virginia.

The beginning of this study, phase I, involved a test of the laser cleaning process and the feasibility of using a hand held laser cleaning system to clean I-beam sections from a bridge. This phase also produced samples for later analysis. After phase I laser testing, phase II consisted of using the laser system to clean I-beams on an actual standing bridge structure. Phase III followed to use the same laser system to attempt cleaning specific components of bridge structures offsite. After obtaining both laser cleaned, grit blasted, and base material samples from phase I, processed I-beams were sectioned for characterization and repainted for both metallurgical and paint adhesion testing. This chapter will detail Phases I, II, and III, as well as the sectioning, sample preparation, and characterization for metallurgical analysis, set-up for PATTI repainting adhesion testing, hardness testing, and tensile and fatigue testing.

### **3.2 Phase I: Laboratory Demonstration**

Phase 1 consisted of sample generation and the initial test to laser clean bridge components. Twenty 1' I-beam bridge sections were removed by VDOT from the bridge on Route 685 (Telegraph Road) over Stinking River located in Pittsylvania County, Structure # 6096, (figure 3.1) and were transported to Norton Sandblasting, in Chesapeake, Virginia, for a LACR demonstration on October 26, 2016. During this demonstration both University of Virginia and VDOT representatives were present, along with an EI Group (industrial hygiene

firm) technician, and a laser operator from Adapt Laser Systems. Along with the documentation and observations made of the LACR process, the EI Group conducted an industrial hygiene survey to monitor and later analyze the worker and environmental safety of the process. The Phase I took place in an indoor office setting, further demonstrating the cleanness of the process due to the vacuum and filtration system present on the laser. (Figure 3.2).



Figure 3.1 (a) The bridge from which the 20 I-beam samples were taken from, as well as (b) a close-up of one of the I-beam sections.

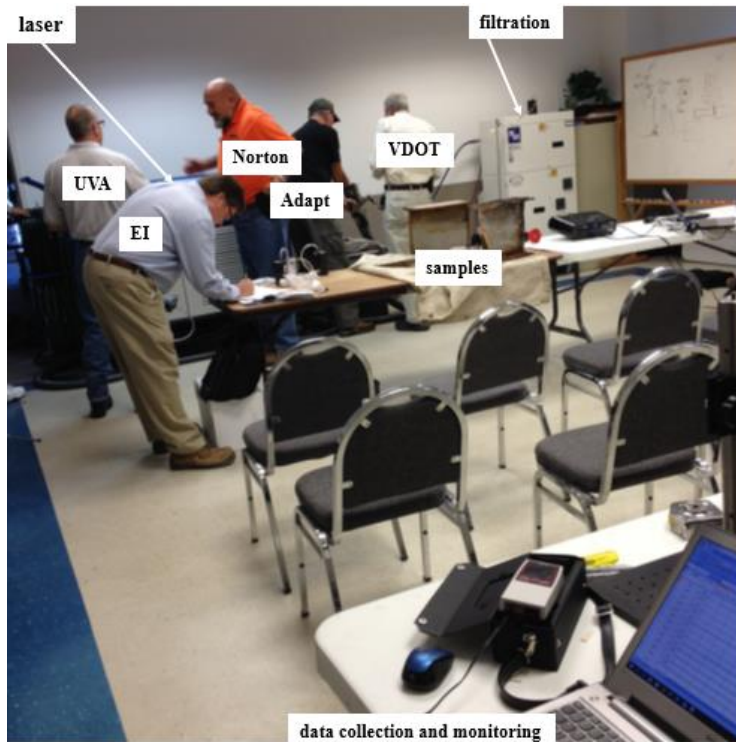
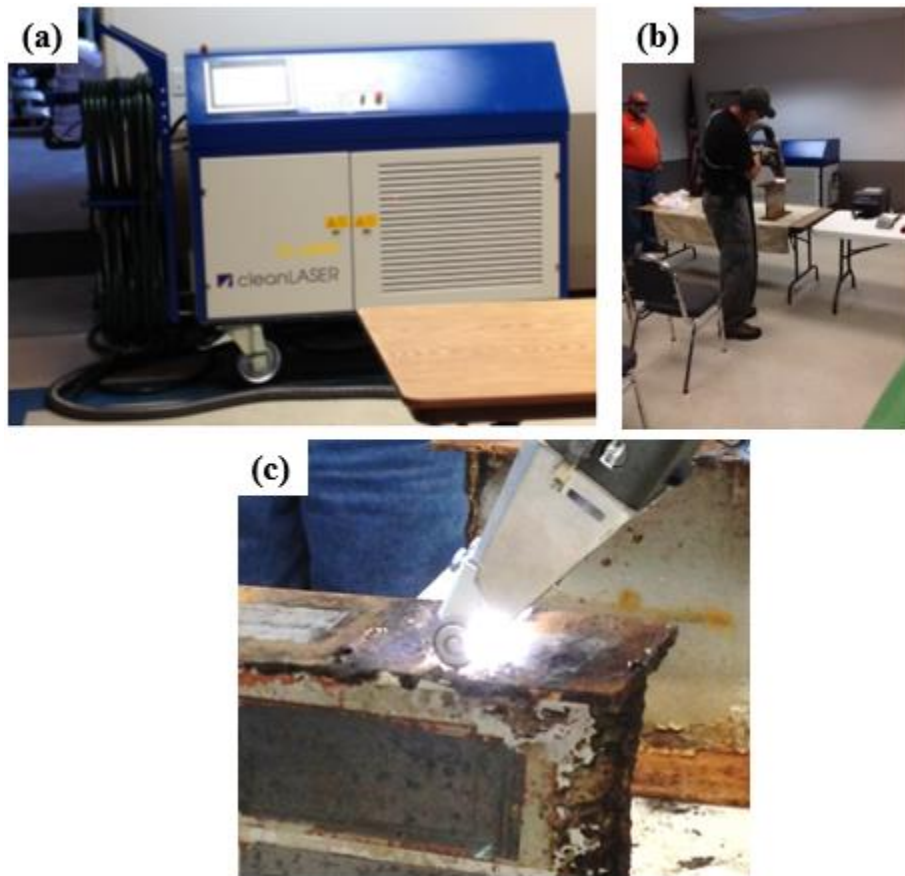


Figure 3.2. The office room at Norton Sandblasting where Phase I took place.

The processing was performed using an Adapt Laser Systems model CL1000QNd:YAG operating at a fundamental wavelength of 1064 nm and delivering 1 kW of average power. As each I-beam section was cleaned the process was documented and recorded in addition to the industrial hygiene analysis. Figure 3.2 shows the laser unit, an operator from Adapt Laser Systems using the laser to clean a sample, as well as a close up of the laser beam surface interaction. It should be noted that the visible light present at the end of the optic head is not the laser light itself (which is invisible to humans due to its infrared wavelength), but actually plasma generated by the laser heat and ablation of the surface coatings.



*Figure 3.3. (a) The CL1000 laser cleaning system, (b) operation of the laser, and (c) a close-up of the laser cleaning process on one of the I-beams.*

The bridge from which the samples were taken from was originally built in 1932, and the beams themselves circa 1925, and as such the I beam sections showed large amounts of corrosion damage, tar, paint, and debris that had accumulated over the years. Due to the thickness of the rust layers, a metal scraper was used manually to remove flakes of rust before laser cleaning began. Figure 3.4 shows an example of a laser cleaned area surrounded by the original condition of the surface. The number of passes required to clean the surface depended on the thickness, composition of the coating, operator experience, as well as the speed and motion used for the laser optic. The heaviest scale required roughly 3-6 passes to remove all visible coatings and reach the substrate.



*Figure 3.4. A visual comparison between the laser cleaned surface area and the surrounding condition of the I-beam surface prior to cleaning.*

### **3.3 Phase II**

Phase II, consisted of an onsite demonstration of the feasibility of using the LACR laser system on a standing bridge structure. After a couple days of preliminary set-up, the laser testing started on August 15, 2017, on Route 695 in Farmville, VA. Figure 3.5 and 3.6 shows the underside of the bridge where the LACR cleaning was attempted. The laser generator, filtration unit, electrical generator, and associated equipment were housed and operated from a trailer that was parked on the side of the road below the bridge and a boom lift was used to bring the laser operator and laser optic within working distance of the bridge components.



*Figure 3.5. (a) Underside of the bridge on Rt. 605 in Farmville VA, where the onsite LACR testing took place. (b) Boom crane used to elevate the operator to the cleaning area.*

In addition to the onsite LACR documentation and observation, VDOT contracted industrial hygiene work again with the EI Group, to determine the worker and environmental safety of the process. During the demonstration a tarp was hung behind the laser operator in the lift to ensure that no reflected laser light was allowed to escape to the surrounding area, and routine laser safety protocols such as wearing laser safety glasses were in place.

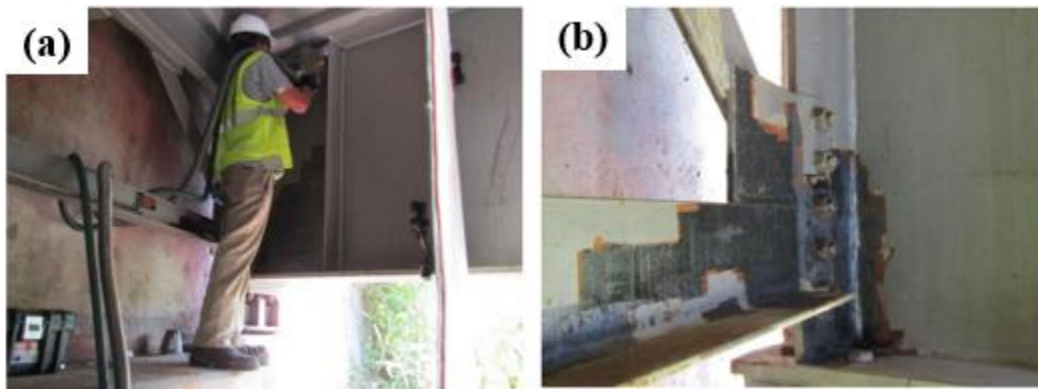


*Figure 3.6. (a) The LACR system in use to clean a component of the beam end. (b) The exposed surface after laser cleaning.*

Phase II showed that the deployment and operation of the laser system from an onsite location was possible, however it also revealed some shortcomings of the implementation of the LACR process on bridge structures. While cleaning of open flat areas of the I-beams proved to be

problem free, the beam ends and bearings were difficult to reach for cleaning due to the limited space and tight and unusual geometries present in these areas. Due to the length of the laser optic head and the exiting optic and vacuum lines from the back (figure 3.7<sup>43</sup>), it was not possible to fit and use the laser properly to clean these parts of the beams, which are the priority areas for cleaning due to excessive corrosion damage that occurs here as discussed in the introduction.

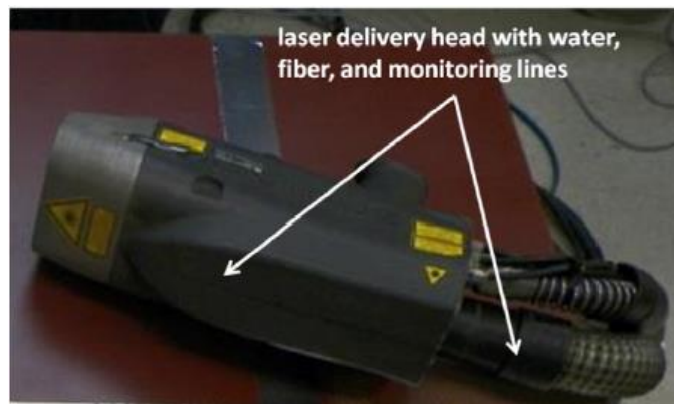


*Figure 3.7<sup>43</sup>. Photo showing the bulky and lengthy cables exiting the back of the laser optic.*

Figure 3.8 shows some of the areas on beam ends that were difficult or impossible to reach with the laser system. In order to address these concerns, a further laser test was planned as Phase III.

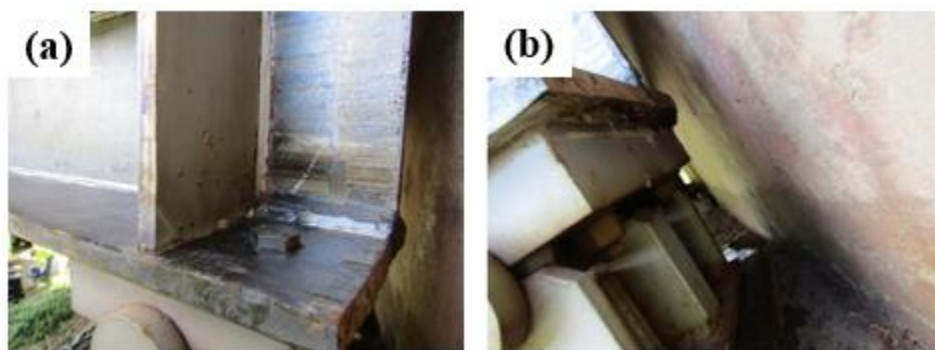


*Figure 3.8. Areas on the bridge structure that could not be reached with the laser for cleaning: (a) Beam ends facing concrete abutments. (b) Beam bearing also directly next to a concrete abutment.*

### 3.4 Phase III: Cleaning Tight Geometry Demonstration

Phase III consisted of a third laser test designed to determine the capability of the Adapt Laser system to effectively clean harder access areas such as bridge beam ends and bearings. For this demonstration, which took place on November 9, 2017, a bridge bearing that was provided by VDOT was transported to Norton Sandblasting in Chesapeake, VA, to perform the laser cleaning. A bridge bearing was chosen due to the recessed areas that could be used in this phase III test. The bearing consisted of 5 different pieces, three of which made up the actual bearing and three other flat pieces that were part of the full assembly. (Figure 3.9).



*Figure 3.9. The partially disassembled bridge bearing used in Phase III.*

In order to evaluate the ability for the laser to clean tighter areas, the Clean Laser 500W system was used with the CleanCUBE H15 head, which consists of a laser optic head with a light

aperture that is 90 degrees to the incoming optic cable line, allowing for a more maneuverable optic that also takes up less space. (Figure 3.10).



*Figure 3.10. CleanCUBE H15 optic used with the 500 Watt laser.*

The targeted area for the laser test was one of the recessed areas underneath the bearing pin because this was the toughest part of the bearing to get access to with the laser (figure 3.11). After surface scale and dirt was removed by hand with a metal scraper and wire brush, the first attempt at laser cleaning used the 500 Watt laser and Clean Cube H15 optic.



*Figure 3.11. Underside of the bearing used for testing.*

Ideally a handheld model of the CleanCube H15 that is also manufactured by Clean Laser would have been used, however for this test only a robot-mountable version was available. The robot mountable head was not ergonomically designed for human use, and hindered the ability to effectively use the laser. In addition, the laser could not be triggered on or off at the optic head itself, requiring another operator to trigger the laser on and off from the laser generator unit itself.

Another one of the downsides to the use of this optic head was the absence of an integrated vacuum system, which had to be externally mounted in the vicinity of the area being cleaned. This meant that environmental hygiene and safety was not as strictly enforced as it typically is when a vacuum nozzle is built into the laser optic head. During this demonstration an industrial hygiene survey was not in place and therefore the effectiveness of the external vacuum system could not be determined, although it is presumably not as effective as when an integrated vacuum nozzle is used with the optic head, which ensures that the material removal follows the precise position of the laser. Figure 3.12 shows the set up used with the external vacuum nozzle in use.



*Figure 3.12. External vacuum hose placement near the site to be laser cleaned.*

Various apertures with different corresponding laser focal lengths can be used with the CL500 Watt laser, and different combinations of lenses and laser parameters were tested until an optimal set up was found. The first laser set up used the 150mm lens which has a focal length of 6 inches, and later was changed out for the 250mm lens which increased the focal length to 10 inches. Various laser parameters such as pulse frequency and scan width were adjusted until optimal settings were found. After adjusting the settings on the laser, a test scan was performed on a sample piece of scrap metal to determine the characteristics of the beam before using the laser on the bearing. Table 3.1 below shows the different laser parameters that were tested in the

sequential order shown, ending with the perceived best configuration. The specific laser parameters can and likely will vary depending on the specific area and geometry of the part to be laser cleaned, as well as the nature of the coating being removed.

**Table 3.1: Various Laser Parameters that were Varied During the Testing**

Test #	Aperture	Pulse Frequency	Scan Width
1	150mm	22 KHz	75%
2	250mm	18 KHz	75%
3	250mm	18 KHz	50%
4	250mm	18 KHz	30%

The 500W laser and CleanCUBE optic appeared to remove most of the outer layer of rust and remaining paint after multiple passes, however the 1000W laser was also tested afterwards. In order to test the 1000W laser which had a lengthier sized optic unit, the vacuum nozzle was removed in order to shorten the length of the laser head by a couple of inches (figure 3.13<sup>2</sup>). As expected the 1000W laser easily removed any remaining rust and left a surface that looked almost the same as the bearing surface after the 500W laser cleaning. However even with the vacuum nozzle on the 1000W optic laser head removed, the device was still too large for use in cleaning bridge beam ends and bearings. This leaves the 500W laser with the

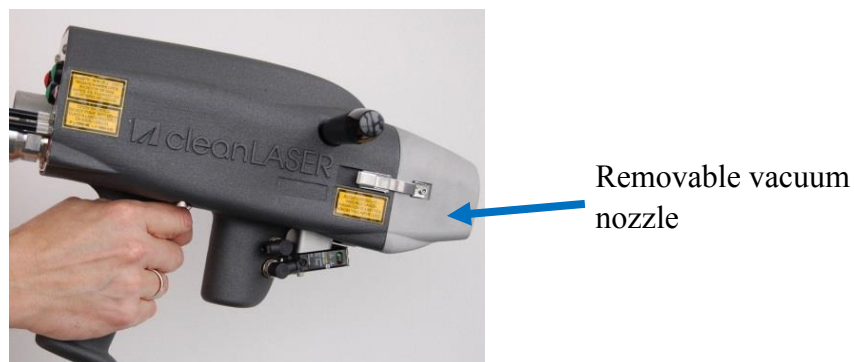


*Figure 3.13. The CL1000 laser optic with the removable vacuum nazzle labeled.*

CleanCUBE H15 head as the only potentially viable option for cleaning these harder access areas. Figure 3.14 shows a before and after photo of the bearing after laser cleaning using both the 500W, and 1000W system.

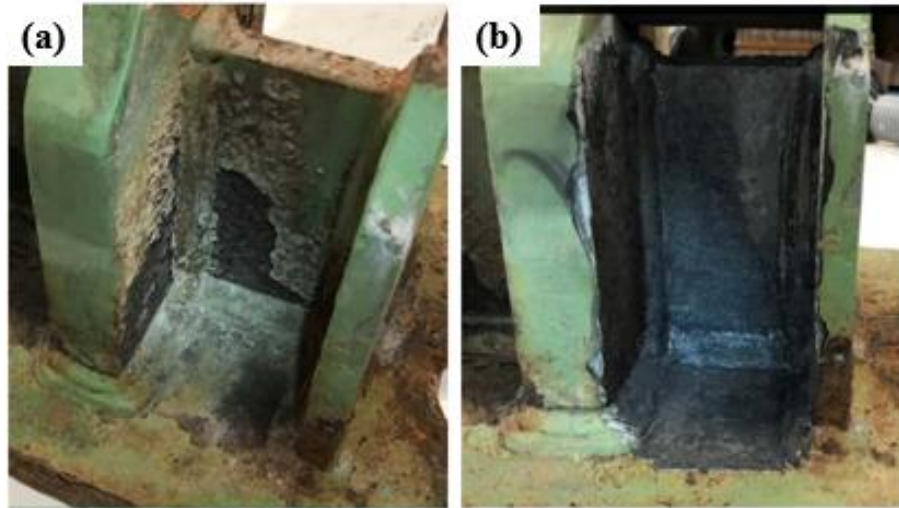


*Figure 3.14. The bearing both (a) before and (b) after cleaning using the 500W and 1000W laser systems.*

### **3.5 Phase IV: Testing for Lead Abatement**

In addition to the Phase I, Phase II, and Phase III parts of the project, a further LACR test for lead abatement was conducted in July and August of 2018 by VDOT and VTRC. The purpose of this study was to determine the effectiveness of LACR in removing lead from steel substrates, in order to provide a lead free surface for further torch cutting of metal samples, a routine task performed by VDOT. Because of the direct high heat and lack of a vacuum system, torch cutting and other methods of hot metal cutting and shaping can result in large amounts of heavy metal fumes such as lead to be released into the surrounding environment. Therefore VDOT is interested in using LACR specifically for the removal of possible contaminants such as lead before the hot cutting of metal work pieces.<sup>44</sup>

In order to characterize the effectiveness and safety of lead removal by LACR, multiple testing methods such as industrial hygiene air sampling, X-ray fluorescence (XRF), and lead wipes were used, in addition to SEM and EDS analysis performed at the University of Virginia. The first stage of the study took place on July 30<sup>th</sup>, 2018 at Norton Sandblasting on Chesapeake, VA. In this stage, bulk samples, wipe samples, XRF readings, and air samples for lead, hexavalent chromium, and polychlorinated biphenyls were collected while two Norton Sandblasting employees utilized a CleanLaser ablation system to remove 55 linear inches of coating from beams provided by VDOT. Following this initial stage, on August 1<sup>st</sup>, 2018, personal and area industrial hygiene samples for lead were collected while a VDOT employee completed oxyacetylene torch cutting, plasma torch cutting, and grinding on the two beams where coating had been removed previously using the CleanLaser system. This portion of the study took place at the Hampton Roads VDOT District office.

During the lead removal operation at Norton Sandblasting lead was detected in one area sample, however the concentration was well below the action level (AL). Also, contaminants were below laboratory detection limits for all sampled analytes on personal samples. Leaded dust levels were measured to have the potential to contribute to worker exposure following removal operations, and therefore protective equipment such as gloves will be needed when handling cleaned samples. Personal and area sample monitoring during hot work operations showed that when the coating has been removed with the laser that the concentrations of leaded containing fumes are not likely to exceed the permissible exposure limit (PEL) or the AL during typical operation. However, an increase in leaded fume was measured when the laser system couldn't remove hidden or encapsulated leaded coating, and this presence of lead could lead to worker exposure during the cutting operation.

During this study two beams were transported to Norton Sandblasting by VDOT to be laser cleaned. These beams were labeled beams A and B, and varied in appearance. Beam A consisted of rolled beams with a silver/grey paint with an obvious rust colored secondary layer that adhered to the base metal during scraping and which broke away as a powder. Beam B was a welded C-beam also with a silver/grey paint which was easily scraped from the beam to base metal during the scraping in large chips, as shown in figure 3.15. Four inch by four inch grids were outlined in tape and paint samples were scraped off of each beam (shown in figure 3.16) for chemical analysis by the contract chemical company, Marine Chemist Service. Samples were screened for lead, chromium, cadmium, and polychlorinated biphenyls (PCBs).

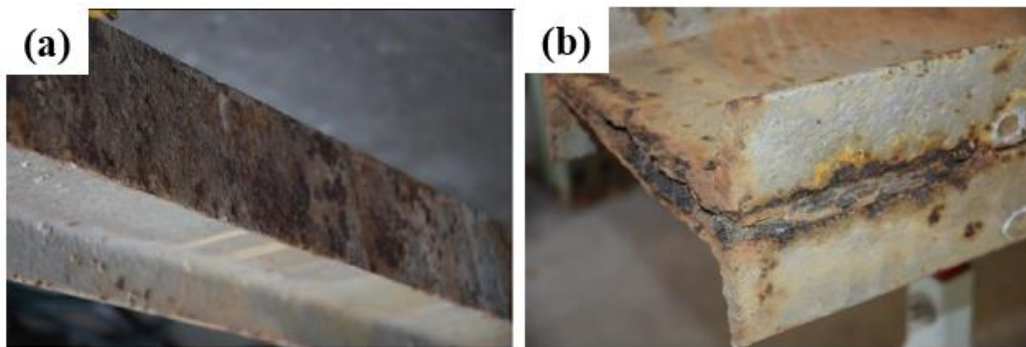


Figure 3.15. (a). Beam A, and (b) Beam B, both used in the VDOT lead abatement study.<sup>44</sup>

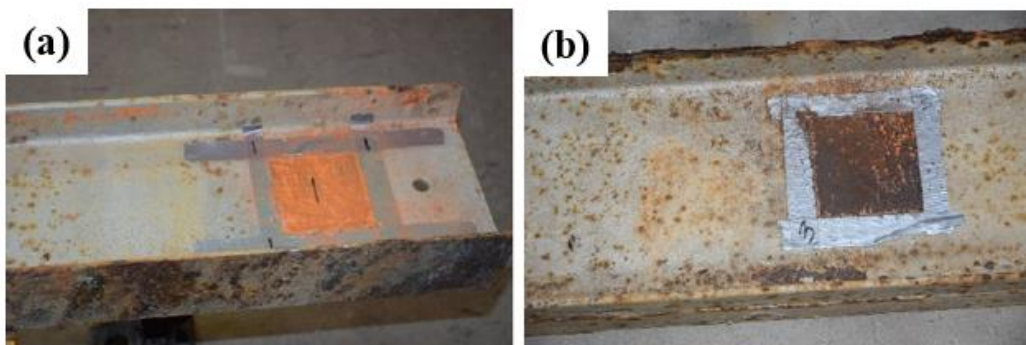


Figure 3.16. The 4 x 4 inch grids where scraped paint samples were taken from. (a) Beam A, (b) Beam B.<sup>44</sup>

During the laser cleaning operation a CL1000 laser system equipped with a TEKA CM 500 laser fume extractor unit consisting of a HEPA filter and activated carbon filter to capture lead debris before releasing the air as exhaust. This is the same filter and containment setup as was used in Phase I, Phase II, and Phase III. During the operation personal samples were worn by each operator in their breathing zone for metal fume, PBCs, and hexavalent chromium. The lead, cadmium, and chromium metal fume samples were collected from both employees on a single 37mm Mixed Cellulose Esther Filter (MCEF), at the end of the two beams, and at the laser air filter exhaust, which had a flow rate of approximately 2.0 liters per minute. After laser removal, lead wipe samples were also collected on a web and flange of each beam (4 total samples) and were analyzed by Marine Chemist Service. XRF samples were collected by an employee of Marine Chemist Service both before and after laser cleaning to document the amount of lead remaining on the beams and to compare the effectiveness of removal using the laser with and without the roller guide. Figure 3.17 shows a laser operator using the laser during LACR cleaning of one of the beams.



*Figure 3.17. A laser operator using the CL 1000 system to remove contaminants from a steel I-beam at Norton Sandblasting.* <sup>44</sup>

After the initial laser cleaning was conducted at Norton Sandblasting, the beams underwent various hot work operations at the VDOT Hampton Roads District location to evaluate whether the laser cleaning system effectively removed enough leaded coating to reduce worker exposure hazard to lead containing fumes during hot work operations. Table 3.2 summarizes the hot work that was completed on each beam and the time associated with each task.

**Table 3.2: A Summary of the Hot Beam Cutting Work Performed at the VDOT Hampton Roads Location <sup>44</sup>**

<b>Task</b>	<b>Beam</b>	<b>Time</b>	<b>Observations</b>
Oxyacetylene Torch Cutting of Flange	A	0905-0917 (13 Min)	29 Flange Cuts
Oxyacetylene Torch Cutting of Flange	B	0919-0930 (11 Min)	19 Flange Cuts Rusting and pitting hammered off prior to cuts
Plasma Torch Cutting of Flange	A	0940-0953 (13 Min)	35 Flange Cuts
Plasma Torch Cutting of Flange	B	0959-1010 (11 Min)	13 Flange Cuts Beam must be prepped before cutting- rust hammered off after heating with torch. Coating inside weld begins to burn and smoke. Web not cut as coating appeared flammable.
Grinding	A	1020-1034 (14 Min)	Nothing Noted
Grinding	B	1044-1053 (9 Min)	Nothing Noted

Figure 3.18 shows a VDOT employee plasma cutting an I-beam and the resulting sparks and fumes that are released from the process. The resulting spark and fumes seen in the photograph are the cause for hazardous contamination concern, and therefore it is the aim of the industrial

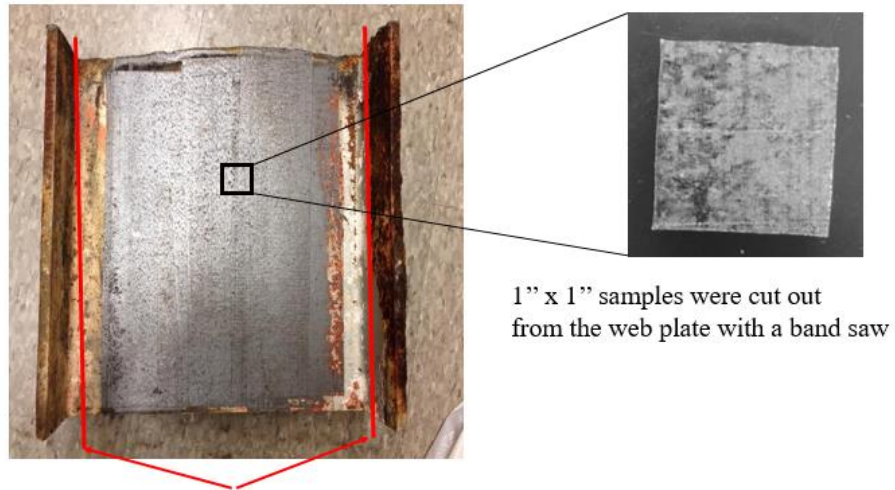
hygiene survey to characterize the potential for lead and other contaminants that may be present within the surrounding work area.



*Figure 3.18. A VDOT employee plasma cutting an I-beam that was previously laser cleaned.*<sup>44</sup>

### **3.6 Preparation of Metallurgical Samples for Analysis**

The I-beams that were processed in Phase I of the project were used for cross sectional, planar, and metallurgical analysis, as well as for providing dog bone samples later used in tensile and fatigue tests. For metallurgical, cross sectional, and planar analysis, the flanges of the beams were removed using a cutting torch, and a band saw was subsequently used to cut out roughly 1'' by 1'' pieces for analysis. (Figure 3.19). The samples were cut from the middle of the I-beam web to avoid any metallurgical effects of thermal damage from torch cutting heat applied to the sides.



1" x 1" samples were cut out from the web plate with a band saw

Flanges were cut away from the webbing using a welding torch

*Figure 3.19. Preparation of samples for cross sectional and metallurgical analysis.*

Several of the laser processed beams and one of the grit blasted beams were brought to Valley Precision Inc. (Waynesboro, VA), for cutting out dog bone samples. Dog bones were water jet cut out from the webs of the processed I-beams according to ASTM E8, and one of the sides of the dog bones specimens was then surface ground to a smooth finish. Sharp edges were also rounded using the same surface grinding tool. Figure 3.20 shows the dimensions that were used for the dog bone specimens, and figure 3.21 shows a schematic of how the dog bones were cut from the I-beams.

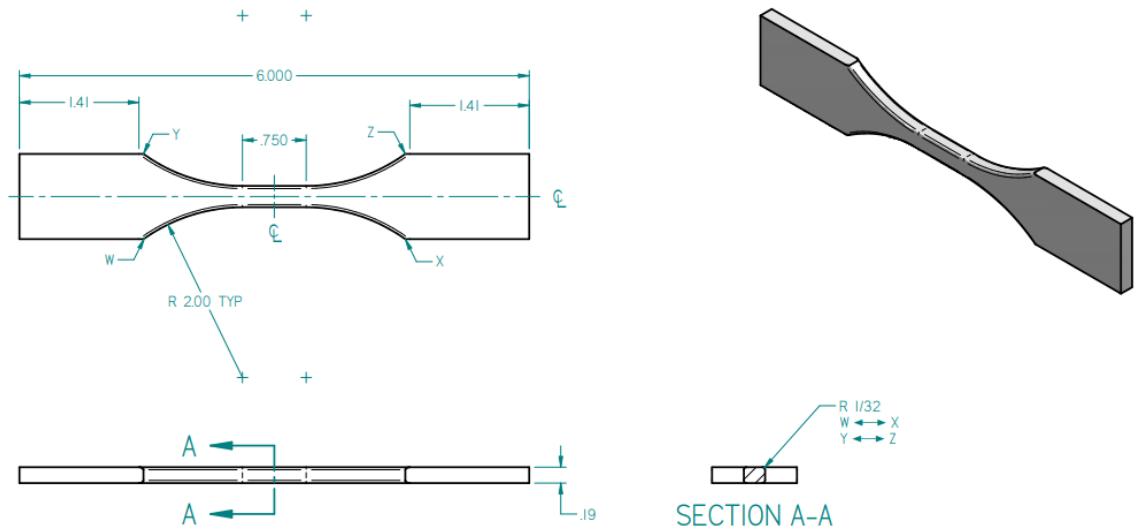


*Figure 3.20. Dog bone sample dimensions.*



*Figure 3.21. Outline of how the dog bone samples were water jet cut from the I-beams.*

Metallurgical samples were polished using conventional polishing techniques up to 1200 grit size polishing paper, and then followed with 3  $\mu\text{m}$ , 1  $\mu\text{m}$ , and colloidal polishing solution. Samples were etched using a 2% Nital etchant (2 % nitric acid, 98% ethanol v/v). Metallographic analysis was performed on all the conditions, including the base material, laser cleaned, and grit blasted samples.

Both planar analysis and cross sectional analysis of the roughly 1'' by 1'' sections of base, grit, and laser cleaned material were examined under optical microscopy, using the Hirox optical microscope (model KH-7700), and scanning electron microscope (SEM) models FEI Quanta 200 and FEI Quanta 650. In addition to microscopy, composition was determined in samples of all three processing conditions using energy dispersive spectroscopy, (EDS). EDS spot, line scans, and maps, were used to measure the elemental composition of cross sections, surface layers, and top planar surfaces of all three processing conditions. A x-ray diffraction scan was completed using a Panalytical X'Pert x-ray diffractometer.

### 3.7 Coating Adhesion Testing

After the beams in phase 1 were laser cleaned, a set number were repainted with standard epoxy paint for coating adhesion testing, using the pneumatic adhesion tensile testing instrument (PATTI) device. The PATTI device is used to test the coating adhesion of the paint to the underlying substrate, and conforms to ASTM D4541 and D7234 standards for coating adhesion testing. It works by slowly leaking in pressurized gas to a piston that is screwed to an aluminum 'stub' that is attached to the paint coating with a high strength epoxy. As the pressure inside the piston increases, the force applied to the stub also increases until it reaches the adhesion strength of paint at which point the stub and paint layer suddenly break away from the surface, and the corresponding burst pressure is recorded. Figure 3.22<sup>45</sup> shows a schematic of the PATTI piston assembly, illustrating how the increasing air pressure inside the chamber applies a force to the rubber gasket, in turn creating an upward pulling force on the stub. The recorded burst pressure is used to calculate the tensile pull-off tensile strength using the equation [3.1]<sup>45</sup>:

$$\text{eq. [3.1]}^{45} \quad POTS = \frac{(BP \times Ag) - C}{Aps}$$

where the pull of tensile strength (POTS) is equal to the recorded burst pressure (BP) times the contact area between the gasket and reaction plate ( $A_g = 4.06 \text{ in}^2$ ), minus a piston constant specific to the piston itself ( $C = 0.286 \text{ lbs.} \pm 1.5\%$ ), all divided by the area of the pull stub, ( $A_{ps} = 0.1963 \text{ in}^2$ ).

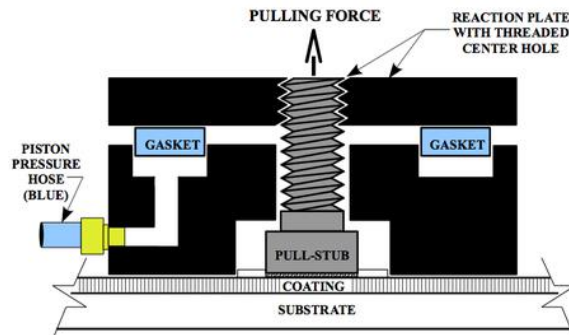


Figure 3.22. Schematic cross section of the PATTI adhesion testing device.<sup>45</sup>

Figure 3.23 shows the surface of a laser cleaned flange, and then the repainted surface with the PATTI pull-stubs attached.

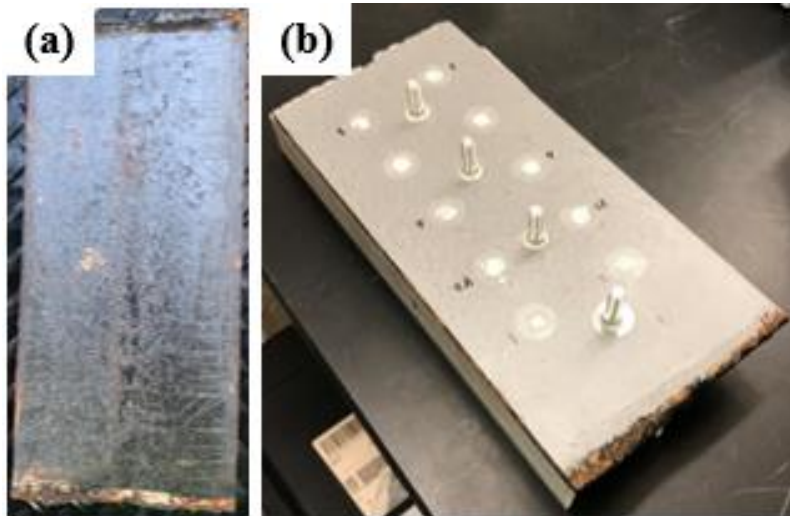


Figure 3.23. LACR cleaned I-beam flange (a) before and (b) after repainting with PATTI stubs attached.

Using conversion tables that use equation [3.1], the burst pressure can be correlated to a pull of tensile strength of the coating, giving a representation of the strength of the coating adhesion to

the underlying substrate. Figure 3.24 shows the PATTI testing set up and labels for each of the parts and functions of the device.

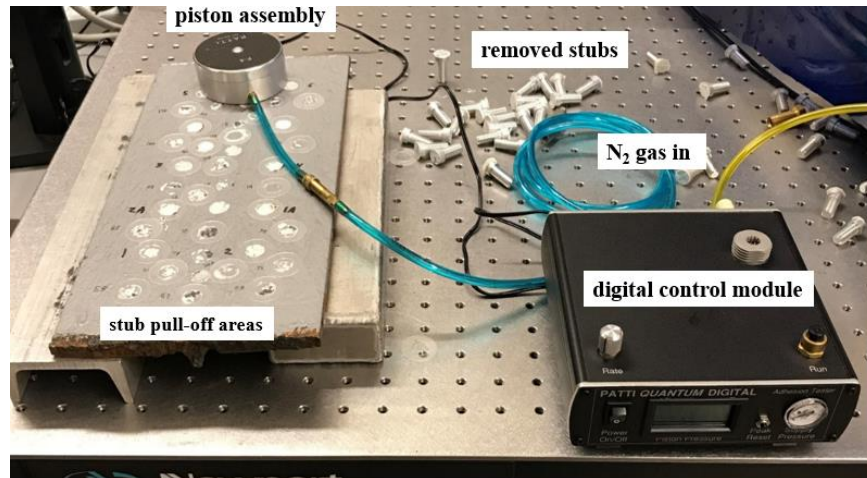


Figure 3.24. PATTI testing set up with each component labeled.

### 3.8 Mechanical Testing

In order to determine the effects of laser cleaning on the mechanical properties of the underlying metal, tensile, fatigue, and hardness tests were performed. Tensile testing included pulling dog bones of the base metal, grit blasted metal, and laser cleaned samples. Tensile tests were performed on an Instron MTS Series 793 servohydraulic UTM and used a laser extensometer to measure the initial gauge length, and the gauge length elongation during the test.

Fatigue testing was performed on the same Instron UTM frame that was used for tensile tests, and fatigue samples were run in a pull-pull configuration, so that the dog bones were always under tensile stress, with a fatigue ratio  $R$  of 0.1, and at 10 hertz frequency. Samples that did not fail before five million cycles were considered run out tests and were stopped upon reaching this number of cycles.

Hardness tests were performed on cross sections for each respective processing condition.

Vickers hardness measurements were taken as a function of depth from the surface of the metal

down into the middle of the cross sections. A standard diamond tipped Vickers Hardness indenter was used with a mass of 0.5 kg and indentation time of 15 seconds.

## **Chapter 4 Results**

### **4.1 Introduction**

The results gathered in this project range from general observations and the documentation of processes, to the characterization of samples and results of mechanical testing and other material property tests such as coating adhesion. Observations were made during the phase I, II, and III tests, and material characterization provided technical data that gave both qualitative and quantitative results to the effects of laser cleaning the bridge I-beams. In addition to the documentation of the different tests and sample characterization, industrial hygiene survey's provided data about the worker and environmental safety of the laser cleaning process, especially during the phase IV testing, where laser cleaning for lead removal was investigated.

During the laser cleaning of I-beam sections in phase I, onsite bridge components in phase II, and a bridge bearing in phase III, notes and photographs were used to document the processes as they took place and to record the overall demonstrations, in addition to industrial hygiene surveys in phases I and II. At the University of Virginia, sample characterization and testing took place, which began with macroscopic optical microscopy of the planar surface in all three conditions, and then scanning electron microscopy (SEM). After this cross sections for each of the samples were polished and etched, and again these were analyzed using both optical and electron microscopy. Energy dispersive spectroscopy (EDS) and x-ray fluorescence spectroscopy (XRF) analysis allowed for determination of the elemental composition of the cross sections, surface layers, (oxides, paint coatings), and microstructure of the steel itself. Mechanical testing included hardness, tensile, and fatigue testing. Results gave insight to the structural integrity of the samples, as well as how different processing conditions affected the mechanical properties of the material.

## 4.2 General Coating Removal Observations

The first results that were obtained in this project were the general observations made during the phase I processing of the I-beam sections at Norton Sandblasting. During this demonstration, the process of laser coating removal was documented and provided a sense of the effectiveness and feasibility of using the laser to remove paint, rust, tar, and dirt from the beams. The I-beam sections used were from a bridge built in the 1930s, and were covered in thick rust, scale, paint tar, and dirt. Before any laser cleaning was attempted, the large scale debris was scraped away using a metal hand scraper. After bulk flakes of scale were removed mechanically, the laser testing began. Figure 4.1 shows a typical I-beam section that was used in phase 1.



*Figure 4.1. Sample I-beam section used in phase I.*

Due to the heavily decayed and dirty state of the I-beams, multiple laser passes were required to reach the substrate of the beams. In general it required between 3 and 6 passes before all the rust, paint, tar, and other detritus was removed. The number of passes needed depended on the operator experience, the speed of the laser movement and motions, as well as the state of the portion of the I-beam undergoing cleaning. The thickness and composition of the coating affected the rate of laser cleaning. Figure 4.2 shows what a portion of the cleaned I-beam looks like compared to the original state of the beam.

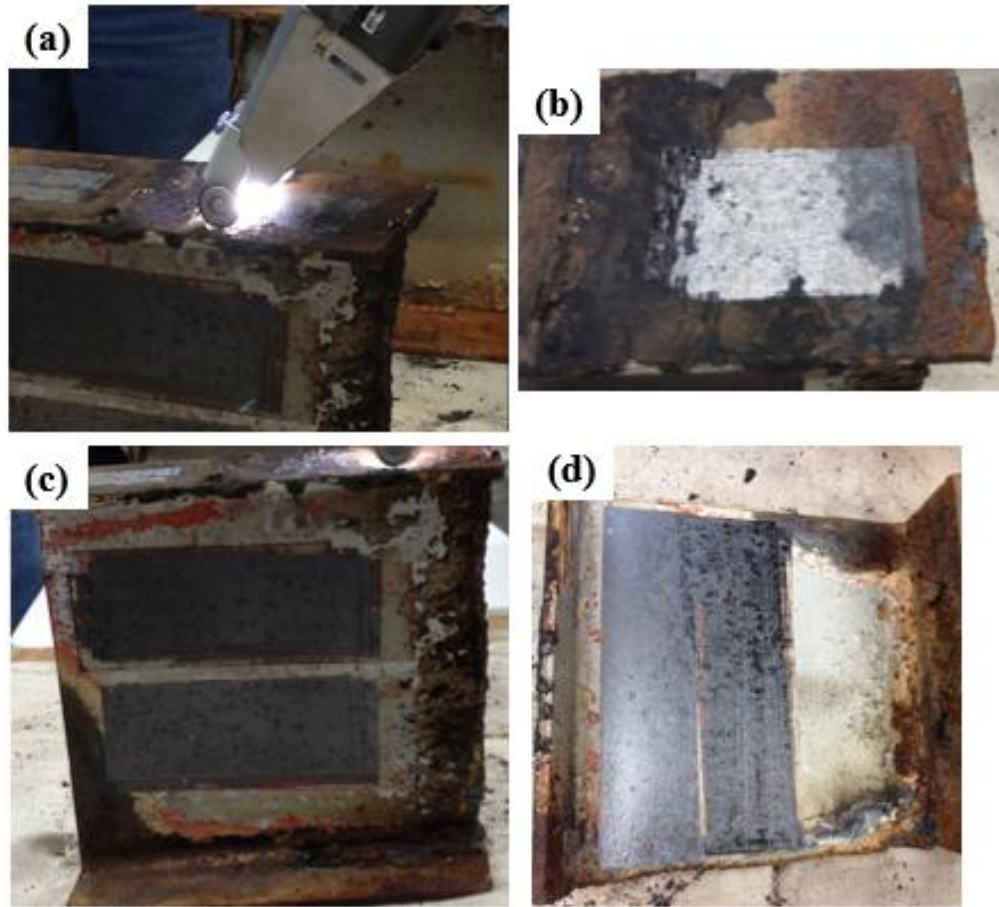


*Figure 4.2. (a) Laser cleaning interaction, (b) cleaned I-beam surface on a beam flange, (c,d), two parallel laser cleaned tracks.*

Upon initial cleaning of the I-beams, some of the first observations also included the presence of laser “tracks”, streaks that were parallel to the scanning laser beam and appeared darker in color than the surrounding substrate (figure 4.3). The appearance depended on the laser parameters that were used, including scan speed, pulse frequency, and the actual motion of the laser by the operator. In addition to the “darker” and “lighter” color of these laser tracks, there also appears to be splotchy areas consisting of this darker color and lighter colored areas surrounding these spots as well.

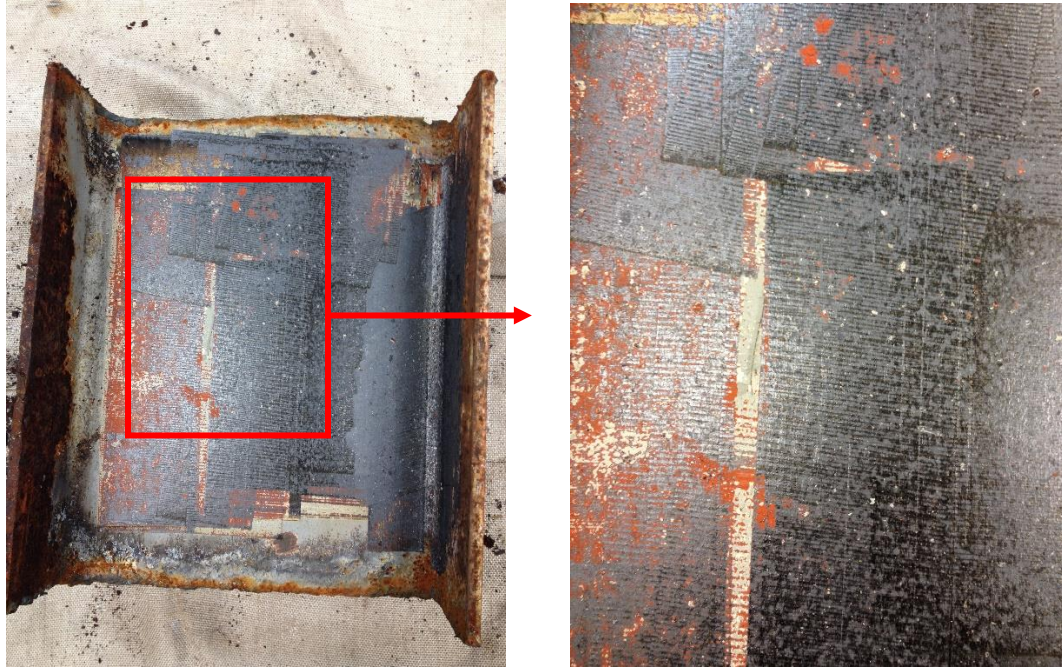
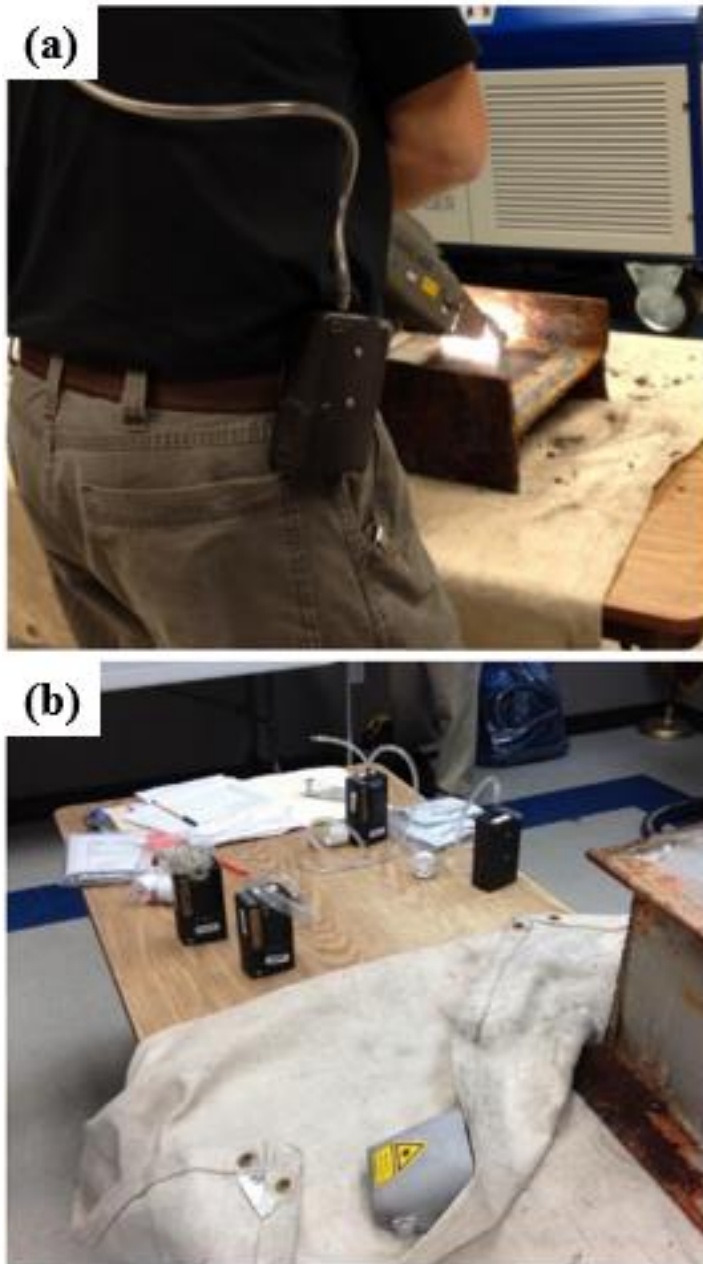


*Figure 4.3. Laser “tracks” left behind on the surface after laser cleaning. Between the tracks the random surface pattern of darker and lighter colored regions can be seen.*

Aside from the appearance of the laser cleaned surface, it was also noted that the red paint was more difficult to remove compared to the other paint coats. With a greater number of laser passes this red paint could be completely removed, however it often required more passes with the laser than the other paint coats needed for “complete” removal. Therefore a noticeable amount of surface area still contained the red paint layer on the surface. Of the twenty 1’ I-beam sections, eighteen were laser cleaned and two were grit blasted onsite at Norton Sandblasting as a comparative processing condition for further material characterization.

#### **4.3 Phase I Industrial Hygiene**

For the industrial hygiene survey, a project manager from The EI Group, Inc. collected both personal and area samples during the laser coating removal demonstration. The survey documented personal and area concentrations of a 31 profile scan of volatile organic compounds (VOCs) using an Assay 566 badge and included a nine metal profile sampling in accordance



with NIOSH method 7300 to capture contaminants emitted in the air associated with the simulated bridge coating removal operation. Figure 4.4 shows the personal samples worn by the laser operator.

After completion of the laser removal process, the particle filter system of the CleanLaser CL1000 unit was disassembled, sampled, and three bulk samples, one from each stage of the filtration system, was submitted to an environmental laboratory for toxicity characteristic leaching procedure (TCLP) analysis for eight metals (silver, arsenic, barium, cadmium, chromium, mercury, lead, and

*Figure 4.4 Personal industrial hygiene sampling set up. (a) The laser operator wearing a VOC collector on his belt with a tube leading to his breathing zone. (b) VOC collecting units used for area placement.*

selenium) by SW846 Method 6010C and SW7470A. The purpose of this survey was to evaluate the concentrations of various heavy metals and VOCs in the work area and to investigate whether the laser operator is exposed during the laser coating removal process even when using a laser equipped with a near HEPA filtration system and carbon filter. This survey was conducted

to determine compliance with Occupational Safety and Health Administration (OSHA) General Industry Standard – Subpart Z, Toxic and Hazardous Substances.

Throughout the approximately 8 hour shift both laser operators wore nine-metal profile area samples and VOCs assay badges clipped to their collars near their breathing zone.

The air monitoring results indicated that the personal and area concentrations of the 31 selected VOCs and nine metals (cadmium, chromium, cobalt, copper, iron, lead, manganese, nickel, and zinc) during the sampling period were below the OSHA Permissible Exposure Limit (PEL) as an 8-hour Time Weighted Average (TWA). All of the area and personal samples were below laboratory detection limits for all sample contaminants, with the exception of lead, however the measured concentrations of lead were well below the action level (AL, 0.03 mg/m<sup>3</sup>) at 0.0043 mg/m<sup>3</sup> for one of the operators and 0.0014 mg/m<sup>3</sup> for the other, both of which were also below the Permissible Exposure Limits for lead (PEL, .05 mg/m<sup>3</sup>).

The TCLP sampling results for metals in the activated carbon filter, HEPA filter, and particle debris filter of the laser system determined that the particle debris filter was hazardous for lead, and therefore the filter must be disposed of as hazardous waste and that appropriate personal protective equipment (PPE) should be worn during the removal of the filter for disposal. Of the three TCLP samples for each filter, TCLP 1 in the activated carbon filter showed all results below the reporting limit (non-hazardous), TCLP 2 in the HEPA filter showed all results were below the reporting limit except for lead (0.141 mg/L) (non-hazardous level), and TCLP 3 in the particle debris filter showed all results below the reporting limit, except for lead at 464 mg/L (hazardous for lead above 5 mg/L), and chromium at 0.302 mg/L (chromium reporting limit 0.1000 mg/L). However this result is unsurprising, due to the fact that the demonstration involved removal of lead based paint from the bridge beams. Also, because all area samples

collected had no detectable amounts of heavy metals or VOCs confirms that the filters were working as expected to, collecting contamination before recirculating air back into the surrounding environment.

#### 4.4 Planar Surface Analysis

Analysis of the laser cleaned, grit blasted, and base material included optical and electron microscopy. Figure 4.5 shows the interface between the laser cleaned surface and the paint coating that was present on the base material before cleaning. Optical microscopy shows a fairly clean interface with a distinct boundary between the cleaned and exposed substrate and the paint.



*Figure 4.5.* (a) Macroscopic and (b) optical microscopic view of the interface between the painted and laser cleaned surfaces.

However, under closer examination using electron microscopy, it becomes clear that the interface between the paint and the underlying substrate is broken without a clean boundary between the paint layers and the underlying substrate. The thickness of the paint coatings that taper down to the substrate depend on how the different paint layers have been removed, meaning that the laser parameters are one factor that dictate the interface between the paint and the underlying substrate. Figure 4.6 shows this paint substrate interface as imaged in the SEM.

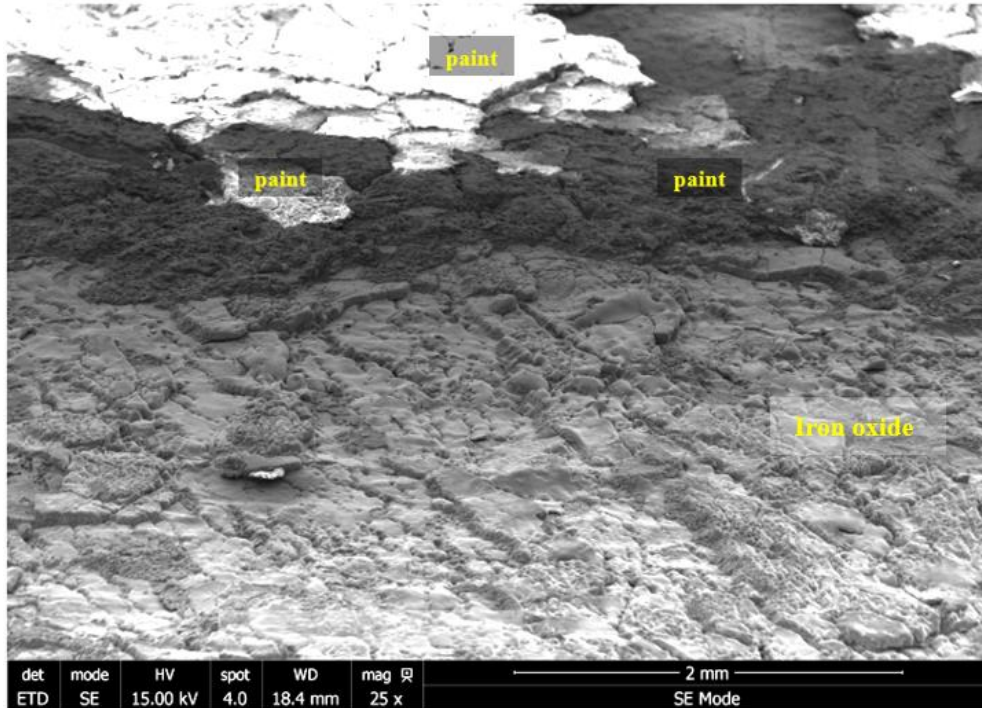


*Figure 4.6. SEM micrograph showing the paint to substrate interface.*

In certain places along this paint to laser cleaned surface, the effect of the laser scan can be observed. As the laser scans back and forth it removes the top most layer of paint before removing lower paint coats and eventually reaching the underlying substrate. In figure 4.7, arrows indicate the areas of removed upper paint coat and the exposed lower paint coat, as well as the removed bottom paint coat which exposes the substrate. These areas of removed coatings match up with the laser tracks which can be seen on the completely cleaned surface adjacent to the paint.

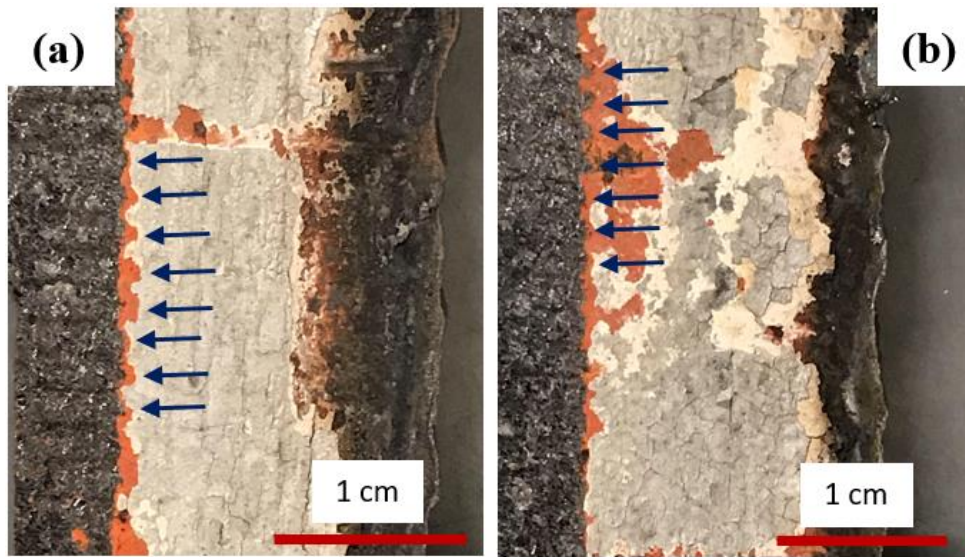


*Figure 4.7. a.) Arrows indicating where the top layer of paint has been removed by the laser scan path. b.) Arrows indicating where all the paint has been removed by the laser scan exposing the underlying substrate.*

Further planar microscopy on the laser cleaned surface shows how clusters of red paint remain on some spots on the surface (figure 4.8). It is suspected that further laser passes would allow for complete removal of all the residual paint. It is interesting to note the difference in appearance of the laser cleaned surface in some areas, depending on the specific laser parameters that were used in combination with the coating system, in other words the varying condition of the paint layers at different areas of the beams. Figure 8 shows a “rocky” mineral type of surface which contrasts to a shinier, more metal surface present in other regions.



*Figure 4.8. Macro scale optical micrograph of the laser cleaned surface showing the remaining clusters of “red” base coat paint.*

Optical microscopy of the laser cleaned surface reveals areas of high reflectance, and areas that appear darker with lower reflectance of light, that correspond to the random disordered distribution of reflective to non-reflective regions on the laser cleaned surface. These regions seem to vary throughout the surface randomly. Figure 4.9 shows optical micrographs of the laser cleaned surface that show these different areas.

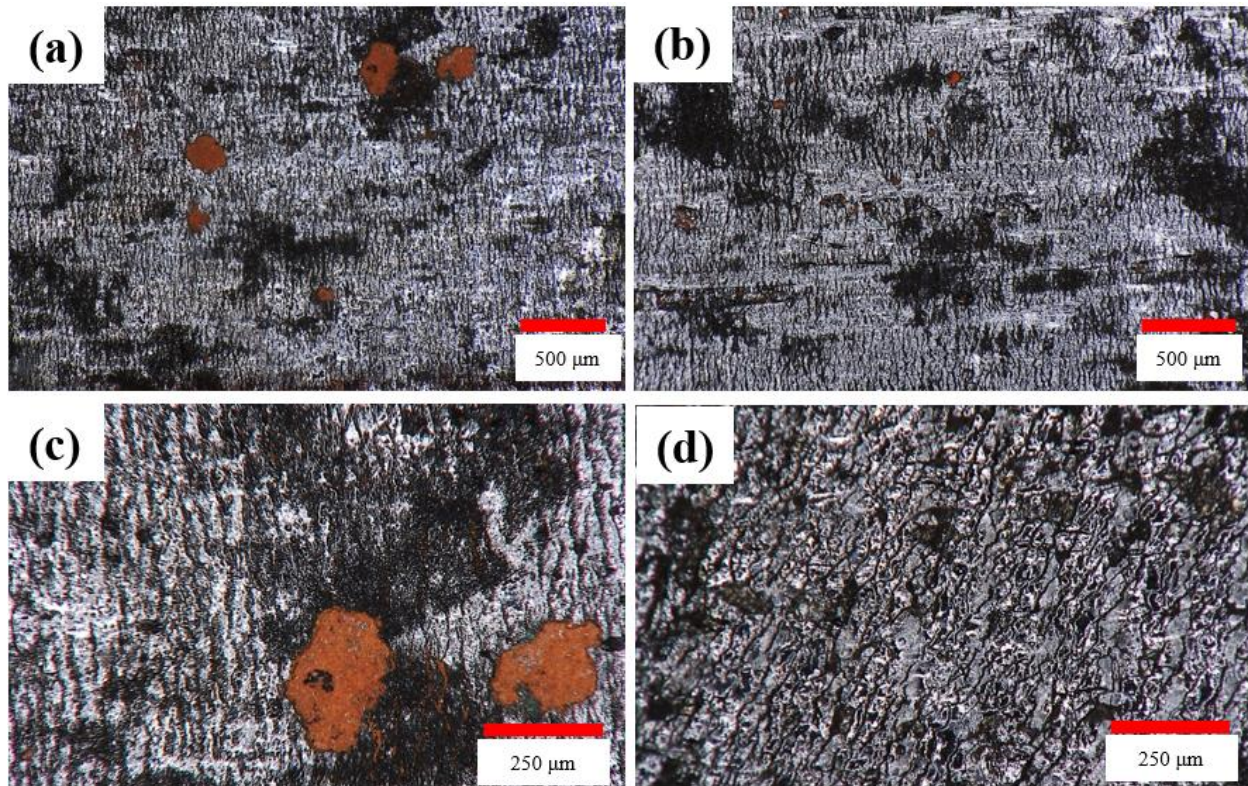


*Figure 4.9. Optical micrographs showing the bright high reflective surface and the darker less reflective areas. A,b.) Clusters of red paint remaining on the surface, that vary in size depending on the number of laser passes. c.) Higher magnification optical micrograph of the clusters of paint remaining on the surface. d.) A laser cleaned region free from paint.*

Using electron microscopy to gain a more detailed view of the surface, the surface topology is revealed more accurately. It is observed that the reflective “shiny” regions of the surface are relatively flatter, and therefore can reflect ambient light more efficiently than the rougher, courser areas, which are much less reflective to visible light and therefore appear dark. In figure 4.10, SEM micrographs of the surface show how regions on the surface with different roughness cause the light to be reflected differently, resulting in the shiny or dark appearance of the surface in different regions.

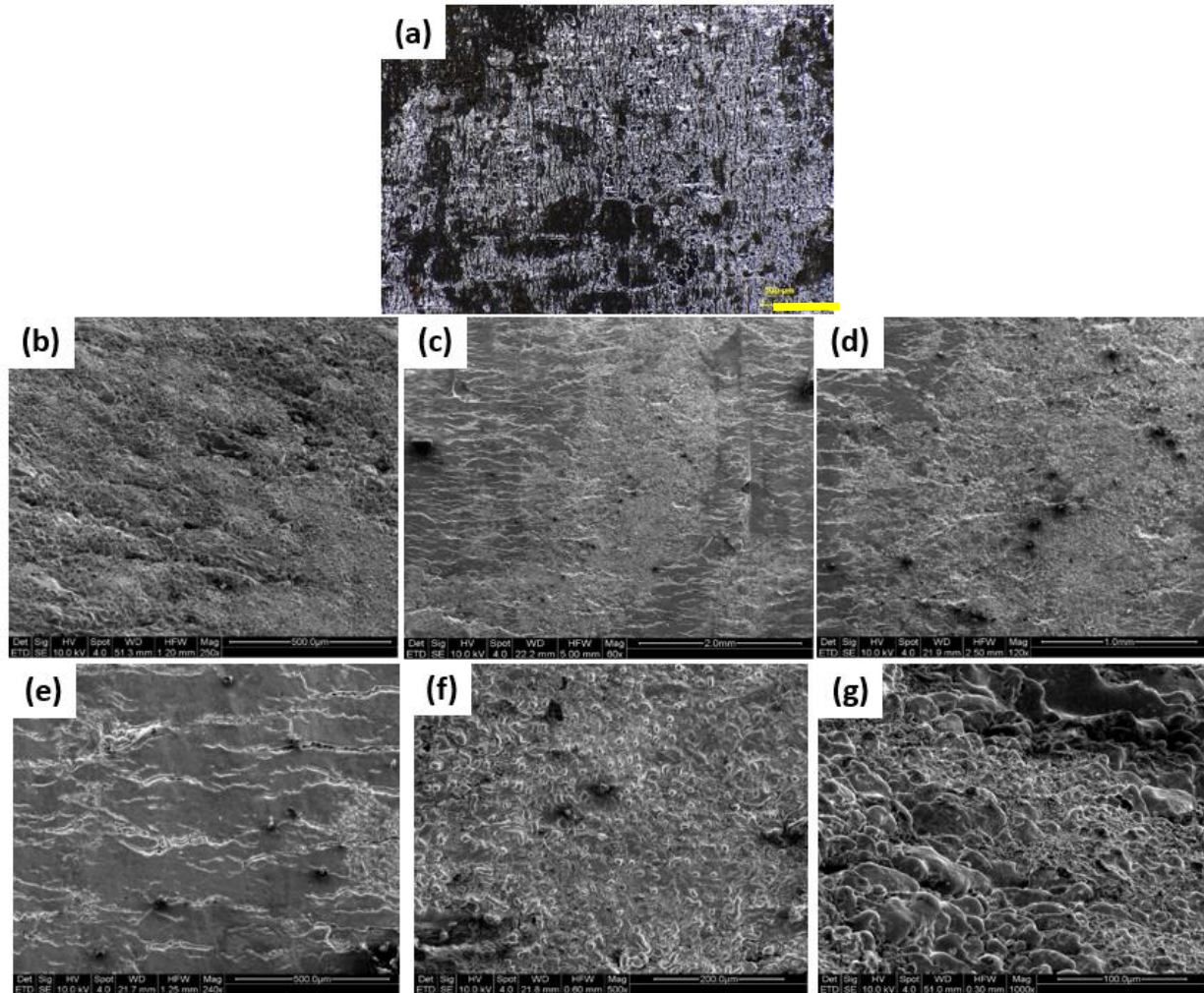
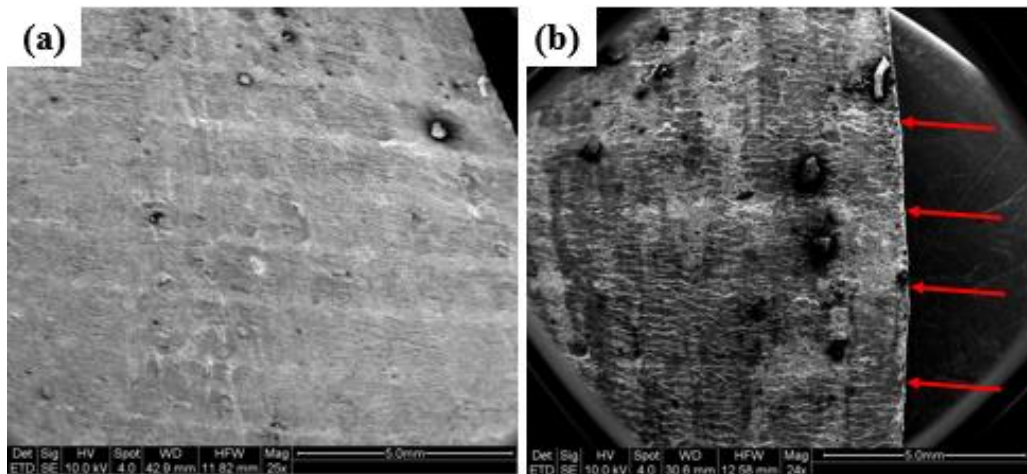


Figure 4.10. (a.) Optical micrograph showing the random distribution between the optically bright, reflective surface and the darker rougher surface regions. Scale bar = 500  $\mu\text{m}$  (b.) SEM micrograph of the surface topology in the darker, less reflective surface area. (c.) SEM micrograph showing the difference in surface topology between the smoother surface and the rough surface (streaking down the middle of the image). (d.) Higher magnification of region shown in c. (e.) High magnification SEM of the smooth reflective surface. (f.) SEM micrograph of a rougher, darker surface region. (g.) High magnification of the region shown in f.

SEM also helped to reveal the laser tracks that were observed simply by eye. In order to see these tracks the sample had to be tilted to a high angle of approximately 60 degrees, at which point the tracks become apparent using a secondary electron detector. Figure 4.11 shows the laser tracks that were observed by tilting the sample in the SEM.



*Figure 4.11. a.) Tilting the sample in the SEM allows visualizing the laser tracks produced on the surface due to the laser material interaction. b.) Using higher contrast helps to define each individual “track”, indicated with red arrows.*

Despite the shiny metallic appearance of the laser cleaned surface, compositional analysis with energy dispersive spectroscopy (EDS) shows that the laser cleaned surface actually consists of an iron oxide. At higher magnifications tiny “mud” cracks can be observed in the iron oxide surface that remains (figure 4.12).

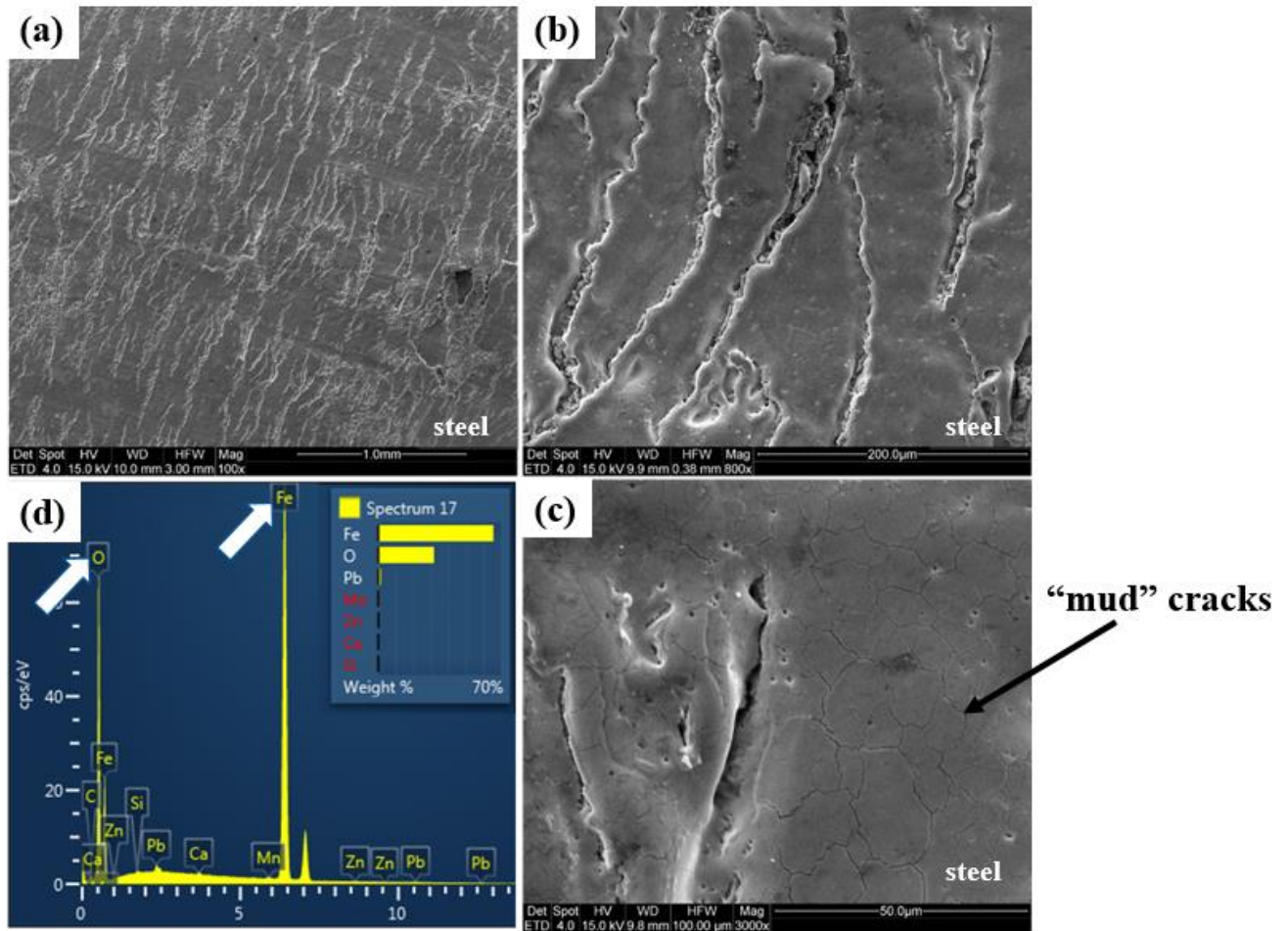
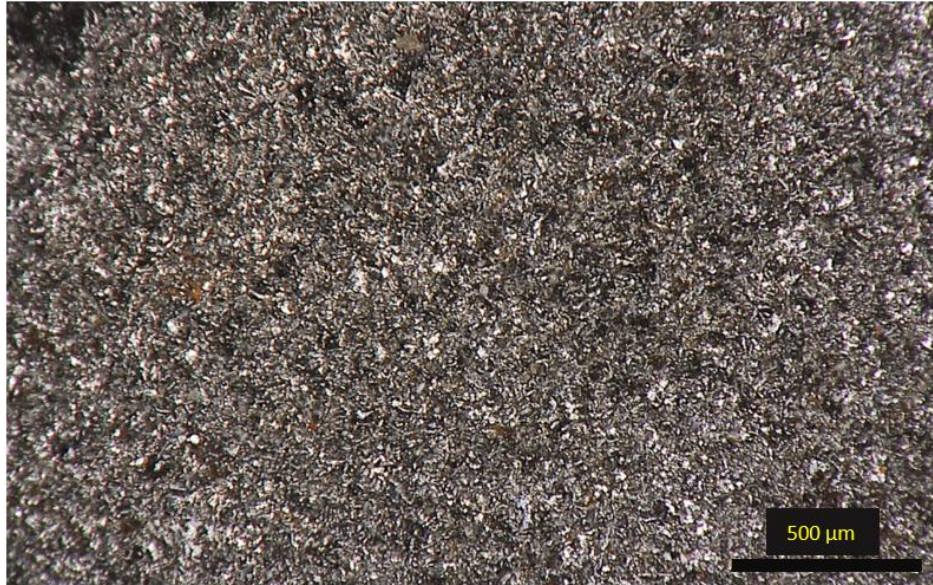


Figure 4.12. a,b.) SEM micrographs showing the laser cleaned surface topology. c.) “Mud” like cracks seen at high magnification. d.) EDS scans showing the iron oxide composition of the laser cleaned surface.

In contrast to laser cleaning, grit blasting appeared to do a more thorough job of removing all the layers of paint. While spots with paint or rust may remain in areas of the I-beam depending on how meticulously a specific area of the surface was blasted, in general the grit blasted surface was devoid of paint and/or oxides, as seen by the naked eye. In addition, the grit blasted surface has a different macroscopic appearance, and seems to be rougher as well as cleaner to the naked eye. Figure 4.13 shows the grit blasted surface as seen with optical microscopy.



*Figure 4.13. The grit blasted surface seen using optical microscopy.*

In addition to planar analysis of the laser cleaned and grit blasted surfaces, the base material that was still covered in paint was also studied. Figure 4.14 shows the paint layers that cover the I-beams before any processing, and the paint coat from bottom to top can be observed. The red paint makes up the first coat, followed by the white colored paint and then the grey top coat.

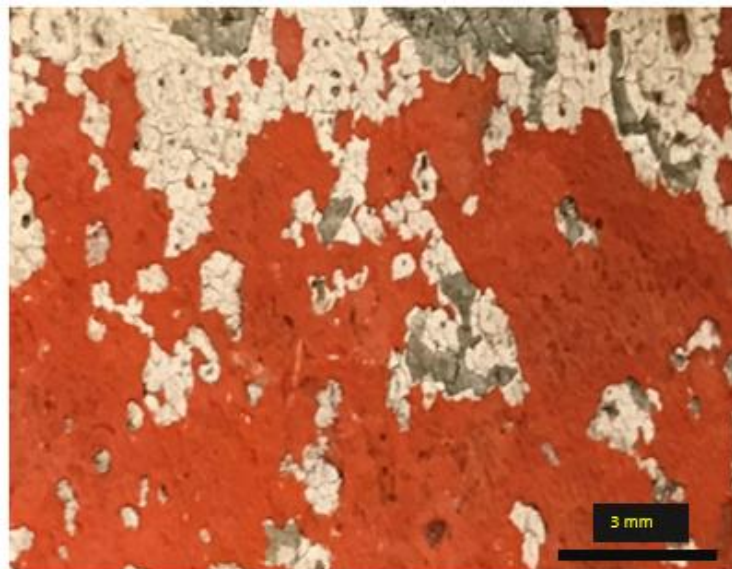


*Figure 4.14. Macro optical image of the paint layers covering the I-beams. From bottom to top: red paint, white coat, and grey top paint coat.*

#### 4.5 Cross Section Analysis

Cross sectional analysis of all processing conditions, including the base material, provides information about the laser-material interaction process, as well as the effect of grit blasting the metal. Comparison with cross sections of the base material allow study of how either process, grit blasting or laser cleaning, affects the metallurgical structure of the material.

Cross sections of the laser cleaned substrate revealed the presence of a semi-continuous iron oxide layer. It varies roughly from 100  $\mu\text{m}$  to 20  $\mu\text{m}$  across the surface, and in some places is not present at all. Figure 4.15 shows a cross section of the laser cleaned substrate and the oxide layer that remains.

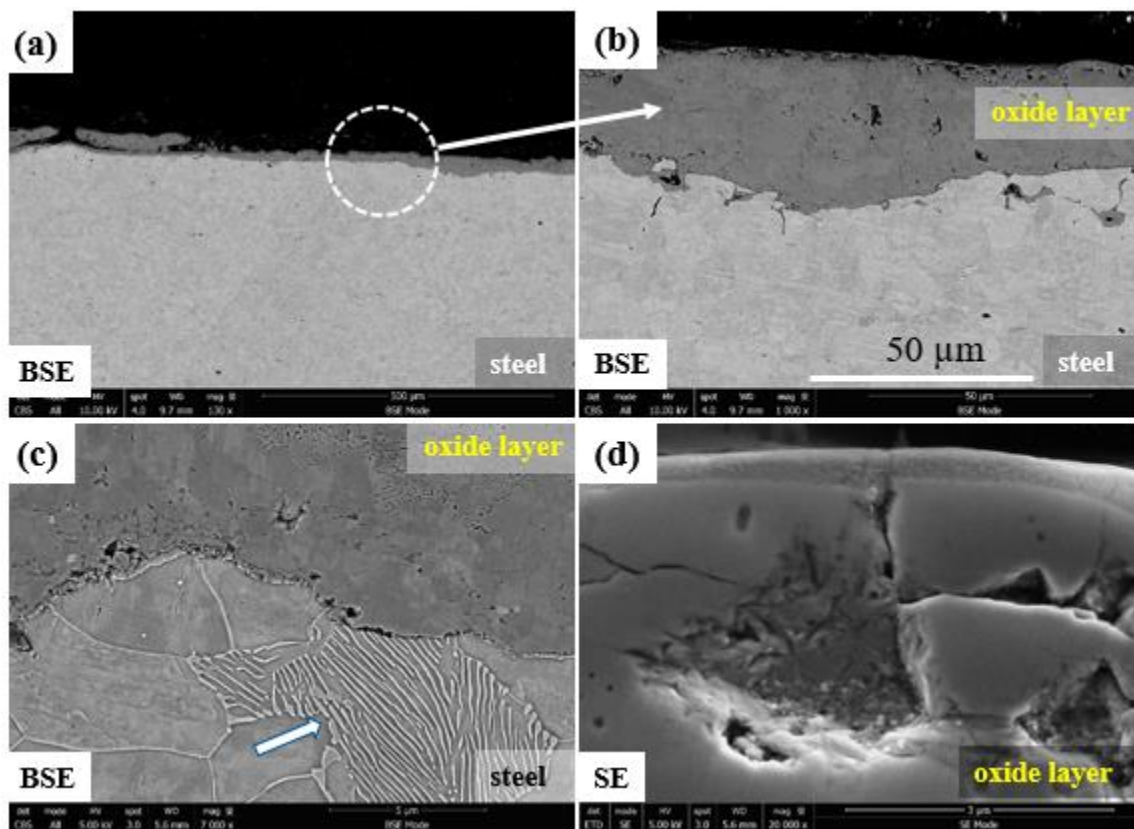
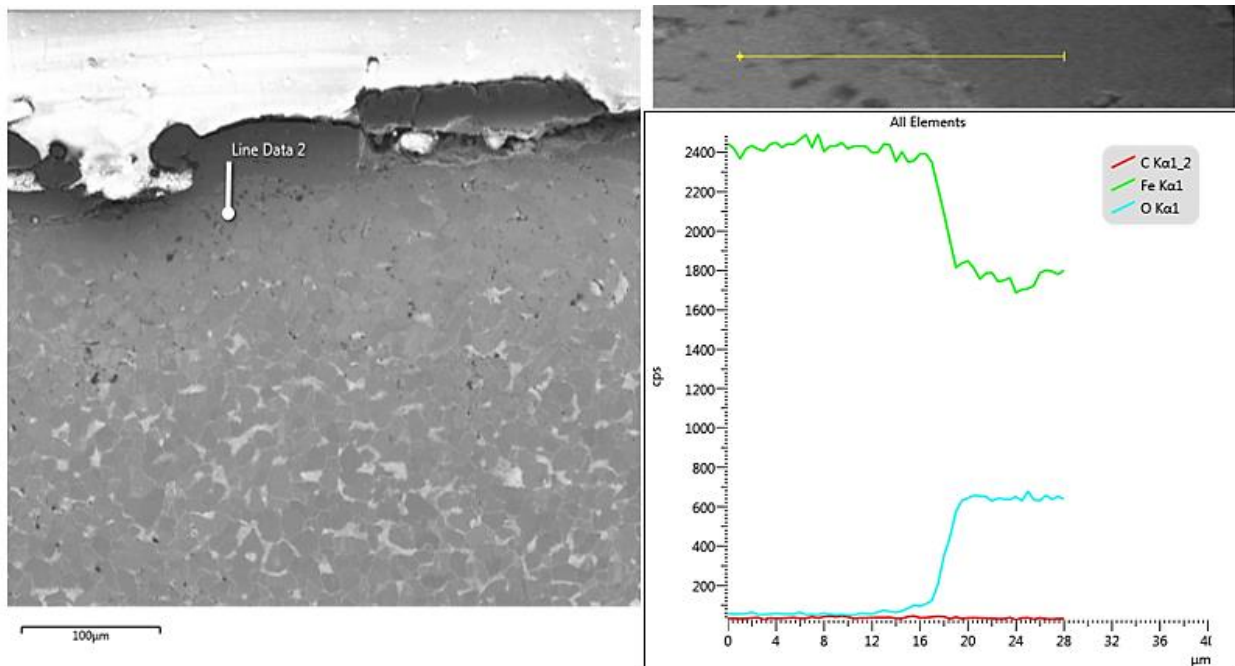


Figure 4.15. Cross section analysis of the laser cleaned surface shows the a,b.) Iron oxide layer on the surface, c.) intact metal microstructure directly below the iron oxide surface layer, and d.) the laser melted top most region of the iron oxide surface.

Underneath the iron oxide layer, the pearlite microstructure of the steel is observed, suggesting that any heat transferred to the underlying steel, if any at all, is not enough to cause significant melting or thermal damage to the steel microstructure. Using EDS, a line scan (figure 4.16) shows the abrupt transition from the iron oxide layer to the underlying steel, which compositionally as well as structurally appears to be unaffected by the laser heat.



*Figure 4.16. Line scan between the I-beam metal and the iron oxide surface layer.*

At high magnifications the melting of a thin surface region of the iron oxide, on the order of 1  $\mu\text{m}$  or less in depth below the oxide surface, can be seen. This finding corroborates the observation of surface melting, and it indeed seems to be the case that the very near surface region of the iron oxide layer undergoes melting due to the laser heat input. Figure 4.17 shows in detail the oxide layer with the melted region indicated.

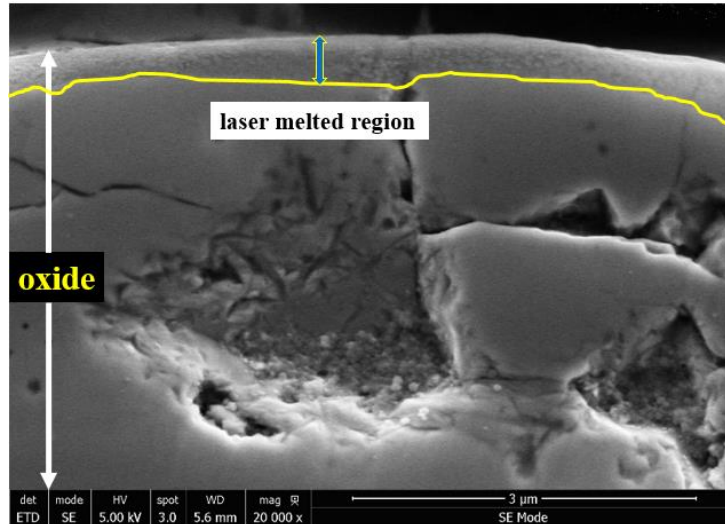


*Figure 4.17. High magnification SEM shows the melted surface region of the iron oxide layer. As expected, grit blasted sample cross sections lack the oxide layer that is found on laser cleaned samples. Instead, the near surface region of the cross sections revealed the deformation of grains due to the forces imparted to the metal during grit blasting. Up to a depth of roughly 10 μm, the grains are flattened and disfigured compared to the undeformed grains below them. Figure 4.18 shows SEM micrographs of grit blasted sample cross sections, and the near surface grains that have been deformed due to grit blasting.*

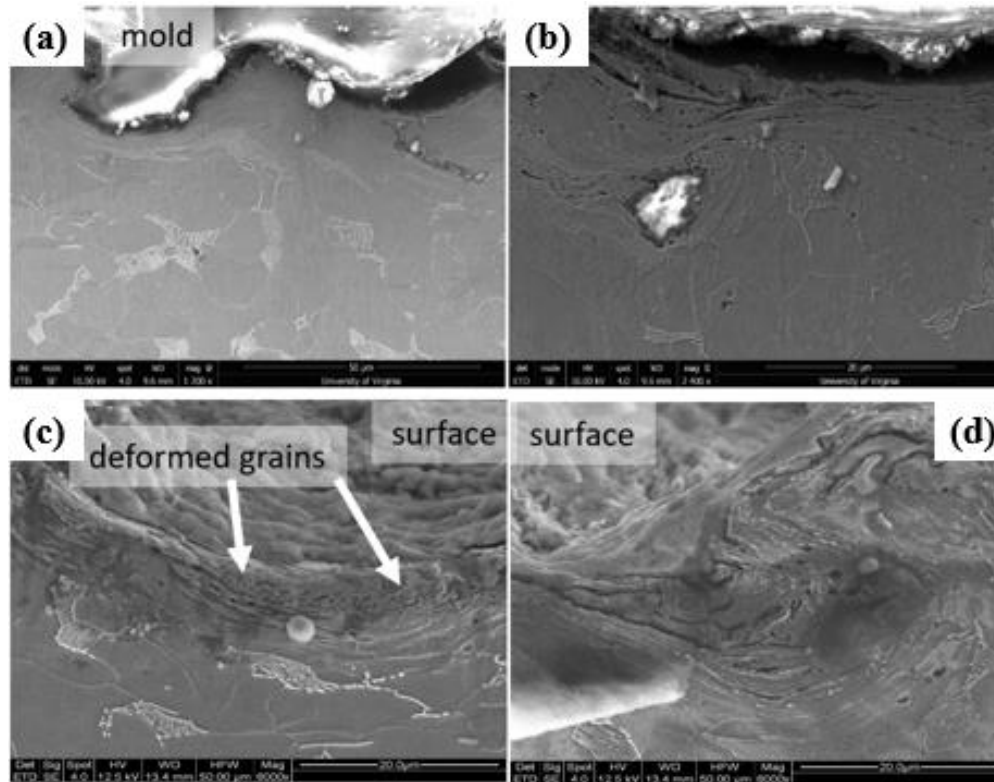


Figure 4.18. Grit blasted sample cross sections showing the deformed grains in the surface region. (a) scale bar = 50  $\mu\text{m}$ , (b) = 20  $\mu\text{m}$ , (c) = 20  $\mu\text{m}$ , (d) = 20  $\mu\text{m}$ .

Aside from the deformed grains at the surface, the roughness of the grit blasted surface is implied by the high amplitude of peaks and valleys in the profile view of the cross section surface. This is in contrast to the relatively smooth cross section surface profile of the laser cleaned samples.

Cross sections of the base metal show that underneath the three paint coats, the iron oxide layer that is observed after laser cleaning is already present. Therefore the I-beams used in Phase I were never originally grit blasted, and the process of laser cleaning removes the top paint layers in turn exposing the iron oxide that is observed on laser cleaned samples. Figure 4.19 shows a cross section of the base metal using both electron microscopy and optical microscopy. This clearly shows the different layers of paint as well as the iron oxide layer and steel.

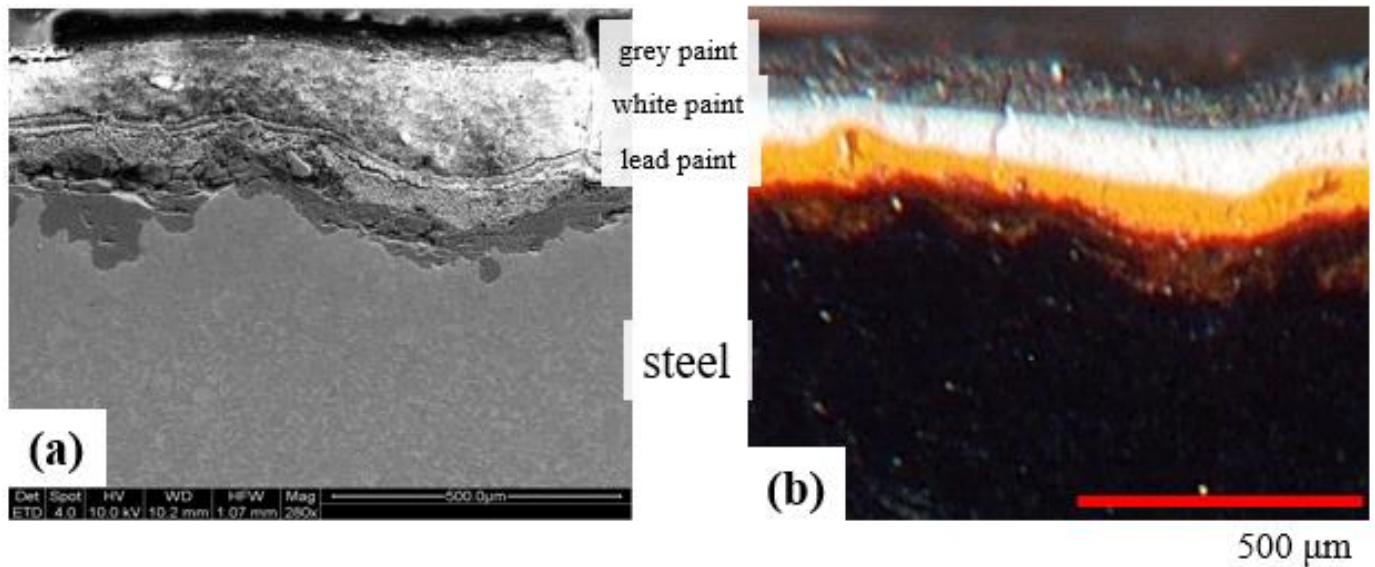


Figure 4.19. SEM (a) and an optical micrograph (b) of a cross section of the base material showing the layers of paint and iron oxide.

Because this oxide layer is present on the steel even before it was originally painted, this suggests that it is oxide that has formed after the I-beam was made in a steel mill, and has since remained on the surface of the steel.

SEM backscatter electron (BSE) imaging also helps to provide an idea of the composition of the paint and oxide layers. Because backscatter images provide z contrast, meaning that higher atomic weight elements appear brighter than lighter elements, which appear darker, certain paint layers such as the lead paint and the iron oxide will stand out from other layers with different compositions. Figure 4.20 shows SEM backscatter micrographs of the base metal cross sections. The lead containing base coat appears the brightest as expected, because of the high atomic weight of lead atoms. In addition to the lead paint the iron oxide layer is strongly contrasted from the steel because of the relatively high oxygen content of the oxide. Aside from the composition of the paint and iron oxide layers, these micrographs further characterize the aged and rough state of the coatings on these beams. In Figure 20 (a) and (b) large pores can be observed within the oxide layer, which ideally would not be present on freshly coated steel. Parts (c) and (d) also

clearly show particulate that has been forced into the coating, creating an opening to the underlying substrate.

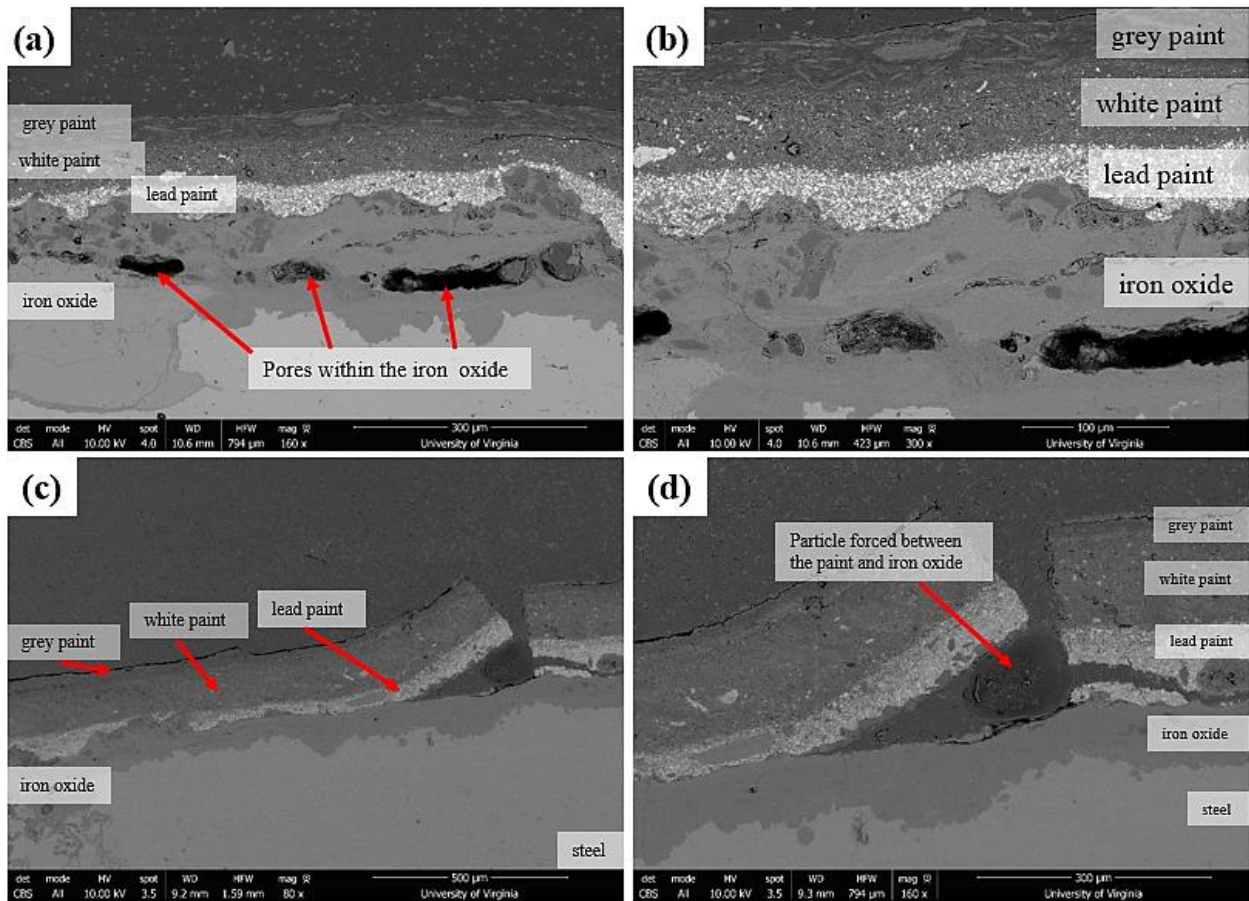
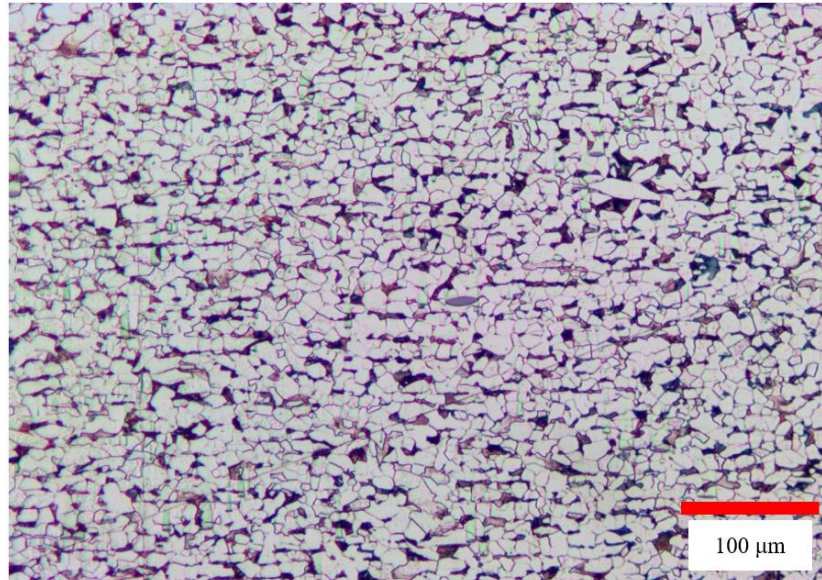


Figure 4.20. (a) BSE micrograph showing the steel, iron oxide, and three paint layers. (b) High magnification micrograph of (a), showing the pores that are present in the oxide layer. (c) BSE micrograph of an embedded particle between the iron oxide and the adjacent paint layers. (d) Higher magnification micrograph of (c), detailing the region containing the embedded particle.

#### 4.6 Microstructure

Below the surface regions in any of the samples, the microstructure is the same in each sample. Both optical and electron microscopy were used to examine the microstructure of the A36 steel. As expected, the microstructure was typical of a low carbon steel. At low magnification, the texture in the microstructure due to the rolling of the steel in the mill can be observed. As shown

in figure 4.21, the grains have a lateral shape that seems to be “stretched” out in the horizontal direction. This is due to the rolling during the manufacturing of the I-beam, which shapes the grains into the laterally stretched shape that they exhibit.



*Figure 4.21. Optical microscopy showing the textured microstructure due to the rolling of the steel into the I-beam shape.*

In figure 4.21 the darker grains are pearlite colonies, and the lighter grains are alpha ferrite. The darker pearlite grains help to bring out the rolling direction by providing contrast to the microstructure in the optical micrograph. Steel stringers or inclusions, were also observed in the microstructure as well. Figure 4.22, shows a higher magnification view of the etched microstructure. Dispersed between the alpha ferrite and pearlite, the steel stringers appear as dark grey “metallic” colored particles. These stringers are also stretched out along the rolled direction of the beam along with the adjacent grains showing the same texture. MnS inclusions are common impurities in steels and can be categorized as specific types. In this case the MnS inclusions appear to be type II inclusions (more information in appendix A1).

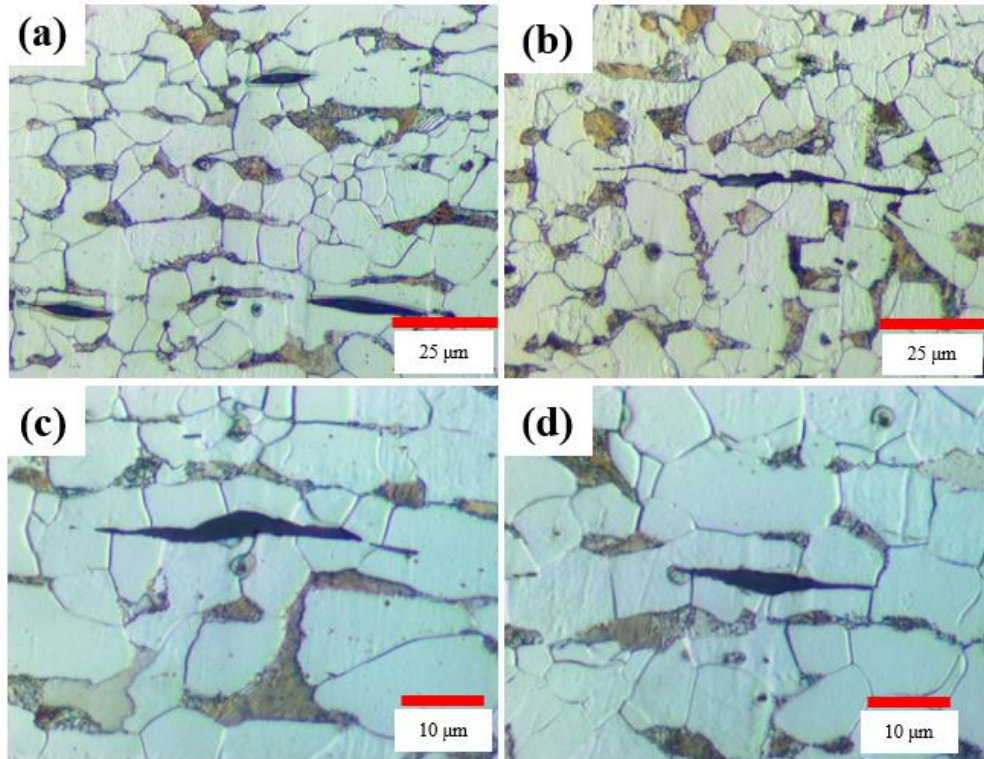


*Figure 4.22. Steel stringers present in the A36 steel microstructure. (a,b): 50x magnification, (c,d): 100x magnification*

In addition to optical microscopy, electron microscopy provided further characterization of the steel microstructure. With the higher resolution and magnification provided with electron microscopy, more detail in the microstructure can be observed. In high magnification micrographs the lamellar structure of the pearlite phase can be discerned much more easily than in the optical micrographs, and the steel stringers can be observed in more detail. (Figure 4.23).

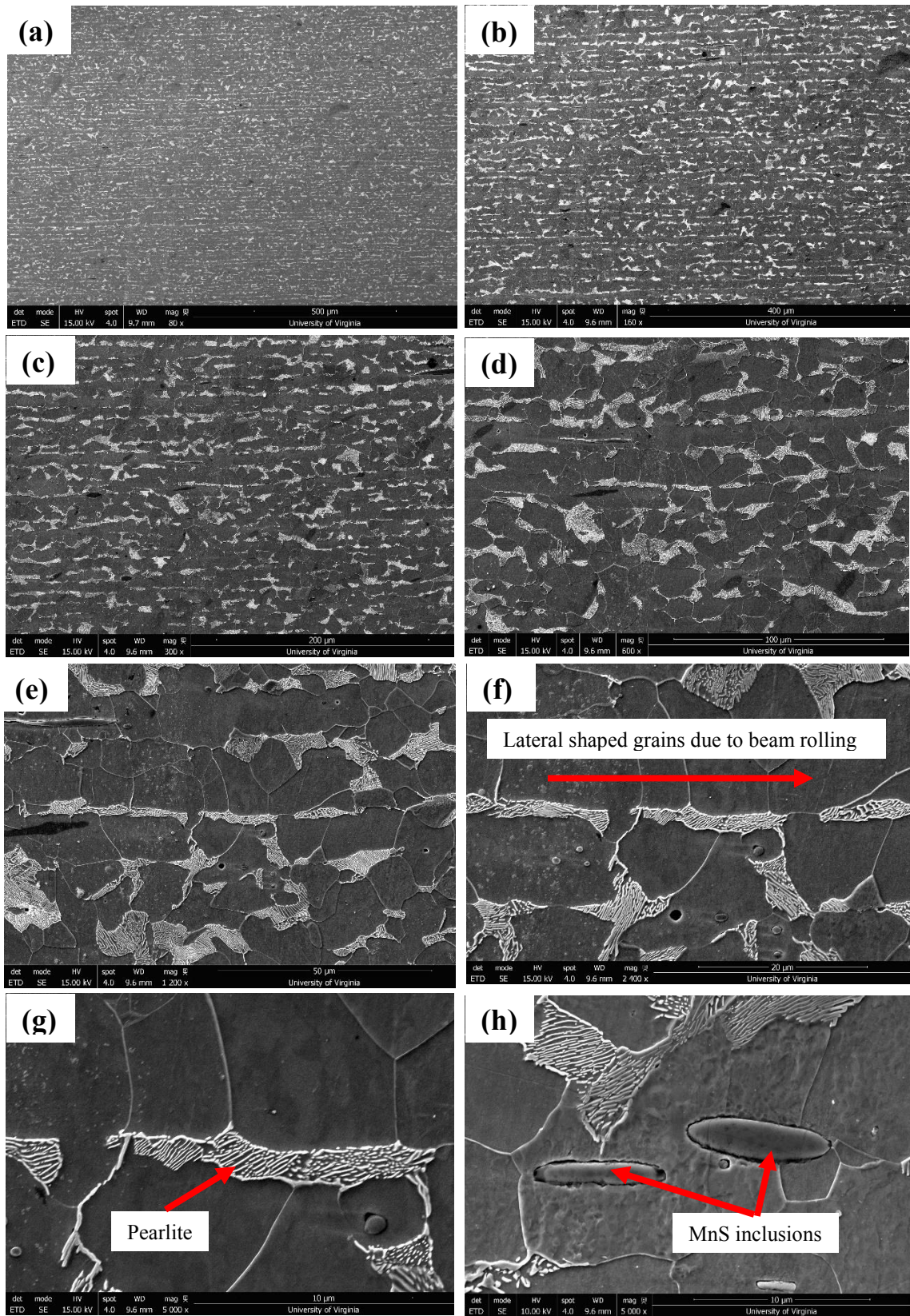


Figure 4.23. SEM micrographs of increasing magnification showing the steel microstructure and texture. a.) 80x, b.) 160x, c.) 300x, d.) 600x, e.) 1200x, f.) 2400x, g., h.) 5000x.

#### 4.7 EDS Paint Composition Analysis

To study the layers of paint present on the base material, cross sections were analyzed with both optical and SEM, and in addition, EDS was used to study the composition of the different paint coats. It was determined that there are three different layers, a red base coat, white layer, and a top coat of grey paint. Figure 4.24 shows an EDS line scan from the top paint layer through to the steel, and by plotting the oxygen and iron content, the transition from steel, to the iron oxide layer, and to the top layers of paint can be seen.

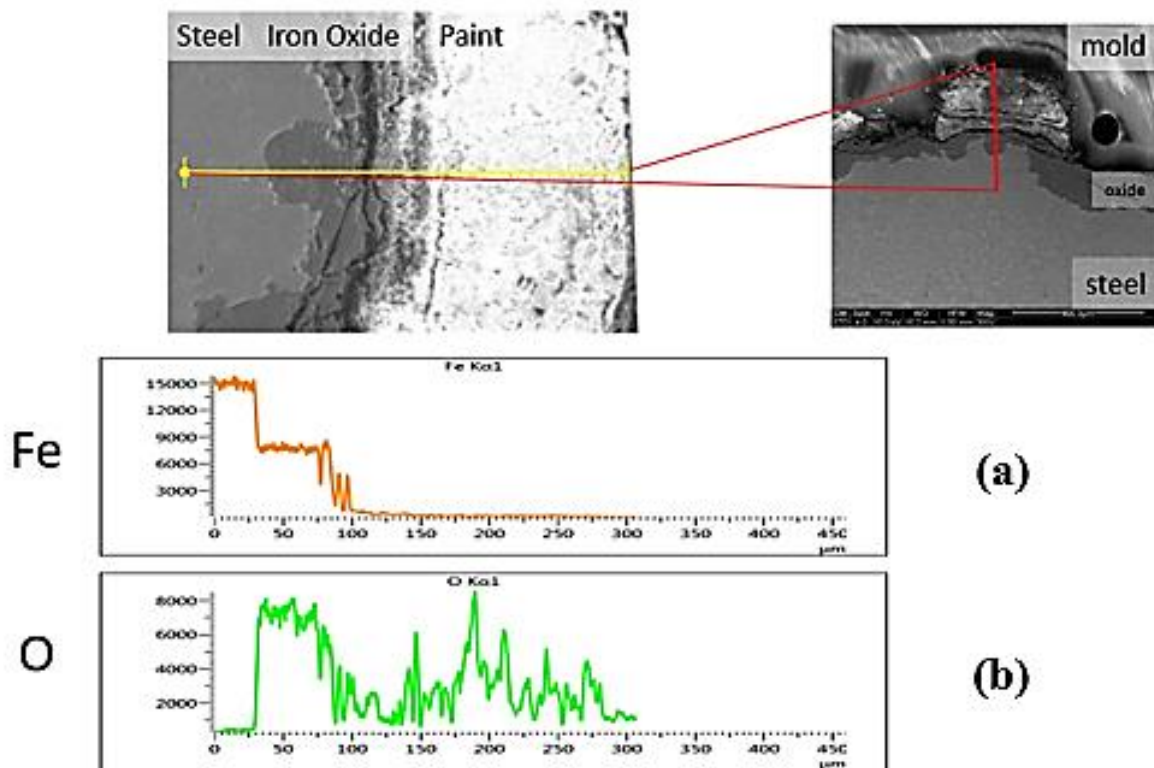


Figure 4.24. EDS line scan delineating the transition from paint to iron oxide surface layer to steel. (a) Shows a clear transition in iron content from steel, to iron oxide, and paint. (b) Likewise shows the low oxygen content of the steel compared to the high oxygen content within the iron oxide layer, followed by the variable amount of oxygen present in the paint.

It is clear that the steel is nearly devoid of oxygen, or that it is at least present in a low enough amount to not be detected by EDS, and therefore the steel can be considered to be unaffected chemically by the adjacent iron oxide layer. The oxide layer is easily detected by the EDS line

scan as the oxygen rises (to about 8000 counts) corresponding to the simultaneously decrease in the iron signal (from 15000 counts in the steel to roughly 8000 counts in the oxide). Throughout the outer layers of paint there seems to be little iron present, however the oxygen content varies throughout the paint layers.

Using the same line scan to analyze the lead paint layer, it is apparent that the lead is mostly present in the base coat of paint (reaching a maximum of 13000 counts), with lead levels varying throughout the upper layers as well. (Figure 4.25). There also appears to be Zn, Na, Ti, and Si present in the outer paint layers as measured with EDS line scans (figure 4.26).

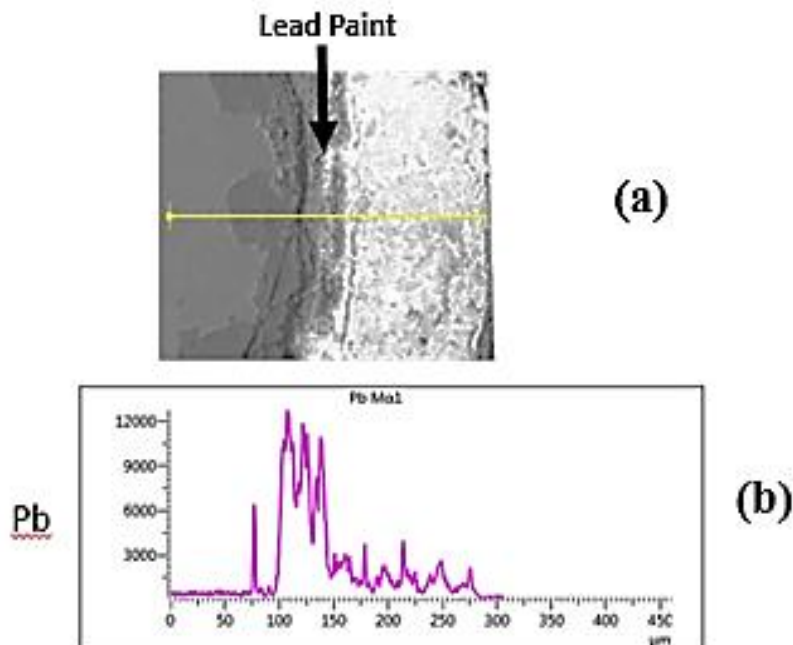


Figure 4.25. EDS line scan shows the concentration of Pb within the red lead paint base coat. (a) Indicating the line scan that was measured on the sample cross section. (b) Lead  $M_{\alpha 1}$  EDS spectrum shows the concentration of lead in the base coat of paint.

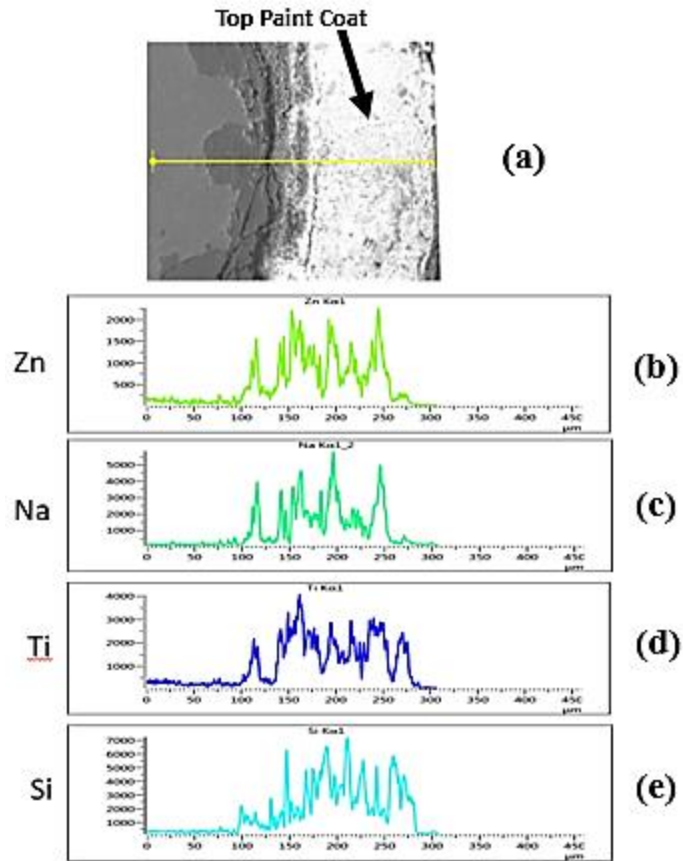


Figure 4.26. EDS line scan providing a compositional profile of the paint layers. There is a strong correlation between Zn (b) and Na (c), slightly less with Ti (d), and peaks mismatched the most with Si (e).

While EDS line scans help to show the distribution of elements between the various paint layers and iron oxide above the steel, using map scans of cross sections of the surface near surface region containing these layers shows a rough indication of the amount of each of these elements. Figure 4.27 shows compositions of this region as determined from several EDS map scans. Because the paint layer thickness is not constant across the surface there is some variation in elemental composition, however this variation is minimal.

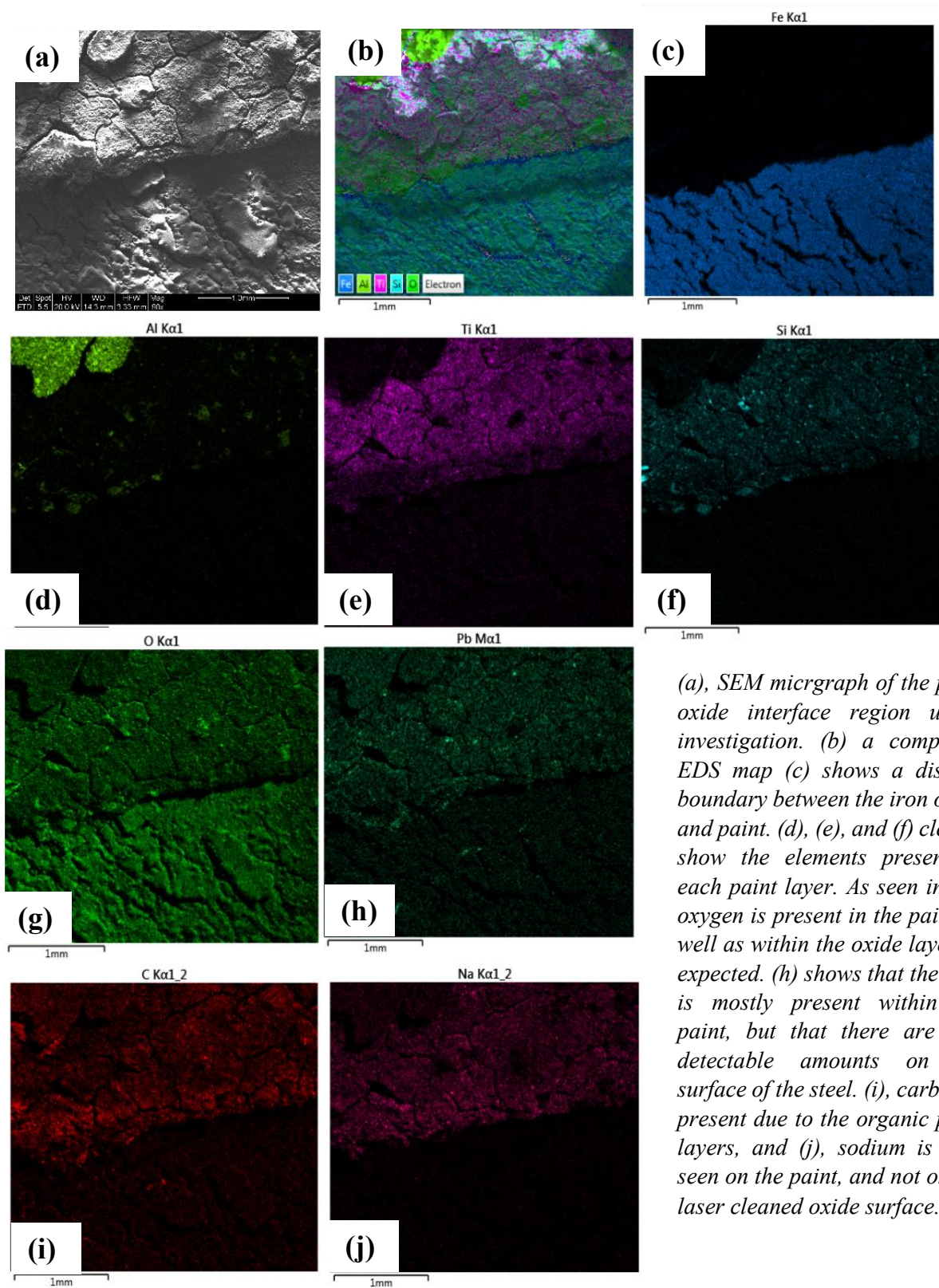
Map Sum Spectrum			Map Sum Spectrum			Map Sum Spectrum		
	Wt%	$\sigma$		Wt%	$\sigma$		Wt%	$\sigma$
Fe	43.9	0.1	Fe	39.9	0.2	Fe	35.4	0.1
O	25.8	0.2	O	29.2	0.2	O	30.2	0.1
Pb	15.4	0.1	Pb	14.6	0.2	Pb	14.4	0.2
Al	4.4	0.0	Al	6.7	0.1	Al	8.0	0.0
Si	4.3	0.0	Si	3.6	0.0	Si	4.0	0.0
Zn	2.2	0.0	Zn	2.6	0.1	Zn	3.0	0.0
Mg	1.6	0.0	Mg	1.6	0.1	Mg	1.9	0.1
Na	0.9	0.1	Ti	1.4	0.0	Ti	1.2	0.0
Ti	0.9	0.0	Ca	0.3	0.0	Na	1.0	0.1
Ca	0.2	0.0				Ca	0.6	0.1
K	0.2	0.0				Ca	0.3	0.0
C	0.1	0.0					0.1	0.0

Figure 4.27. EDS map compositions from several map scans of the near surface region which contains the three paint layers and iron oxide.

Using EDS maps of the paint to substrate interface between the laser cleaned surface and the base paint layers, the different layers of paint as well as the surface iron oxide interface with the paint can be seen.

Figure 4.28 shows an EDS color map of a select location along the paint and iron oxide surface interface. (Also see Appendix A2) These EDS maps help to distinguish the features that are observed in the accompanying SEM micrographs.

Location 1:



*Figure 4.28. Several different locations along the paint substrate interface shown using EDS color maps to help identify the composition of different paint coats. (Appendix A2).*

Comparing these EDS maps reveals the composition of each paint layer as well as the cleanliness of the laser cleaned surface. There is a sharp distinct boundary between the paint and the substrate as observed in a majority of the maps, and even between some of the paint layers. For example, in location 1, C, Na, Si, and Al are not detected on the iron oxide surface in large amounts, but only on the paint regions. Also at location 1, the laser cleaned surface has high signals of iron, and oxygen. This helps confirm that the iron oxide surface nearly exclusively consists of iron and oxygen, with minimal contamination that may have possibly been introduced during the laser cleaning process. In addition, there is a clear distinction between the top aluminum containing paint coat and the middle titanium paint, as seen in the EDS maps. These suggests that some each paint layer is composed of distinct elements that can be used to characterize them. Furthermore, by comparing EDS map scans to optical images allows identification of what paints contains which pigments and elements. Near the edges of samples, the paint tends to flake off to varying degrees, this reveals the separate paint layers. By revealing different paint layers in various areas this allowed for direct EDS characterization of each paint coating. Figure 4.29 shows optical micrographs of the painted surface, where each paint layer is clearly seen.

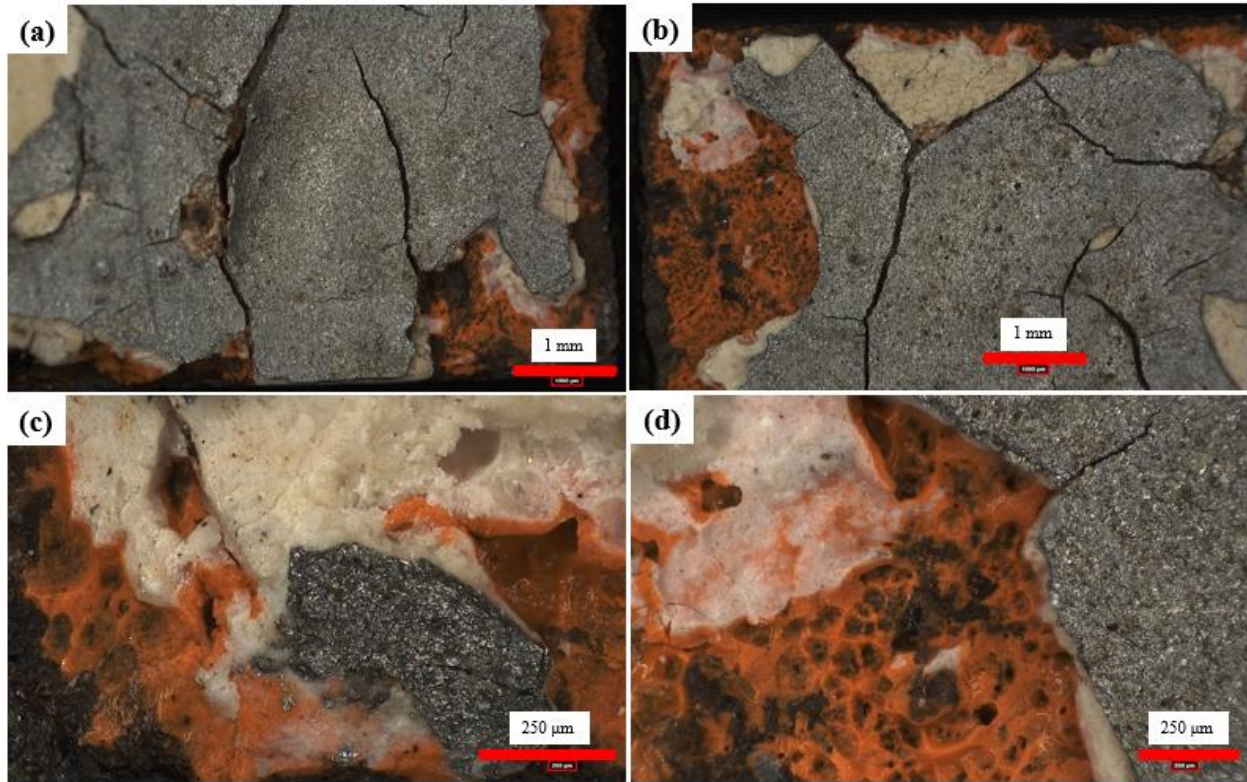


*Figure 4.29. Optical micrographs of the base metal surface, containing several layers of paint that were removed during LACR.*

It is apparent from optical microscopy that the top layer of paint is the silver or grey colored layer, the layer below that is white colored, and that the base coat is a bright orange color. Aside from the colors of the paint, other characteristics such as the texture can be observed. The top grey paint has cracks continuously running throughout the surface, likely due to aging and exposure to sunlight over the decades of use that these bridge beams have been through. The white colored paint has a "mineral", rocky, look, as does the orange base coat that seems to mix, or adhere more strongly to the adjacent white paint than the top coat does. By direct comparison of these optical micrographs with EDS maps collected in the SEM, this leads to easy identification of each paint layer by composition. Figure 4.30 shows optical micrographs along with EDS maps of the same surface location in order to identify paint compositions. (More EDS maps are shown in appendix A3).

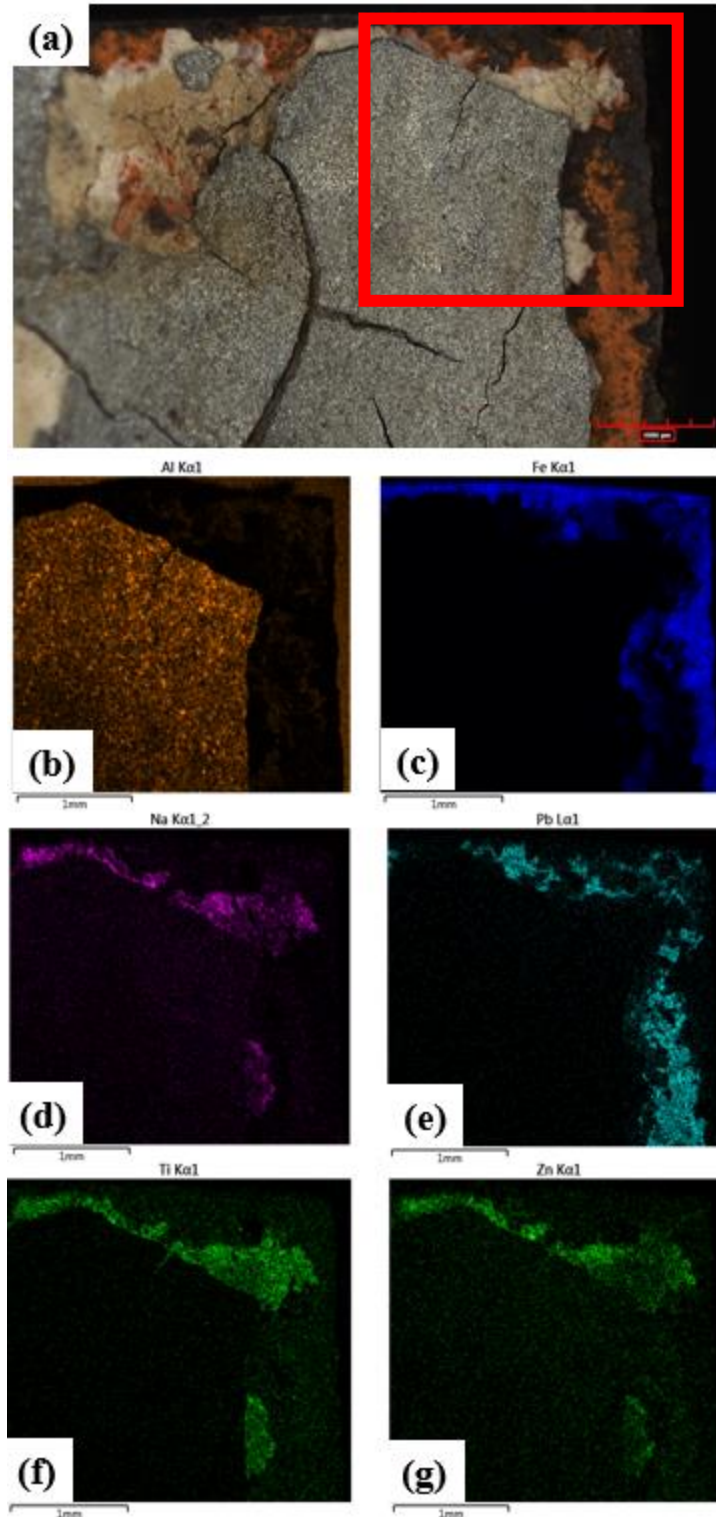
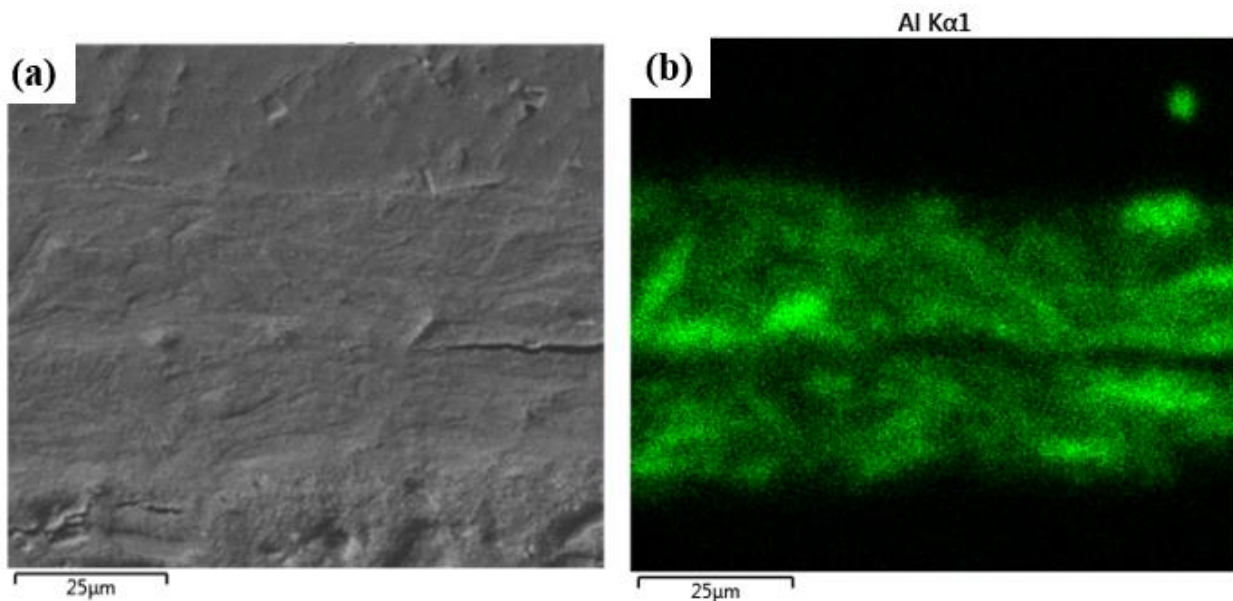


Figure 4.30. A red box over the optical micrograph (a), shows the region mapped in EDS. The elements in each map are as follows: (b): Al (c): Fe (d): Na (e): Pb (f): Ti (g): Zn. All scale bars = 1 mm. (Appendix A3).

From EDS analysis each layer can distinctly be identified. The top paint layer is clearly high in aluminum content, the second white colored layer is high in both zinc and titanium, whereas the base orange paint coat contains lead. Analyzing base metal samples still containing paint, the morphology of the paint constituents or pigments can be identified. For example figure 4.31 show EDS maps of a cross section of the top most, aluminum, paint layer. It is clear that the aluminum is concentrated in round disc-like shapes, and because this is a cross sectional view, it provides a side cut viewing angle of these aluminum flakes. A common top coat of paint is aluminum flake paint, containing flakes of aluminum, which is likely the type of paint that was used as a top coat in this bridge coating system.



*Figure 4.31. (a) SEM micrograph of the area examined by EDS. Above the aluminum paint is the epoxy mold used to mount samples, and below is the white titanium and zinc layer. (b) The aluminum K-alpha one EDS map, showing the aluminum paint layer, especially highlighting the individual aluminum flakes within the paint.*

EDS has determined that the main elements constituting the paint are lead in the orange base layer, zinc and titanium in the white middle coat, and aluminum flakes in the top paint coat.

However, in addition to these majority elemental components, other elements seem to be present

throughout the paint in smaller, or even trace amounts. These include elements such as silicon, magnesium, sodium, and calcium. Figure 4.32 shows another composition EDS map of an area with all three paint layers exposed. Again, it is obvious that the top layer of paint is aluminum, followed by the white colored titanium and zinc paint, and then the base lead paint. However, these maps also reveal another feature of the paint, as seen on the silicon and magnesium maps, these are specific spots that shows localized high levels of specific elements, particularly titanium, calcium, silicon, and magnesium. Through higher magnification EDS analysis, the reasons for these elements presence is explained by the observation of pieces of inorganic minerals that are embedded within the paint. In figure 4.33 a higher magnification sequence of EDS maps shows one of these particles. Through EDS it is clear that this inorganic particle embedded in the paint consists of silicon, magnesium, and oxygen, and it's outline is clearly traced by the zinc and titanium paint matrix that surrounds it. These and other inorganic silicates are scattered throughout the white paint layer, and therefore explain the concentration of elements that are seen in the EDS maps of figure 4.31. This suggests that the second "white colored" layer of paint is a mineral silicate paint, a type of epoxy paint often used due to its hydrophobicity and great weathering properties. Due to the application at hand, bridge coating protection, it is logical that this type of paint was chosen as a component in the coating system.

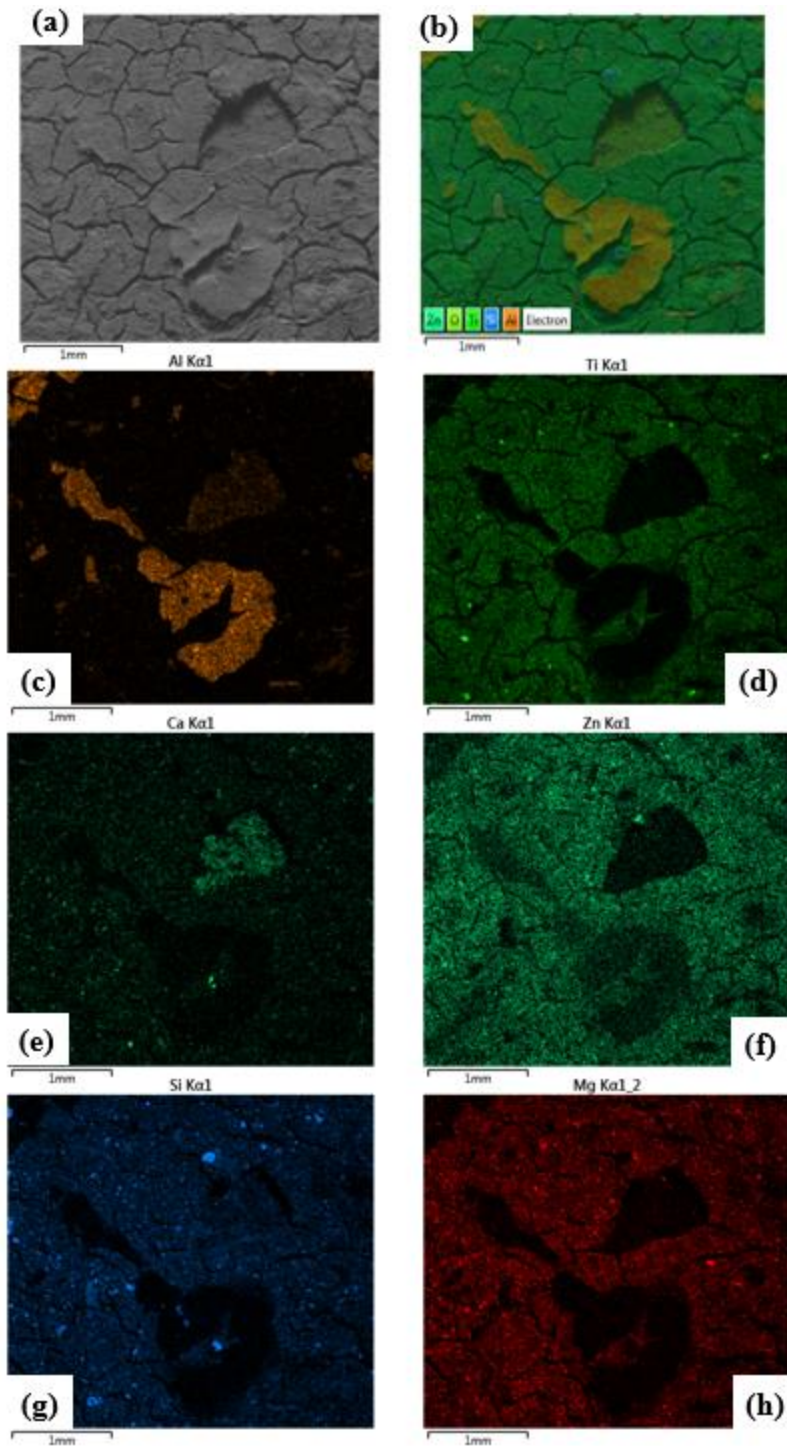


Figure 4.32. Paint EDS mapping not only confirms the composition of each paint layer, but also reveals the presence of specific concentrated signal points for some elements, such as Ti (d), Ca (e), Mg (f), Si (g), and Mg (h). Scale bar = 1 mm in each micrograph.

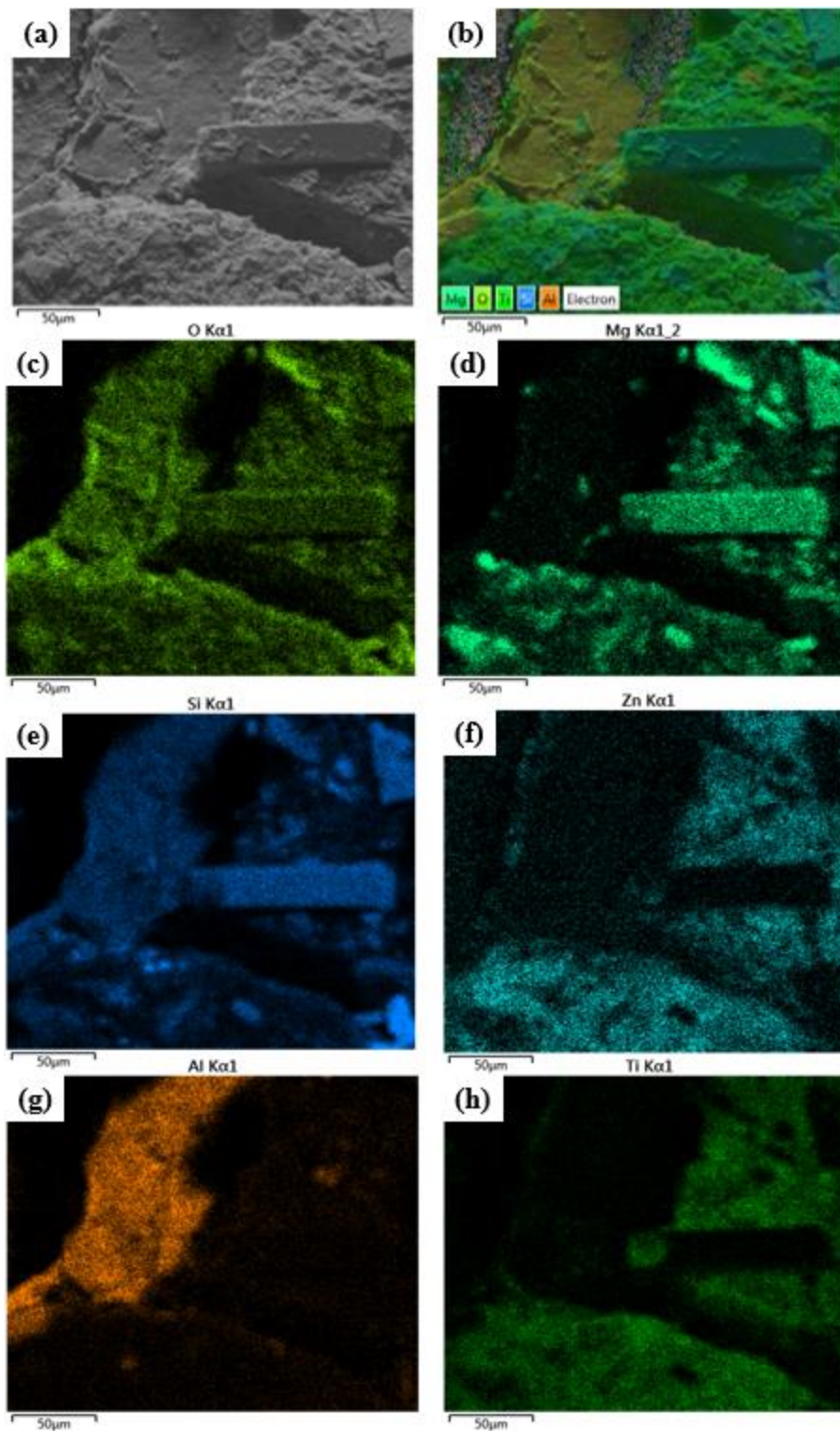
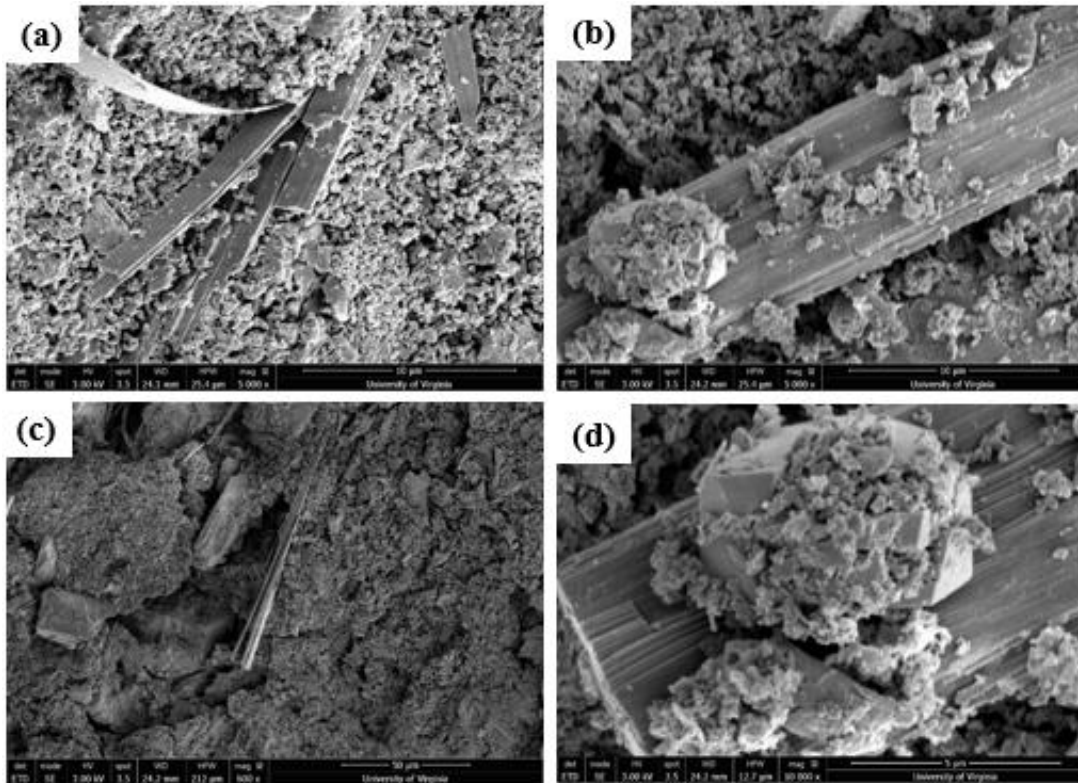


Figure 4.33. EDS maps detailing a piece of inorganic mineral that is embedded within the titanium and zinc paint. These are scattered throughout the paint and explain the highly concentrated elemental points seen in figure 31. Scale bars = 50 μm.

Apart from the large scale, macroscopic view of the paint, upon closer examination in the SEM these microscopic components can be observed. Figures 4.34, 4.35, 4.36, and 4.37, show examples of different particles that were found to exist within the white titanium and zinc paint layer. Figure 4.34 shows wooden “plank” like crystals that are scattered throughout the paint matrix, figure 4.35 shows particles with distinct crystal like morphologies, and figure 4.36 and 4.37 show SEM micrographs of spherical particles that were scattered throughout the white paint layer.



*Figure 4.34. Morphology of crystals that are scattered throughout the zinc/titanium paint.*

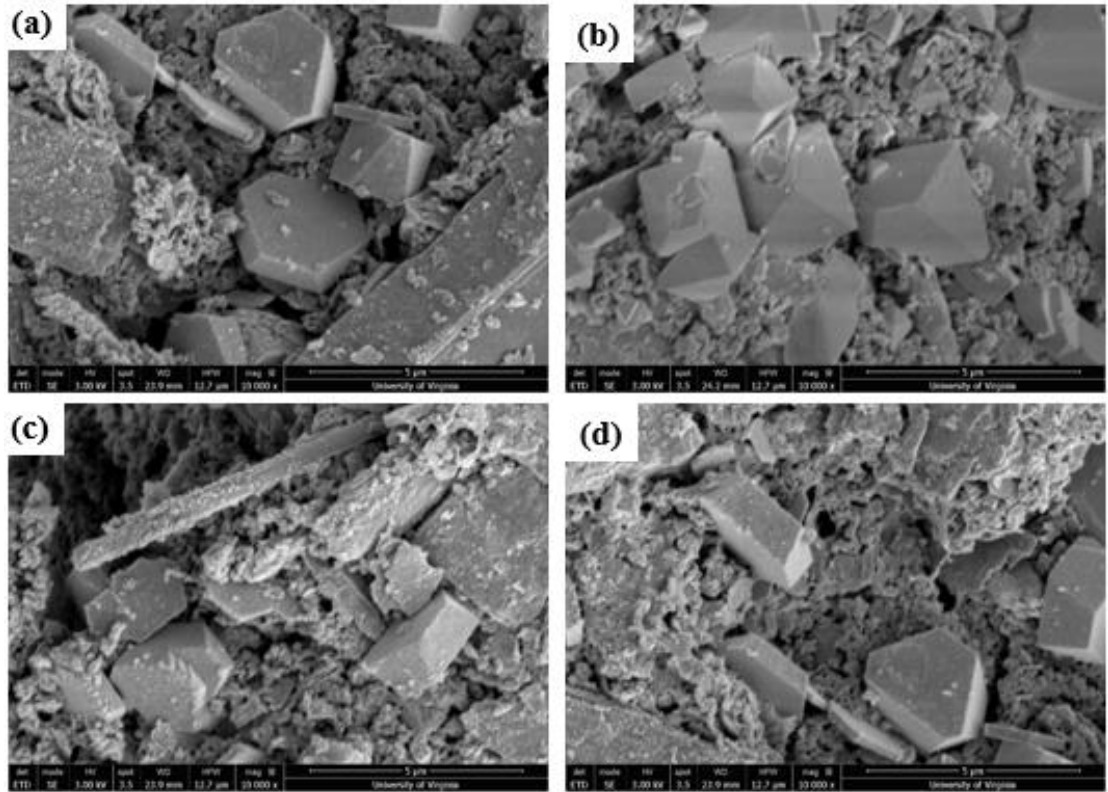


Figure 4.35. Various crystals that are present throughout the zinc/titanium paint.

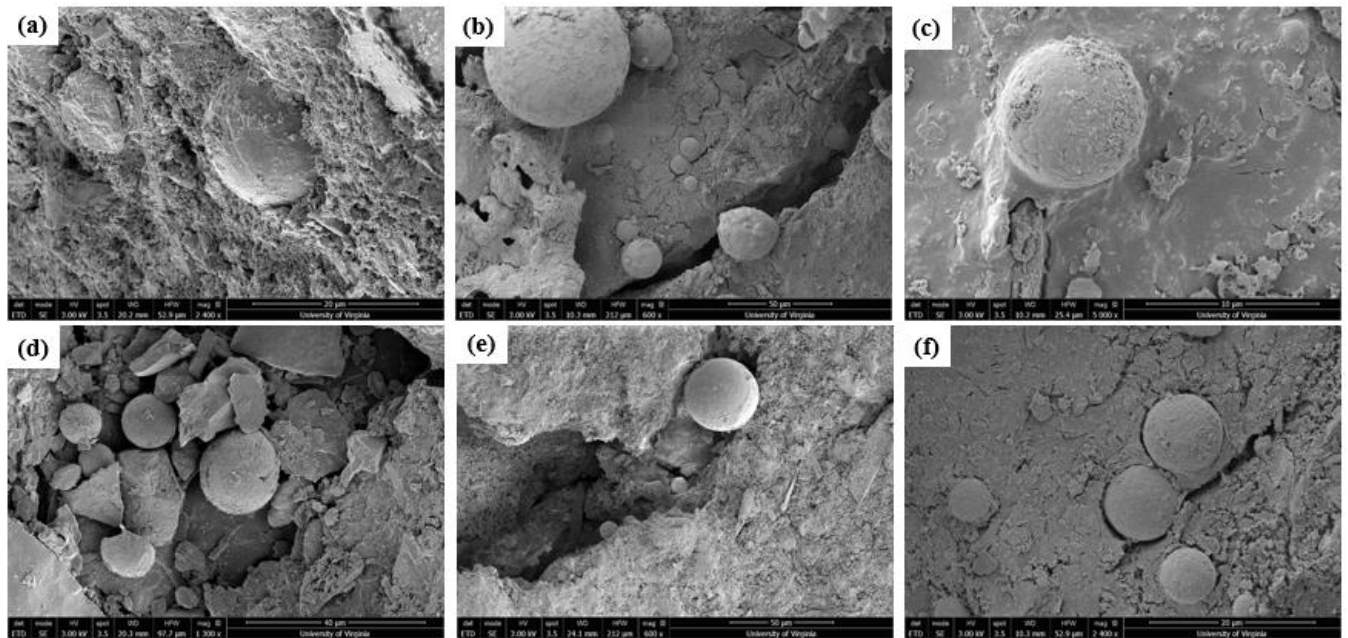


Figure 4.36. SEM micrographs of spherical particles found within the zinc and titanium paint.

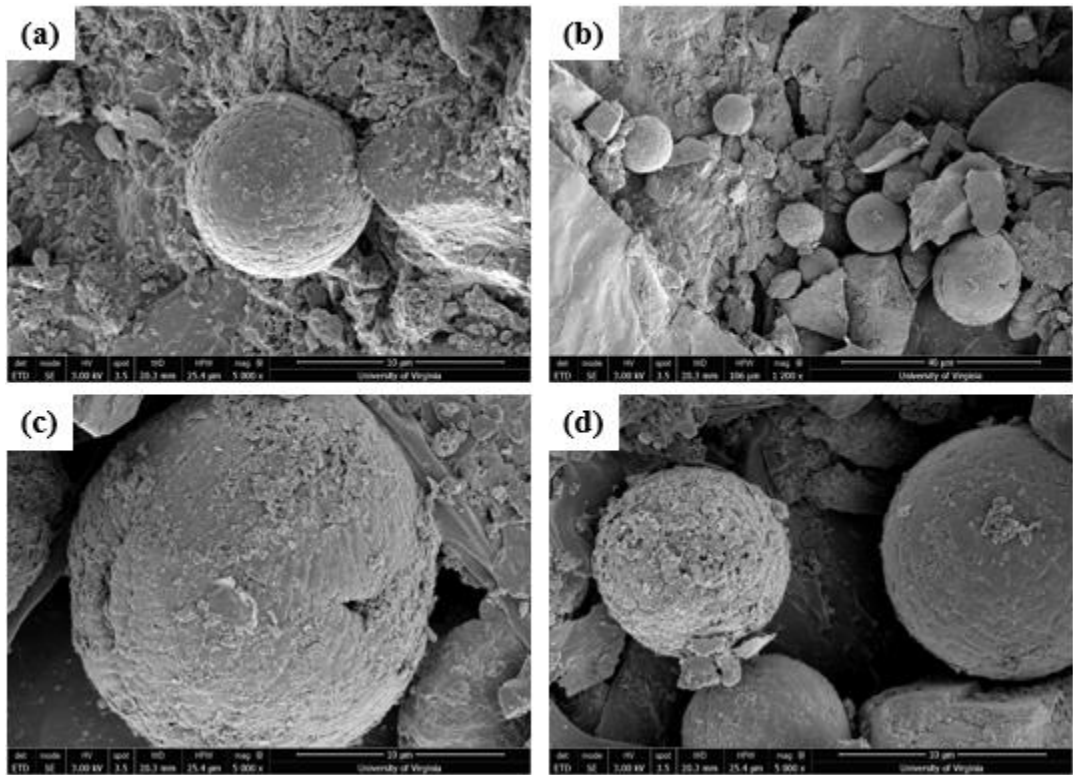


Figure 4.37. High magnification SEM micrographs of the spherical particles shown in figure 35.

All of these components within the paint are examples of particulate within the paint that the laser must ablate in order to remove the paint from the I-beam surfaces, and provide a visual sense of the microscopic objects that make up the paint layers.

#### 4.8 XRF and XRD Analysis of LACR Surfaces

In addition to EDS and SEM analysis of base samples and laser cleaned samples, XRF testing was also performed at the University of Virginia to provide another means of confirming the elemental composition of the base and laser cleaned samples.

In table 4.1 the surface composition of pre-laser cleaned samples containing all layers of paint is shown for several different samples. It can be seen that the composition varies between the different samples, which reflects the inhomogeneity of the original beam coating surface.

**Table 4.1: Composition of the Base Material Painted Surface as Determined via XRF**

Element	Sample 1 (%)	Sample 2 (%)	Sample 3 (%)	Average (%)
Na	0.088	0	0	0.029
Mg	0.493	0.650	0.204	0.449
Al	38.18	50.29	37.99	42.15
Si	4.616	4.359	3.839	4.271
P	0	0	0.145	0.048
S	0	2.483	2.568	1.684
K	0.510	0.219	0.298	0.342
Ca	2.715	1.159	1.349	1.741
Ti	0.300	6.333	7.604	4.746
V	0.114	0.100	0.125	0.113
Cr	0.255	0.004	88.4 ppm	0.130
Mn	0.121	0.073	0.106	0.100
Fe	6.481	4.669	7.609	6.253
Ni	0.036	0	0	0.012
Cu	0.043	0	0	0.014
Zn	36.91	29.64	38.16	34.90
Mo	0.141	0	0	0.047
Sn	0	0.023	0	0.008

Because base material with all the paint layers has a thickness of about 300  $\mu\text{m}$ , and XRF penetration depth depends on both the x-ray energy and the material undergoing analysis, based on the XRF data the XRF source x-rays do not reach the substrate beneath the paint, (no Fe signal is detected), and therefore is only a representation of the composition of the top paint layers.

Table 4.2 shows the elemental composition of the surface of several laser cleaned samples, as well as the average composition of these samples. As expected, the bulk of the

surface reflects the A36 steel's composition (0.26% C, 0.75% Mn, 0.2% Cu, <0.04% P, <0.05% S, balance Fe), in addition to the residual lead that is left on the surface. Aside from these elements, others such as Si, Ca, Cr, and Zn are also remaining as artifacts from the various paint coats that had been removed.

***Table 4.2: Composition of the Laser Cleaned Surface as Determined via XRF***

Element	Sample 1 (%)	Sample 2 (%)	Sample 3 (%)	Average (%)
Si	0.051	0.036	0.028	0.038
Ca	0.167	0.063	0.100	0.110
Cr	0.081	0.055	0.057	0.064
Mn	0.554	0.631	0.628	0.604
Fe	98.00	98.53	98.60	98.38
Ni	0.131	0.124	0.116	0.124
Cu	0.128	0.114	0.085	0.109
Zn	0.022	0.035	0.045	0.034
Mo	0.014	0.013	0.013	0.013
Sn	0.028	0.030	0.030	0.029
Pb	0.819	0.331	0.288	0.479

In addition to EDS and XRF compositional analysis, which showed that the laser cleaned surface is an iron oxide mill scale, or rust, x-ray diffraction (XRD) helped to confirm the presence of the iron oxide, as well as give insight to the various types of iron oxides present, which have different crystal structures. Figure 4.38 shows an XRD scan performed on the laser cleaned surface with the different iron oxide phases present.

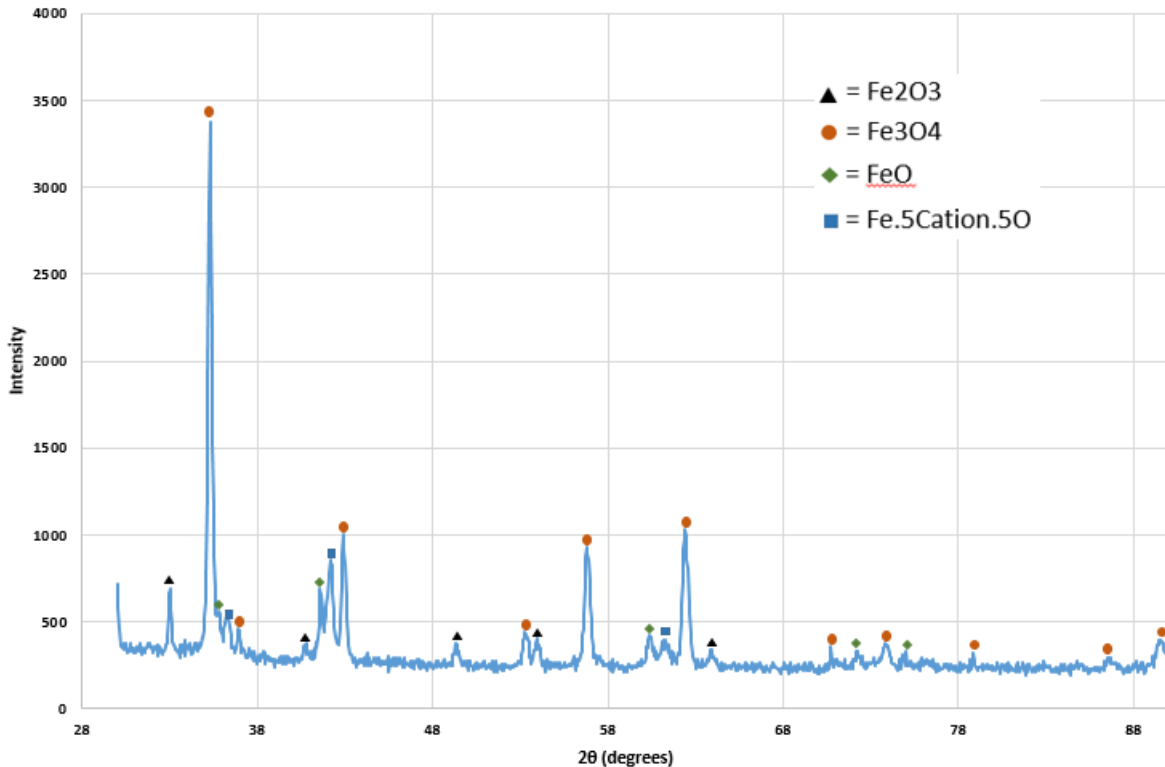


*Figure 4.38. X-ray diffraction scan of the LACR surface. Four different iron oxide phases were observed, as indicated in the plot.*

XRD analysis shows that four different iron oxide phases were present, Fe<sub>2</sub>O<sub>3</sub>, Fe<sub>3</sub>O<sub>4</sub>, Fe<sub>2</sub>O, and a variation of the Fe<sub>2</sub>O phase in which half the iron cations are replaced with different cations, Fe<sub>0.5</sub>Cation<sub>0.5</sub>O. The cations that replace iron (II) may be a different size and therefore can distort the unit cell, thereby causing a slight shift in the peak positions. The precise identity of the cation was not identified, however it could possibly be a transition metal element that was introduced to the molten oxide from the paint during laser irradiation.

#### **4.9 Phase IV: LACR Testing for Lead Abatement**

Phase IV testing was conducted by VDOT and VTRC and included both industrial hygiene surveys for the lead removal phase using the CL1000 laser system, as well as for the hot cutting phase during which laser cleaned I-beams were cut using a welding torch. In addition to the

industrial hygiene survey's, samples were returned to the University of Virginia for further surface analysis using SEM and EDS.

For industrial hygiene sampling during the plasma cutting operation personal samples were collected throughout each task and one area sample was collected during the hot working operations approximately 16 feet and down-wind from the work area.

Sample results were compared to both the OSHA PELs and ALs as outlined in contaminant specific regulation or, where applicable, OSHA Subpart Z-Toxic and Hazardous Substances, the same standards used for industrial hygiene testing in Phases I and II. Contaminant limits are outlined in table 4.2.

**Table 4.2. Contaminant Limits as Determined by OSHA Standards<sup>44</sup>**

<b>Contaminant</b>	<b>OSHA PELs (mg/m<sup>3</sup>)</b>	<b>OSHA Action Level ( mg/m<sup>3</sup>)</b>
Cadmium (1910.1027)	0.005	0.0025
Chromium	1	NA
Hexavalent Chromium (1910.1026)	0.005	0.0025
Lead (1910.1025 and/or 1926.62)	0.05	0.03
Lead Wipe (Brookhaven National Laboratory Safety and Health Services Division, 2017)	Change Areas/Storage Facilities/Lunchrooms: <200 µg/ft <sup>2</sup> recommended OSHA Regulated Areas: >= 4,645 µg/ft <sup>2</sup> recommended *Non-Regulatory Recommended Limit	
PCB Aroclars	1.0 for PCBs with 42% Cl 0.5 for PCBs with 54% Cl	NA

Bulk paint samples were analyzed for the percent weight of lead, cadmium, chromium, and PCBs, and they did not indicate a presence of cadmium or chromium above the level of detection. The lead concentration on both beam's coatings exceeded 50%, and the PCB samples results were below the level of detection for all analyzed aroclars (a specific class of PCB).

Based on the paint composition, beam coatings would not likely contribute to measurable concentrations of hexavalent chromium, cadmium, or PCBs during the laser cleaning process.

Wipe samples were completed following laser cleaning and HEPA vacuuming of remaining dust. Remaining levels of leaded dust were compared to Brookhaven National Laboratory recommended lead dust concentration levels for “containment areas”. The measured levels from Beam A were well below the Brookhaven criteria for acceptable containment dust levels, and the levels from Beam B were in excess of the Brookhaven criteria for acceptable containment lead dust levels. The presence of lead dust means that careful handling of beams after laser cleaning including wearing gloves and handwashing is needed. Table 4.3 shows the results from the lead wipe tests.

***Table 4.3: Data from Lead Wipe Tests: Beam B has a Higher Concentration of Lead Overall Compared to Beam A<sup>44</sup>***

<b>Beam</b>	<b>Flange</b>	<b>Web</b>
A	1,177 µg/ft <sup>2</sup>	1,555 µg/ft <sup>2</sup>
B	8,836 µg/ft <sup>2</sup>	5,291 µg/ft <sup>2</sup>

In summary of the industrial hygiene survey, bulk sample, and lead wipe tests, personal samples from the laser cleaning process did not show any measurable levels of lead, cadmium, hexavalent chromium, or PCBs during the first stage of laser cleaning at Norton Sandblasting. Only one area sample showed a low concentration of lead particulate, and this level was measured to be well below the AL.

During the hot work operation at the Hampton Roads District Headquarters, work on Beam A, the rolled I beam with complete coating removal, didn’t show a concentration of lead likely to exceed the AL over the course of a normal workday, for which case a cutting time of 1.5 hours is

assumed. In contrast, beam B, the welded C beam, indicated a presence of lead at a concentration that could potentially contribute to lead exposure over the course of a workday, and as noted earlier, these beams must be handled with the proper PPE (personal protection equipment) in order to maintain operator safety.

After VDOT conducted the laser cleaning and hot cutting of the beam, the industrial hygiene survey, and contracted lead testing, cut sections of the I-beams were transported to the University of Virginia for further surface characterization. After cutting out smaller (roughly 1 inch by 1 inch) metal samples from the I-beams, the surfaces were studied in the SEM with the primary goal of measuring the remaining amount of lead on the surface. Figures 4.39 and 4.40 show SEM micrographs and accompanying EDS data for the surface region shown. As expected, EDS shows a high content of iron and oxygen, due to the iron oxide layer that remains on the surface. Iron weight percentages obtained from EDS typically fell within the 70 to 80% range, and oxygen weight percentages approximately around 15 percent. Aside from these two dominate elements, smaller amounts of other elements such as carbon (roughly 10 weight percent, although percentages vary with surface region), and manganese and sodium were also present. These trace elements were attributed to dirt and detritus that were left remaining on the I-beam surface.

Regarding lead, the element under investigation, lead consistently appeared in EDS analysis, however only in trace amounts. In fact, computer EDS data analysis consistently placed lead at the bottom of the list of trace elements, (shown in red on the EDS spectra composition list), suggesting that while lead is present, it is only scattered throughout the surface in very small amounts. This agrees with the results of the lead wipe tests and prior chemical analysis performed by the VDOT contracted company, Marine Chemist Service. While lead definitely

remains on the surfaces of these I-beams, it is safe to conclude that it is only present in very minute amounts.

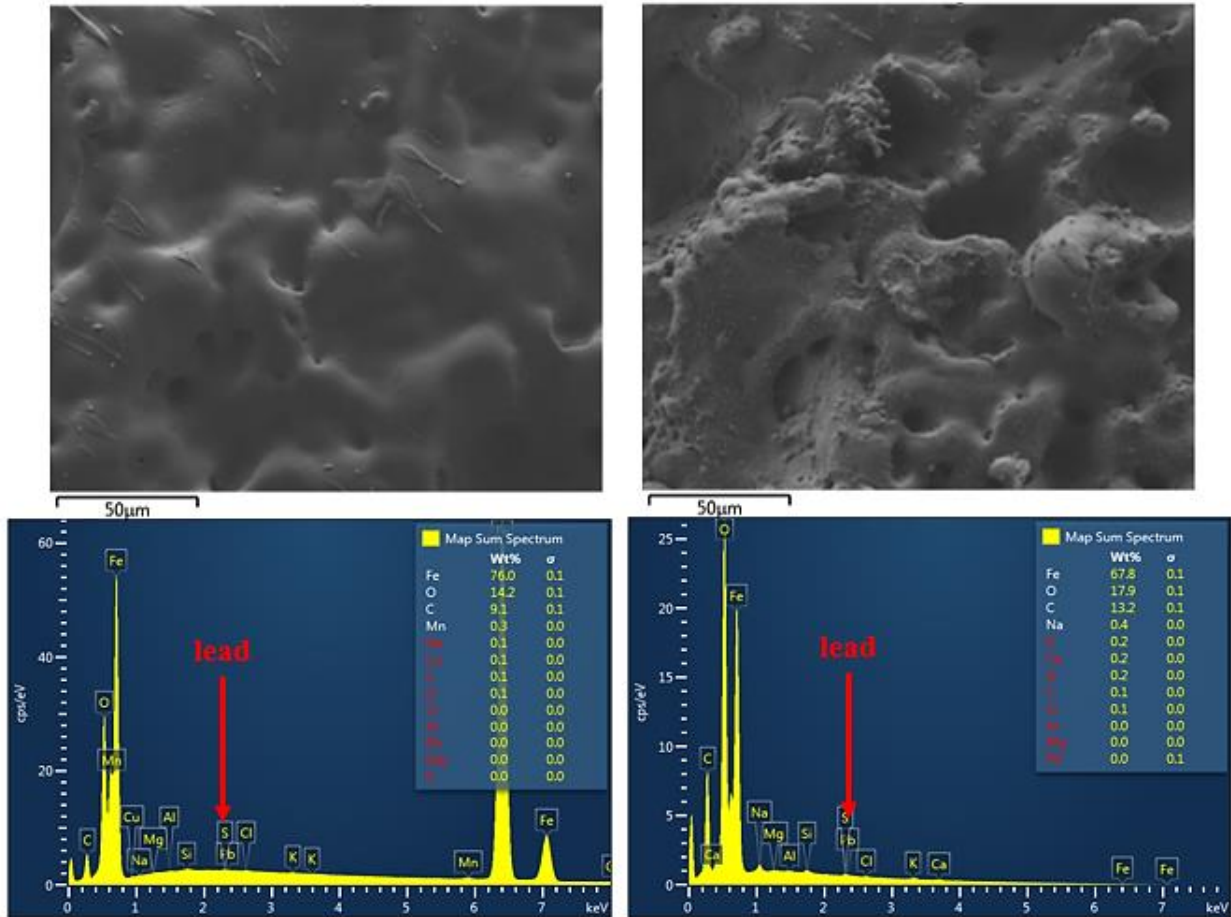


Figure 4.39 (i). SEM micrographs of two different surface areas of the LACR cleaned surface. In both regions Fe, O, and C predominate the composition of the surface, with the remaining elements only present in trace amounts.

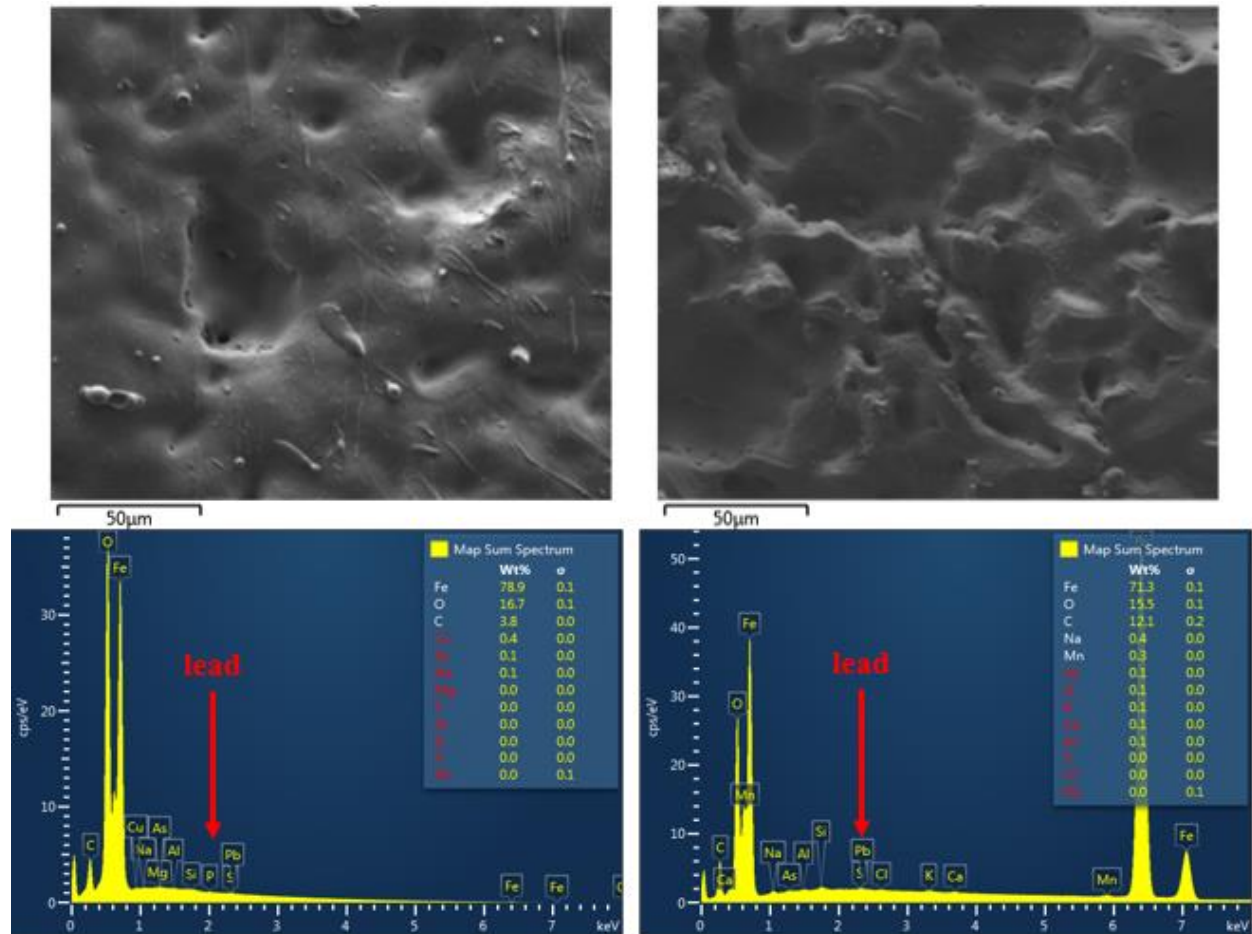


Figure 4.40 (ii). Two more surface areas that were selected for EDS analysis. Again, lead is only present in very small amounts.

#### 4.10 Coating Adhesion Testing

Using the PATTI adhesion testing device, the adhesion of repainted epoxy paint on laser cleaned beams was assessed. As could be roughly observed macroscopically, the reapplied paint appeared to vary in roughness and therefore thickness, across different repainted beams and within beams themselves. Beams with a heavily applied paint coating left brush strokes easily visible, whereas thinner coatings seemed to be smoother. Figure 4.41 shows macroscopic photographs of these two different paint conditions.

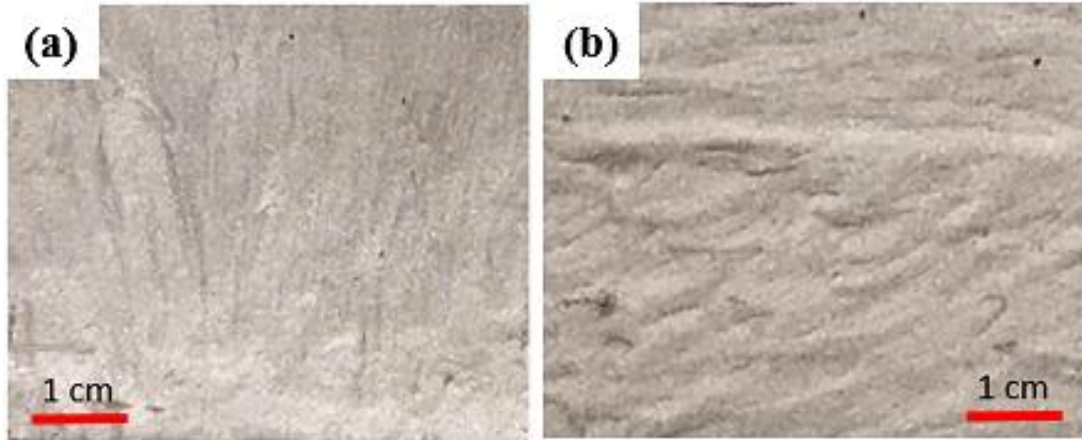
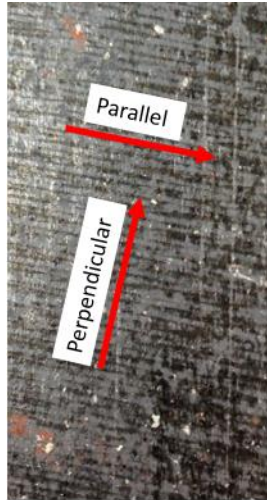


Figure 4.41. (a): thinner smoother paint, (b) thick, rough paint surface texture.

Upon testing these different painted regions, a course correlation between the paint thickness and the adhesion strength of the paint was observed, with a higher coating adhesion for thicker, rougher paint areas. For thin paint coat areas the average pull off tensile strength was determined to be 1721 psi, as opposed to 2094 psi for the thicker regions. These values were determined by averaging the pull off tensile strength recorded for over 50 pull tests for each paint condition.

#### 4.11 Surface Roughness

Using a surface profilometer, the surface roughness of different processed surfaces was investigated. The biggest variable for surface roughness was the grit blasted surface condition versus the laser cleaned surface. Besides the difference in processing condition, for the laser cleaned surface there are laser tracks present from the laser surface interaction. In order to determine if these tracks were associated with any roughness of the surface, profilometry measurements were taken both parallel and perpendicular to the tracks, as shown in figure 4.42.



*Figure 4.42. Profilometry measurements that were recorded in parallel and perpendicular directions to the laser tracks.*

As expected, the gritblasted surface had a rougher profile, with an average roughness value of  $9.86\ \mu\text{m}$ . Both laser cleaned surface measurements had lower average roughness values, of  $5.41\ \mu\text{m}$  and  $5.26\ \mu\text{m}$  for the profiles perpendicular and parallel to the laser tracks respectively.

#### **4.12 Mechanical Testing**

##### **Hardness**

Vickers hardness tests were performed on samples in the as-received, grit blasted and laser-cleaned conditions. The focus of hardness testing was to determine whether there was any effect on the hardness of the steel due to laser cleaning, and to compare the hardness of laser cleaned samples with the hardness of the grit blasted condition. Hardness was measured as a function of depth into the material from the processed surface, at roughly  $75\ \mu\text{m}$  intervals. Ten hardness measurements were made at each depth into the steel and averaged. Figure 4.43 shows the hardness results for the three different processing conditions. The base metal showed little variation in hardness with depth, with an average hardness of  $\sim 140\ \text{HV}$  were observed. Laser-cleaned metal also showed essentially no change in hardness with depth. At  $75\ \mu\text{m}$  below the surface a Vickers hardness of about  $139\ \text{HV}$  is seen, and three millimeters into the metal, roughly

in the middle of the entire beam cross section, the hardness is measured to be 138 HV. The highest value of hardness is 141 HV at roughly 1.75 millimeters in the metal, whereas the lowest hardness measured is 138 at roughly 1.2 millimeters into the metal. This small range of hardness values shows how little variation in hardness is present in laser cleaned samples. Cross sectional analyses showed that the near surface region was heated and melted (to a depth of  $\sim 1 \mu\text{m}$ ), however the underlying metal seems to be unaffected by the heat. In contrast, grit blasted samples have a higher hardness near the surface (149 HV), but the hardness quickly drops off and reaches the values observed in the base metal, and nearly constant into the middle of the cross section. At 75  $\mu\text{m}$  below the surface in the grit blasted samples the hardness is 149 HV, and quickly drops to 140 HV within 0.25 millimeters into the steel. The elevated hardness at the surface is due to the deformation imparted by the grit blasting.

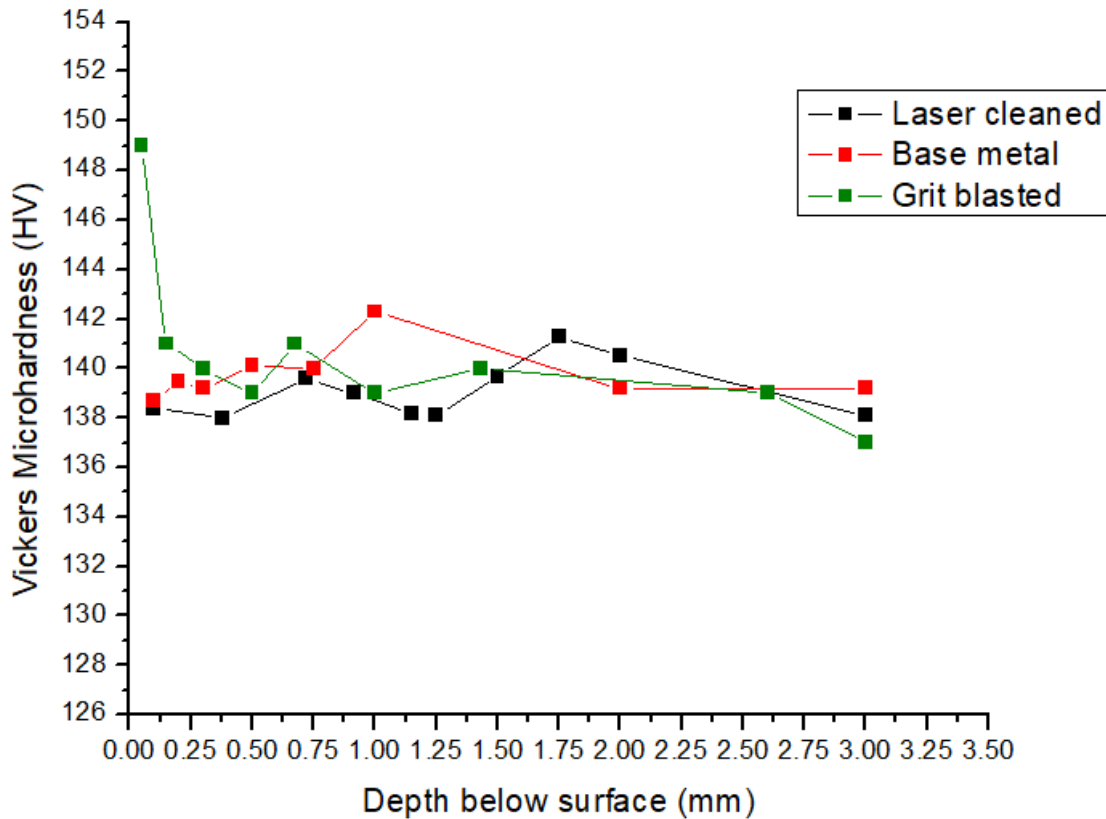
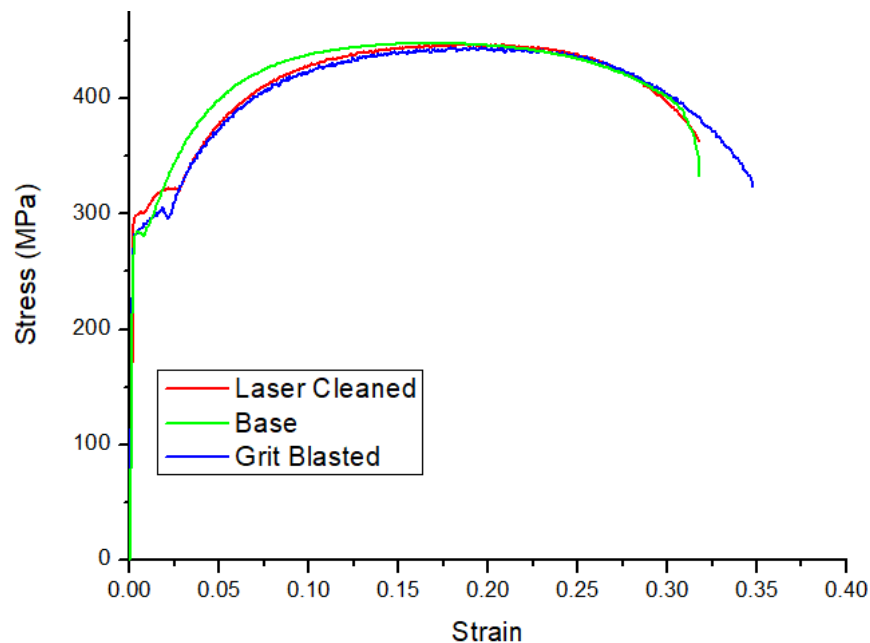


Figure 4.43. Hardness profile of all three processing conditions from the surface into the bulk of the material.

## Tensile Testing

Tensile testing was completed on base metal, grit blasted, and laser cleaned samples to determine the effects of different processing conditions on the strength of the metal. It was shown that laser cleaning had negligible effects on the strength, as all three processing conditions showed the same yield and ultimate tensile strength of 280 MPa and 440 MPa, respectively, which matches the mechanical properties of A36 steel which has a minimum yield strength of 275 MPa and an UTS ranging from 400-550 MPa.<sup>46</sup> No appreciable differences in the ductility were observed either, with all samples falling between 30% and 40% elongation vs. the minimum value of 23% for A36. (Figure 4.44).



*Figure 4.44. Stress strain curves for base, grit blasted, and laser cleaned metal.*

## Fatigue Testing

Fatigue testing was completed on the laser cleaned samples to investigate the effect of laser cleaning on the fatigue life of the steel. The same laser cleaned samples that were used for tensile

tests from phase I were also used in fatigue testing. Using a pull-pull set up in which the sample is always in tension, with a fatigue ratio,  $R$ , of 0.1, and 10 Hz frequency, the fatigue tests were run with a maximum stress ranging from 258 to 368 MPa, to fill out a SN curve. Figure 4.45 shows a fatigue SN curve for the fatigue tests.

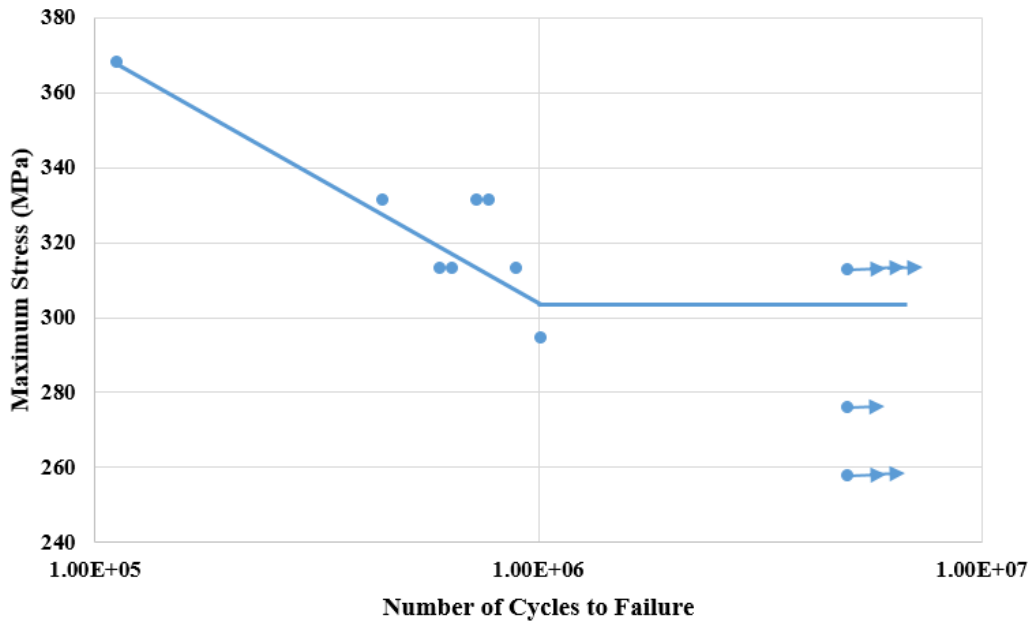
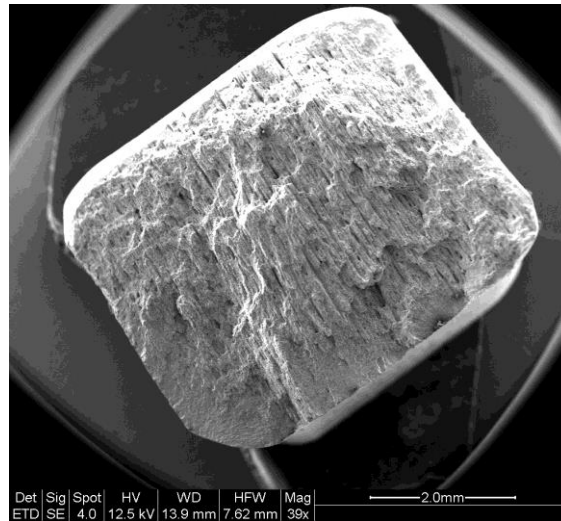


Figure 4.45. SN curve for LACR fatigue samples. Arrows on points at  $5 \times 10^6$  represent run out tests. The blue line provides a guide for the eye through the data.

The first dog bone sample that was tested used a maximum stress of 368 MPa, where the dog bone broke within a relatively short amount of cycles, roughly 122,000. Figure 4.46 shows the fracture surface of this sample.



*Figure 4.46. Fracture surface of a specimen stressed at the yield strength of the material.*

On this sample, two crack initiation sites were observed, which grew and eventually caused failure. In figure 4.47, the initiation sites are marked in yellow and the crack growth regions can be seen radiating outward from these spots.

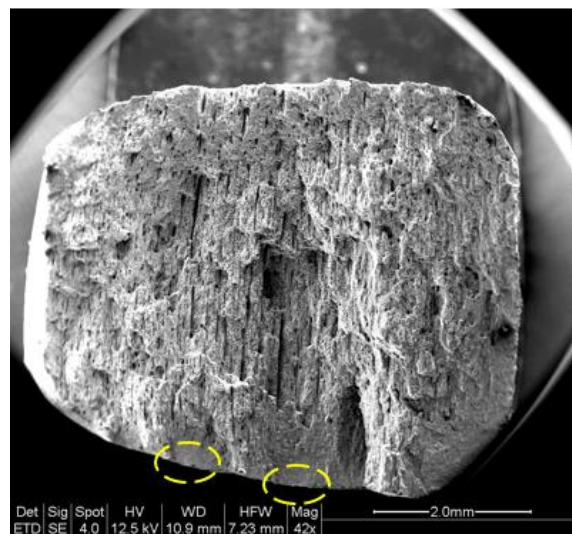


*Figure 4.47. Fatigue surface of the sample fatigued at the yield strength of steel. Crack initiation sites are marked in yellow.*

After this initial test, the maximum stress was decreased to 295 MPa. For this sample, which ran for approximately 1,000,000 cycles, the oxide layer debonded from the steel and left the layer

exposed on one of the fracture surfaces. Figure 4.48 shows SEM micrographs of the fractured surface and the exposed oxide layer that was left remaining on one of the fracture surfaces.

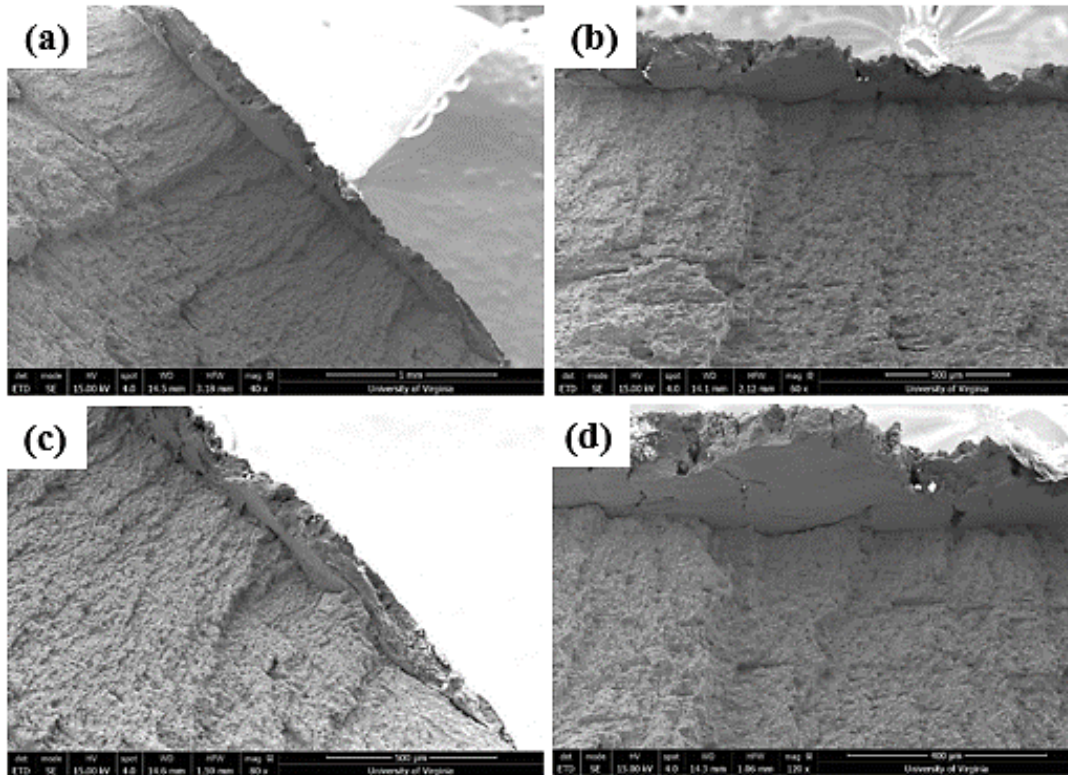


*Figure 48. The exposed oxide layer left on one of the fracture surfaces of the sample that failed at 1,000,000 cycles.*

The region of crack propagation and growth appeared similar on all the fatigue samples, figure 49 shows a representative micrograph of the crack growth surface. Fatigue crack growth striations can be observed at higher magnifications.

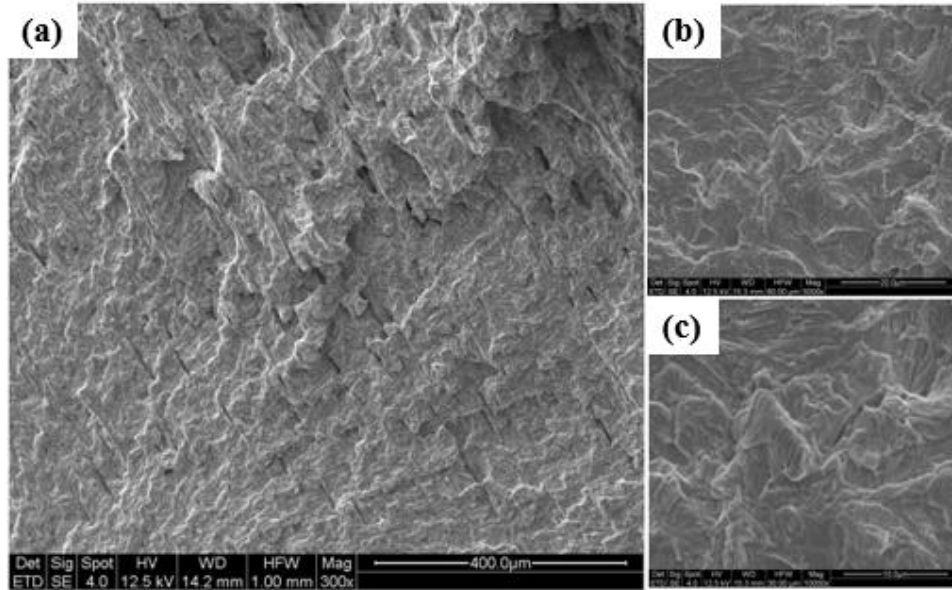


Figure 49. Representative SEM micrograph of the crack growth surface on LACR fatigue samples. a.) 300x, b.) 1000x, c.) 10,000x.

All of the samples also exhibited debonding between the steel matrix and intermetallic MnS particles embedded into the steel matrix. Figure 50 shows the ductile fracture surface of the 368 MPa sample, where crevices of varying depth were observed surrounding the intermetallic particles.

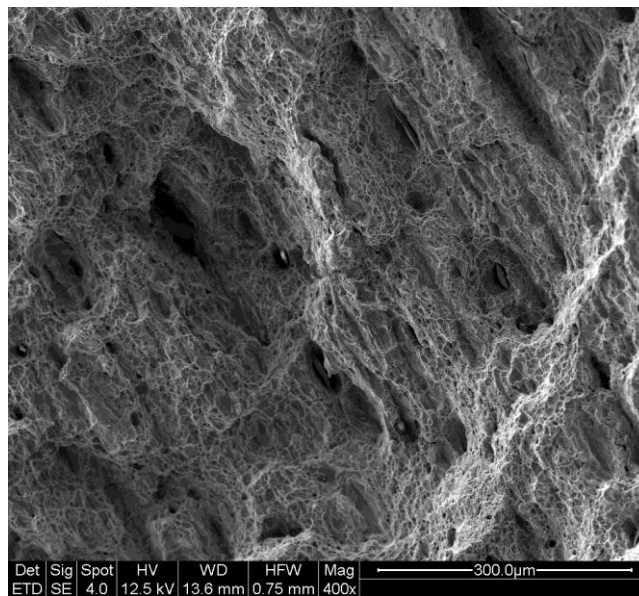
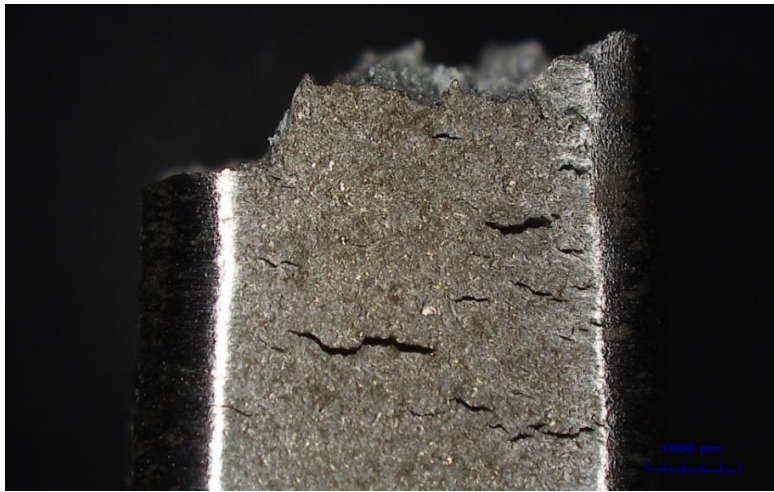


Figure 50. Ductile fracture surface showing the debonding between intermetallic particles and the steel matrix.

In addition to the fracture surface itself, observations were made on the outer surface of the fracture samples. Secondary cracks were observed on both sides of the final fracture of the dog bone samples. Figure 51 shows secondary cracks that could be seen near the final fracture of the 368 MPa maximum stress fatigued dog bone.



*Figure 51. Secondary cracks observed on the outside surface near the final point of failure.*

Looking directly at the fracture surface provides a different angle of the crack growth and debonding of the steel inclusions from the matrix. Figure 52 is a SEM micrograph of the fatigue surface as viewed from this angle. In these micrographs the traces of the aftermath of the crack can be seen radiating downward from the iron oxide layer, and splitting or changing direction once one of the intermetallic inclusions is reached.

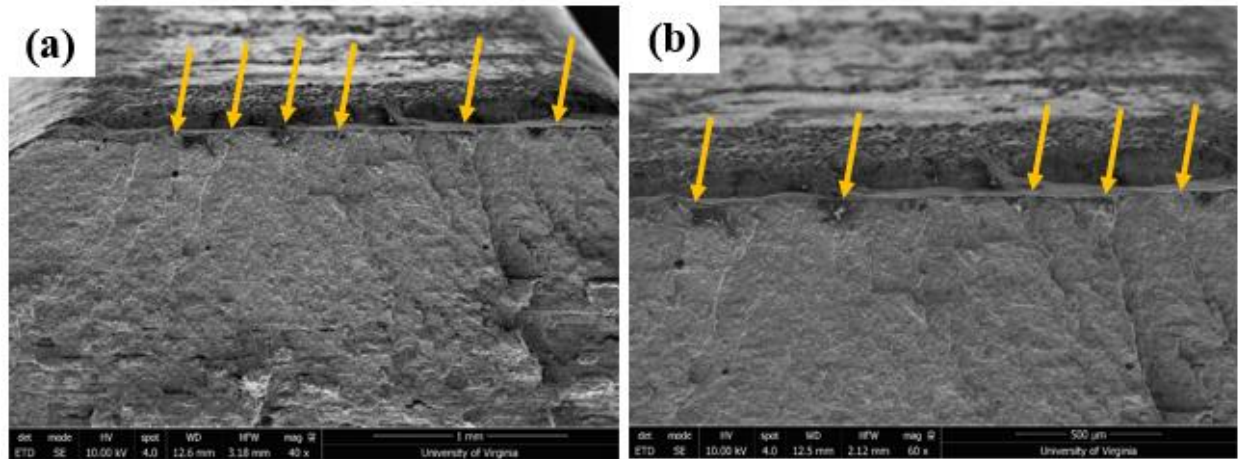


Figure 52. (a) Direct view of the crack propagation from the iron oxide surface layer through to the bulk material showing the interaction of the crack growth with the inclusions. (b) Higher magnification micrograph of (a). Yellow arrows indicates regions below the iron oxide surface where cracks appear to have initiated.

## Conclusion

The results in this project ranged from observational documentation and industrial hygiene work to technical material characterization. During phase I the initial laser demonstration of coating removal was observed, and provided samples for later analysis at the University of Virginia. In addition, industrial hygiene surveys showed that the entire process met OSHA worker safety regulations and requirements. It was determined however, that the filter became a source of hazardous waste as lead paint was involved in the laser coating removal, but nonetheless there were no dangerous levels of heavy metals or VOCs found on either personal or area samples placed throughout the room where the laser demonstration took place.

Later characterization studies revealed that the laser cleaned surface actually consists of a semi-continuous iron oxide layer, and that this layer is present on the base metal before laser cleaning takes place. The lead red colored base coat on the steel beams is harder to remove than the other paint layers, and pieces of this lead paint can be observed by eye on the laser cleaned surfaces. In contrast to laser cleaned samples, grit blasted samples are almost completely free of paint and

oxide, however they contain a roughly 10  $\mu\text{m}$  thick surface region of deformed grains due to the forces involved in the grit to surface impact.

Mechanical testing involved hardness measurements, tensile tests, and fatigue tests. There was no difference in hardness between base metal and laser cleaned material, however grit blasted cross sections showed higher hardness in the near surface region due to the compressive forces caused by the grit blasting forces involved. As expected, tensile tests showed no noticeable change in the mechanical properties (yield and ultimate tensile strength) of either of the processed conditions compared to the base metal. Fatigue tests also revealed typical fatigue behavior for A36 steel, as shown with a SN fatigue life curve. PATTI coating adhesion tests determined that repainted beams had high coating adhesion strength, averaging about 1800 psi where a minimum of only 600 psi is required.

## **Discussion**

### **5.1 Introduction**

In the results section, general observations of the LACR coating removal were introduced, along with coating adhesion testing and mechanical testing results. Delving deeper into the interaction between the laser and the coating helps to reveal the efficiency of the coating removal process and explain the different laser-material interaction between the different coating layers.

Furthermore, it is shown that there is more to the PATTI testing results than there seems to be at first glance, including the failure mechanism of the coating-substrate system. Likewise, comparison between the fatigue fracture surfaces of LACR samples and literature A36 fracture surfaces shows close resemblance. The SN fatigue curve of the LACR samples is consistent with a Goodman Diagram and also passes the AASHTO (American Association of State and Highway Transportation Officials) fatigue design guidelines used in bridge design.

### **5.2 EI Group Industrial Hygiene**

The results of the industrial hygiene survey have shown that so far the LACR process is safe with regards to the laser operator and surrounding environment, and that the demonstrations to date have met OSHA worker and environmental health and safety requirements. This includes both the removal of lead based primer paint in phase I of the project and the onsite LACR testing of a bridge in Farmville Virginia. While the end results of the survey are the significant findings, the details of how the survey was conducted, including the placement of sample collectors, the duration of exposure, and the profile of metals and volatile organic compounds that were screened for, are also important.

To summarize, the Phase I industrial hygiene survey consisted of personal samples, area samples, and several samples that were collected from the filter itself as well as just outside the filter exhaust. The personal and area samples consisted of the 31 VOCs profile as well as nine

metals. Table 5.1 summarizes the permissible exposure limit (PEL) and action level (AL) concentrations for the nine metals that were surveyed and collected in the area and personal samples.

**Table 5.1: Exposure Limits Set by OSHA and Regulated in Subpart Z- Toxic and Hazardous Substances**

Contaminant	OSHA PELs (mg/m <sup>3</sup> )	OSHA Action Level (mg/m <sup>3</sup> )
Cadmium (1910.1027)	0.005	0.0025
Chromium	1	NA
Cobalt	0.1	NA
Copper	0.1 (fume)	NA
Iron Oxide	10	NA
Lead (1910.1025)	0.5 (c)	.03
Manganese	5	NA
Nickel	1	NA
Zinc Oxide	5 (fume)	NA

*Note that (c) denotes a ceiling limit.*

Three area samples of the 9 metal profile were collected in addition to two personal samples that were worn by the laser operator and the assistant.

The first metal profile samples was placed about 12 feet away from the work table where the laser removal activities were taking place. The sample was collected between 10:35 AM and 3:35 PM, during the entire period of the LACR demonstration. The second sample was set approximately 2.5 feet from the filter exhaust point of the laser fume extractor. This sample was also collected between 10:35 AM and 3:35 PM, throughout the entire duration of the LACR demonstration. The third area samples was placed about 5 feet away from the rear wall of the room, and once again was collected between 10:30 AM and 3:35 PM, corresponding to the full duration of the LACR demonstration.

Area air sample results from Phase I LACR testing indicated that airborne concentrations of metals (cadmium, chromium, cobalt, copper, iron, lead, manganese, nickel, and zinc) were below

the OSHA PEL and OSHA AL. These results are representative of area concentrations for employees performing routine lead abatement activities, such as the LACR process that was demonstrated here. The two personal samples for the nine metal profile survey were worn by both the laser operator and the assistant to the operator.

The first operator, who was both an operator and a helper, used the laser to remove paint from various pieces of the I-beam sections resting on a table of about waist height. The first operator laser cleaned during the morning portions of the shift and worked as the helper in the afternoon. The sample was placed in the first operator's breathing zone from 10:30 AM to 3:35 PM, including a lunch break of about 35 minutes. Analytical results indicated that the first operator's exposure for the nine metals was below laboratory detection, with the exception of lead. Lead results measured  $0.0014 \text{ mg/m}^3$ , below both the OSHA action level of  $0.03 \text{ mg/m}^3$  and OSHA's PEL for lead of  $0.05 \text{ mg/m}^3$ .

The second operator, who also worked as an operator and helper, spent the morning hours of the demonstration inside of 10 feet of the lead removal operation as a helper while moving I-beam sections to and from the first operator. In the afternoon hours the second operator laser cleaned while the second operator acted as a helper, handling the I-beam sections. The entire demonstration lasted from 10:30 AM to 4:00 PM and no breaks were taken during this period, other than a 35 minute lunch break. Analytical lab results showed that the second operator's exposure to the nine metals was below laboratory levels of detection (LOD), except for lead. Lead concentrations were detected at  $0.0032 \text{ mg/m}^3$  above the LOD, but below both the OSHA PEL and OSHA AL.

In addition to the nine metals, an Assay 56 badge was used to measure 31 different VOCs that may have been created or emitted into the immediate area due to the laser cleaning. The VOCs

that were included in the Assay 56 badge profile included Methyl chloroform, 1,1,2-Trichlorethane, 1,1-Dichloroethane, 1,2-Dichlorethane, acetone, Benzene, Chlorobenzene, Cumene, Cyclohexane, Cyclohexanone, Cyclohexene, Ethyl Alcohol, Etylbenzene, Isopropyl Alcohol, m-dichlorobenzene, Methyl Ethyl Ketone, Methyl Isobutyl Ketone, Methyl n-propyl ketone, Methylene Chloride, n-butyl Acetate, n-hexane, n-propyl acetate, o-dichlorebenzene, p-dichlorebenzene, Pentane, Tetrachloroethylene, Tetrahydrofuran, Toluene, Trichlorethylene, and xylene.

During the Phase I demonstration both area and personal samples were taken for volatile organic compounds (VOCs), which included two personal samples and three area samples.

The first area sample was placed in the left corner of the room, about 12 feet away from the work table where the operator was conducting laser removal activities. This sample was collected between 9:15 AM and 3:20 PM throughout the entire period of the laser removal demonstration. The second area sample was set up about 2.5 feet away from the exhaust port of the laser fume extractor, and was collected from 10:30 AM to 3:20 PM. Another area sample was placed in the back of the room, about 2.5 feet away from the exhaust point of the laser fume extractor, and was also collected from 10:30 AM to 3:30 PM. The analytical results showed that in all area samples the airborne concentrations of all 31 VOCs were below laboratory detection limits.

Two personal VOC samples were also collected, which were worn by the laser operator or the person assisting the operator. One sample was collected from 9:05 AM to 3:50 PM and the other from 9:10 AM to 3:45 PM. Analytical results indicated that airborne concentrations of all 31 VOCs were below laboratory detection limits.

In addition to the area and personal metal and VOCs samples, toxicity characteristic leaching procedure (TCLP) testing was also completed on several of the filter components. The TCLP testing followed EPA methods SW6010C and SW7470A and included silver, arsenic, barium, cadmium, chromium, mercury, lead, and selenium. As presented in the results, the sampling was completed on three different parts of the filter, TCLP 1 was placed in the activated carbon filter, TCLP 2 in the HEPA filter, and TCLP 3 in the particle debris filter. TCLP 1 showed that all metals were below the reporting limit, meaning that the carbon filter is considered non-hazardous. TCLP 2, in the HEPA filter, showed that all metals were below the reporting limit except for lead, which was measured at 0.141 mg/L, where the reporting limit for lead is 0.100 mg/L. This still corresponds to a non-hazardous amount of lead, as determined by OSHA guidelines. The particle filter, which contained TCLP 3, showed all metals were below the reporting limit except for lead and chromium, which were measured to be 464 mg/L and .302 mg/L respectively. The chromium reporting limit is 0.100 mg/L, and lead is considered hazardous above 5 mg/L under RCRA, meaning that the particle debris filter is hazardous waste. Therefore this filter must be disposed of and cleaned using the proper PPE for handling hazardous lead waste. Again, as mentioned in the results, the area sample that was placed directly outside the filter exhaust (2.5 feet away), showed that airborne concentrations of all nine metals were below laboratory detection limits. This confirms that there was a large amount of lead paint removed from the beams as evidenced by the hazardous levels of lead in the particle filter, but that the filter was working correctly and prevented any detectable traces of lead to be released into the surrounding area, as determined by the area sample placed directly adjacent to the filter exhaust.

In conclusion, the industrial hygiene survey determined that airborne contamination of the contaminants included in this evaluation were well below the current OSHA PELs and OSHA ALs for each sample's work area during the Phase I LACR demonstration. This indicates that corrective actions are not needed at this time to further reduce employee exposure associated with LACR of lead containing coatings from steel. However, tests sampling for metals in the activated carbon filter, HEPA filter, and particle debris filter of the CleanLaser CL1000 showed that the particle filter debris was hazardous for lead, and must be disposed of correctly.

### **5.3 Laser Cleaning of Lead Paint**

After EDS analysis revealed that the composition of the red base paint coat was the lead containing paint, it was theorized that this was consistent with red lead paste, a bright orangey-red colored anti-corrosive primer base paint coating that was commonly used throughout the early 1900s. During this time it was liberally applied to structural metals for corrosion protection, including the Golden Gate Bridge when it was originally built (1937), which interestingly gave the bridge its iconic "international orange" color. Around the mid 1960's red lead paste was slowly phased out of use due to the invention of more effective and environmentally friendly anti-corrosion coatings.<sup>47,48</sup>

Red lead paste is a simple mixture of the mixed valence  $Pb_3O_4$  (II, IV) oxide crushed powder and linseed oil, which is used as the organic binder to keep the powdered red lead pigment in suspension and make it spreadable for application. This paint mixture was made by crushing  $Pb_3O_4$  (II, IV) oxide powders to smaller particle sizes and then dispersing the thin powder into linseed oil, a mixture of fatty acids that were extracted from a flax plant and that had great binding and suspension properties for paints during this time.<sup>49-54</sup> Figure 5.1<sup>48</sup> shows SEM micrographs of the dry  $Pb_3O_4$  (II, IV) oxide powder as well as after it is applied as a slushy to an iron cathode.

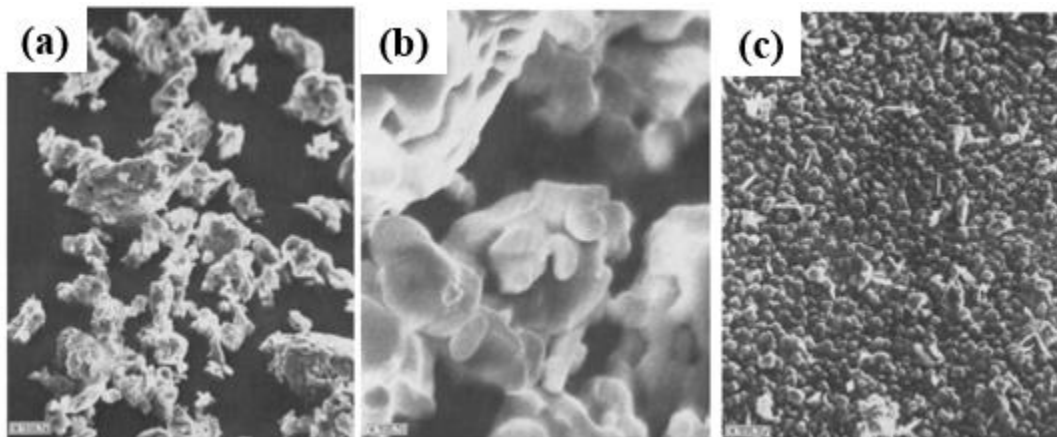


*Figure 5.1. SEM micrographs of  $Pb_3O_4$  (II, IV) oxide powder. a.) The dry powder at 2,400x magnification. b.) the dry powder at 12,000x magnification. c.) Lead oxide powder applied in solution to an iron cathode, magnification 2,400x.<sup>48</sup>*

EDS analysis of base metal samples revealed that the base paint layer was high in lead and oxygen, and contained carbon as well, which correlates well with the composition of red lead paste due to the lead oxide and organic linseed oil that provided the binding and adhesiveness of the paste. (Figure 5.2). In addition the base paint layer has a bright orange-red color very similar to that of  $Pb_3O_4$  (II, IV) oxide. (Figure 5.3).

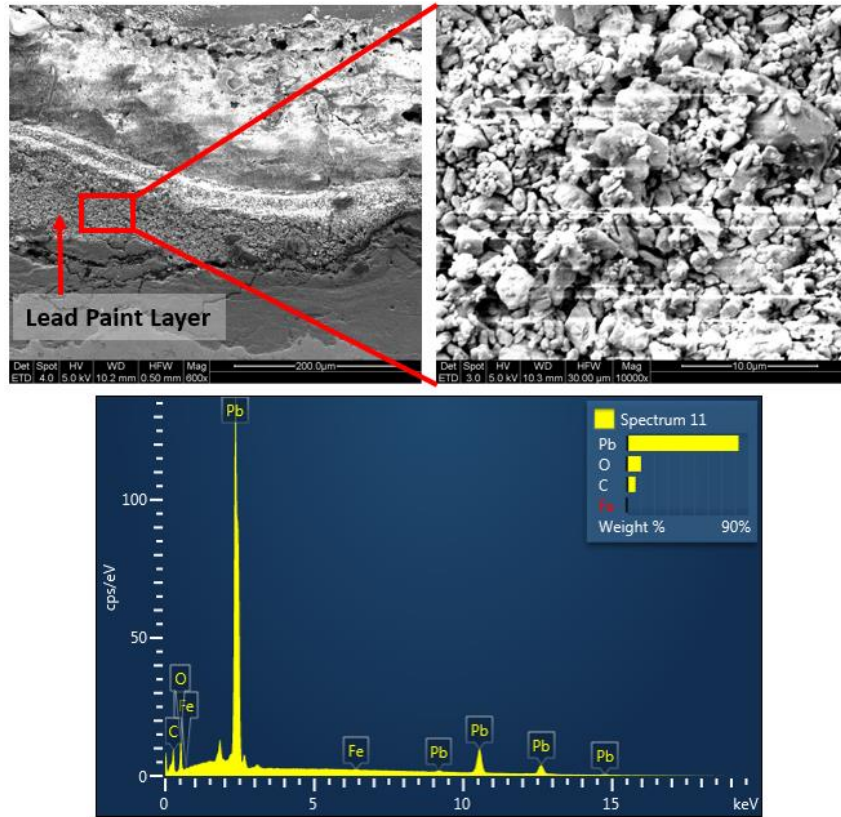


Figure 5.2. SEM micrographs show the details of the red base paint layer on the base sample cross sections. The variation in particle size is comparable to that seen in figure 5.1, where the particles are presumably the crushed  $Pb_3O_4$  (II, IV) oxide crystals used for the red lead paint. EDS confirms the presence of lead in the coating.



Figure 5.3. Macroscopic appearance of crushed  $Pb_3O_4$  (II, IV) oxide, the inorganic pigment used in the red leaded base coat of paint applied to the bridge beams.

In this mixture, the red lead oxide acts as a pigment, providing the characteristic orange red color to the paste. Pigments are organic or inorganic compounds that provide color through the selective

absorption or scattering of specific wavelengths and the reflection of others, in turn giving the pigment its perceived coloration. Pigments are different from dyes

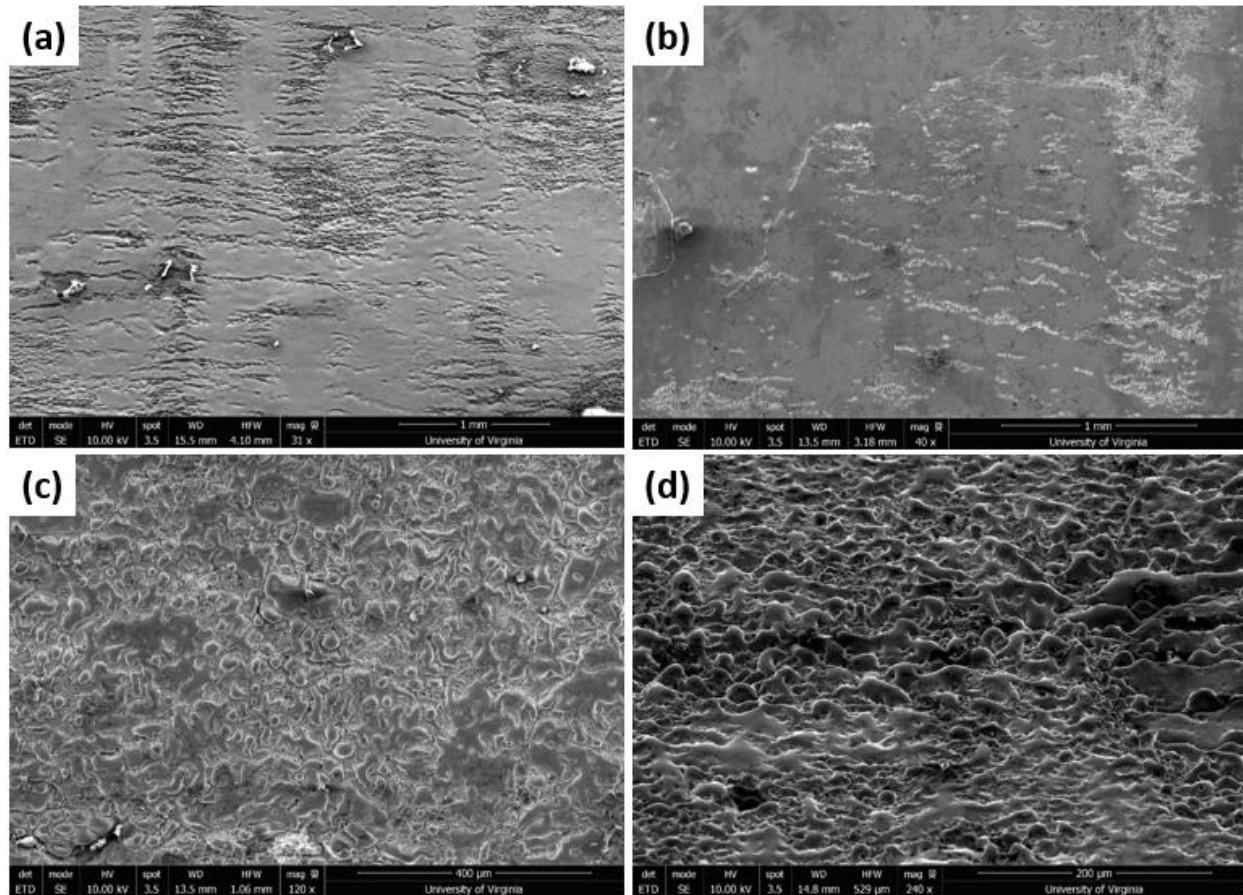
in that pigments are not water soluble and therefore act as suspensions in a mixture, whereas dyes are water soluble and are true solutions when dissolved in aqueous solvents.<sup>55</sup> Because clusters of the red lead paint remained on the surface after laser cleaning, the efficacy of the laser in removing the red lead oxide was questioned. Due to the possible perceived difficulty to

remove the red colored base paint specifically during the LACR process, it is theorized that the  $\text{Pb}_3\text{O}_4$  (II, IV) oxide crystals present in the coating interact with the laser light as to diminish the effect of laser ablation. One possible explanation is that the lead oxide crystals do not absorb the laser wavelength well, and therefore are not easily ablated from the surface. After further literature searches comparing the absorptivity of the  $\text{Pb}_3\text{O}_4$  (II, IV) oxide to that of titanium dioxide and zinc oxide that is present in the white paint layer, it was determined that the absorptivity of these pigments are very similar to each other and therefore could not be attributed to the observed differences in paint removal. (see appendix B). Due to this it was concluded that the base  $\text{Pb}_3\text{O}_4$  (II, IV) oxide paint simply appeared to remain on the laser cleaned surface because it was the deepest paint layer and therefore would require a greater number of laser passes to fully remove after the top coats of paint had been removed.

#### **5.4 LACR Surface Analysis**

In the results, the different surface features after LACR were briefly introduced. These mostly consisted of the smoother “reflective areas” and the rougher, darker, or less reflective areas which were distributed across the surface. These observations were attributed to the difference in surface topology as seen in the SEM, and further SEM analysis helps to reveal more detail about the LACR surface. In figure 5.4, SEM micrographs show the distribution between these two different surfaces. In figure 5.4 (a), there is an even amount of rough surface area to smoother surface area, and these two regions are both evenly spread over the surface. This is in contrast to (b), in which a large area of the surface in the micrograph is the flat and reflective type, with relatively very little area consisting of the rougher surface profile. This exemplifies how the distribution of these two surface profiles varies over the entire LACR surface, and that large swaths of surface area can be dominated by the flatter or the rougher profiles. Figure 5.4 part (c)

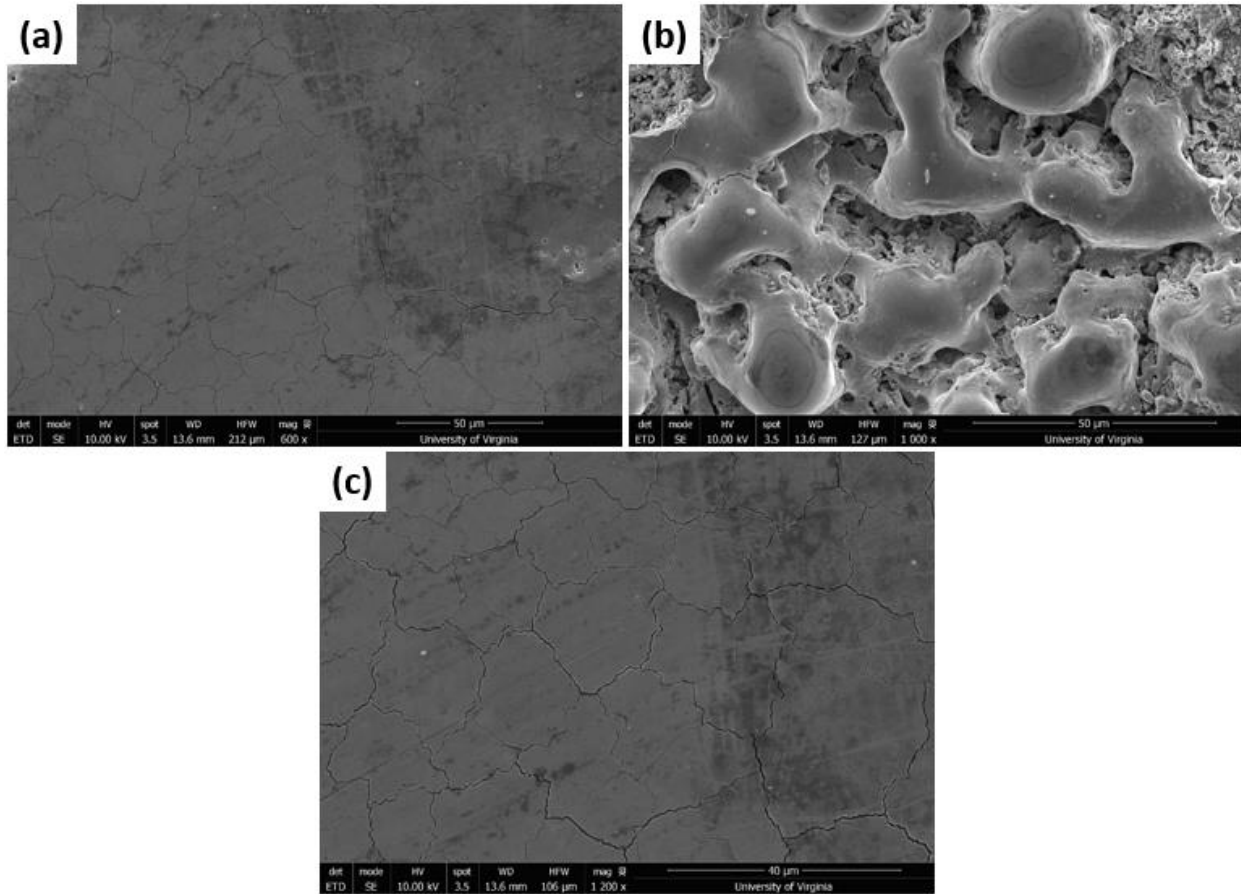
and (d) show higher magnification images of the rougher surface profiles, from a top down view and at a high tilting angle respectively.



*Figure 5.4. Low magnification SEM micrographs showing the different types of surfaces left after LACR, and their distribution throughout the surface. (a). A relatively even distribution of the flat surface and the rough surface topology. (b). An area that predominately consists of the flat surface, with a few rougher regions present. (c). A top down view of the rougher surface region. (d). a tilted side view of the rougher surface region.*

Figure 5 shows how the rougher area contains raised areas, with valleys in between these peaks, giving rise to the roughness of the surface. The scale bars in part (a) and (b) are the same, and this gives a sense for how the rough surface compares to the bright reflective smooth surface, which is very flat in this particular area. Also apparent from these images are the “mud” cracks that are present throughout the LACR surface. They are even present on the rougher areas,

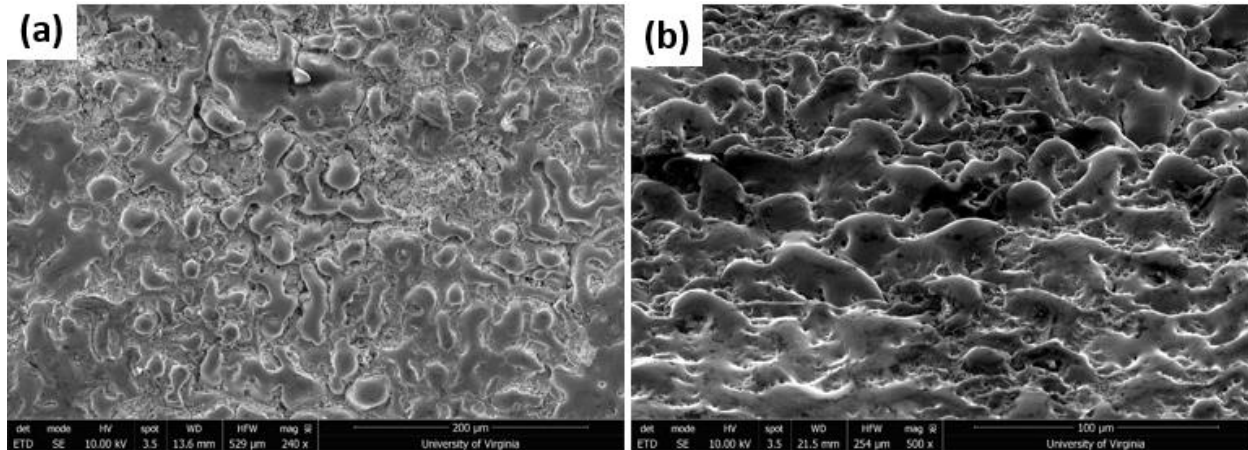
however they are more difficult to see due to the peaks and valleys of the raised and lowered surface compared to the flat surface of the smoother areas.



*Figure 5.5. A comparison between the flat surface regions and the rough surface regions. In (a) and (b) both scale bars are 50 μm and allows direct comparison between the scale of the rough surface features compared to the flat surface. (c) shows the flatter surface at higher magnification, where the mud cracks can be easily seen.*

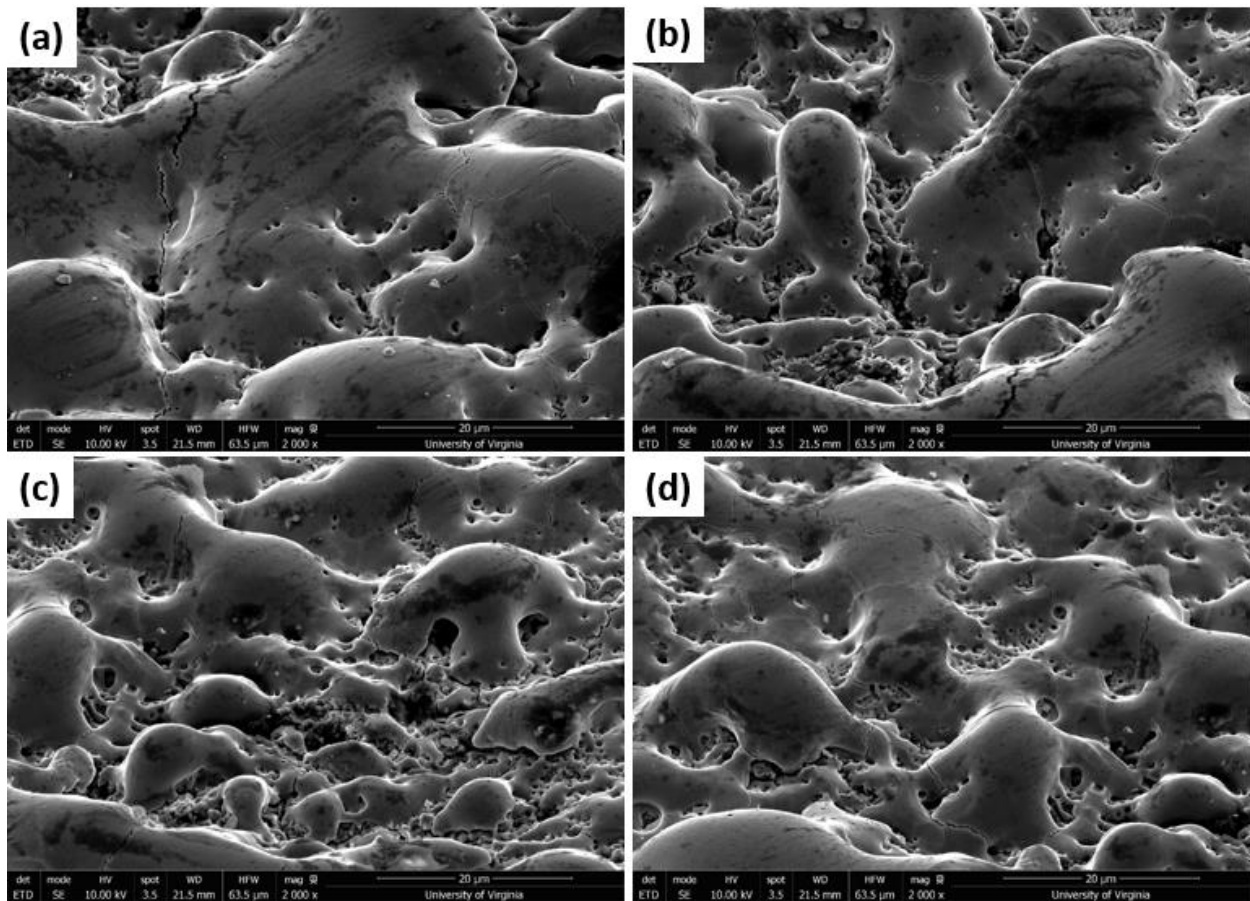
Higher magnification SEM micrographs helps to further characterize the rougher surface regions.

Figure 5.6 (a) shows another top down view of this surface, whereas figure 5.6 (b) shows a profile view from a tilted angle. When viewed directly downward the detailed feature of the valleys can be seen whereas from a side view the smoother sides and tops of the peaks are the focus of the image. The tops and sides of the peaks are smooth in appearance whereas the valleys are much rougher and tortuous.



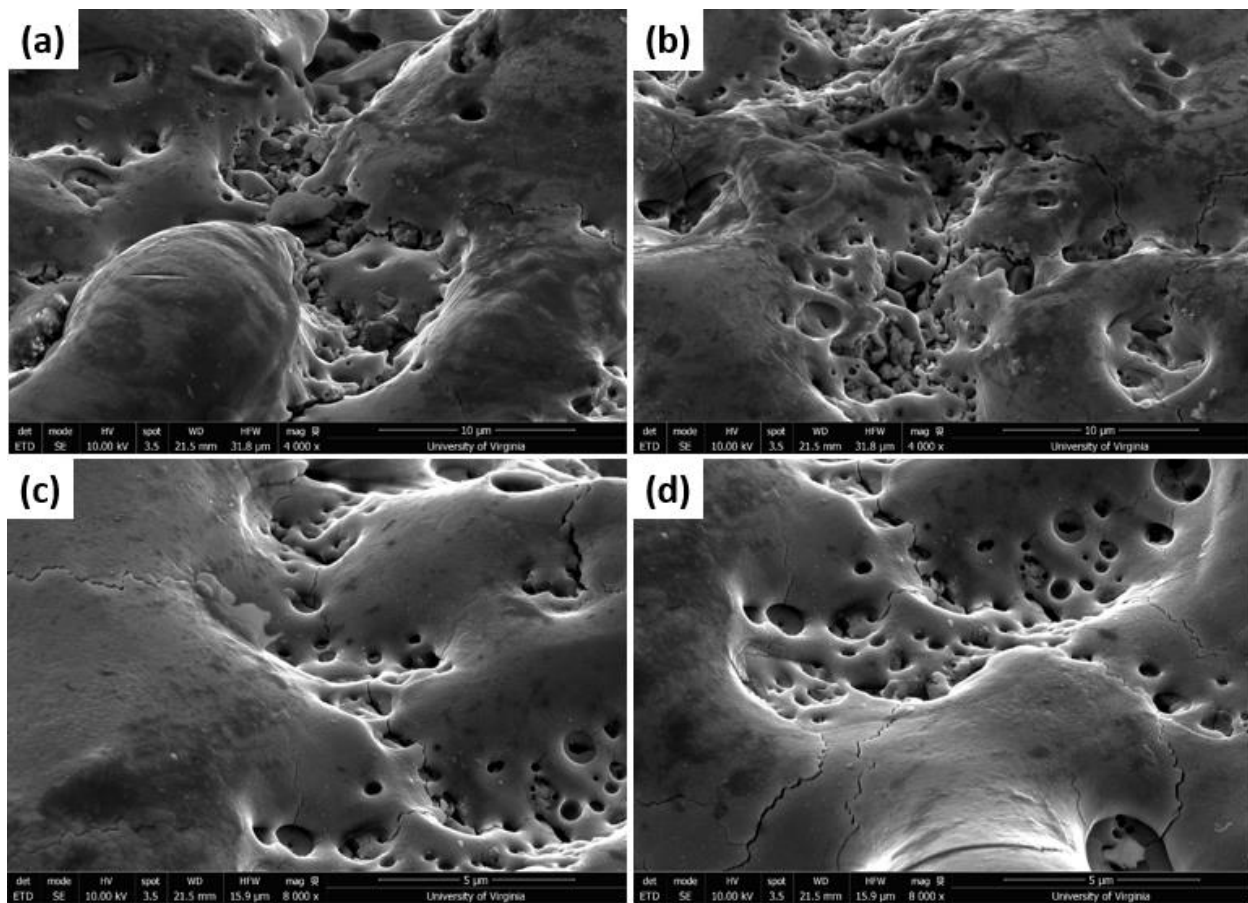
*Figure 5.6. (a) A Top-down view allows views of the valleys in the rough regions of the surface, as well as gives an idea for the area taken up by the peaks compared to the area filled by the valleys. (b) A tilted SEM view gives a side profile of the rough region where the smooth surface of the peaks is visible and the rough tortuous valley are hidden from view.*

Figure 5.7 shows higher magnification SEM micrographs from a tilted view of the same rough surface region. The variability of the surface topology at this length scale becomes obvious once viewed from this tilted angle. In some spots the surface is smoother and rounded, as in figure 5.7 (a), however in others it is rougher and the peaks are not as well defined, as seen in figure 5.7 (c). Figure 5.7 parts (b) and (d) also contrast the difference in height between the valleys and peaks within this overall rougher region of the surface, where in (b) the peaks are relatively high from the surrounding valleys compared to peak to valley distance in (d).



*Figure 5.7. SEM micrographs of the tilted sample at high angles ( $\sim 55^\circ$ ). Tilting allows a better visualization of the heights between the peaks and valleys that are not discernable from top down perspectives. Comparing (a) and (c) shows the difference between areas containing more of the smooth “peak” like surface compared to surface with more of the tortuous rough “valley” like appearance of the surface. (b) and (d) show the range of distances observed between the peak to valley heights.*

At higher magnifications tiny (roughly  $0.5 - 3.0 \mu\text{m}$ ) holes are seen in the valleys, however not on the peaks of the rough LACR surface regions, (figure 5.8). Also, the cracks in the surface can still be seen in these images.



*Figure 5.8. Holes are observed in the valleys of the rougher regions, however they are not as commonly seen on the tops of the peaks. Also in (c) and (d), the mud cracks can be seen on the surface, across the valleys and peaks in this region.*

### 5.5 LACR Cross Section Analysis

Multiple cross sections of the LACR samples helped to study the iron oxide layer that was left on the surface after LACR treatment. Cross sections helped also reveal the two different surface topologies, the smooth and the rough regions. In the rough surface regions, cross sections show a tumultuous surface where the peaks and valleys that were observed on the surface are now presented as cross sections. As seen on the surface, there is a variation in the shape of these features, as shown in figure 5.9. It can be noted that the spacing and height of these peaks is different from one area to another, matching the observations from surface microscopy.

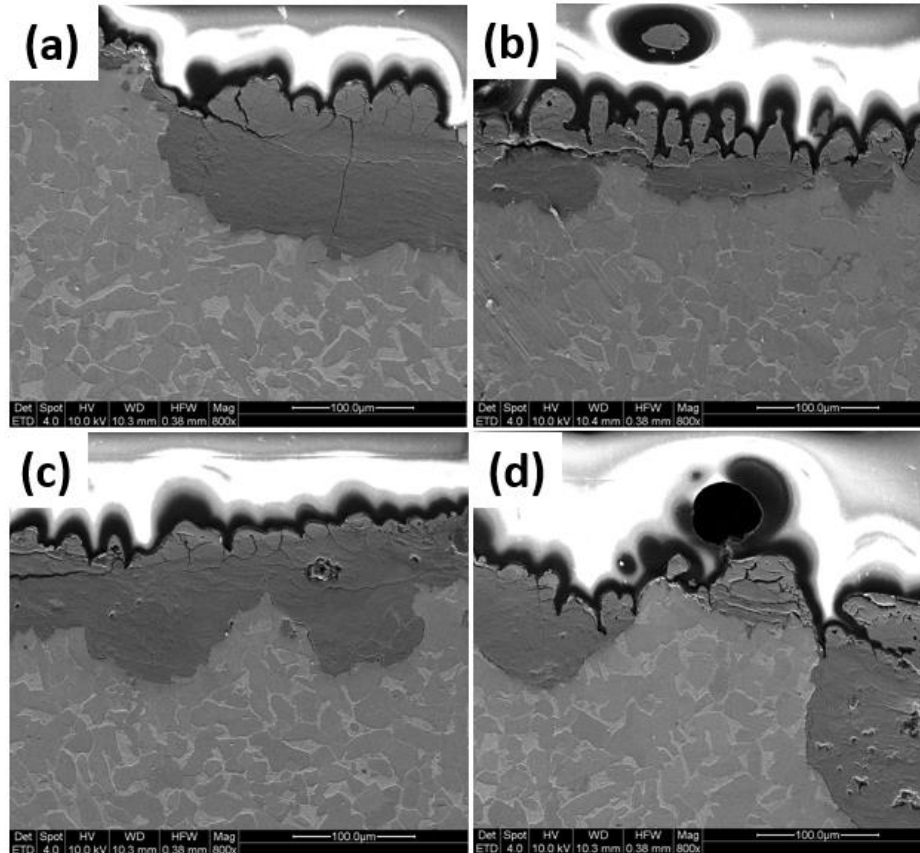


*Figure 5.9. Cross sectional SEM micrographs of LACR sample surfaces showing the variation in the oxide layer surface throughout one of the rough surface regions. (a) The oxide surface peaks are relatively spaced out compared to (b), where they are very close together and have large peak to valley distances. In (c) and (d), cross sections show how the peaks can be smaller in some areas and that the oxide layer is not always continuous across the entire surface, respectively.*

In contrast, the smooth reflective parts of the LACR surface are much flatter in cross section as expected. As shown in figure 5.10, the microstructure of the underlying steel seems to be unaffected up to the iron oxide surface layer as evidenced by the unaltered pearlite ferrite grains right up to the oxide.

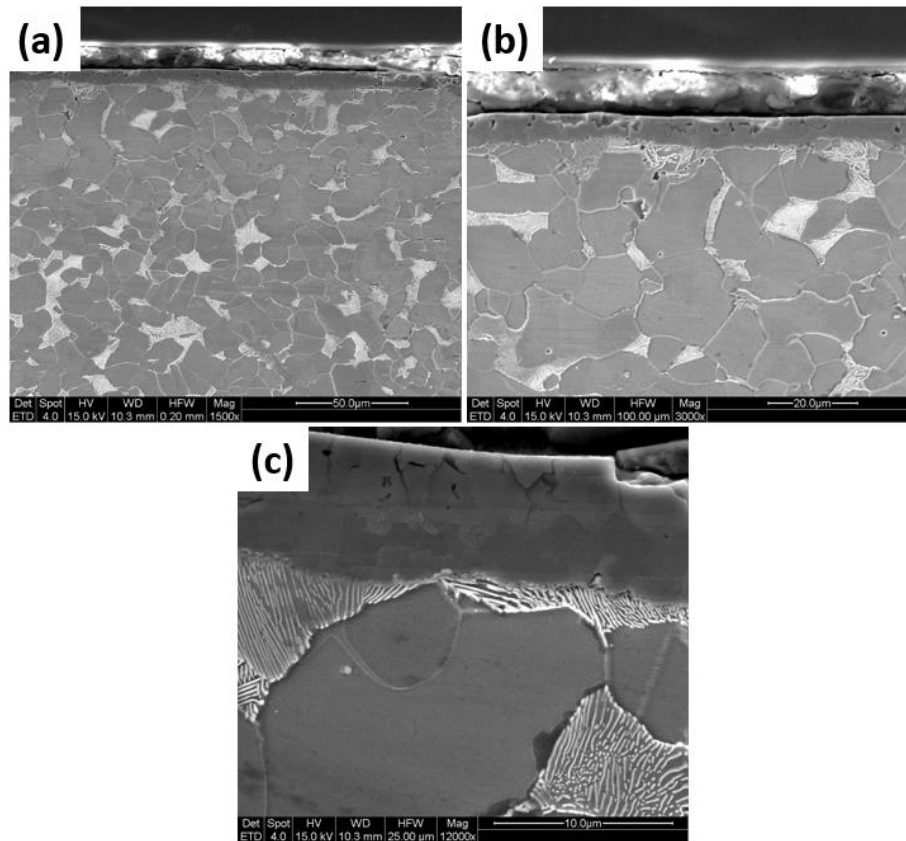


*Figure 5.10. SEM micrographs of LACR sample cross sections. (a) Showing the flat oxide surface corresponding to the reflective flat LACR surface regions. (b) higher magnification of (a). (c) High magnification SEM showing that the steel microstructure is unaltered all the way up to the oxide surface layer.*

As already mentioned, the iron oxide layer across the steel surface is not continuous at every point, and in some places exposes the steel directly to the laser beam. In these regions there is an effect on the surface that alters the appearance of the near surface region of the metal, along with the microstructure further into the steel. In figure 5.11, an exposed part of the steel adjacent to an end of the iron oxide is seen in cross section, revealing the effect of the laser on the metal. At lower magnifications, the decrease in grain size compared to the bulk material can be seen, and at higher magnifications the near surface region that was affected by the direct laser light is outlined in red.

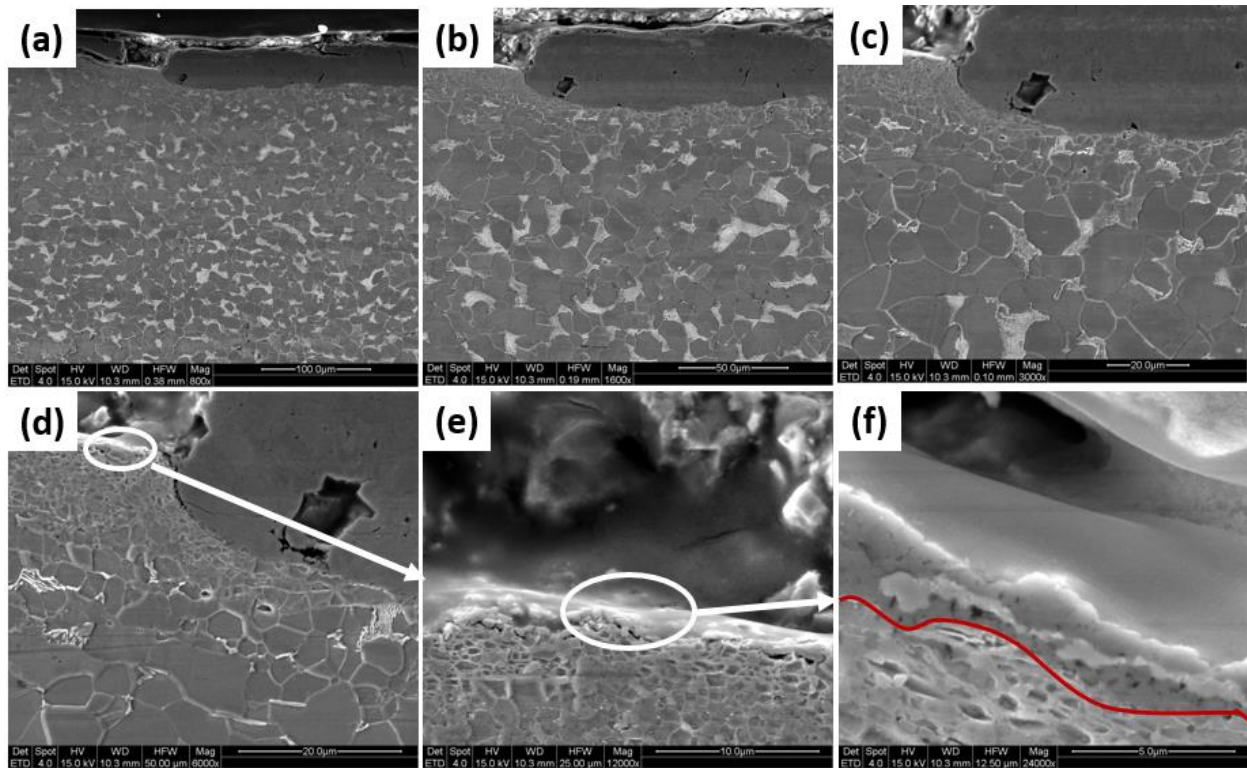


*Figure 5.11. SEM micrographs of a LACR sample cross section showing the effects of laser damage directly on exposed steel adjacent to the iron oxide surface layer. (a), (b), (c), Successively higher magnification micrographs showing the effect of laser heat on the near surface steel compared to the bulk microstructure. (d), (e), (f), Higher magnification micrographs showing the surface region that was affected by the laser heat, outlined specifically in red in (f).*

Throughout the surface of the laser cleaned steel, there are chips and surface scratches that change the surface topology and roughness, mostly due to the initial rough surface of the I-beams before undergoing LACR. Figure 5.12 shows a piece of steel that is lying on top of the oxide layer, confirmed to be steel by the microstructure. Because this piece of steel is outside the bulk I-beam material, the microstructure is different than that of the bulk steel, as seen in the micrographs. For example there is no indication of a texture due to hot rolling, and the size distribution of ferrite grains and pearlite is much different from that of the bulk steel. This may be due to multiple factors such as deformation of the metal if scraping is what caused it to pull

away from bulk material, or even that it was exposed to more heat energy from the laser beam due to the fact that more surface area is exposed compared to the steel underneath the surface.

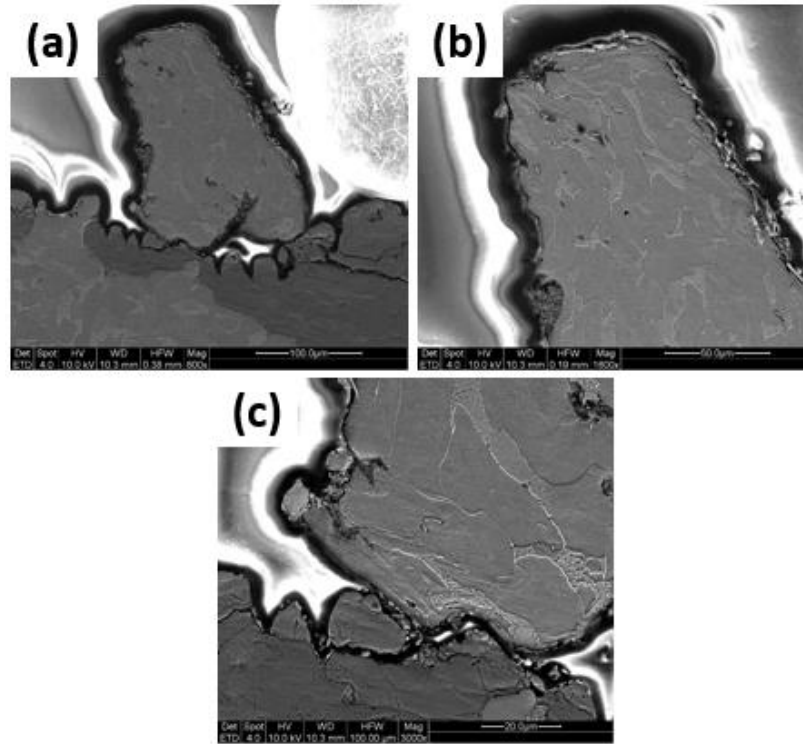


*Figure 5.12. A chipped piece of steel laying on top of the surface of the laser cleaned steel. (a), the full view of the chipped steel particle. (b) The top portion of the chip, (c) and bottom where the chip interfaces with the iron oxide surface layer.*

In addition, cross sections with rounded edges between the steel and the iron oxide layer help to show the transition between the two materials. Figure 5.13 shows cross sections of laser cleaned samples with rounded edges at the transition between these two regions. These micrographs also show the roughness throughout the oxide layer. Towards the right side of 13a, a step in the oxide thickness can be seen, and in the in the background of 5.13b a similar step can be observed across the entire surface.

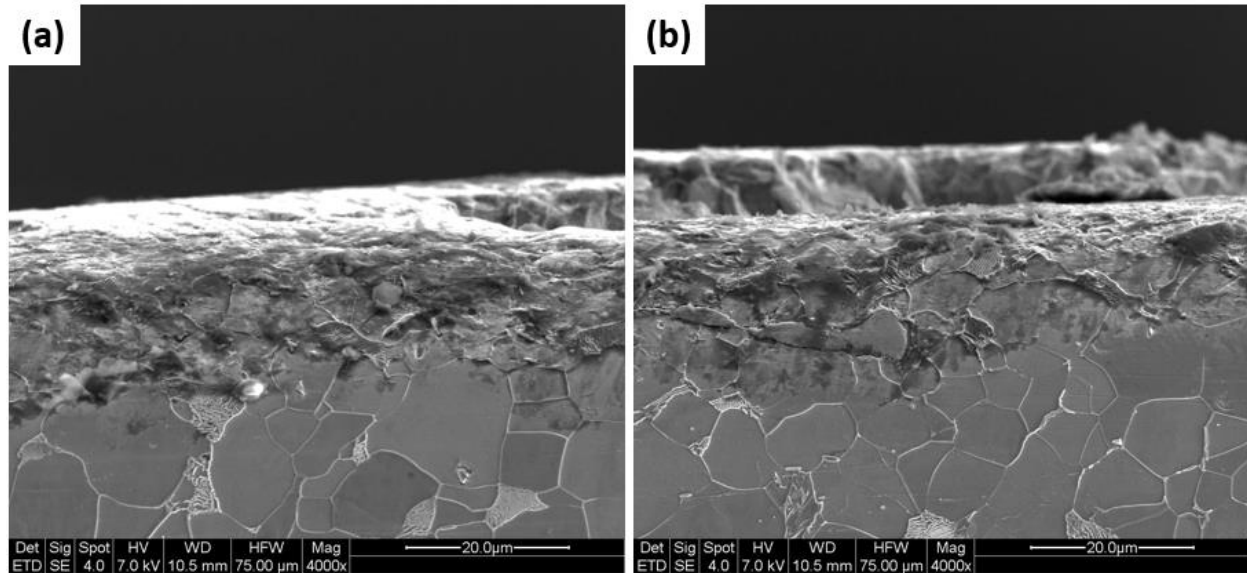


*Figure 5.13. Rounded polished edges on cross sectional samples show the transition from steel to iron oxide. Also both (a) and (b) shows the roughness of the iron oxide surfaces.*

In addition to SEM analysis of laser cleaned cross sections, EDS helped to confirm the cleanliness of the steel after LACR. By comparing cross section samples in EDS before and after laser cleaning, the removal of the paint is clear. Figure 5.14 shows EDS maps of a base metal sample in cross section showing each layer of paint. As explained in the results, the composition of each layer in cross section is consistent with what was observed using planar EDS maps of the paint surface, where a base paint layer of lead is covered with the white colored paint which contains both titanium and zinc, followed by a top layer of aluminum paint.

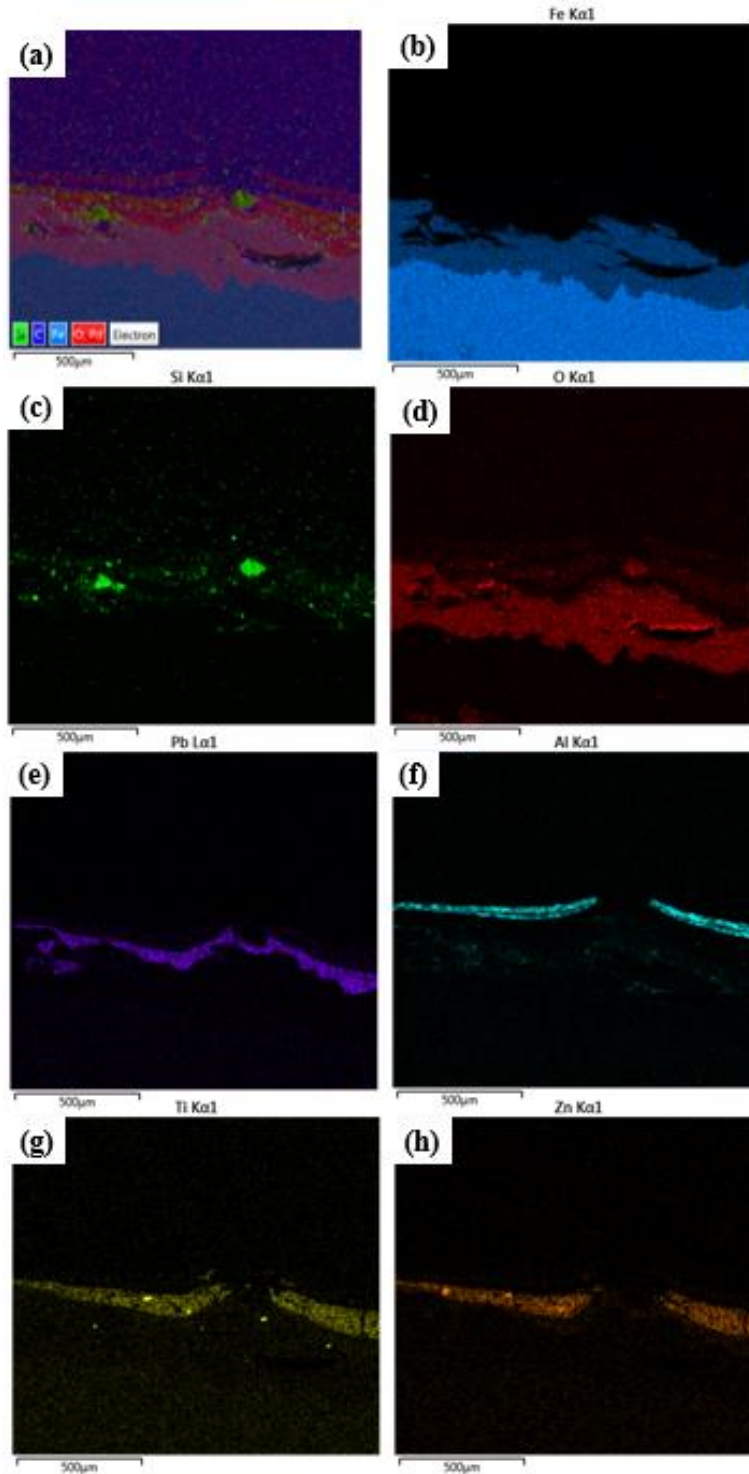


Figure 5.14. EDS maps of base metal cross sections. As described in the results, the base layer paint contains Pb (e), the middle layer Ti (g) and Zn (h), and the top paint coat consists of Al (f). The Fe (b) and O (d) maps also depict the oxide layer. Pieces of silicate minerals are observed in the silicon map (c), which are dispersed throughout the Ti and Zn paint layer.

In addition to EDS maps of base metal paint cross sections, BSE micrographs provide another method of determining each layer apart from each other. Figure 5.15 shows BSE micrographs of cross sections prior to laser cleaning in increasing magnification.

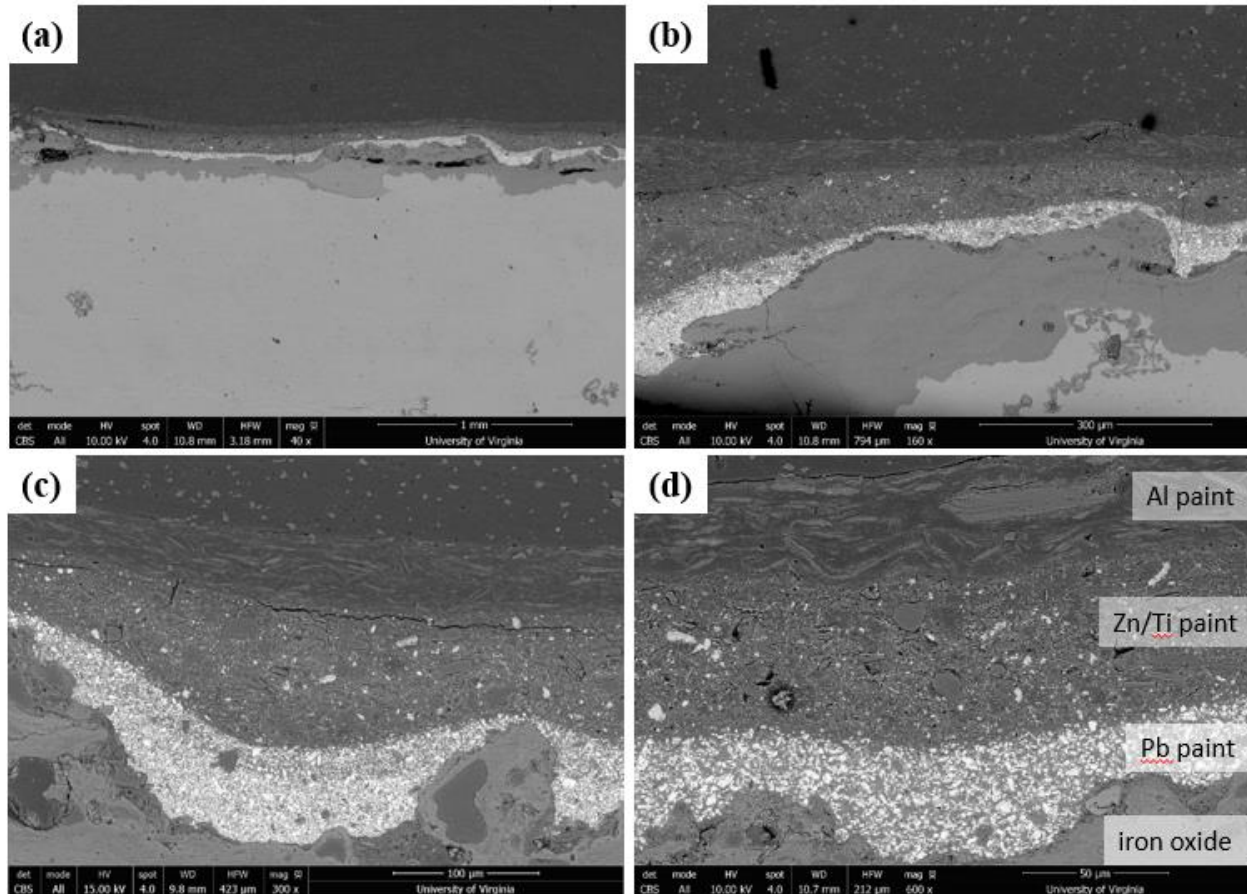
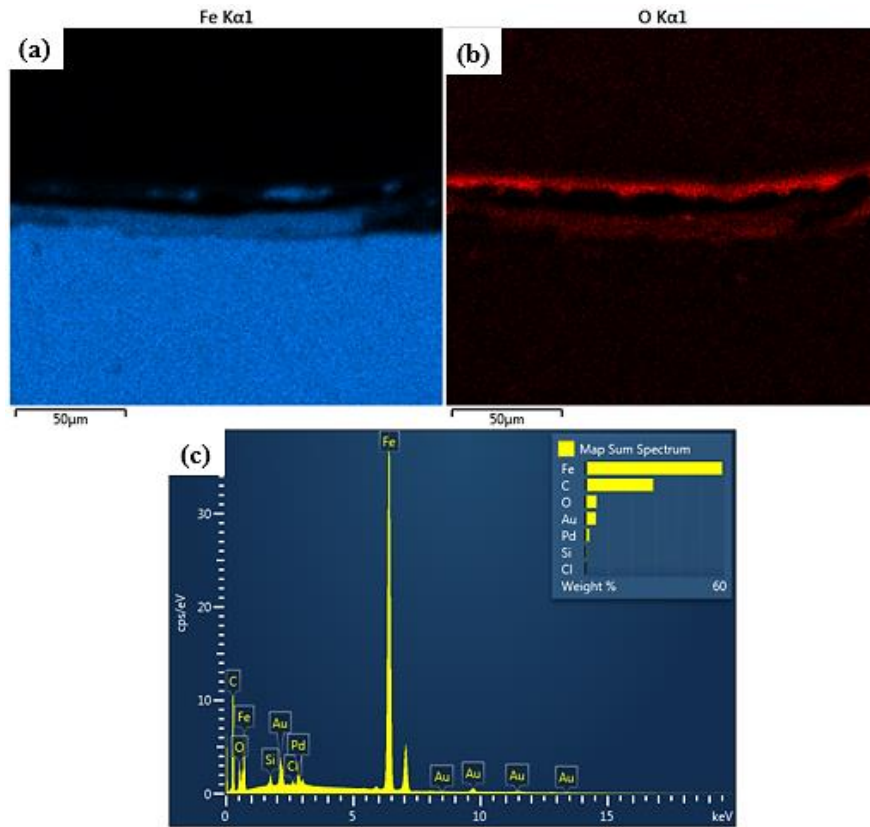


Figure 5.15. BSE micrographs of the paint and iron oxide layers on the base metal surface. (a) 40x magnification show a large scale size of the surface coatings compared to the bulk material. (b) 100x magnification. (c) and (d), showing the variation in coating thickness across the surface. The bottom layer is the iron oxide, followed by the lead paint, appearing brightest in BS imaging mode, zinc/titanium middle paint layer, and the aluminum flake paint top coat.

EDS map scans of laser cleaned surface cross sections showed that the iron oxide remained, but that all of the paint layers have been removed. Figure 5.16 shows EDS maps and an EDS spectrum of a cross section of a laser cleaned sample. The iron oxide surface layer can be seen as well as the bulk steel of the samples, which is very high in iron content. EDS confirms the

cleanliness of the sample by showing no residual paint, which would show up either as lead, zinc or titanium, or aluminum.



*Figure 5.16. EDS maps and spectrum for a laser cleaned sample cross section help to confirm that the coating has been removed, and show the iron oxide layer that remains on the surface. The carbon peaks are due to the sample epoxy mold, and the Au/Pd peaks are from sputter coating.*

## 5.6 Coating Adhesion

Due to the importance of coating bridge structures for protection, many state Departments of Transportation (DOTs), including VDOT, have conducted research into various coating systems and their effectiveness.<sup>56,57,58, 59</sup> One of the primary factors in the success of a coating in protecting the structural integrity of bridge steel is the adhesion of the coating to the metal substrate. Many factors can contribute to the adhesion strength, including the coating thickness, the coating system used, the environmental conditions at the time of the application of the

coating<sup>60</sup>, the surface condition of the substrate (such as roughness), among others. Although this study focuses on the effectiveness of LACR for coating removal operations, because the metal must be repainted for corrosion protection coating adhesion is just as important.

Paint adhesion to substrates is mainly classified into several distinct mechanisms: adsorption, chemical, and mechanical adhesion. Adsorption refers to the physical “bond” or attachment between the coating and the substrate on the atomic level. This includes factors such as Vander Waals forces that can keep polymeric or other organic binders in paints adsorbed to the substrate surface. Because this type of adhesion depends on forces at atomic and molecular dimensions, it requires very close contact between the coating and the substrate, which in turn depends on the wettability of the coating and substrate surface in question. To take advantage of strong adsorption effects, good wettability is needed to ensure that the paint is easily spread across the surface and that intimate contact is made between the paint molecules and the substrate.<sup>61</sup>

Chemical adhesion occurs when an actual chemical bond is formed between the coating and the substrate. In some applications and depending on the substrate, specific functional groups are incorporated into the paint polymer chain to react with the substrate and form covalent bonds to the substrate surface. These covalent bonds can be very strong and help to create strong adhesion between the coating and the underlying substrate.<sup>62</sup>

In mechanical adhesion, which was originally thought to be the only method of paint adhesion, the liquid paint flows over the substrate surface filling holes, pores, crevices, and micro-voids, and then once hardened the paint has a mechanical grip onto the surface. This mechanical interlocking with the surface is what provides the strength to the interface, and accounts for why abrasive blasting or mechanical roughening are common surface preparation treatments, by providing a sufficiently rough surface for the paint to hold on to.<sup>63</sup> Another way that surface

roughness increases adhesion strength is by increasing the surface area at the substrate-coating interface, allowing for even more interaction between the coating and the substrate, especially if chemical and/or adsorption adhesion is taking place.

For different applications various combinations of these three adhesion mechanisms are employed, and in many circumstances simply one or two of them is all that is needed for sufficient coating adhesion strength.

When testing coating strength and adhesiveness, it is important to understand different types of coating failures. In general, coating failure can be grouped into two types, adhesive failure and cohesive failure. Adhesive failure refers to a breaking of the bond between the coating and the substrate, resulting in the overall failure of the coating due to loss of adhesiveness between the coating and the substrate. In contrast, cohesive failure is when the coating or substrate itself mechanically fails, also resulting in ultimately breaking the coating-substrate piece into two separate pieces, however in this instance the coating to substrate bond is never truly broken. These two modes of coating failure are diagrammed in a schematic in figure 5.17.

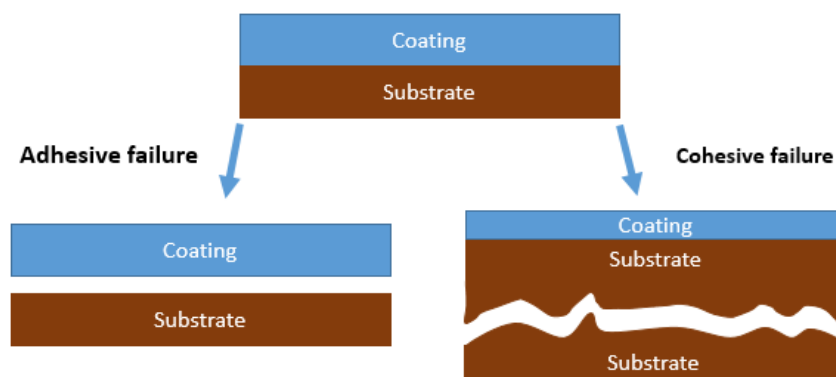


*Figure 5.17. Schematic showing adhesive versus cohesive failure between a coating and substrate. Note that in adhesive failure the coating to substrate bond is actually broken whereas in cohesive regime the bond between the substrate and coating is left intact, and the overall failure is due to a mechanical break in the substrate or coating itself.*

During PATTI coating adhesion testing of the repainted LACR treated beams, it was observed that not only was the reapplied paint coating removed from the substrate (the iron oxide layer on top of the steel), but that the oxide layer itself was sometimes broken away from the underlying steel. A schematic explaining how this occurs is shown in figure 5.18.

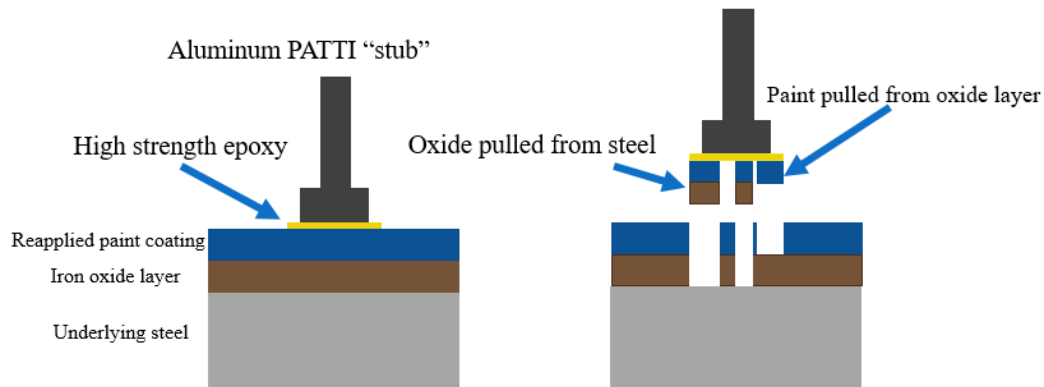


*Figure 5.18. A schematic diagram explaining how PATTI test stubs removed both reapplied paint from the surface oxide, as well as the oxide from the underlying steel. This implies that the paint to oxide bond is stronger in many cases than the oxide to metal interface.*

The significance of this is that the recorded coating adhesion is not only representative of the adhesion strength between the reapplied paint and the substrate, the iron oxide layer, but also includes the adhesion strength of the iron oxide to the steel. This also implies that the paint adheres so well to the iron oxide layer that this interface is more strongly bound together than the iron oxide layers adherence to the steel.

Figure 5.19 shows SEM micrographs of the PATTI stub surface, and shows the region on the stub surface where the paint was removed from the oxide, which shows up as paint on the stub, and also shows regions where the oxide itself has broken off of the steel, appearing as the iron oxide layer on the stub itself. In addition to the removed paint and oxide, the high strength epoxy is also seen, mostly on the perimeter of the stub. The insulating epoxy and paint both charge in

the SEM very easily compared to the iron oxide, and therefore this helps with identifying these materials.

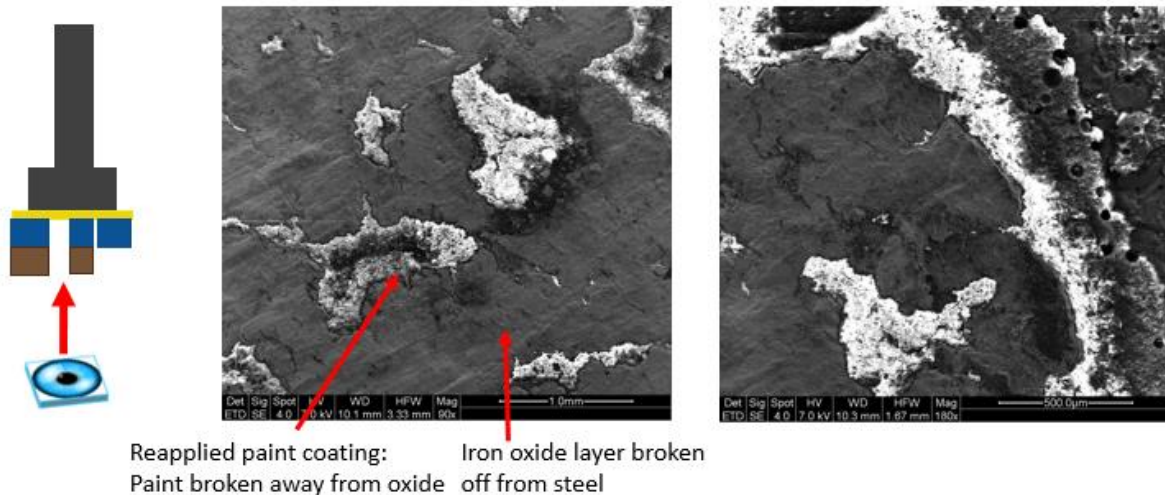


*Figure 5.19. SEM micrographs of the PATTI stub surface after testing. Both iron oxide and paint was found on the stub surface, proving that the adhesion of the paint to the oxide as well as the oxide to the steel was measured during PATTI testing.*

Another unique feature to LACR, aside from the preservation of the iron oxide layer when compared to grit blasting, is the absence of embedded grit in the metal surface. Aside from the possible detrimental effects that embedded grit can have on the fatigue life of the steel, it has been shown that the surfaces of grit blasting media, such as almandine garnet, do not bind as strongly with organic additives used in paints as well as steel surfaces do.<sup>64</sup> This implies that embedded grit blasting media can decrease the coating adhesion strength of the substrate surface to paint due to the weaker bonds between garnet surfaces and binding agents in the paint. While large amounts of embedded grit particles were not found in the blasted steel used in this study, depending on the specific steel used it has been shown that abrasive blasting can leave up to about a third of the treated steel surface covered in blasting residues, with potentially significant consequences for coating adhesion.<sup>64</sup>

The results for PATTI testing correlate well with previous coating adhesion tests that were performed in other LACR studies. The PATTI tests performed on the laser processed steel ranged from a low of roughly 10 MPa up to nearly 20 MPa, roughly depending on the thickness and roughness of the paint coating, although the average value was around 14 MPa. In LACR Part I, another LACR project conducted at the University of Virginia, paint adhesion strengths were measured to be roughly 14 MPa, ranging from 13.7 to 14.1 MPa, regardless of the laser processing parameters used, or the thickness of the paint. Others have reported a wide range of coating adhesion strength as well. It was determined that the coating adhesion strength depends on both the surface processing condition prior to painting and the thickness of the coating, and the coating system used<sup>65</sup>. For example, Toubia et al. has shown that paint coating adhesion on steel substrates can have a wide range of adhesion strengths (13 – 27 MPa)<sup>66</sup>, again dependent on the coating system used and the environment the painted surface is exposed to after painting. Adhesion strengths as low as 3.43 MPa have been measured for epoxy coatings on sandblasted carbon steel, where adhesion strength was also slightly dependent on coating thickness. In addition, it has been shown that coating adhesion strength is lower on conversion coating protected metals<sup>67</sup>, however that is not of concern as they are not commonly used as part of bridge coating systems.

Overall, despite the iron oxide layer present on the steel surface, there seems to be no detrimental effects from LACR on the coating adhesion properties of the substrate. As discussed earlier, the oxide layer may even act to enhance the coating adhesion, providing a bond to the epoxy paint that is stronger than the adherence between the iron oxide and the steel itself.

## 5.7 Fatigue Testing

The fatigue fracture surfaces that were analyzed were typical for those of low carbon steels, including the presence and effect of MnS stringers (inclusions).<sup>68-70</sup> MnS inclusions are the most common impurities found in steels and produce a recognizable microstructure as seen in the results, as well as a recognizable fracture surface.<sup>68, 71</sup>

MnS inclusions have been known to cause detrimental effects to the fatigue behavior of steel, and in the I-beam steel used in this study the failure mechanism reflected the presence of MnS inclusions and matched the commonly seen appearance of fracture surfaces of other manganese sulfide inclusion containing steel. This included the “woody” appearance of the fatigue fracture surface that is caused by the inclusions, which can introduce or accentuate anisotropic mechanical responses to the host steel when placed under certain stress states. This type of fracture surface is well documented in MnS inclusion containing steels, as seen in figure 5.20.<sup>68,72</sup> These fracture surfaces are from sulfur containing steels that have fatigued and left a “grainy” surface appearance due to the nonmetallic inclusions in the steel.

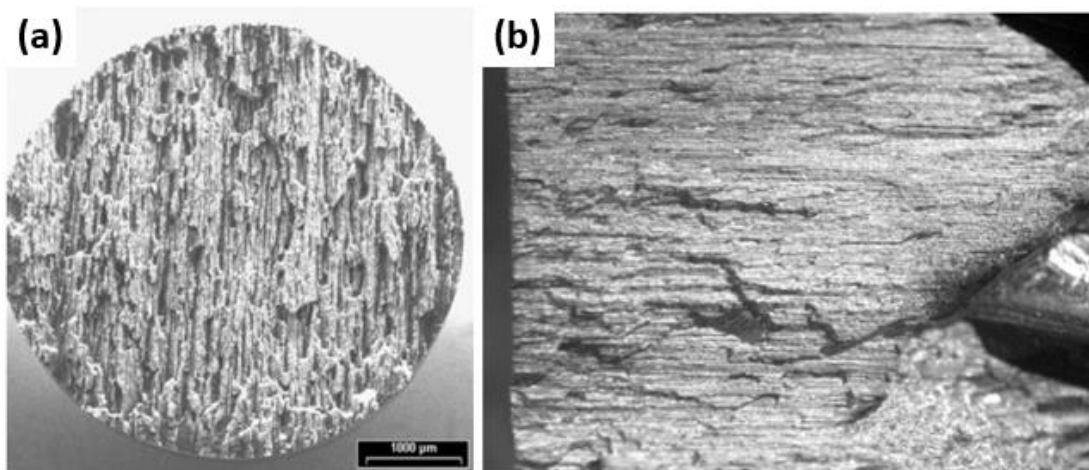


*Figure 5.20. Typical fracture surface of high sulfur steel. a.) Fracture surface of high sulfur steel with 40 HRC at strain amplitude 0.275%<sup>72</sup> b.) Optical image of the typical woody appearance of a resulfurized steel in ductile overload on a plane parallel to the longitudinal direction.<sup>68</sup>*

The same surface texture is apparent from the LACR fatigue samples. This was easily attributed to the MnS inclusions that were originally observed in the microstructure of the I-beam metal. Figure 5.21 shows low magnification SEM images of representative fracture surfaces of the LACR dog bones.

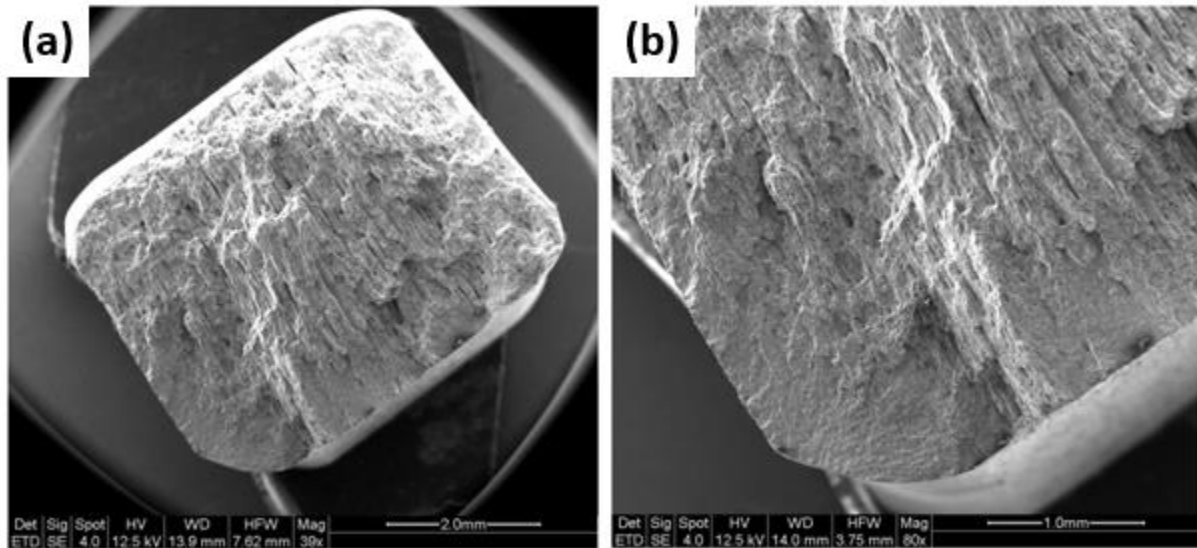


*Figure 5.21. Low magnification SEM micrographs of a fatigue fracture surface stressed at the highest maximum highest stress level tested (368 MPa). a.) 39x b.) 40x magnification.*

It was interesting to note holes of different depths on the fracture surface which had inclusions of varying dimensions present at the bottom. Upon closer examination of the fracture surface the dimpled texture of the surface is brought out, a typical surface texture for the ductile failure of low carbon steel. Figure 5.22<sup>73</sup> shows the holes that were observed on the fracture surface and how the surface texture compares to a literature SEM micrograph of a ductily failed A36 steel sample. The dimpled surface is easily distinguished and the similarity to the literature micrograph can be directly observed.

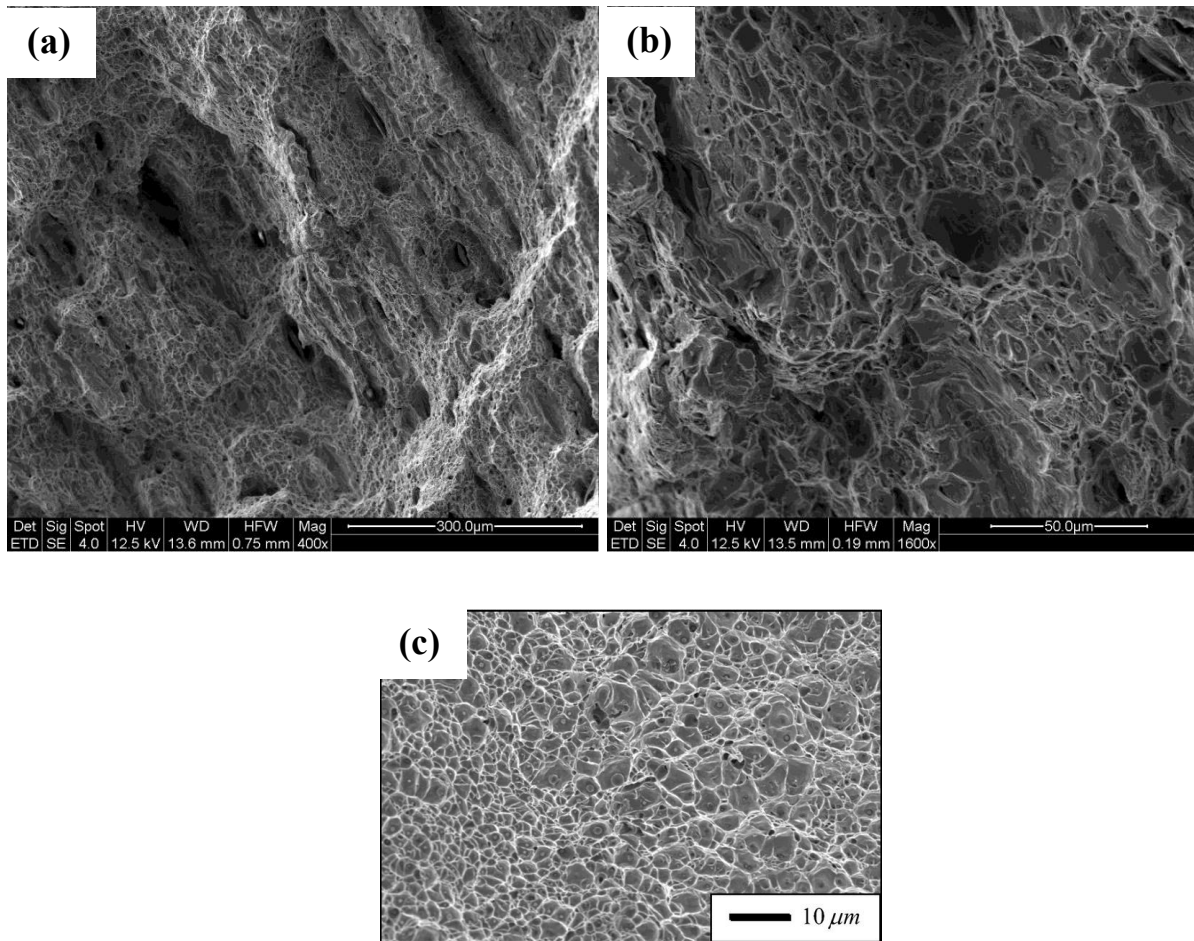


Figure 5.22. a.) SEM micrograph of the fracture surface showing the holes of varying depths surrounding the MnS inclusions. b.) Higher magnification of image (a). c.) Literature SEM micrograph showing the dimpled surface of a ductile A36 steel fracture surface.<sup>73</sup> One can note the similarity seen in the surface texture to image (b).

At even higher magnifications in the SEM, individual fatigue striations can be seen on the fracture surface (figure 5.23)<sup>68</sup>. These correspond to the incremental growth of the crack from the point of initiation to the beginning of ductile failure at which point the remainder of the thickness of the sample is quickly broken apart by plastic deformation of the metal, corresponding to the region with the “woody” grainy appearance at lower magnifications. In contrast to the ductile fracture region the area of crack growth is much flatter and does not exhibit the deep holes surrounding the MnS inclusions that are present on the ductile fracture surface.

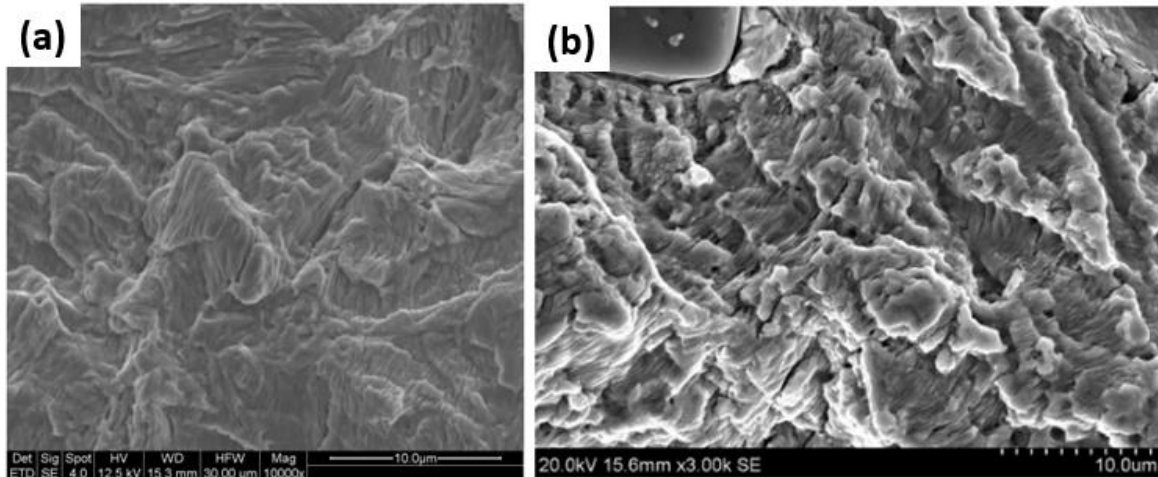


Figure 5.23. a.) Higher magnification SEM micrograph showing individual fatigue striations that are observed on the area of slow crack growth and propagation. b.) Literature SEM micrograph showing fatigue striations next to a MnS inclusion (top left).<sup>24</sup>

Figure 5.24 shows MnS inclusions on the flat crack propagation surface region. Their positions relative to each other are consistent with the inclusions that were observed on the cross sections. This makes sense considering that the steel between the inclusions is not plastically deformed, and therefore the inclusions maintain the same spacing or separation distance between them.

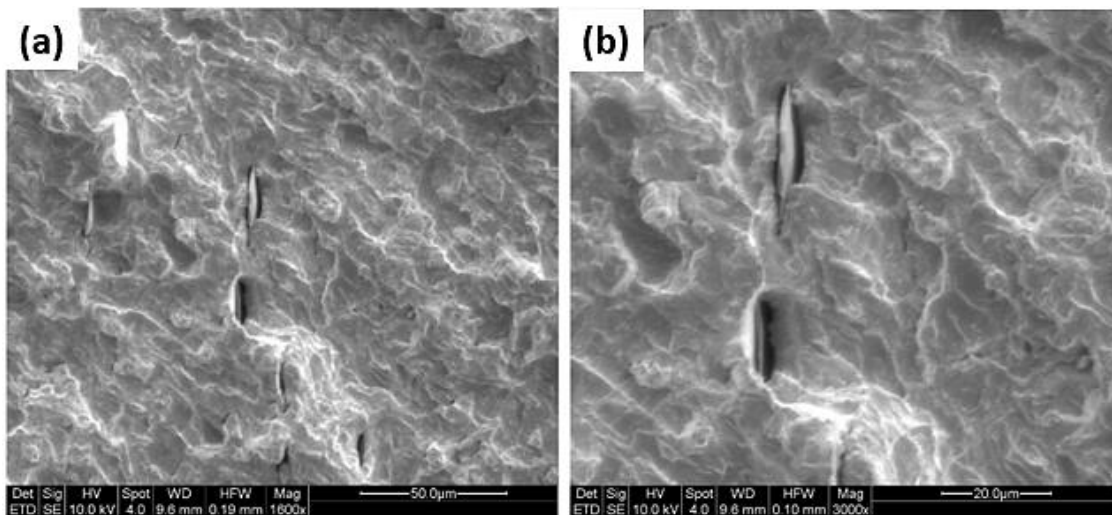
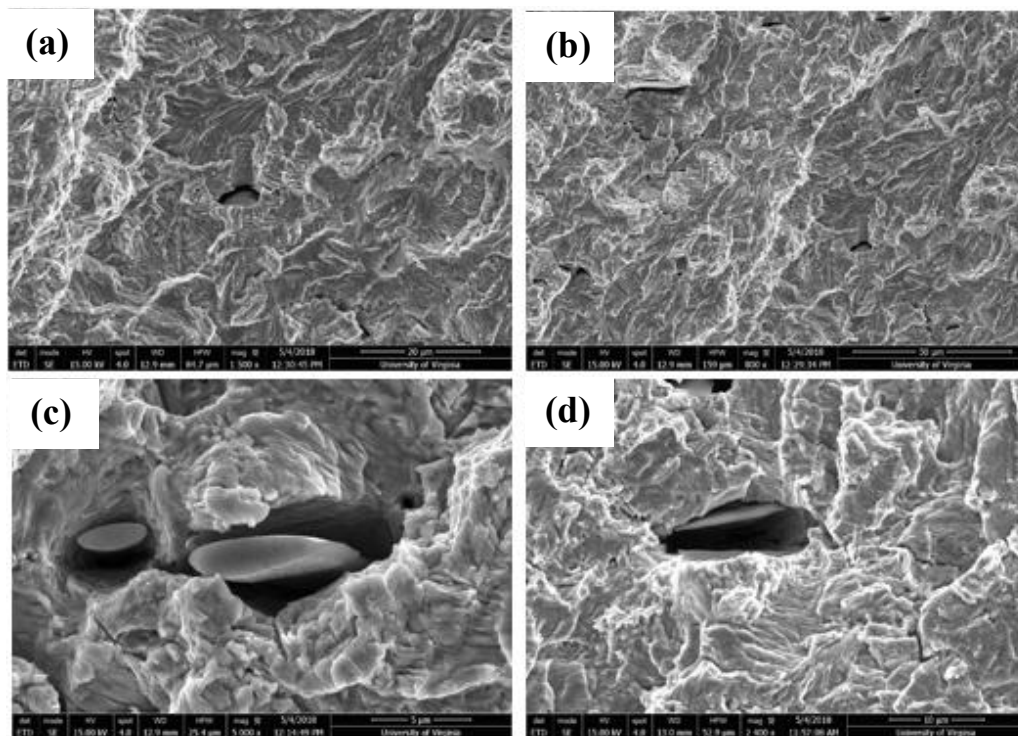


Figure 5.24. a.) SEM micrograph of the crack propagation area showing MnS inclusions. Notice that they are still located relative to each other as they were before fatigue testing, (same distance apart) determined by comparisons with cross sections. B.) higher magnification of the left image.

It is interesting to note that compared with high magnification micrographs from the literature of fatigue failed samples containing nonmetallic inclusions, on the LACR fatigue fracture surfaces the inclusions are often not flush with the fracture surface, even in flatter regions of crack propagation. (Figure 5.25). In some cases the inclusions appear to be “below” the surface, and there often seem to be a gap between the inclusion itself and the surrounding steel matrix. In some cases, the inclusion seems to have split into two separate pieces itself. (Figure 5.25 d).



*Figure 5.25. SEM micrographs showing the different state of MnS inclusions on the fatigue surface. a.),b.) Inclusions that are recessed below the surface, and not fully exposed. c.) High magnification SEM showing the size of the gap that exists between some of the inclusions and the surrounding steel matrix. d.) A MnS inclusion that appears to be split in two, presumably from the growth of a fatigue crack.*

Figure 5.26 plots the SN curve of the LACR dog bones. A line has been drawn through the data to represent the fatigue behavior, including an endurance limit of 135 MPa. When compared to literature data, the fatigue behavior of the LACR metal was similar to that of A36 steel, suggesting that the LACR process has very little if any effect on the fatigue life of the steel.

Analysis of the fatigue surface also revealed the typical appearance for that of A36 steel. Crack initiation sites were found on both the LACR surface as well as the sides of the dog bones, which were the sides exposed to the water jet cutting. This means that the LACR surface was not the only surface that caused crack site initiation, and therefore the surface topology due to LACR may not be much more detrimental than the surfaces formed by other processing methods such as water jet cutting.

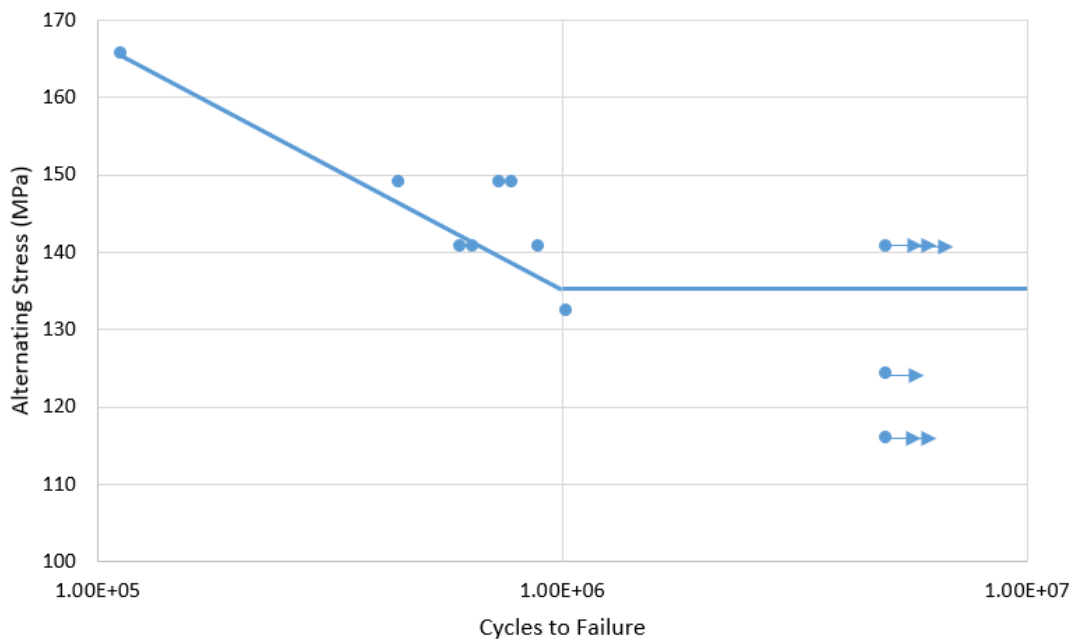


Figure 5.26. SN fatigue curve for the LACR dog one specimens. A line as a guide for the eye is included through the data as well as an endurance limit at roughly 135 MPa. Single arrow points denote run out tests, and double and triple arrow points represent two unfailed samples at the same stress value.

In order to validate the fatigue performance of laser cleaned steel, the endurance limit determined from the SN curve was plotted on a Goodman Diagram, which also includes the Soderberg Line and Berger Curve (figure 5.27). These models are used to predict the effect of varying mean stresses and stress amplitudes on the fatigue life of a component. Fatigue data points inside these boundaries are predicted to have an infinite life without failure, whereas fatigue points outside these boundaries are expected to have a finite life and break due to fatigue

at some future point in time. The Gerber curve usually matches the test data for ductile metals, however the more conservative Goodman line is often used in practice. For an even higher margin of safety the Soderberg line can be used, which is based off of the yield strength as opposed to the ultimate tensile strength which is used for the Goodman model. The mathematical relationships for the three models are expressed as [eq. 5.1]:

$$[\text{Eq. 5.1}] \quad \sigma_a = \sigma_e \left[ 1 - \left( \frac{\sigma_m}{\sigma_u} \right)^x \right]$$

Where  $x = 1$  for the Goodman line,  $x = 2$  for the Gerber curve,  $\sigma_u = \sigma_y$  for the Soderberg line, and  $\sigma_e$  is the fatigue limit for fully reversed ( $R = -1$ ) loading.<sup>74</sup>

As can be seen in figure 5.27, the stress levels corresponding to the endurance limit falls directly onto the Goodman line, marked with an X. Because this value is outside the boundary of the Goodman line this substantiates that LACR treatments do not appear to degrade the fatigue performance of the laser cleaned steel.

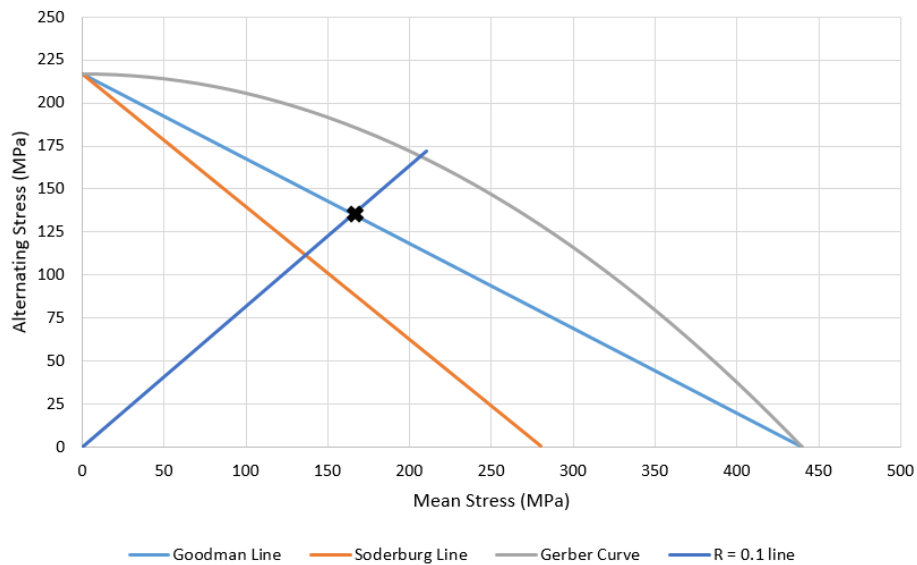


Figure 5.27. A Goodman diagram demonstrates that LACR treated samples do not appear to show any degradation in fatigue performance. An X placed along the fatigue ratio of  $R = 0.1$  line represents the endurance limit and falls nearly directly onto the Goodman line.

In the design of bridges, the material guidelines for bridge component follow design rules that are published by AASHTO. AASHTO provides fatigue specifications in the form of different categories, with specify varying degrees of fatigue failure resistance depending on what design feature geometry and the design detail type.<sup>75</sup> The AASHTO fatigue categories are presented in the form of lines on an S curve, where Category A represents the highest fatigue performance, followed by B, and eventually reaching category F, the lowest fatigue performance. The fatigue category lines were determined from experimental data that was produced during the National Cooperative Highway Research Program (NCHRP). The line for each fatigue category has a slope of -3 on a log-log plot, as shown in the below equation used to plot each fatigue category [eq. 5.2]:

$$[\text{Eq. 5.2}] \quad \Delta F = \left(\frac{A}{N}\right)^{1/3}$$

Where A is a constant that defines the fatigue category, N is the number of stress cycles, and  $\Delta F$  represents the nominal fatigue resistance, the red line drawn in figure 5.28.

After the sloped region, a flat line represents the “infinite life” fatigue region, in which the endurance limit is reached, and where infinite life is expected for the specimen if the applied stresses remain within the limits indicated in this region of the fatigue category. The stress level for the infinite region is different for each fatigue category and decreases with lower fatigue level performance categories.

The LACR samples fall within the AASHTO Category A fatigue, meaning that a value of A = 25,000,000,000 applies and a stress value for the infinite life region of 24 ksi (165 MPa) is used.<sup>76</sup> Figure 5.28 shows a plot of the LACR fatigue data along with the AASHTO category A

fatigue specification. It can be seen that all the fatigue data points fall above this line, except for the sample at the highest stress value, which failed below this category guideline.

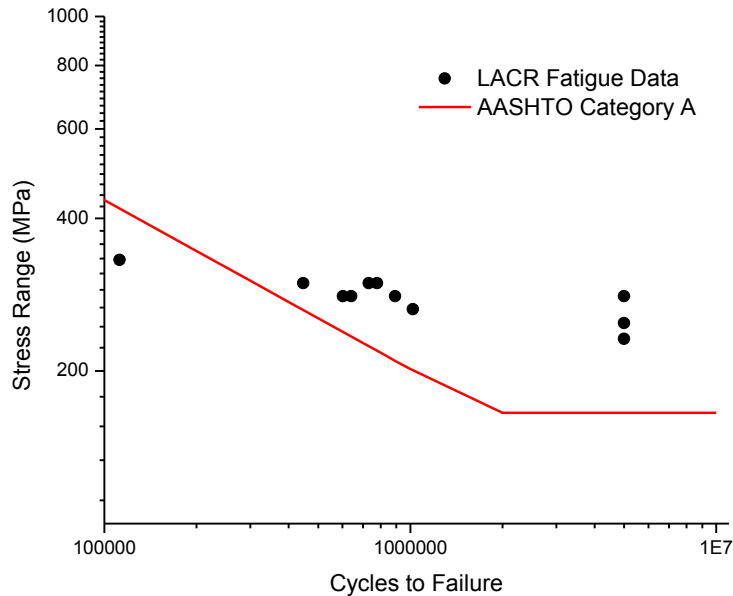


Figure 5.28. LACR fatigue data graphed with the AASHTO Category A Fatigue, demonstrating how LACR samples meet AASHTO fatigue requirements, other than for the highest stressed sample.

In summary, the fatigue surfaces of the LACR dogbones presented features typical of low carbon steel fatigue failures, with crack initiation sites present both on the LACR surface at the oxide layer, as well as on the waterjet cut side of the dogbones in some cases. In addition, the characterization of the fatigue fracture surface at all length scales, from the macroscopic appearance due to the MnS inclusions, to the effect of the inclusions on the region of slow crack growth, to the fatigue striations, shows that the fatigue behavior is no different from standard nonmetallic inclusion containing low carbon steel. In other words, the MnS inclusions seemed to play a bigger part in the fatigue behavior of the steel than any effect due to the LACR surface processing had, meaning that the LACR process does not seem to have any significant effect on the fatigue life of the steel.

## **Chapter 6 Conclusions and Future Work**

This chapter summarizes the main conclusions made from this project, as well as future directions for further research on coating removal from bridges. Overall, material characterization showed that laser cleaning had no detrimental effects on either the mechanical properties or the coating adhesion strength. In addition, industrial hygiene surveys conducted on personal samples as well as area samples showed that no heavy metals or volatile organic compounds are released during laser cleaning, and that while lead was detected, that it was well below OSHA action levels. Further industrial hygiene surveys conducted in VTRC studies further confirmed that LACR can effectively remove lead from metal substrates.

As this project progressed various areas for improvement of the coating removal process were noted, including the investigation of other commercial laser systems that would better address certain technical issues related to coating removal, as well as alternative methods of coating removal that may potentially offer advantages when used in conjunction with laser coating removal. These alternative coating removal methods are presented in the future work section.

### **6.1 Conclusions**

First, it was determined that LACR effectively removes the coatings investigated, including Pb-based paints. As was observed in previous studies and by the present, LACR can effectively remove epoxy and other polymer based coatings from steel substrates. The bridge steel examined in phase 1 of this study (A36) was never subjected to grit blasting and contained mill-scale from its manufacturing, resulting in a distinct appearance after laser removal. Although microscopic investigation reveals that small paint particles remain on the surface after cleaning, this did not affect subsequent coating adhesion. It is suspected that a greater number of laser passes would remove this remaining paint, in the case that complete removal is desired for a specific application.

Coating adhesion of LACR surfaces was determined to be satisfactory with adhesion testing revealing average pull-off pressures of 1800 psi. This observation may require revision of recoating requirements, since roughness requirements applicable to decoating by grit blasting do not appear to apply to LACR surfaces. Traditionally it has been held that high roughness values were required to provide mechanical interlocking between the coating and substrate, necessary to resist pull-off, however in this study, average roughness values of laser cleaned surfaces were lower than grit blasted surfaces roughness, at 5.26 and 5.41  $\mu\text{m}$  parallel and perpendicular to the laser scan direction, compared to 9.86  $\mu\text{m}$  for grit blasted samples.

In the scope of this study, LACR processing did not detrimentally affect the mechanical properties of the steel (ASTM structural steel A36) that was used in this study. Despite the fact that microscopic investigation reveals very local ( $\sim 1 \mu\text{m}$  thick) surface melting of the metal substrate (or oxide if present), hardness measurements revealed no degradation, averaging 139 HV across from the surface to the center of cross sections. Similarly, the tensile yield strength, ultimate strength, ductility, and fatigue strength were all on parity with expected values of A36 steel alloy. Field studies in Phase II to perform coating removal on bridge beams ends and bulk heads with the selected laser system was problematic due to tight space limitations and geometry. This is unfortunate because present productivity rates do not appear sufficient to warrant broad application of the technique, rendering such niche applications attractive. In order to address this dilemma alternative laser systems that were smaller, lighter, and more powerful were observed, although not tested in detail. A laser system with these characteristics could improve both the productivity and address the tight space limitation that was of concern for the current system used. Due to these potential improvements, further investigation of LACR and of other potential LACR systems and

coating removal methods is warranted. The manufacturers of other LACR systems can provide higher productivity rates than the system presently considered, due to higher laser power (1.6 kW vs. 1 kW), and other coating removal methods such as induction coating removal (ICR) can provide the advantages of rapid, large area, wider interaction angles, as discussed in the future works section.

The results from the Industrial Hygiene (IH) studies show that LACR poses little risk to either the laser operator or to the surrounding environment. All measurements were well below the current OSHA Permissible Exposure Limit (PEL) and OSHA Action Limit (AL) for each sample's work area. Of particular interest to this study was the detection of lead. The PEL for lead is of 0.05 mg/m<sup>3</sup>, while the AL is 0.03 mg/m<sup>3</sup>. The highest operator lead levels observed was 0.0043 mg/m<sup>3</sup>, which is below the AL and PEL for lead. The results of the IH study also show that LACR provides a potential cost-benefit, since it does not require the type of containment that traditional grit-blasting approaches require. Further, the hazardous waste generation is greatly reduced, and restricted to the LACR vacuum particle filtration system. However, it is noted that this particle filtration system must be disposed of as hazardous waste and that appropriate personal protective equipment (PPE) should be worn during the removal of the filter for disposal.

In an external phase conducted by VDOT and VTRC, LACR was employed as a lead-abatement technique in preparation for other processes, such as hot working (torch cutting) and welding which are widely used by VDOT. Industrial hygiene personal monitoring showed that the hazard levels were below laboratory detection limits for all contaminants. Dust levels on beams indicated that remaining dust levels have the potential to contribute to worker exposure and therefore appropriate protective equipment should be worn during handling of cleaned beams.

## 6.2 Future Work

One area for improvement is in the area of effective access to tight areas or spaces with odd geometries. In order to address this a search for alternative laser companies was undertaken to determine whether other laser systems were commercially produced that could fix this issue. Several other companies have been identified during the course of this research program. The products provide for a smaller and more portable laser optic head. In addition, for some products, the laser aperture is located 90 degrees from the incoming fiber optic and cooling lines, suggesting that it would allow superior access to the tighter geometries that proved difficult to reach with the system used. Further research is warranted for the coating removal for bridge applications where tight, small spaces are critical.

As a complementary process to LACR for coating removal operations, induction coating removal (ICR) should be considered. ICR is an established coating removal technology that has already been implemented for use on marine structures, as well as pipelines and other infrastructure. As implied by the name, ICR operates on the principal of electromagnetic induction, where heat is generated in the near surface of the steel substrate (~0.3 mm) which subsequently dissociates the bonds at the substrate - coating interface without disintegration of the coating system. Using a hand operated induction coil, a high frequency alternating current is placed close to the coating and substrate, in turn creating electron eddy currents within the steel substrate which causes the metal to rapidly heat up. While the fundamental operating principal behind ICR is different from LACR, the ICR process has additional benefits beyond the LACR process, including the minimal production of volatile organic compounds (VOCs), minimal waste production and consumables, high removal rate, and small scale equipment with nominal power requirements. However, there is a variation between LACR and ICR regarding the final substrate appearance. LACR processing

results in a substrate with a clean visual appearance; removing coatings, rust, and other contaminants that are present on the substrate surface. In comparison, ICR removes the bulk coating layer, leaving behind levels of residual rust, primer layers, or adhesives. A proposed two step method of ICR to first remove the coating system in rapid fashion followed by processing with LACR should be explored.

## Appendix A

### A: Results

#### A1: MnS Inclusions

Microstructural analysis of the A36 low carbon steel presented showed the presence of many MnS steel stringers, a common impurity found in steel making. Manganese is added to steels to prevent the formation of iron sulfide, which is a brittle compound that can have even more detrimental effects on the steel than manganese sulfide, MnS. Iron sulfide is also a low melting point phase that results in hot forming difficulties and ruptures, and by adding sufficient manganese the sulfur preferentially converts to the higher melting point manganese sulfide which are elongated during hot working because of their high plasticity at these temperatures.<sup>68,</sup>

<sup>71</sup> Usually small amounts of manganese are added to the melt in order to capture remaining sulfur, however some types of steel are resulfurized, meaning that sulfur and manganese are intentionally added in correct stoichiometric proportions to increase the concentration of MnS inclusions, which has been shown to significantly increase machinability. However, this practice must be done in balance because MnS inclusions have also been known to have detrimental effects on fatigue, welding, and corrosion properties of steels. Due to the large number of ways MnS inclusions can impact steel properties, MnS inclusions have been studied in detail.<sup>72-78</sup>

According to the original classification of MnS inclusions proposed by Simms and Dahle, MnS inclusions are roughly categorized into three types for cast steel, depending on their morphology; type I, type II, and type III. Type I consists of randomly dispersed globular MnS inclusions, type II fine rod-like inclusions, and type III angular sulfides. Type I inclusions are often found in silicon-killed steels where oxygen content is high, and are spread throughout the matrix of the steel. Type II inclusions tend to have dendritic structures in cast steel, are located at grain boundaries, and are present in de-oxidized steel. Type III inclusions are also usually found in

close proximity to each other unlike types I and II, and are sometime referred to as “colony” inclusions. Type III are more isolated than type II, but are also found on grain boundaries. The types of MnS inclusions in wrought steels depends on the type of sulfide inclusions formed in the original cast steel, as well as any processing such as rolling or extruding that can cause a change in the morphology of the inclusions compared to the unprocessed cast morphology.

Although the details of the processing and manufacturing history of the I-beams that were tested in this study are not known, studying the microstructure of the steel and compositional data from EDS analysis have helped to identify the type of inclusions present in the I-beams, and therefore their impact on the mechanical behavior of the steel.

From comparison of the MnS inclusions observed in the microstructure of the I-beam steel, it was determined that they are likely type II MnS inclusions. This conclusion was mainly based off of the fact that the inclusions are located between grains, in other words at grain boundaries, and also that these inclusions are often found in close proximity to each other, indicative of the colony characteristic seen in type II MnS inclusions. Figure A1 shows unetched micrographs of some of the inclusions found in the cross sections of the I-beam steel. When compared to type II inclusions from the literature, it is resemblance between these morphologies is clear.

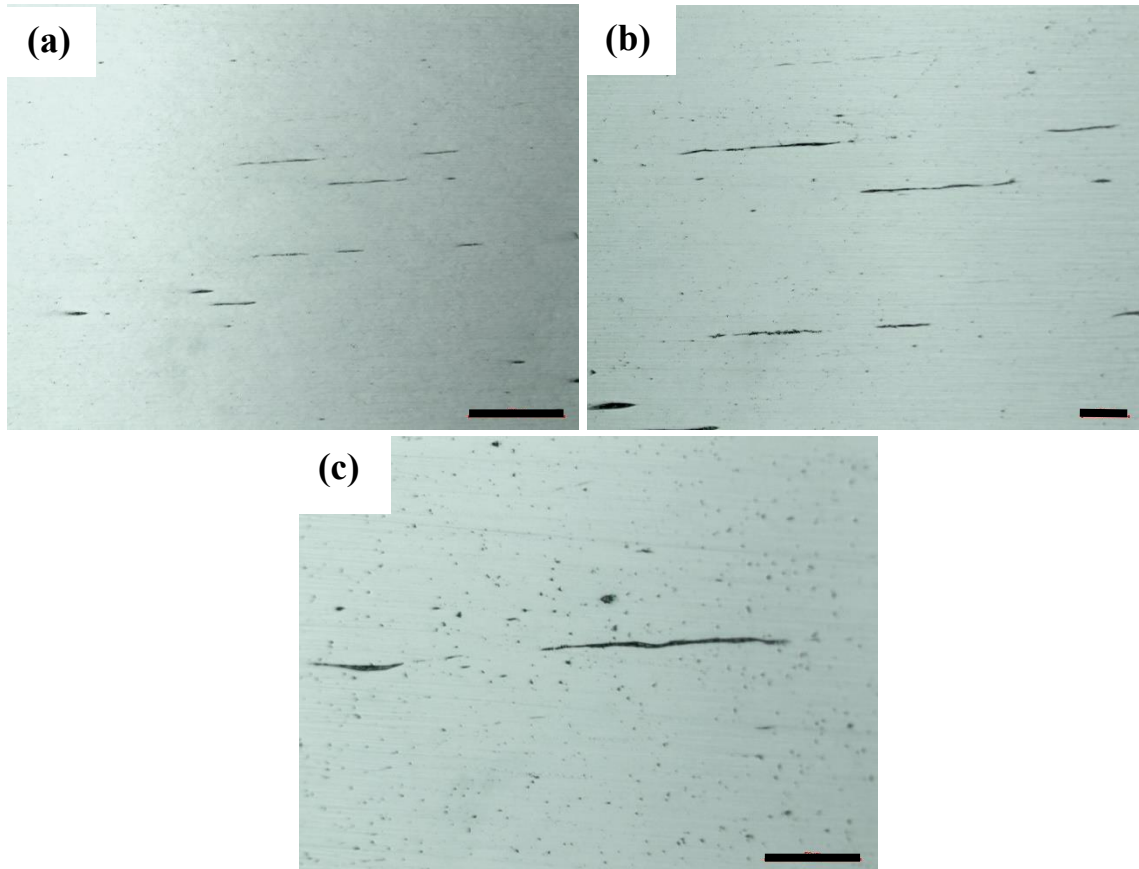


*Figure A1. Unetched micrographs of I-beam cross sections showing the morphologies of the MnS inclusions in the steel at different magnifications. The groupings of inclusions and the flat drawn out shape due to rolling are indicative of type II MnS inclusions. a.) scale bar = 200  $\mu\text{m}$ , b.) scale bar = 100  $\mu\text{m}$ , c.) scale bar = 50  $\mu\text{m}$ .*

Figure A2<sup>78</sup> shows classified MnS type II inclusions from literature in a low carbon steel with a sulfur content of 0.013%, whereas in ASTM A36 steel the sulfur content is kept below 0.05% sulfur as a maximum concentration.

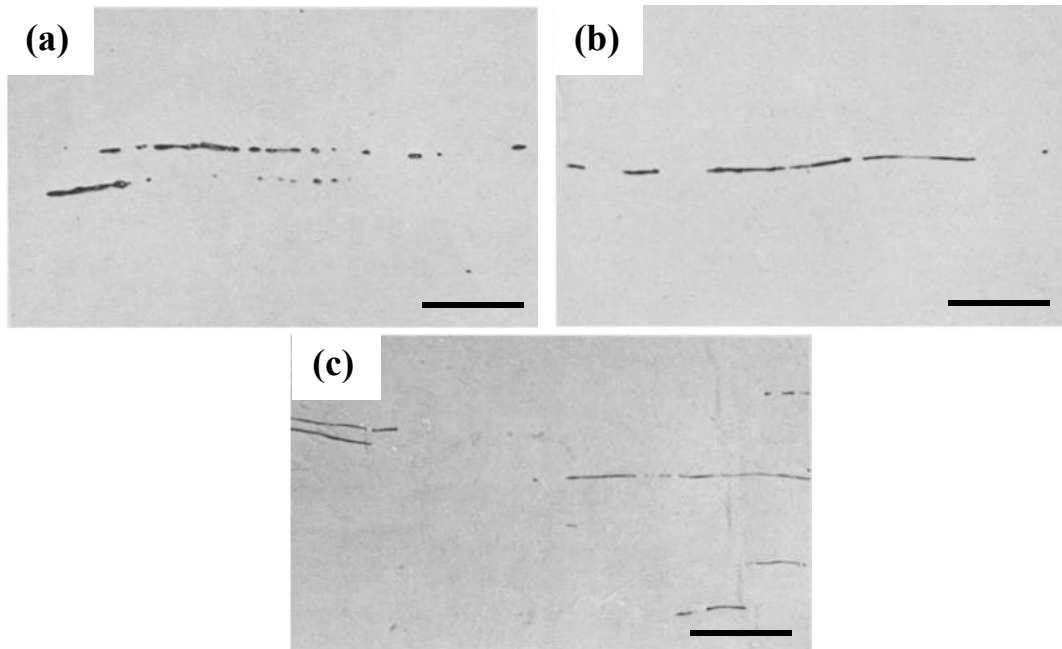
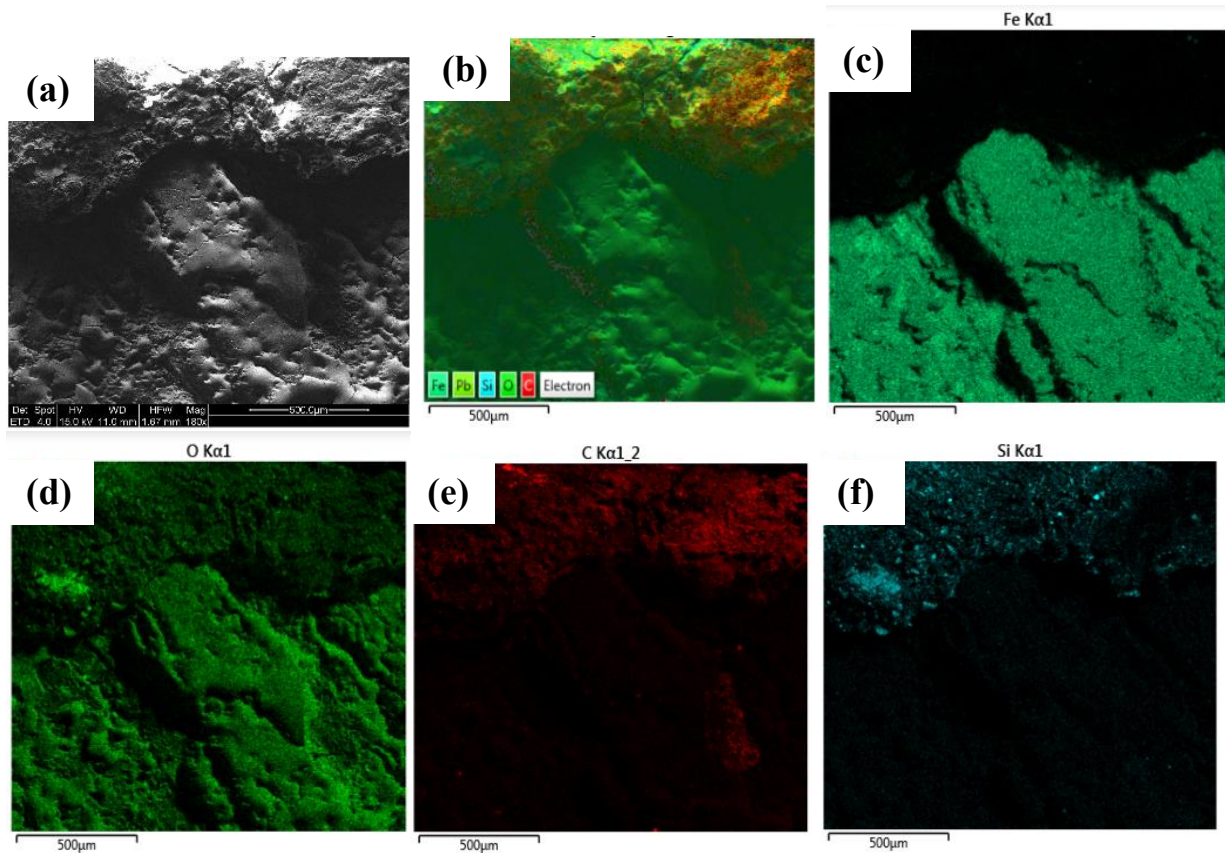


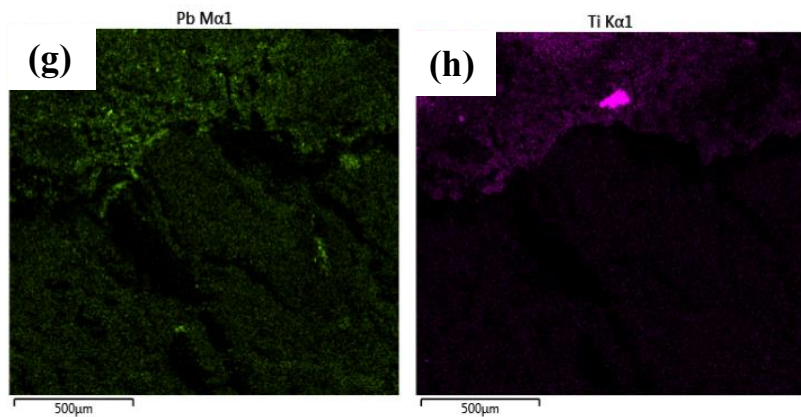
*Figure A2. Literature micrographs of MnS type II inclusions in unetched steel with a sulfur content of 0.013%, with heat treatments at 925°C. a.) No heat treatment, b.) 5 hr heat treatment, and c.) 10 hr heat treatment. (All scale bars at 20  $\mu\text{m}$ .)<sup>78</sup>*

This means that both steels have roughly the same sulfur composition for type II MnS inclusions. In addition, EDS analysis shows no measurable amount of oxygen left in the steel matrix, which rules out the possibility of type I MnS inclusions which are usually found in oxygen containing steels. In addition, the thin elongated plate like morphologies can be seen in both the literature and I-beam MnS inclusions, which is indicative of hot rolling, where the originally spherical like inclusions become elongated along with the steel grain as they are deformed from the hot rolling process.

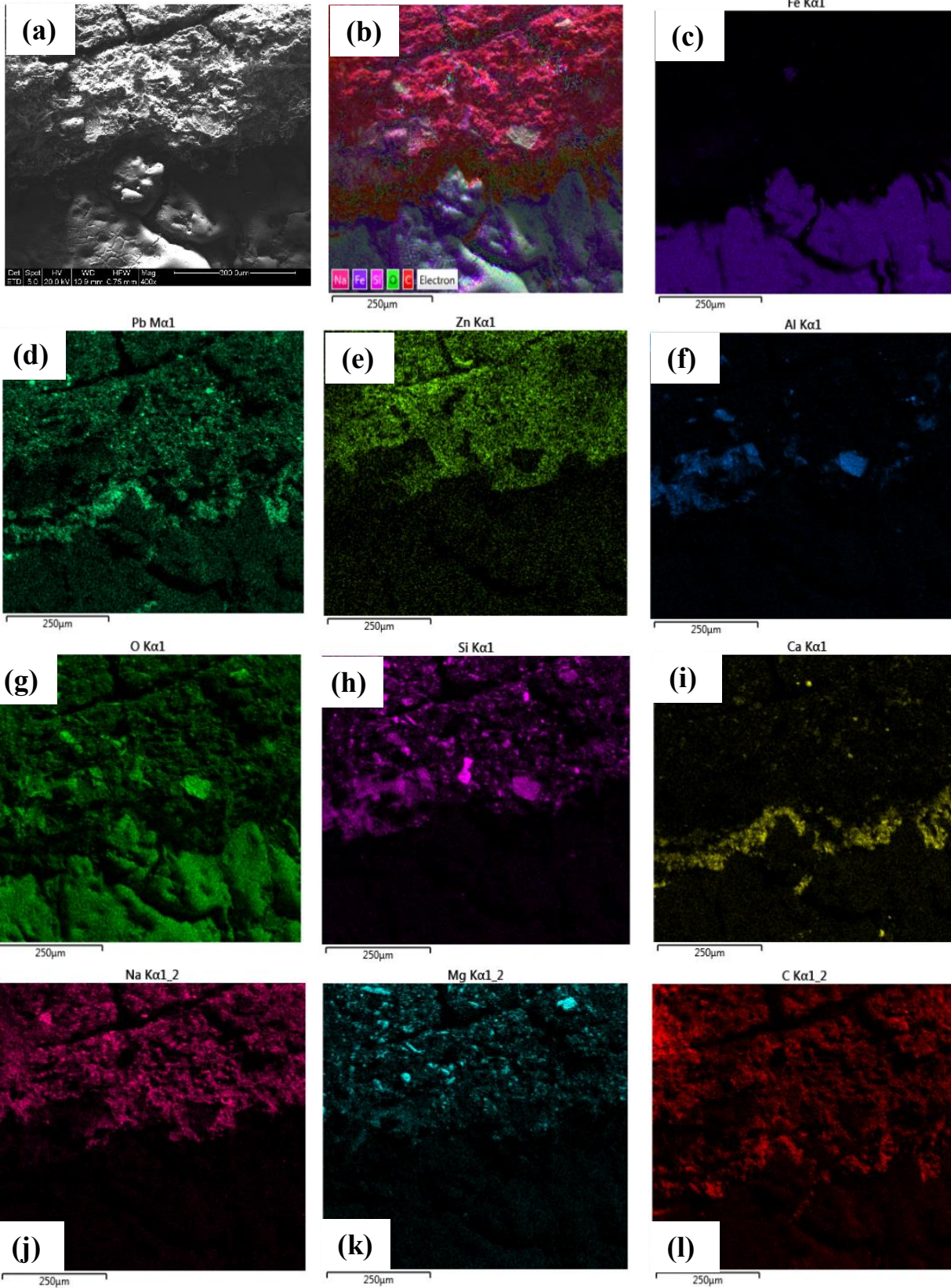
A2: Paint Interface EDS Maps: Location 2:



(a), SEM micrograph of the paint oxide interface. Again, (c) shows a clear distinction between the paint and the cleaned iron oxide surface. (d) oxygen is present throughout the paint as well as iron oxide. (e) Carbon is mostly contained within the paint, and not on the cleaned surface. (f), shows sporadic locations of silicon within the paint, but not on the cleaned surface. (g) shows that lead is still present on the cleaned oxide, however in smaller amounts compared to the painted regions. (h) Titanium is clearly present within the paint only, but is not detected on the cleaned iron oxide surface.



Location 3:



*Location 3: (a), SEM micrograph of the paint oxide interface region to be analyzed with EDS. (b) composite map showing all elements measured. (c) Clear boundary between the iron oxide and paint is delineated by the iron EDS signal. (d) shows that lead is present mostly within the paint, however also on the cleaned surface, albeit to a lesser extent. (e) and (f), Zinc and aluminum are representative of specific paint layers. (g), oxygen map showing the high oxygen content of the iron oxide, (h), silicon map showing that it is associated with the paint. (i), calcium is present within the paint however it is concentrated along the paint to oxide interface. (j), sodium is also only present within the paint. (k) magnesium is similar to silicon in that it is only appears in sporadic locations within the paint. (l), carbon is mostly due to the organic materials used in the paints, although it is also found on the cleaned surface in smaller quantities.*

A3: Paint EDS Maps paired with Optical Microscopy

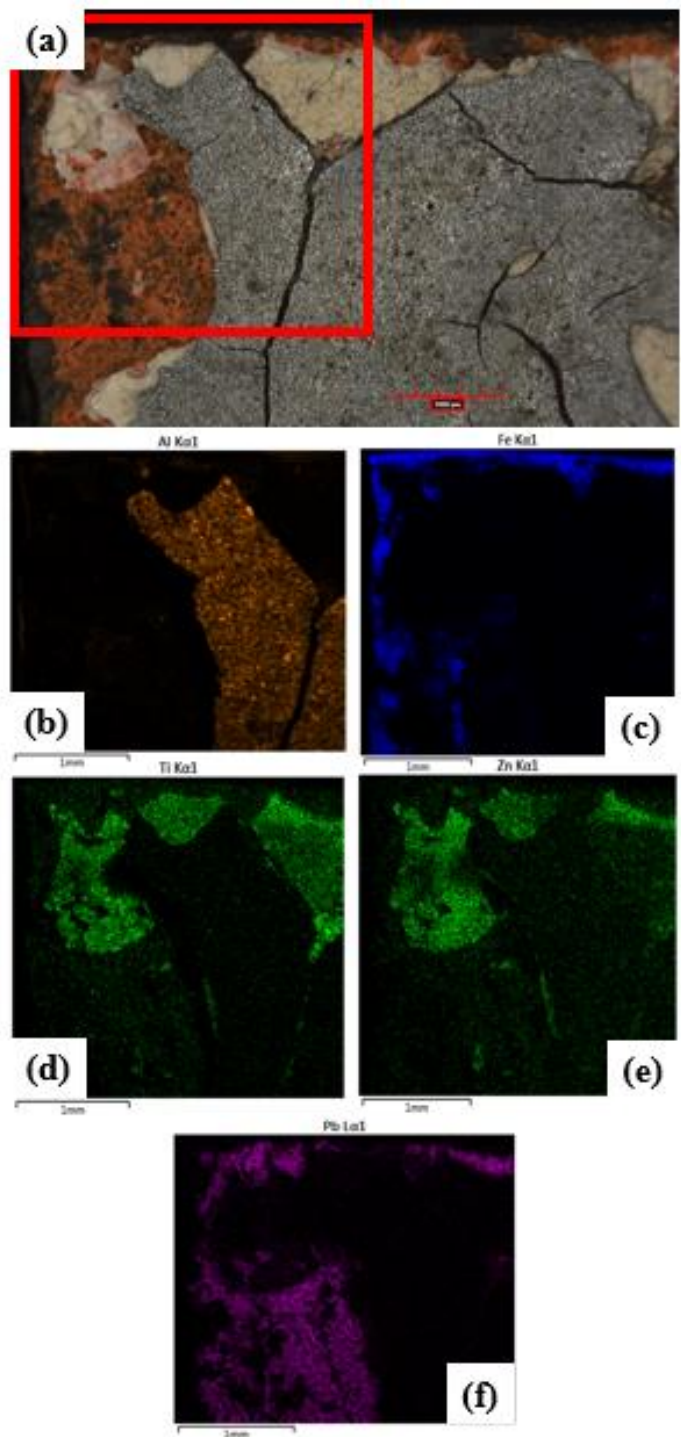


Figure A3 (ii). A red box over the optical micrograph (a), shows the region mapped in EDS. The elements in each map are as follows: (b): Al (c): Fe (d): Ti (e): Zn (f): Pb. All scale bars = 1 mm.

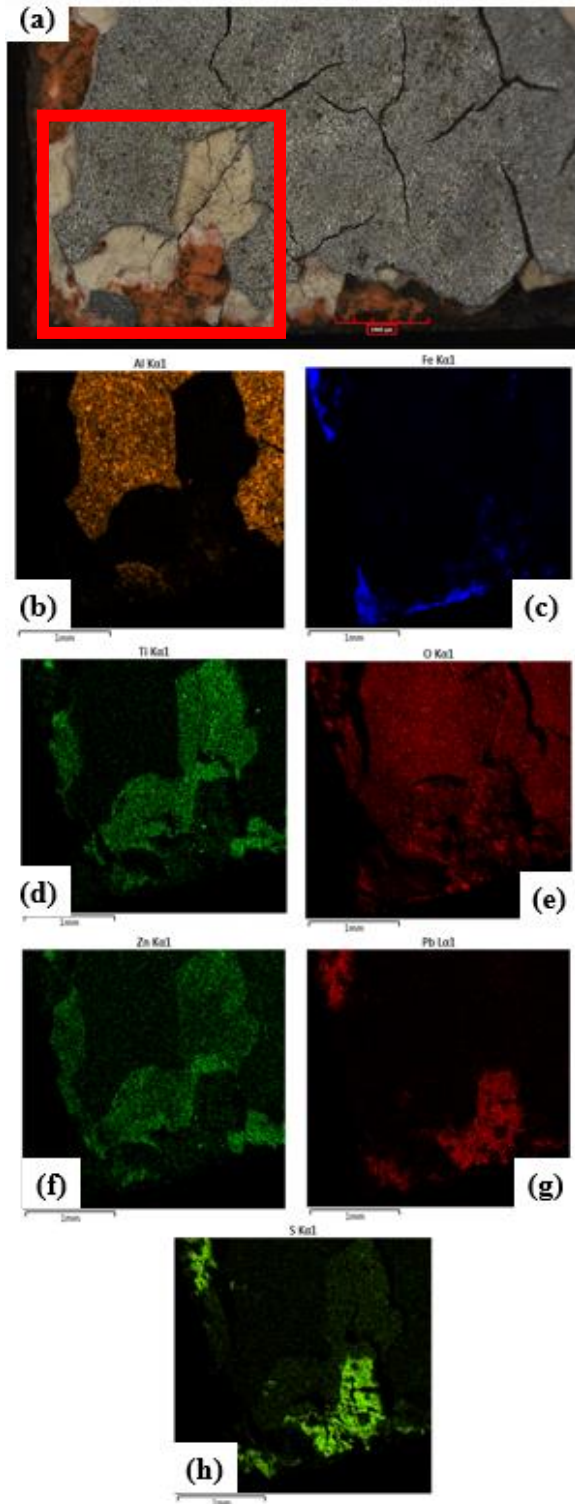


Figure A4 (iii). A red box over the optical micrograph (a), shows the region mapped in EDS. The elements in each map are as follows: (b): Al (c): Fe (d): Ti (e): O (f): Zn (g): Pb (h): S. All scale bars = 1 mm.

## Appendix B

### B: Discussion: Lead Paint Reflectance

Due to the presence of lead paint in some areas even after laser cleaning the I-beam surfaces, it was theorized that the  $\text{Pb}_3\text{O}_4$  (II, IV) oxide crystals that constitute the paint may have optical properties that diminish the effect of the laser light on ablating the paint from the surface. In order to investigate whether this was the case the optical reflectance of this pigment at the wavelength used by the CL1000 laser (1064 nm) was determined from literature. Upon investigating the literature it was clear that  $\text{Pb}_3\text{O}_4$  (II, IV) oxide is in fact highly reflective in this region (absolute reflectance of roughly 80%), which would substantiate the fact that the lead paint appeared to be more difficult to remove. However, after comparing to the light reflectance of the zinc and titanium oxide white paints, these pigments also have about the same reflectance spectrum over the same range of wavelengths, and therefore it was determined that the optical reflectance alone could not account for the remaining spots of lead paint left on the surface.

Literature shows that  $\text{Pb}_3\text{O}_4$  (II, IV) oxide pigment is very reflective in the region of infrared light that the laser operates in. The Nd:YAG laser used for LACR produces light at 1064 nm, and at this wavelength the reflectance of lead oxide is roughly 0.80 absolute reflectance as measured by near-infrared spectroscopy. Figure B1<sup>79</sup> shows a near infra-red reflectance spectra of various lead oxides, and the most notable feature is a large absorption edge at about 550 nm, where the reflectance quickly rises from around 0.05 to 0.80 absolute reflectance. This explains the color of the pigment as observed in the visible light spectrum range. As described in Chapter 4, pigments alter the appearance of a coating by the selective absorption or scattering of light, in addition to possible transmittance. Electromagnetic radiation encountering an object meets one of these three fates, and any or all three can occur completely or partially on any part of the

electromagnetic spectrum. This means that the reflectivity and absorptivity of pigments are independent of each other, and the visible light coloration bears no saying on the optical behavior of the pigment in ranges outside the visible range of the spectrum. In this case, the  $\text{Pb}_3\text{O}_4$  (II, IV) oxide is highly reflective at visible wavelengths of 550 nm to 750 nm, corresponding to yellow, orange, and red light, thus giving the pigment is bright orangey-red color. This high reflectivity continues into the near infrared spectrum, (750 to 1,400 nm).

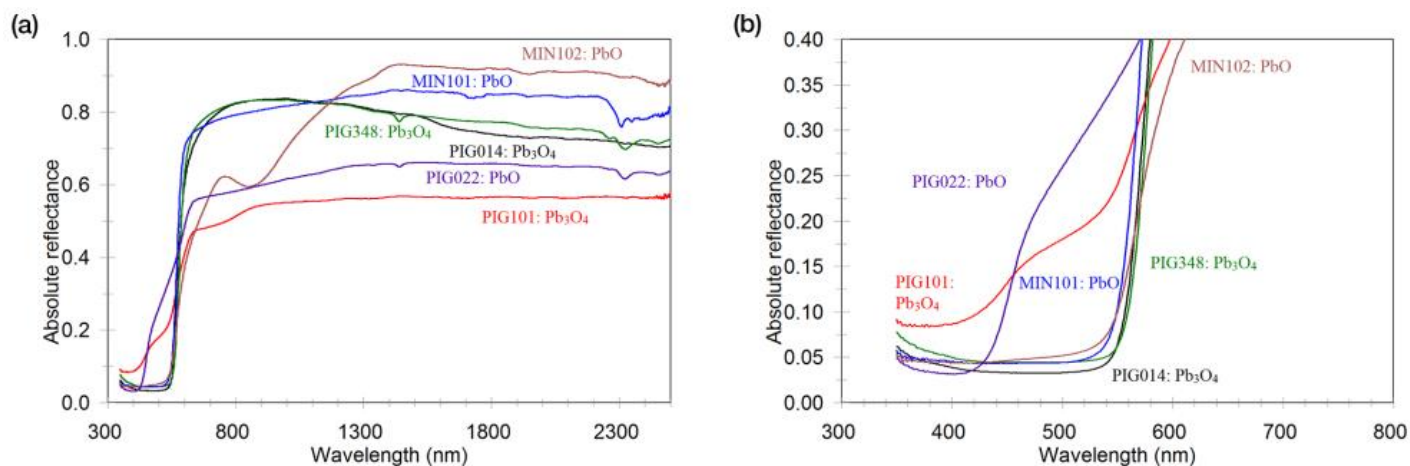


Figure B1. a.) 350-2500 nm reflectance spectra of powdered lead oxide pigments. b.) Same as (a), showing the details in the low wavelength-low reflectance region. The Nd:YAG laser used for LACR produces infrared light at 1064 nm, as marked in (a).<sup>79</sup>

The very low reflectance (0.05 absolute reflectance) between wavelengths of 380 nm to 550 nm correspond to the violet, blue, and green colored parts of the visible spectrum, and the low reflectance is likely balanced by high absorption. This means that in the visible part of the spectrum the longer orange and red wavelengths are reflected from lead oxide, whereas the shorter blue green wavelengths are absorbed.

Figure B2<sup>79</sup> shows another near infrared spectra of lead oxides, similar to figure B1a, however this time the lead oxides were mixed with boiled linseed oil, giving an even better indication of the optical properties of the red lead paint which uses linseed oil as the binder medium for the pigment.

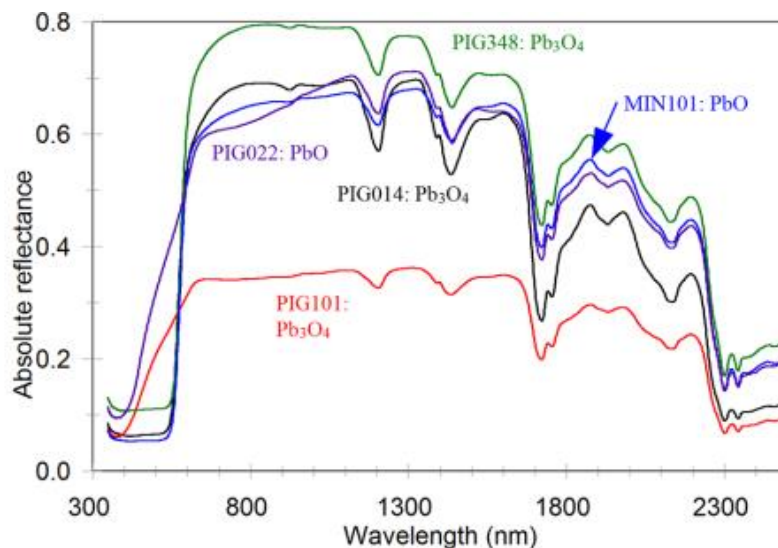


Figure B2. Same reflectance spectra as shown in figure 1, however for lead oxide pigments boiled in linseed oil, the common binder used in red lead paste. Above roughly 1100 nm the spectra are dominated by the linseed oil spectral features, however the organic binder does not affect the spectral properties of the lead oxides, as the position of the absorption edge and the spectral slope are generally unaltered.<sup>79</sup>

At first glance the impact on the spectra due to the linseed oil is readily seen. At wavelengths above about 1100 nm sharp dips are attributed to the organic linseed oil molecules, however the sharp absorption peak position and slope does not seem to be affected by the presence of the oil. This is important because this means that neither the visible appearance of the pigment nor the laser reflective behavior is altered by mixing with linseed oil, both of which match observation. When compared to the reflectance values of  $Pb_3O_4$  (II, IV), both titanium dioxide and zinc oxide have almost identical reflectance behaviors. Figure B3<sup>80,81</sup> shows reflectance values for both titanium dioxide and zinc oxide as a function of wavelength. Each of these pigments has a sharp absorption edge within the visible light spectrum (roughly 450 nm for  $Pb_3O_4$  (II, IV), 400 nm for  $TiO_2$ , and 380 nm for  $ZnO$ ), which imparts the given color to each of these pigments. More importantly, each of these pigments is also highly reflective at a wavelength of 1064 nm (0.80 absolute reflectance for  $Pb_3O_4$  (II, IV), 0.95 absolute reflectance for  $TiO_2$ , and roughly 0.80

absolute reflectance for ZnO), which corresponds to the wavelength of the CL1000 laser used for LACR in this project. Because each of these pigments has about the same reflectance values at the laser wavelength used, this means that optical reflectivity cannot account for any difference in the ease of coating removal for each paint layer.

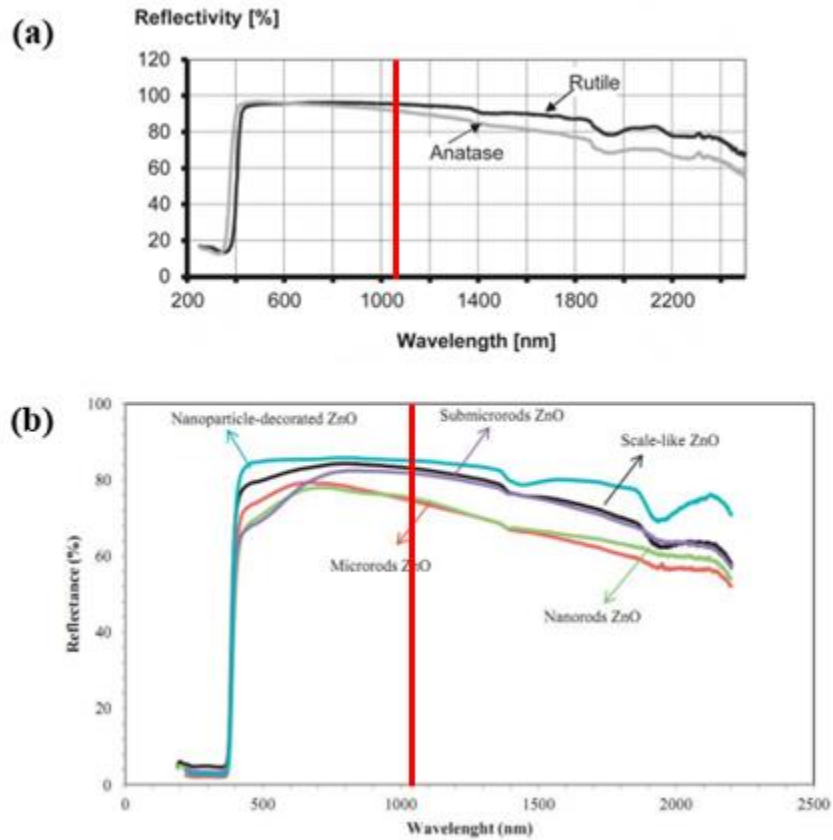


Figure B3. Near UV/VIS and NIR reflectance values for (a) TiO<sub>2</sub> and (b) ZnO pigments. Red vertical lines mark 1064 nm, the wavelength used by the CL1000 laser used for LACR<sup>80,81</sup>

## References

---

- 1.) LACR Research Proposal Fitz-Gerald, James M., et al. "Implementation Of Coating Removal Technique For Steel Components On VDOT Bridges." Charlottesville, VA. (2016).
- 2.) Sharp, Stephen R, et al. "Preliminary Assessment of Procedures for Coating Steel Components on Virginia Bridges", Report 14-R1, pg. 3, Virginia Center for Transportation Innovation and Research, October 2013, Available from NTIS.
- 3.) Castillejo, Marta, "Analytical study of the chemical and physical changes induced by KrF laser cleaning of tempera paints." *Analytical chemistry* Vol. 74, Issue 18 (2002): 4662-4671.
- 4.) de Cruz, Adele, Myron L. Wolbarsht, and Susanne A. Hauger. "Laser removal of contaminants from painted surfaces." *Journal of Cultural Heritage* Vol. 1 (2000): S173-S180.
- 5.) Maravelaki-Kalaitzaki, P., V. Zafiropulos, and C. Fotakis. "Excimer Laser Cleaning of Encrustation on Pentelic Marble: Procedure and Evaluation of the Effects." *Surface Science* 148.1-2 (1999): 92-104.
- 6.) Oujja, Mohamed, et al. "Laser cleaning of terracotta decorations of the portal of Palos of the Cathedral of Seville." *Journal of cultural heritage* Vol. 6 Issue 4 (2005): 321-327.
- 7.) Cooper, M. I., D. C. Emmony, and J. Larson. "Characterization of laser cleaning of limestone." *Optics & Laser Technology* Vol. 27 Issue 1 (1995): 69-73.
- 8.) Siano, S., "Laser cleaning in conservation of stone, metal, and painted artifacts: state of the art and new insights on the use of the Nd: YAG lasers." *Applied Physics A* Vol. 106 Issue 2 (2012): 419-446.
- 9.) Salimbeni, Renzo, "Assessment of the state of conservation of stone artworks after laser cleaning: comparison with conventional cleaning results on a two-decade follow up." *Journal of cultural heritage* Vol. 1 Issue 4 (2000): 385-391.
- 10.) Liu, Katherine, and Elsa Garmire. "Paint removal using lasers." *Applied optics* Vol. 34 Issue 21 (1995): 4409-4415.
- 11.) Delaporte, Ph, et al. "Dry excimer laser cleaning applied to nuclear decontamination." *Applied Surface Science* Vol. 208-209 (2003): 298-305.
- 12.) Mateo, M. P., T. Ctvrtnickova, E. Fernandez, J. A. Ramos, A. Yanez, and G. Nicolas. *Laser Cleaning of Varnishes and Contaminants on Brass*. *Applied Surface Science* Vol. 255 Issue 10 (2009): 5579-583.
- 13.) Daurelio, G., G. Chita, and M. Cinquepalmi. "Laser surface cleaning, de-rusting, de-painting and de-oxidizing." *Applied Physics A* Vol. 69 Issue 1 (1999): S543-S546.
- 14.) Guan, Y. C., "Laser surface cleaning of carbonaceous deposits on diesel engine piston." *Applied Surface Science* Vol. 270 (2013): 526-530.
- 15.) USAF's Travis AFB Tests Laser Technique to Remove Corrosion. *Airforce Technology*, 15 Mar. 2018, [www.airforce-technology.com/news/usafs-travis-afb-tests-laser-technique-remove-corrosion/](http://www.airforce-technology.com/news/usafs-travis-afb-tests-laser-technique-remove-corrosion/)
- 16.) Naguy, Tom, and Randy Straw. "Technical AFRL Laser Technology for Aerospace Maintenance and Sustainment Applications." AFRL. (2009).

- 
- 17.) Chen, G. X., "High-power fibre laser cleaning for green shipbuilding." *Journal of Laser Micro/Nanoengineering* Vol. 7 No. 3 (2012).
  - 18.) Head, J. D., and J. Peter Niedzielski. *Laser paint stripping*. Final Report, Laser Technologies Inc. South Lyon, MI, Wright Laboratories, Wright-Patterson Air Force Base, 1991.
  - 19.) D'Addona, D. M., "Laser ablation of primer during the welding process of iron plate for shipbuilding industry." *Procedia Cirp* Vol. 33 (2015): 464-469.
  - 20.) "Laser Paint Stripping, Laser Cleaning and Coating Removal Solutions." Lasertronics.com, General Lasertronics Corporation, [www.lasertronics.com/wp/applications/ship-maintenance/](http://www.lasertronics.com/wp/applications/ship-maintenance/).
  - 21.) Cargill, Robert R. "Closed-Loop Laser Ablation for Navy Maintenance Applications." ASNE 2011 Symposium Paper, General Lasertronics Corporation, [www.lasertronics.com/wp/wp-content/uploads/2011/10/ASNE-2011-Symposium-Paper.pdf](http://www.lasertronics.com/wp/wp-content/uploads/2011/10/ASNE-2011-Symposium-Paper.pdf).
  - 22.) Cleaning US Capitol Building, "Project Overview." [Conservationsolutionsinc.com](http://conservationsolutionsinc.com/projects/view/518/laser-cleaning-of-marble-at-the-us-capitol-north-wing/), Conservation Solutions Inc., [conservationsolutionsinc.com/projects/view/518/laser-cleaning-of-marble-at-the-us-capitol-north-wing/](http://conservationsolutionsinc.com/projects/view/518/laser-cleaning-of-marble-at-the-us-capitol-north-wing/).
  - 23.) Public Works and Government Services Canada. *How Parliamentary Buildings Are Rehabilitated*. PSPC, Government of Canada, Public Services and Procurement Canada, 15, Nov. 2017, [www.tpsgc-pwgsc.gc.ca/citeparlementaire-parliamentaryprecinct/rehabilitation/parlement-parliamentary-eng.html](http://www.tpsgc-pwgsc.gc.ca/citeparlementaire-parliamentaryprecinct/rehabilitation/parlement-parliamentary-eng.html).
  - 24.) D. Baüerle, *Laser Processing and Chemistry*, 4th ed., Springer, 2011.
  - 25.) Razab, Mohammad Khairul Azhar Abdul, et al. "A review of incorporating Nd: YAG laser cleaning principal in automotive industry." *Journal of Radiation Research and Applied Sciences*, Vol. 11, Issue 4, (2018).
  - 26.) Matthew S., Brown Craig B., Arnold, *Fundamentals of Laser-Material Interaction and Application to Multiscale Surface Modification*, Chapter 4
  - 27.) Bergström, David, John Powell, and A. F. H. Kaplan. "The absorptance of steels to Nd: YLF and Nd: YAG laser light at room temperature." *Applied Surface Science* Vol. 253 Issue 11 (2007): 5017-5028.
  - 28.) Toftmann, B., et al. "UV and RIR matrix assisted pulsed laser deposition of organic MEH-PPV films." *Thin Solid Films* Vol. 453 (2004): 177-181
  - 29.) Mercado, A. L., et al. "Pulsed laser deposition vs. matrix assisted pulsed laser evaporation for growth of biodegradable polymer thin films." *Applied Physics A* Vol. 81 Issue 3 (2005): 591-599.
  - 30.) Forrest, Stephen R. "The path to ubiquitous and low-cost organic electronic appliances on plastic." *Nature* Vol. 428.6986 (2004): 911.
  - 31.) Hohnholz, Dirk, Hidenori Okuzaki, and Alan G. MacDiarmid. "Plastic electronic devices through line patterning of conducting polymers." *Advanced Functional Materials* Vol. 15 Issue 1 (2005): 51-56.
  - 32.) Romoli, Luca, G. Tantussi, and Gino Dini. "Experimental approach to the laser machining of PMMA substrates for the fabrication of microfluidic devices." *Optics and Lasers in Engineering* Vol. 49 Issue 3 (2011): 419-427.
  - 33.) Liu, Hao-Bing, and Hai-Qing Gong. "Templateless prototyping of polydimethylsiloxane microfluidic structures using a pulsed CO2 laser." *Journal of Micromechanics and Microengineering* Vol. 19 Issue 3 (2009): 037002.

- 
- 34.) Gabriel, Ellen Flávia Moreira, Wendell Karlos Tomazelli Coltro, and Carlos D. Garcia. "Fast and versatile fabrication of PMMA microchip electrophoretic devices by laser engraving." *Electrophoresis* Vol. 35 Issue 16 (2014): 2325-2332.
  - 35.) Trokel, Stephen L., R. Srinivasan, and Bodil Braren. "Excimer laser surgery of the cornea." *American journal of ophthalmology* Vol. 96 Issue 6 (1983): 710-715.
  - 36.) Jako, Geza J. "Laser surgery of the vocal cords An experimental study with carbon dioxide lasers on dogs." *The Laryngoscope* Vol. 82 Issue12 (1972): 2204-2216.
  - 37.) Srinivasan, R., and Bodil Braren. *Ultraviolet laser ablation of organic polymers*. Chemical Reviews Vol. 89 Issue 6 (1989): 1303-1316.
  - 38.) Bityurin, N., et al. *Models for laser ablation of polymers*. Chemical reviews Vol. 103 Issue 2 (2003): 519-552.
  - 39.) Lippert, T., UV Laser Ablation of Polymers: From Structuring to Thin Film Deposition, *Laser-Surface Interact. New Mater. Prod.*, ed. A. Miotello and P.M. Ossi, Springer, Berlin (2009), Chapter 7, pp. 141-175
  - 40.) François Brygo, A., Semerok R., Oltra J.M., Weulersse S., Fomichev "Laser heating and ablation at high repetition rate in thermal confinement regime" *Applied Surface Science*, Volume 252, Issue 23, (2006), p. 8314-8318
  - 41.) Madhukar, Yuvraj K., et al. *Effect of laser operating mode in paint removal with a fiber laser*. *Applied surface science* Vol. 264 (2013): 892-901.
  - 42.) Young, Hugh D., *University Physics*, 7<sup>th</sup> Ed. Addison Wesley, 1992
  - 43.) Shamsujjoha, Md., et al. "Effects of Laser Ablation Coating Removal (LACR) on a Steel Substrate: Part 1: Surface Profile, Microstructure, Hardness, and Adhesion." *Surface and Coatings Technology*, vol. 281, 2015, pp. 193–205
  - 44.) "VDOT Industrial Hygiene Survey Report: Norton Sandblasting Laser Ablation" August 2018.
  - 45.) PATTI Digital Model Operator's Manuel
  - 46.) A36/A36M-14: Standard Specification for Carbon Structural Steel. (*ASTM International*, West Conshohocken, PA, 2014
  - 47.) Kline, Eric. "Durable Bridge Coatings." *Modern Steel Construction*, Nov. 2009.
  - 48.) Lindqvist, St.-Å., and N.-G. Vannerberg. "Corrosion-Inhibiting Properties of Red Lead—I. Pigment Suspensions in Aqueous Solutions." *Materials and Corrosion/Werkstoffe Und Korrosion*, vol. 25, no. 10, 1974, pp. 740–748.,
  - 49.) Sabin, Alvah Horton. *Red Lead and How to Use It in Paint*. Nabu Press, 2010.
  - 50.) Boughton, E.w. "Effect of Certain Pigments on Linseed Oil." *Technologic Papers of the Bureau of Standards*, 1916
  - 51.) Tumosa, Charles S., and Marion F. Mecklenburg. "The Influence of Lead Ions on the Drying of Oils." *Studies in Conservation*, vol. 50, no. sup1, 2005, pp. 39–47.,
  - 52.) Kanmaz, Evrim Özkaynak, and Gül den Ova. "Genotypic Variation on Oil Content, Fatty Acid Composition and Phenolic Compounds in Linseed (*Linum Usitatissimum* L.)." *Ege Üniversitesi Ziraat Fakültesi Dergisi*, vol. 52, no. 3, 2015, p. 249.,
  - 53.) Plater, M.john, et al. "The Characterisation of Lead Fatty Acid Soaps in 'Protrusions' in Aged Traditional Oil Paint." *Polyhedron*, vol. 22, no. 24, 2003, pp. 3171–3179.,
  - 54.) Higgitt, Catherine & Spring, Marika & Saunders, David. (2003). Pigment-medium Interactions in Oil Paint Films containing Red Lead or Lead-tin Yellow. *The National Gallery Technical Bulletin*. Vol. 24. 75-95.

- 
- 55.) Malshe, Vinod C., and Ashwini K. Bendiganavale. "Infrared Reflective Inorganic Pigments." *Recent Patents on Chemical Engineering*, vol. 1, no. 1, Sept. 2010, pp. 67–79.,
  - 56.) Pyć Wioleta Agata. *Field Performance of Epoxy-Coated Reinforcing Steel in Virginia Bridge Decks*. Virginia Polytechnic Institute and State University, 1998.
  - 57.) Vaca-Cortes, Enrique, et al. Adhesion testing of epoxy coating. *Conducted for the Texas Dept. of Transportation by the Center for Transportation Research Bureau of Engineering Research*, The U. of Texas at Austin, 1998.
  - 58.) Toubia, Elias, and Sadra Emami. *Performance Comparison of Structural Steel Coating Systems*. The Ohio Department of Transportation, Office of Statewide Planning & Research, 2016, Performance Comparison of Structural Steel Coating Systems.
  - 59.) Vinik, Paul, *Successful Preservation Practices For Steel Bridge Coatings*. Scan Management, 2016, Successful Preservation Practices For Steel Bridge Coatings.
  - 60.) Petrie, Edward M. *Adhesion & Bonding*. Metal Finishing, vol. 107, no. 10, 2009, pp. 48–50.,
  - 61.) Lambourne, R., and T. A. Strivens. Paint and Surface Coatings: Theory and Practice. Woodhead Publishing, 2004.
  - 62.) Sunkara, Vijaya, and Yoon-Kyoung Cho. "Investigation on the Mechanism of Aminosilane-Mediated Bonding of Thermoplastics and Poly(Dimethylsiloxane)." *ACS Applied Materials & Interfaces*, vol. 4, no. 12, Dec. 2012, pp. 6537–6544.,
  - 63.) Momber, A. W., S. Koller, and H. J. Dittmers. "Effects of surface preparation methods on adhesion of organic coatings to steel substrates." *Journal of Protective Coatings and Linings* vol. 21 issue 11 (2004).
  - 64.) Poon, Jeffrey, et al. "Characterizing Surfaces of Garnet and Steel, and Adsorption of Organic Additives." *Langmuir*, vol. 34, no. 26, Nov. 2018, pp. 7726–7737.,
  - 65.) Baek, Yun Ho, et al. "NACE International 2009." NACE International, *Reliability on Coating Pull-Off Adhesion Strength Test*, 2009.
  - 66.) Toubia, Elias Anis and Emami, Sadra, "Experimental Evaluation of Structural Steel Coating Systems" (2016). Civil and Environmental Engineering and Engineering Mechanics Faculty Publications. Paper 22
  - 67.) Ramezanzadeh, B., et al. "The Effects of Addition of Poly(Vinyl) Alcohol (PVA) as a Green Corrosion Inhibitor to the Phosphate Conversion Coating on the Anticorrosion and Adhesion Properties of the Epoxy Coating on the Steel Substrate." *Applied Surface Science*, vol. 327, 2015, pp. 174–181.,
  - 68.) Maciejewski, J. (2015). The Effects of Sulfide Inclusions on Mechanical Properties and Failures of Steel Components. *Journal of Failure Analysis and Prevention*, Vol.15 Issue 2, 169-178.
  - 69.) Luo, S., Wang, B., Wang, Z., Jiang, D., Wang, W., & Zhu, M. (2017). Morphology of Solidification Structure and MnS Inclusion in High Carbon Steel Continuously Cast Bloom. *ISIJ International*, Vol. 57, Issue 11, 2000-2009.
  - 70.) Ånmark, N., Karasev, A., & Jönsson, P. (2015). The Effect of Different Non-Metallic Inclusions on the Machinability of Steels. *Materials*, Vol. 8 Issue 2, 751-783.
  - 71.) Ito, Y., Masumitsu, N., & Maysubara, K. (1981). Formation of Manganese Sulfide in Steel\*. *Transactions ISIJ*, Vol. 21

- 
- 72.) Cyril, N., Fatemi, A., & Cryderman, B. Effects of Sulfur Level and Anisotropy of Sulfide Inclusions on Tensile, Impact, and Fatigue Properties of SAE 4140 Steel. SAE International (2008).
  - 73.) Myers, A. T., et al. "Calibration of the SMCS Criterion for Ductile Fracture in Steels: Specimen Size Dependence and Parameter Assessment." *Journal of Engineering Mechanics*, Vol. 136, Issue 11
  - 74.) Campbell, Flake C., ed. *Elements of metallurgy and engineering alloys*. ASM International, 2008.
  - 75.) Fisher, John W. "Bridge fatigue guide-design and details." American Institute of Steel Construction (1977).
  - 76.) *AASHTO LRFD Bridge Design Specifications*. Washington, D.C. :American Association of State Highway and Transportation Officials, 8<sup>th</sup> Edition, 2017
  - 77.) Wang, R. (2016). *Three-Dimensional Investigations of Different Sulfide Inclusions in Steels by Using the Electrolytic Extraction Method*, Master's thesis, KTH Royal Institute of Technology School of Industrial Engineering and Management. KTH.
  - 78.) Murty, Y. V., Kattamis, T. Z., Mehrabian, R., & Flemings, M. C. (1977). Behavior of sulfide inclusions during thermomechanical processing of AISI 4340 steel. *Metallurgical Transactions A*, Vol. 8 Issue 8, 1275-1282.
  - 79.) Cloutis, Edward, et al. "Spectral Reflectance (350–2500 Nm) Properties of Historic Artists Pigments. II. Red–Orange–Yellow Chromates, Jarosites, Organics, Lead(–Tin) Oxides, Sulphides, Nitrites and Antimonates." *Journal of Near Infrared Spectroscopy*, vol. 24, no. 2, 2016, pp. 119–140.,
  - 80.) Jochen Winkler, Vincentz Network, "Chapter 1." *Titanium Dioxide Production, Properties and Effective Usage*, 2013, pp. 24–24.
  - 81.) Fang, Vivian, et al. *A review of near infrared reflectance properties of metal oxide nanostructures*. GNS Science, 2013.